Optogenetic interrogation of intercellular propagation of force signals

Artur Ruppel

THÈSE

Pour obtenir le grade de

DOCTEUR DE L'UNIVERSITÉ GRENOBLE ALPES

Spécialité : Physique pour les Sciences du Vivant

Arrêté ministériel : 25 mai 2016

Présentée par

Artur RUPPEL

Thèse dirigée par **Martial BALLAND**, Université Grenoble Alpes
et codirigée par **Thomas BOUDOU**,Chargé de Recherches, Université Grenoble Alpes

préparée au sein du **Laboratoire Laboratoire Interdisciplinaire de Physique**
dans **l'École Doctorale Physique**

Interrogation optogenetique de propagation intercellulaire de signaux de forces

Optogenetic interrogation of intercellular propagation of force signals

Thèse soutenue publiquement le **6 mai 2022**,
devant le jury composé de :

Monsieur FRANÇOIS FAGOTTO
Professeur des Universités, UNIVERSITE DE MONTPELLIER, Président
Madame MARIANNE WEIDENHAUPT
Maître de conférences HDR, GRENOBLE INP, Examinatrice
Madame ELISABETTA ADA CAVALCANTI- ADAM
Chercheur HDR, Max Planck Institute, Rapporteure
Monsieur MATHIEU COPPEY
Directeur de recherche, CNRS DELEGATION PARIS CENTRE, Rapporteur

Abstract

Cell generated forces play a major role in coordinating large-scale behavior of cells, in particular during development, wound healing and cancer. Mechanical signals based on cellular force generation propagate faster than biochemical signals, but can have similar effects, especially in epithelial tissue with tight cell-cell adhesion. However, a quantitative description of the transmission chain from force generation in a sender cell, force propagation across cell-cell boundaries, and the concomitant response of receiver cells is missing due to the lack of appropriate model systems. Here we show that such a setup can be realized by combining optogenetics and micropatterning. Our minimal system are two epithelial cells on an H-pattern ("cell doublet"). After optogenetically activating RhoA, a major regulator of cell contractility, in the sender cell, we measure the mechanical response of the receiver cell by traction force and monolayer stress microscopies. In contrast to single cells on the same pattern ("cell singlet"), whose force generation after half-activation suffers from internal flows, in the cell doublet the cell boundary suppresses global flows and leads to a stable contractile situation. Force propagation and response of the receiver cell strongly depends on the actin organization in the sender cell, which we control by the aspect ratio of the H-pattern. Thus both cell-cell boundary and organization of the sender cell are essential for stimulation of the receiver cell. We quantify the active response of the receiver cell by comparing it with the passive response calculated with a mathematical model. We find that the response essentially matches the signal strength of the sender cell, and that it is the stronger the more organized the actin cytoskeleton is perpendicular to the direction of the cell-cell boundary, reminiscent of the Poisson effect in passive material. We finally show that the same effects are at work in small tissues. Our work demonstrates that cellular organization and active mechanical response of tissue is key to avoid global actin flows and to generate an elastic response that can lead to long-range mechanical signaling across the tissue.

Résumé

Les forces générées par les cellules jouent un rôle majeur dans la coordination de leur comportement à grande échelle, notamment au cours du développement, de la cicatrisation et du cancer. Les signaux mécaniques se propagent plus rapidement que les signaux biochimiques, mais leurs effets peuvent être similaires, notamment au sein des tissus épithéliaux avec une forte adhésion cellule-cellule. Cependant, une description quantitative de la chaîne de transmission (de la génération de forces dans une cellule émettrice se propageant via les jonctions entre cellules, à la réponse induites des cellules réceptrices) manque en raison de l'absence d'outils permettant un bon contrôle spatio-temporel de la force. Nous proposons ici un modèle minimal de deux cellules épithéliales sur un motif en H ("doublet cellulaire"). Après l'activation par optogénétique de RhoA, un régulateur majeur de la contractilité cellulaire, la cellule émettrice se contracte. Nous mesurons ensuite la réponse mécanique de la cellule réceptrice par microscopie des forces de traction et contrainte de monocouche. On observe que la propagation de la force ainsi que la réponse de la cellule réceptrice dépendent fortement de la polarisation mécano-structurelle de la cellule émettrice, que nous contrôlons par le rapport d'aspect du motif en H. Nous constatons que la réponse de la cellule réceptrice est plus forte lorsque l'axe de polarisation mécano-structurelle est orienté perpendiculairement à la direction de propagation de la force, ce qui rappelle l'effet de Poisson dans les matériaux passifs. Nous montrons finalement que les mêmes effets sont à l'œuvre dans les petits tissus. Ainsi, nos travaux démontrent que l'organisation cellulaire et la réponse mécanique active d'un tissu sont essentiels pour maintenir la force du signal et conduisent à l'émergence de l'élasticité, ce qui signifie que les signaux ne sont pas dissipés comme dans un système visqueux, mais peuvent se propager sur de grandes distances, comme dans un système élastique.

Acknowledgments

First and foremost, I want to thank Martial, my mentor over the last four years. I met you as my teacher in the final year of my undergraduate studies and I consider this to be one of the most fortunate moments of my life. Your approach to teaching and science has been, and continues to be, truly inspirational and has instantly made me want to work with you. Moreover, your field of research combines my shared passions for physics and biology, an area of research that I was not even aware of. Fortunately, you have willingly welcomed me into your team and have guided me throughout this PhD journey. You always put my interests before yours, gave me all the freedom that I could wish for and enabled countless opportunities for me to grow as a scientist and as a person and for that I will always be grateful.

Next, I want to thank Thomas, my co-supervisor. Your rigorous approach to science and your strong technical expertise have been invaluable in carrying out this work. You were always there when I needed help to define experiments, to prepare a conference, to analyze data, to discuss results and anything else I needed guidance with. I think that you and Martial differ in many ways in your approach to science and therefore your advice and support were complementary to Martial's, which makes you a great team in my opinion. Thank you so much for all that.

I also want to thank Giovanni, the third and last permanent member of the MicroTiss team. You were not officially my supervisor and yet you followed my work quite closely, helped with revising the manuscript, discussing ideas and giving career advice. Thanks a lot for that.

Special thanks go out to Vanni, former PhD student in the team. You taught me many of the experimental skills that I needed for this work. You always took the time to answer my endless question and your great sense of humour always made lunch and coffee breaks very pleasurable.

Thanks also to Vladimir, a new PhD student in the team. I had a great time showing you how to do the experiments I do, and you learned so fast that you quickly became a great help in finalizing this work. Thank you for your motivation and your investment!

A big thank you also to Ulrich and his PhD student Dennis, my primary collaborators from Heidelberg. They developed all the theory here presented and their

insights were crucial in accomplishing this work. Especially with Dennis I spent countless hours discussing physics and working out problems and I can't imagine having accomplished this work without you. Working with you was such a great experience and I hope we can continue our collaboration in the future. Discussing physics with you is always a lot of fun and I learned so much in doing so.

I also want to thank the jury members François, Marianne and particularly the reviewers Elisabetta Ada and Mathieu for taking their time to read and review my work and to give me so much valuable feedback. All of you had a significant impact on me during my scientific and personal journey and I am very glad that you accepted my invitation to be part of this jury.

On a more personal note I want to thank Adrien. You were one of the very first people I met here in France, and you instantly made me feel welcomed in this country. We quickly became friends and shared not only work and studies, but also drinks and climbing.

Thank you also to Maxime. Sharing an office with you was a lot of fun and your background as an architect always gave a fresh, new, and interesting perspective on things.

Final thanks go out to the people who are the closest to me in my life. Saire, you are the best that has ever happened to me. You supported me emotionally when I needed it, you motivated me when I felt like quitting, you listened to my complaints when things weren't going well, you were the first person I shared my excitement with when things were going well. I cannot imagine having done this without you and I am truly grateful for having you by my side. Und natürlich meine lieben Eltern. Nur dank euch konnte ich studieren gehen, nach Frankreich ziehen und meine Träume verfolgen. Ohne eure bedingungslose Unterstützung wäre nichts davon möglich gewesen. Worte können nicht ausdrücken, wie dankbar ich für euch bin. Und natürlich auch an meinen Bruder Derek. Ich hoffe dass wir trotz der Entfernung den Kontakt zueinander weiterhin beibehalten werden und unsere Lebenserfahrungen miteinander teilen können.

Contents

1 A physics approach to study living systems **1**

1.1 Signalling function of mechanical forces in living systems 4

1.1.1 Forces drive morphogenesis and play a role in its regulation 5

1.1.2 The force generating mechanisms - The actomyosin network 9

1.1.3 The interfaces for mechanosensing - Focal adhesions and adherens junctions 13

1.1.4 Translating mechanical signals into behavior - Mechanotransduction 16

1.2 Building up scale: From single cells to simple multi-cellular assemblies 20

1.2.1 The basic building block - single cells 21

1.2.2 The simplest multicellular assembly possible - Cell doublets 26

1.2.3 Increasing complexity: 2D monolayers and small 3D tissues 29

1.3 Basic idea of my PhD project 32

2 Tools to study intercellular communication through forces **33**

2.1 Traction force microscopy to measure mechanical activity of cells . 33

2.1.1 Displacement field measurement methods 35

2.1.2 Traction force field calculation 39

2.1.3 Cell stress calculation 42

2.1.4 Implementation of the whole analysis pipeline 44

2.1.5 Strategies to improve certain aspects of TFM 49

2.1.6 Applications of TFM outside of cell biology 50

2.2 Optogenetics to modulate cell signalling pathways 53

2.2.1 Optogenetic manipulation of RhoA, major regulator of cell mechanical activity 55

2.2.2 New optogenetic tools to modulate cell contractility 59

2.2.3 Other applications of optogenetics 60

2.3 Micropatterning to impose geometrical boundary conditions on cells 62

2.3.1 Micropatterning to study single cell morphogenesis 64

2.3.2 Micropatterning to study collective cell behavior 65

2.3.3 Micropattern fabrication methods 67

3 Results & discussion **71**

3.1 Optimizing the experimental conditions 72

3.1.1 Substrate rigidity and pattern size 73

3.1.2 Seeding density and incubation time 75

3.1.3 Activation pulse duration and frequency 76

3.1.4 Activation pulse power and activation area 78

3.1.5 Pattern geometry 81

3.1.6 Discussion 82

3.2 Force propagation across cell boundaries depends on actin organization 84

3.2.1 Introduction 86

3.2.2 Results 88

3.2.3 Discussion 104

3.2.4 Materials & Methods 106

3.2.5 Author contributions 111

3.2.6 Acknowledgements 112

3.3 Cell doublets to understand cell-matrix vs. cell-cell adhesion in other contexts 112

3.3.1 Cell doublets of mesodermic *Xenopus* stem cells 114

3.3.2 Cell doublets to decipher the role of EpCAM in breast cancer cells 115

3.3.3 Discussion 117

4 Future perspectives **119**

5 Annex **143**

5.1 Theory supplement 143

5.2 Protocols 163

1. A physics approach to study living systems

Living systems are by far some of the most complex systems one can encounter in the world around us. Living system show complex structure and behavior across multiple length scales; from the micron-sized bacterium, containing thousands of genes coding for proteins that create a complex network of chemical reactions, able to catabolize nutrients to extract energy and raw material from the environment and able to metabolize these to create more copies of oneself, up to the meter-sized human, able to reason about its own existence and to create civilizations that span the whole globe. Although we came a long way in understanding these immensely complex structures, from developing the theory of evolution by natural selection, over the discovery of the cell, to the discovery of DNA, "the heritage molecule", we are still far away from a firm understanding of all the details that explain how life works.

But why has a deep understanding of life been so elusive up to date? There are of course many possible explanations. Here is my attempt of pinning down the main reasons:

First, living systems are highly ordered structures across many length scales. It ranges from the nanometer scale of molecules to the meter scale of some animals and plants. There is no obvious periodicity or higher meta structure that we could exploit to accurately describe the whole system in all its detail on all the different scales. Instead, we have very intricate and incredibly complex structures, that have to be intensely studied on all those different length scales, just in order to accurately *describe*, let alone understand them. Current efforts focus on building theories that explain living systems on a given length scale. Bridging the explanatory gap in between those theories is one of the major future challenges.

Second, living systems self-assemble. It is one of the great mysteries of science up to date: How do these complex structures develop without the external guidance of a creator of some sorts? Or in other words, how can local, short-scale rules lead to coordinated behavior on much larger scale? And how can they robustly do so in so many different environments? These are very challenging questions and we are only beginning to answer them.

Third, living systems show emerging properties on different length scales, due to the incredible interconnectivity of its constituent elements [1]. On top of that, these complex networks span several length scales themselves: On the lower end of the scale we have organelles in a cell, which form a complex network of metabolic and reproductive machinery, constantly transforming external chemicals into heat and more molecules of themselves. On the upper end of this scale, we have billions of specialised cells in a brain, all of them having their own set of metabolic and reproductive machinery, somehow interconnecting in a way leading humans to make art, form societies and explore the universe. Understanding how these properties of networks emerge from the action of its constituent elements has proven to be a central open question in science today, with important implications to fields as diverse as neuroscience, computer science or biology at large [1].

To address this multiplicity of challenges, scientists have employed many different concepts, originating in many different fields of research, such as physics, chemistry, computer science, engineering or architecture. This makes the modern study of living systems inherently interdisciplinary and more and more interdisciplinary approaches will be needed to get a fuller understanding of life.

One angle of approach that has been emerging recently is that of mechanobiology. It studies the mechanical properties of cells and their environment and how they relate to their behavior. One of the first key discoveries, was that mechanical properties of the cells' environment can have a pivotal impact on key cellular processes such as apoptosis or differentiation [2, 3]. With it came the realisation that cells constantly probe the mechanical properties of their environment, which they do by exerting well defined forces onto said environment and evaluating the impact of that force. These mechanisms have been shown to not only probe the external environment, but also as a means of regulating, coordinating and driving

[1] This feature is not unique to life, but seems to be a property of complex networks in general

large-scale collective behavior such as in morphogenesis [4].

In our lab we are interested in this specific aspect of cell generated forces: How cells use them to coordinate their behavior across length scales, or in other words, how cells use forces to communicate with each other. The precise question that I try to address in this work, is: How are cell-generated, mechanical signals transmitted to the surrounding cells and how do those signals influence the behavior and structure of the surrounding cells?

In the team, we try to address this question on multiple length scales, ranging from single cells to simple, multicellular, matrix-embedded systems. By doing so, we hope that we will be able to pin down which properties exactly emerge from the interconnectivity of the network and which can be understood by understanding the elements in the network.

In this specific work we try to understand intercellular, mechanical communication on the smallest scale imaginable: Cell doublets. We use a novel tool, optogenetics, to induce a transient contraction of one of the cells, generating a mechanical signal. We then use live traction force microscopy and live immunofluorescence imaging coupled with image processing tools to analyse how the structure of the system and its contractile state evolve over time in response to that perturbation. Finally we use micropatterning to control (to some extent) and to systematically vary some of its' key structural parameters, and to study their effect on intercellular, mechanical communication.

Before trying to understand something new, we have to understand what is already known first. We will therefore start with a short review of the existing literature in the field. The challenge here is of course to be as detailed and comprehensive as possible without losing the overview. In an attempt to do so, I will first talk about some general notions of mechanobiology. How cells generate forces, how they sense and how they transduce those signals into behavior. I will then review some studies on the mechanical properties of cells and multicellular assemblies, with a focus on the length scales around where this project is situated; From single cells to simple multicellular assemblies.

1.1 Signalling function of mechanical forces in living systems

Complex processes such as migration or morphogenesis can only robustly take place as a consequence of tightly regulated feedback networks. Most research until recently focused on biochemical regulatory networks, but it has become apparent that mechanical feedback networks also play an important regulatory role [4–6]. Figure 1.1 shows the cell as a signal processing network. The regulatory feedback networks that control the cell are numerous and implicate many different structures, such as the nucleus, focal adhesions or the cytoskeleton.

To understand a signal processing system, we need to look at how signals are generated, how they are sensed at interfaces and how they are translated into an output. These three key points will be illustrated in the following chapters.

Furthermore, forces also drive cellular processes. Whenever cells move or change shape, forces are necessarily implied in the process. The importance of forces in regulating and driving biological processes is best illustrated with one of the most puzzling and complex processes in biology: Morphogenesis.

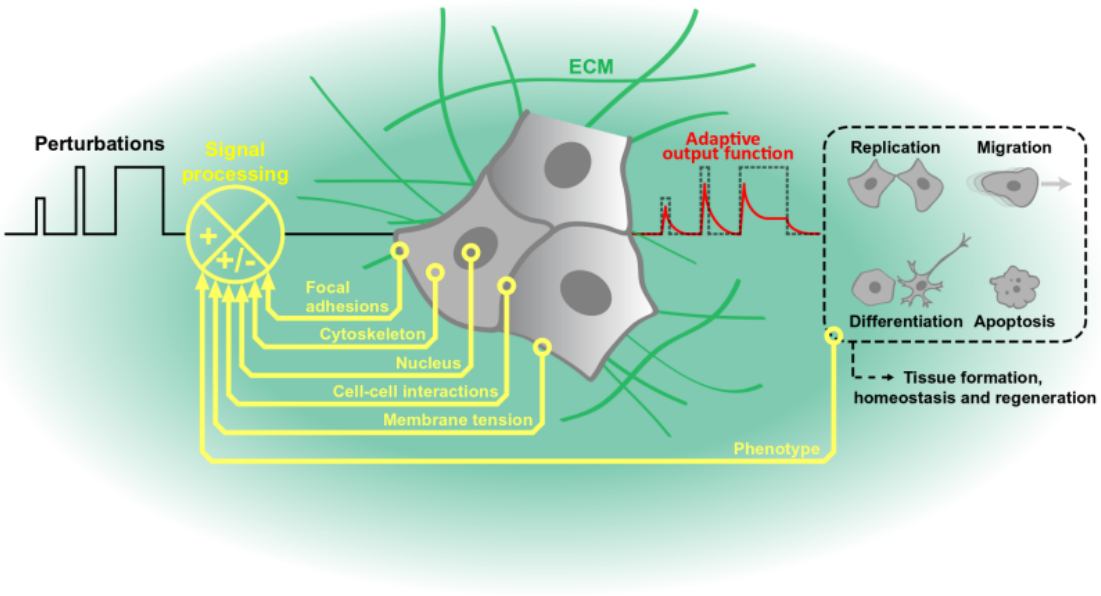

Figure 1.1: Simple multicellular assembly schematized as signal processing system. The cell integrates external perturbations and regulates its behavior in response to those through many different positive and negative feedback loops. Taken and modified from [5]

1.1.1 Forces drive morphogenesis and play a role in its regulation

During the development of an organism, cells constantly rearrange, change shape and migrate. From this observation alone, one can conclude that cells have to exert forces on their environment to drive these processes. Thus, measuring forces *in vivo* in a developing organism has been of great interest to scientists, which has proven to be quite challenging. One approach to tackle this issue consists of analysing movement of timelapse image data and using mathematical models to infer a possible set of equivalent driving forces for the observed movement. The method is called *Video Force Microscopy* and has been used by Brodland et al. to characterize forces that drive ventral furrow formation in *Drosophila* embryos [7].

Figure 1.2 (a) shows a cartoon of a cross-section of an early *Drosophila* embryo. Figure 1.2 (b) A-F show a series of images during ventral furrow formation with fluorescently labelled myosin II [2], allowing to track the deformation of the embryo. Figure 1.2 G-L show a force map that accounts for the measured deformations. One can appreciate for example how ventral furrow formation seems to be primarily driven by apical constriction of mesodermic cells.

Although this method does not allow for an estimation of absolute forces and relies on certain assumptions on the material properties of the tissue, it allows to give an overview of relative forces needed to drive observed deformations. Combining this approach with genetic modifications of the embryo and correlating calculated forces with expression levels of certain proteins, such as myosin II, makes for a powerful tool to study how forces drive tissue formation in development.

The way local contractile forces in subparts of the embryo account for key morphogenetic processes has since been impressively demonstrated by Izquierdo et al. [8] in a recently published work on tissue invagination in *Drosophila* embryos. They used an optogenetic tool, which allows to locally and transiently activate RhoA [3] through the use of light. Using this tool, they showed that local activation of RhoA on the apical surface of the tissue is sufficient to drive tissue invagination, but does not account for closure of invaginations into tubes. Additional, lateral

[2] Myosin II is the main motor protein responsible for force generation in non-muscle cells. For more detail, see subsection 1.1.2

[3] RhoA is an important signalling protein that induces, among other things, cell contraction. For more information about RhoA and optogenetics, see section 2.2

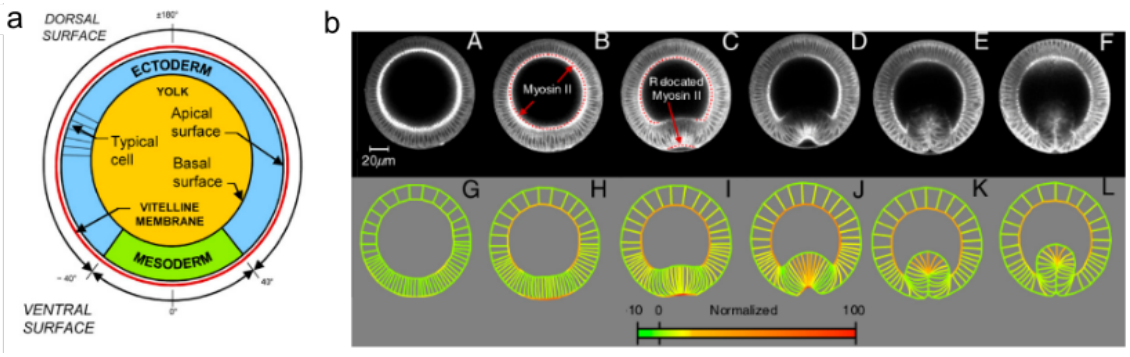

Figure 1.2: (a) A cross-sectional view of an early *Drosophila* embryo. The mesoderm shown in this cartoon is the part that will form the ventral furrow. (b) (A-F) shows a series of images of a cross-section of a *Drosophila* embryo during ventral furrow formation. Myosin II is fluorescently labelled to visualise cells and analyse correlation with calculated forces. (G-L) show a force map in arbitrary unit that account for the observed deformations. Taken and modified from [7].

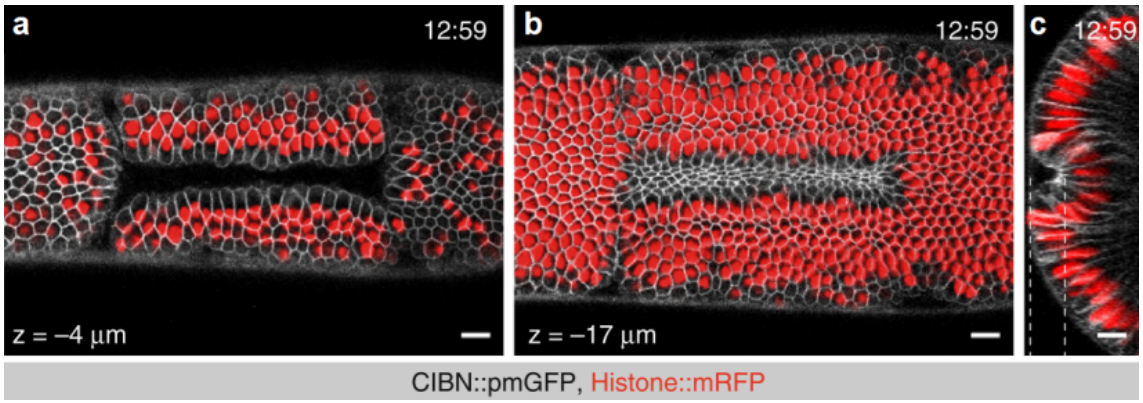

Figure 1.3: Local activation of contraction via optogenetics is sufficient to drive invagination of tissue parts that would not otherwise invaginate in *Drosophila* embryos. (a) and (b) show a confocal image of the tissue at different heights and (c) shows a cross-sectional view of the tissue. The membrane is shown in white and the nucleus in red. Taken from [8]

forces are suspected to be necessary for tube closure. Figure 1.3 shows confocal images of an embryonic tissue undergoing induced tissue invagination, with a and b showing two different focal planes and c showing a cross-section view of the tissue.

These examples show, how complex patterns of cellular contraction can drive morphogenetic processes. But they leave a central question unanswered: How do these complex patterns arise in the first place? There is no central coordination center that orchestrates all these processes. Cells only sense their immediate surroundings and adjust their behavior accordingly. Yet, this seems to be sufficient to yield the vast multitude of complex shapes that we observe in living organisms. In order to understand this very broad and fundamental question of

self-organization, it might be useful to broaden ones view and look into more theoretical work.

John Conway for example, an English mathematician, famously demonstrated in his "game of life", how very simple and local behavioral rules can lead to a multitude of complex patterns. The game of life is a "zero-player computer game", meaning that it evolves autonomously, dependent only on the initial conditions. The game simulates cells in a grid that can either be dead or alive and whose survival and birth after each iteration depends only on the number of their neighbours. By using only this simple rule, one can create a multitude of "organisms" that either go extinct after a while, live an eternal, stable or oscillatory life, or show chaotic behavior.

The game of life needs distinct initial conditions to create its complex patterns though, but living systems generally develop from initially symmetrical objects [4]. The first theory that described how complex shapes can arise from initially symmetrical objects has been developed by Alan Turing in 1952 in his work "The chemical basis of morphogenesis" [9]. He describes pattern formation with *morphogens*, hypothetical molecules that are produced in the organism, diffuse through it and inhibit or stimulate each others production. Although the chemicals Turing described in his work were entirely hypothetical, he gives some examples of what a morphogen could be. Genes themselves for example can be regarded as morphogen, or hormones. Within this framework he formulates a set of coupled differential equations that describe the diffusion of these morphogens and the reactions they catalyse. The solution of these equations can yield very complex concentration patterns through amplification of small disturbances in the initial symmetry via chemical feedback loops. From these results he concludes, that these type of reaction-diffusion systems are sufficient to account for many complex shapes one encounters in living organisms.

Inspired by Turing and limited by the available tools, much focus in experimental science has been put into identifying and describing these biochemical reaction-diffusion systems that lead to pattern formation. It is worth noting that Turing mentioned in the beginning of his work the necessity to couple his theory with a theory of the mechanics of organisms to give a full account of morphogenetic

[4] This is not entirely true actually. Although most organisms start as spherical cells, often times they inherit some initial asymmetric distribution of some protein or RNA molecules, which define an initial polarity axis

processes. However, he conceded this endeavour to its complexity and the impossibility to solve the associated equations without the use of digital computers. Now, 70 years later, the process of developing a comprehensive mechanochemical theory of morphogenesis is still ongoing [10]. On the experimental side, the development of new tools to measure and manipulate the mechanics of living systems enabled scientists to recognize the importance of mechanical signals in the regulation of morphogenetic processes.

For example, Desprat et al. highlighted in a study on *Drosophila* embryos the implication of compressive forces on the regulation of Twist expression, a transcription factor protein that regulates cell differentiation early on in the developing embryo [11]. They observed a correlation between compressive forces, exerted by cells during germ band extension, and the up-regulation of Twist expression in stomodeal cells[5] (Figure 1.4). The upper row shows the embryo before initiation of germ band extension and the bottom row shortly after. Column a and b show the nuclei of the anterior part of the embryo. The authors performed particle image velocimetry (PIV) analyses on those images to obtain the deformation map shown in column c and d. Column e and f shows the Twist expression pattern in the embryo and the red arrows indicate the position of stomodeal cells. From these experiments the authors observed that Twist expression and compressive forces both increase during germ band extension in stomodeal cells.

In order to find out if the compressive forces in stomodeal cells are what causes the up-regulation in Twist expression, the authors conducted following experiments: First, they laser-ablated the ventral part of the embryo that causes the compression of stomodeal cells. They performed the same analyses as described above and observed that this process removes both compression and Twist expression in stomodeal cells (see Figure 1.5 A). Next, they used two different methods to restore compressive forces in stomodeal cells. They used a micro-manipulated needle to manually compress stomodeal cells (Figure 1.5 B), which rescued high Twist expression in those cells, as in unmanipulated embryos. For the second method, shown in Figure 1.5 C, they injected magnetic microbeads into the embryo right before cellularization [6]. They used an electro-magnet to move the beads to an area

[5] Precursor cells of the mouth and the fore-gut

[6] Cellurization is a process that happens very early in the development of *Drosophila*. After fertilization, the nucleus divides rapidly, but without compartmentalization into seperate cells. After 13 cell cycles, membranes form simultaneously around all the nuclei.

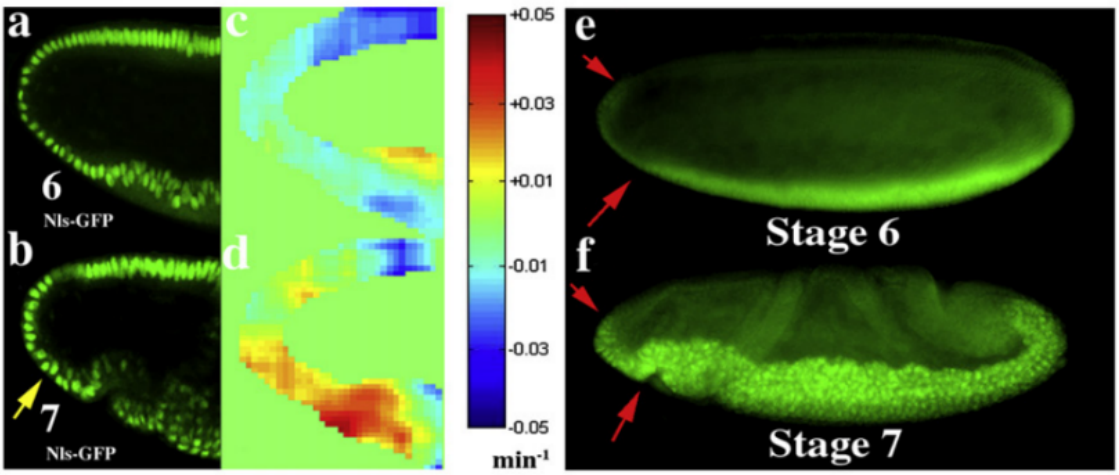

Figure 1.4: The top row shows a *Drosophila* embryo right before germ band extension and the bottom row right after the onset of germ band extension. (a) and (b) show the nuclei of cells in the anterior part of the embryo. (c) and (d) show the results of PIV analysis on those images, showing areas of compression in red and extension in blue. (e) and (f) show Twist expression levels in the embryo, the red arrows show the position of stomodeal cells. Taken from [11].

close to the stomodeal cells, trapping the beads in this part of the embryo after the cellurization process is completed. They then used a magnetic tweezer to push this part of the embryo against the stomodeal cells, effectively recreating a situation close to germ band extension as it happens normally during development. They observed that this process also rescued high Twist expression levels in stomodeal cells. From these experiments the authors concluded that compressive forces exerted during germ band extension are the primary cause for Twist expression in stomodeal cells.

These examples show that cells both react to mechanical cues and adjust their behavior to them, and also exert forces themselves in order to drive morphogenetic events and in order to feel and measure the properties of their surrounding. Thus, in order to understand how cellular forces drive morphogenesis and how cells feel their environment, one also has to understand how cells are able to exert forces in the first place.

1.1.2 The force generating mechanisms - The actomyosin network

The actomyosin network is one of three networks that make up the cytoskeleton. Alongside microtubules and intermediate filaments, it defines the mechanical

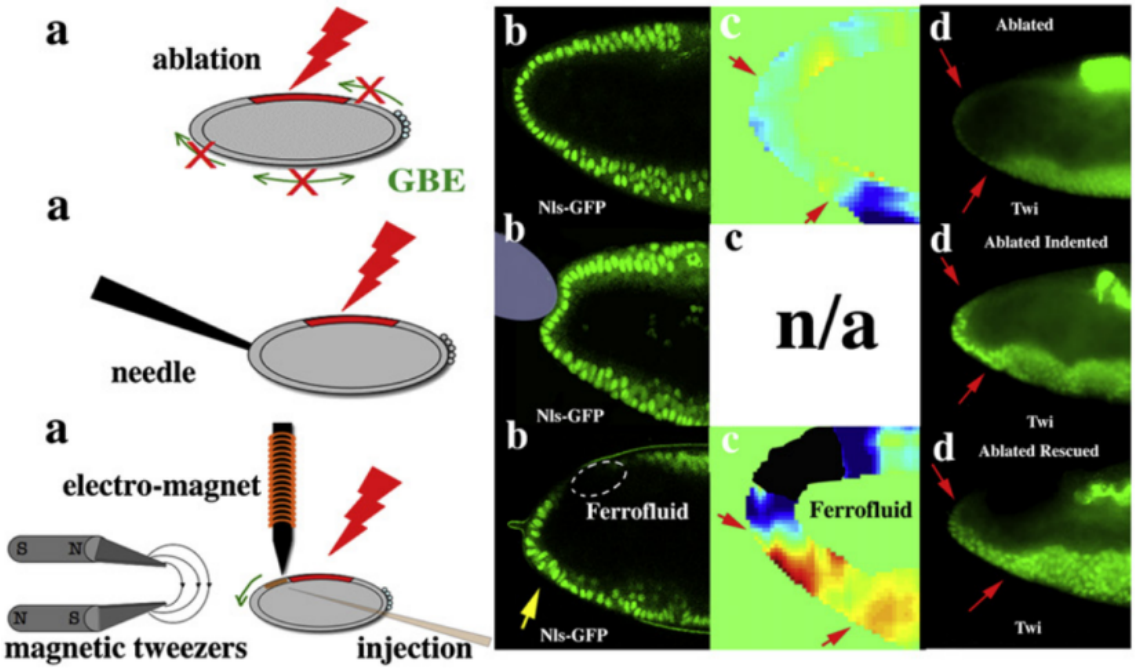

Figure 1.5: Each row shows a separate experiment. In all three experiments, the ventral part of the tissue that is responsible for compression of stomodeal cells is removed. (a) shows a schematic of the conducted experiment. All panels in (b-d) show the anterior end of the embryo, with (b) showing the nuclei, (c) showing tissue deformation analysed with PIV and (d) showing *twist* expression levels. Taken from [11].

properties of the cell, defines its structure, organises molecule transport, coordinates motility and much more [12].

All three filaments are polymers, made out of protein monomers. Their structure and some basic properties are shown in Figure 1.6. An example fluorescence image of each network in fibroblast cells is also shown.

With a diameter of 25 nm, microtubules are the thickest and least flexible of the three filaments. With a persistence length [7] of several millimetres, they behave like rigid rods across the scale of the cell. Microtubule filaments are polar, meaning that one end of a filament behaves differently from the other. This property makes it possible for molecular motors to move along the filaments with a preferential direction. In the case of microtubules, these motors are from the kinesin and dynein family and are for example responsible for vesicle transport in the cell. Another major function of the microtubule network is the segregation of chromosomes during mitosis.

With a diameter of 8 nm to 12 nm, the size of intermediate filaments is, as the name suggests, in between microtubules and actin filaments. They have a

[7] A measure for flexibility. It denotes the length below which a filament behaves like a rigid rod

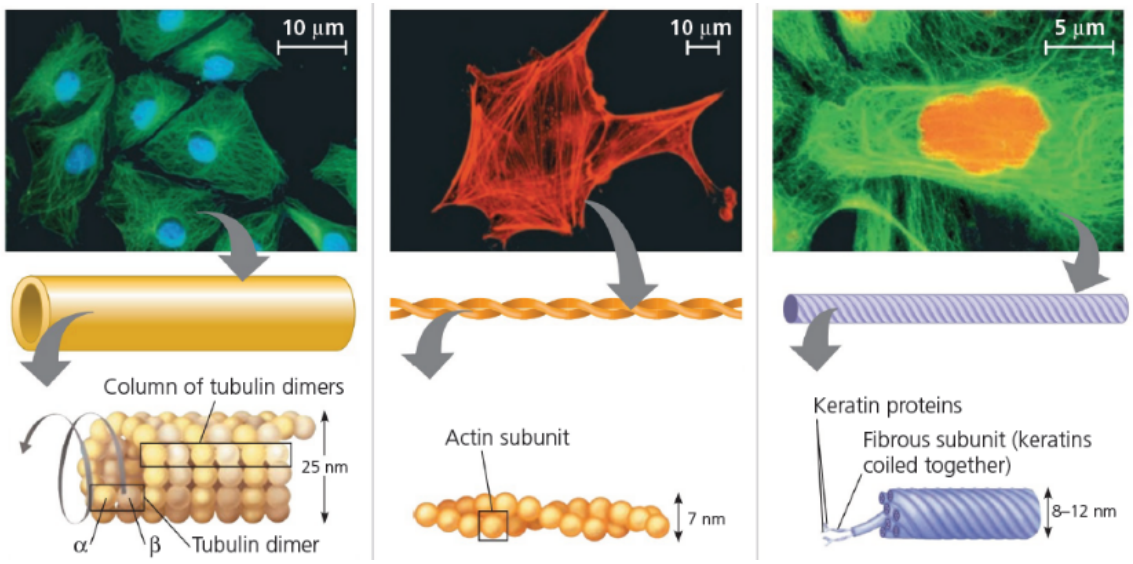

Figure 1.6: The top row shows an image of fluorescently labelled microtubules (left), actin filaments (center) and intermediate filaments (right) in fibroblasts. The nucleus is also labeled in blue in the left and in red in the right image. The bottom row shows a cartoon of the structure of the respective filaments. Microtubules (left) are hollow tubes, composed out of α and β tubulin dimers. Actin filaments (center) are composed of a single monomer, actin, and it forms a double-helical structure. Intermediate filaments are made out of a single type of protein from a large family of proteins, which coil into large suprafilaments. Taken from [13]

persistence length of 0.5 μm and are the most flexible of the three filaments. They are the only non-polar filament type and thus do not bind any motor proteins. They are very resistant to tensile forces and are mostly responsible for mechanical stability of the cell.

With a diameter of 7 nm, actin filaments are the thinnest filament of the three. They have a persistence length of 13.5 μm and are thus semi-flexible at the scale of the cell. Like microtubules, actin filaments are polar and they bind molecular motors which are called myosin, with myosin II being the main protein for contraction in non-muscle cells. The actomyosin network is the main force generating machinery in the cell. As such, it plays a major role in defining the cells shape, in muscle contraction, in the cell's sensing of the mechanical properties of its environment, in cell migration, in cytokinesis and much more. For these reasons it has been subject of extensive research in the field of mechanobiology and is thus the main focus of this section.

Myosin II is also a polar protein, like actin. One of its ends contains two globular units, which serve as "legs" that can "walk" on actin filaments. Myosin II assembles into dipolar minifilaments that bind anti-parallel actin filaments. This

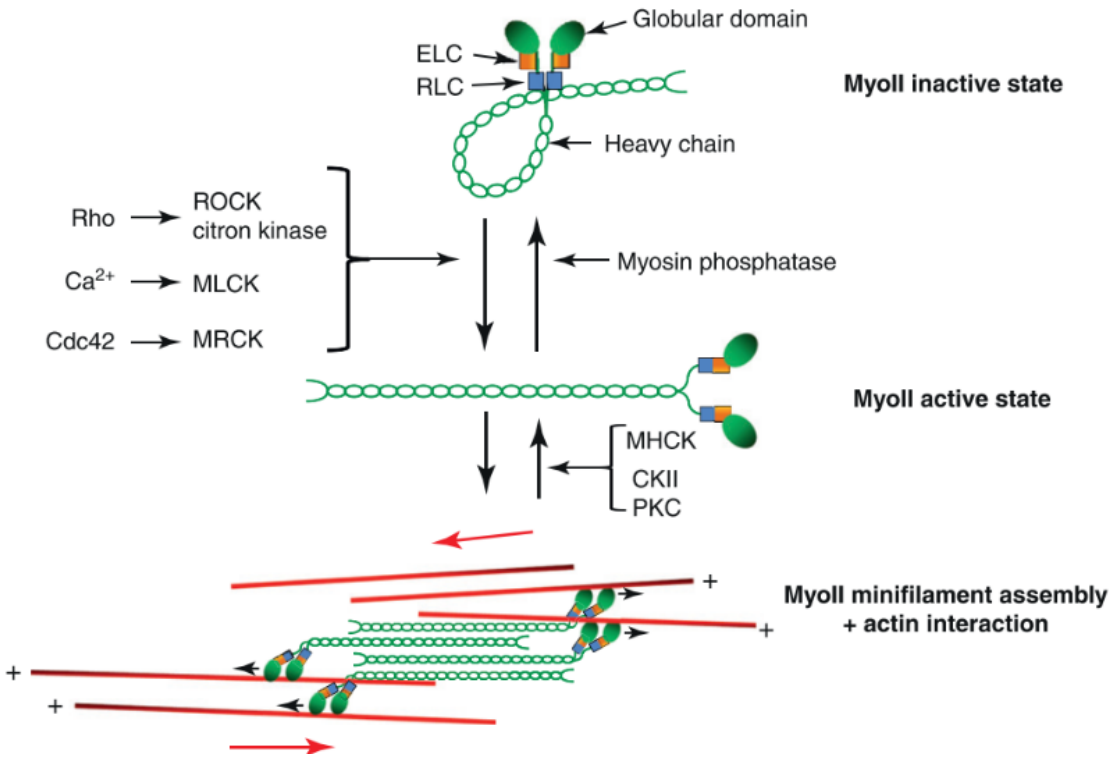

Figure 1.7: The top cartoon shows myosin II in its inactive state. Myosin II is a hexamer with two identical sub-units. Each sub-unit is composed of one heavy chain, which ends in a globular domain and two light chains: The essential and the regulatory light chain (ELC and RLC). The RLC can be phosphorylated by several different kinases, leading myosin II to change its conformation to the active state. Phosphorylation of the heavy chain then enables assembly to bipolar minifilaments. These minifilaments then associate with anti-parallel actin filaments and move along them, thus exerting contractile forces. Taken from [14].

way, they exert opposing forces onto the actin filaments, creating a contractile element, if the actin filaments are attached somewhere. Figure 1.7 shows a cartoon of the structure of myosin II and the biochemical pathways that control its activation, its assembly into minifilaments and its interaction with actin filaments. The formation of contractile actomyosin filaments takes place in two steps: Phosphorylation of the regulatory light chain (RLC) by several kinases activates myosin II and phosphorylation of the heavy chain controls its assembly into minifilaments [14].

The interactions between actin and myosin alone are not sufficient to account for the enormous variety of shapes encountered in cells. Many different proteins are known to interact with actin and modulate its behavior in numerous ways. It includes nucleation factors, which catalyse the formation of new filaments, cross-linking proteins, which form connections in between filaments, adaptor proteins, which attach filaments to the cell periphery, capping proteins which regulate the

length of the filaments and many more. The kind of structures it forms can broadly be categorised into filamentous, as in stress fibers or filopodia, and mesh-like, as in the lamellipodium or the actin cortex. Figure 1.8 shows a schematic of a migrating cell and how the actomyosin network is structured inside, with a selection of the most important implicated binding partners [15].

This contractile actomyosin network is essential for the cell to be able to probe the mechanical properties of its environment. However, it is not sufficient by itself; the cell needs to interface this network to the outside environment. This is the role of cell-cell and cell-substrate adhesions.

1.1.3 The interfaces for mechanosensing - Focal adhesions and adherens junctions

Cells need to be able to adhere to each other and to the extracellular matrix in order to form mechanically coherent tissues - if they didn't, they would just be a loose collection of cells and multicellular organisms could never form. There are two main types of adhesion in cells: Cell-cell adhesions and cell-extracellular matrix (ECM) adhesions. The role of these adhesion sites is not only to ensure the mechanical integration of a cell into its environment, they are also an important signal processing hub, which enable the cell to integrate information of the chemical, geometrical and physical properties of its environment into its behavior. There are numerous types of cell-cell junctions, like adherens junctions, tight junctions, gap junctions or desmosomes, as well as numerous types of cell-ECM adhesion structures, like focal adhesions, podosomes or fibrillar adhesions. Here we will focus on focal adhesions and adherens junctions, since they are, in our current understanding, the most ubiquitous and important sites of mechanosensing.

Both adherens junctions and focal adhesions have been shown to grow in response to externally applied force [16, 17], which is direct evidence for the cell's ability to sense and respond to forces. This self-fortifying properties enable the cell to adapt to a high variety of mechanical environments. Focal adhesions and adherens junctions are not only subject to external forces, they are also under self-generated tension. This tension is generated by the actomyosin network and is transmitted to the adhesion sites via adaptor proteins.

Central to all types of cell adhesions are trans-membrane adhesion proteins.

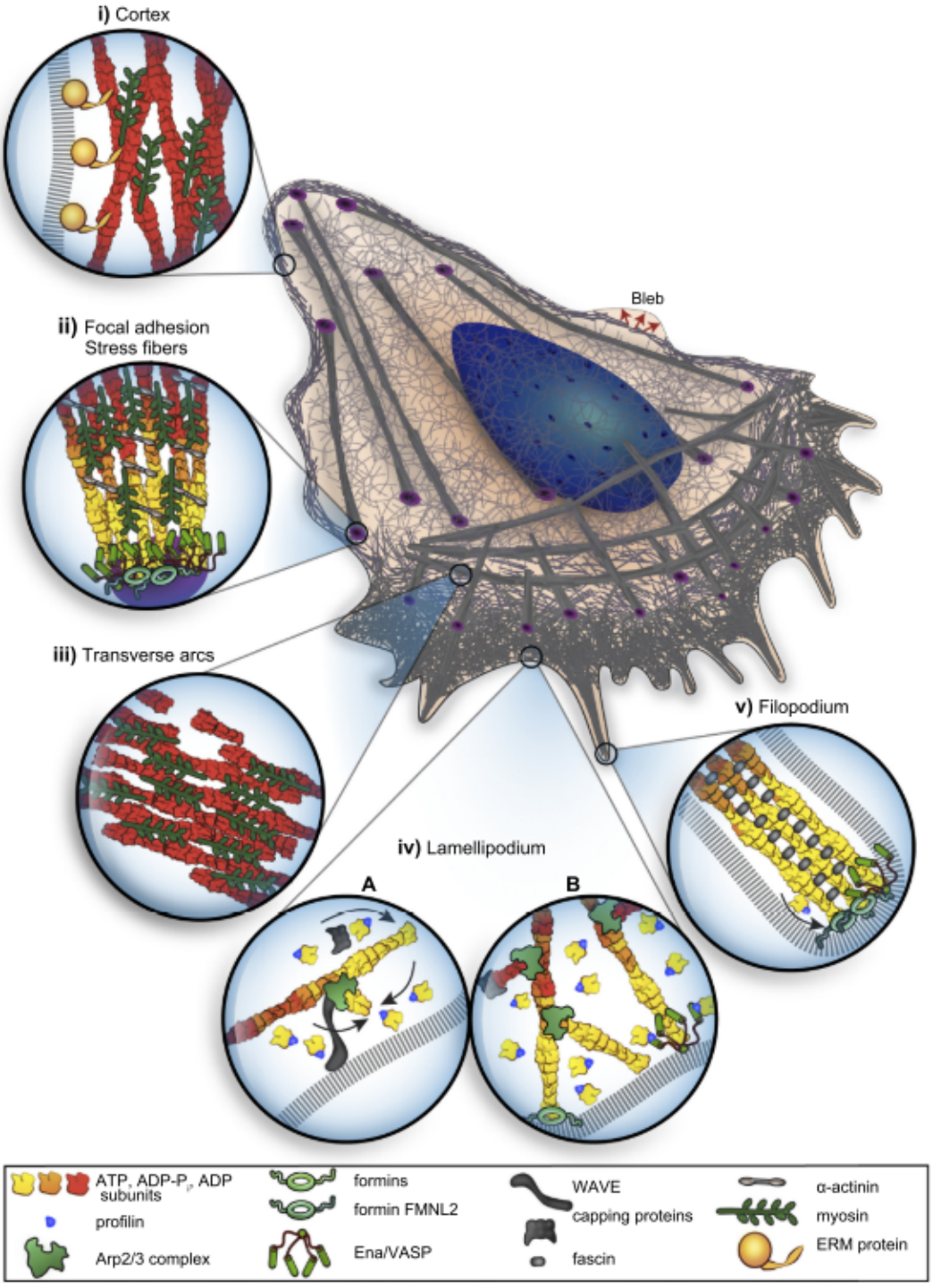

Figure 1.8: Actin and the numerous proteins modulating its assembly into polymers to form a variety of different structures. They form a dense, contractile mesh that attaches to the cell membrane, giving the cell stability and putting the membrane under tension. They form large contractile stress fibers, which are attached to the extracellular matrix through focal adhesions. Migrating cells form lammelipodia on their leading edge, where the cell pushes the membrane forward by assembling the lamellipodium against the cell membrane. They form transverse arcs, which are stress fibers that are not directly linked to focal adhesions but serve as attachment point for other stress fibers. They also form non-contractile fibers like filopodia, which are extensions used to sense the environment. Taken from [15]

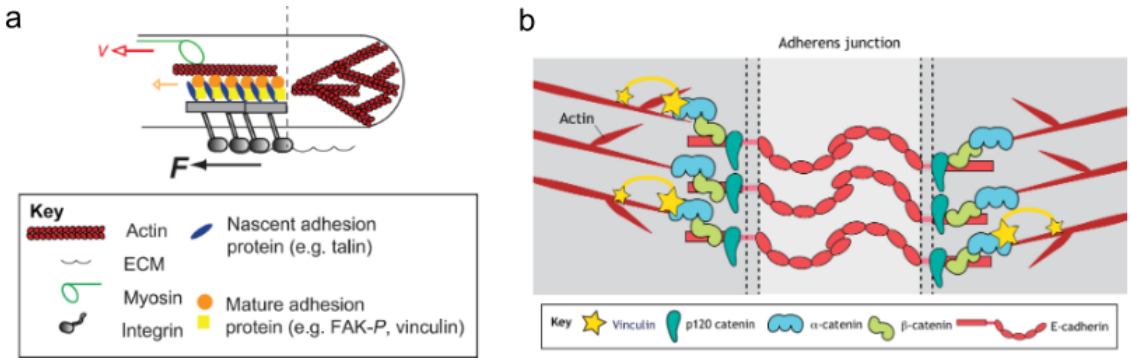

Figure 1.9: (a) Focal adhesions form at the boundary between lamellipodium and lamella of a spreading or migrating cell. Integrins bind to the ECM in a force-dependent manner outside of the cell and adaptor proteins like talin or vinculin connect them to the actomyosin network. Taken and adapted from [18]. (b) The extracellular domain of E-cadherins, the cadherin isoform of epithelial cells, attach to E-cadherins of neighboring cells to initiate adhesion. The cytoplasmic domain then binds to adaptor proteins like catenins or vinculin which then in turn binds to the actomyosin network. Taken and adapted from [19].

The main ones in focal adhesions are called integrins and the main ones in adherens junctions are called cadherins. Their extracellular domain interacts with their counterpart to form a mechanical bond. Those counterparts are for example other cadherins for adherens junctions or fibronectin for focal adhesions. The cytosolic part of those adhesion proteins then binds to the actomyosin network through several adaptor proteins like talin, vinculin or cathenins. A cartoon for the basic structure and the main proteins involved in focal adhesions and adherens junctions are shown in Figure 1.9 (a) and Figure 1.9 (b).

To be able to respond to changing mechanical forces, there needs to be a mechanosensitive element in this adhesive chain that changes its properties in response to forces in the physiological range and induces a physiological answer of the cell. The exact mechanism for this is still subject of intensive study, but there are some known elements already. Both cadherins and integrins have been shown to have catch-bond properties, meaning that the dissociation rate to their binding partners decreases with increasing force [20, 21]. Some adaptor proteins like talin or α-catenin have been shown to unveil cryptic binding sites to more adaptor proteins like vinculin in response to an increased force [22, 23]. Other possible mechanisms of mechanosensing include steric considerations. An applied torque could for example align actin filaments with a wide angle to each other, allowing cross-linking proteins to bind them together. Last but not least, actin filaments themselves can be mechanosensitive due to their intrinsic material

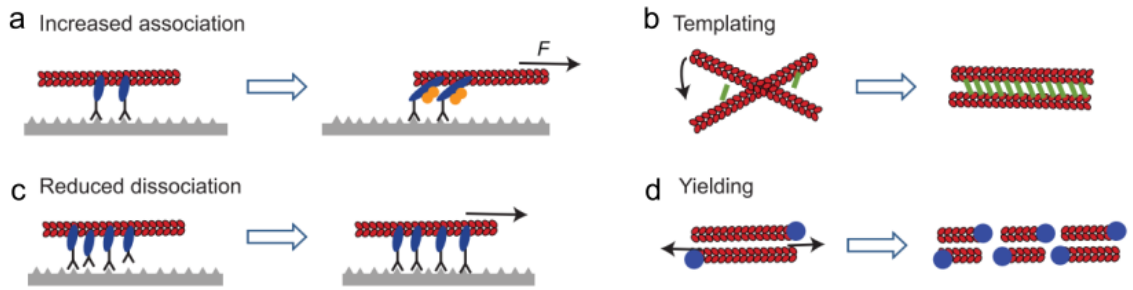

Figure 1.10: (a) shows the mechanosensitive mechanism where a force applied onto a protein unveils cryptic binding site, which increases its association rate to certain binding partners. (b) shows how an applied torque to two unaligned actin filaments can align those, allowing the association of additional cross-linking proteins to the filaments. (c) represents a catch-bond mechanism, where the dissociation rate of a protein to its binding partner is reduced upon force application. (d) shows how an applied force to actin filaments can lead to their rupture, unveiling additional binding sites for capping proteins. Taken from [18]

properties. Tensile forces can lead to rupture of filaments, unveiling binding sites for capping proteins. Compressive forces can lead the filaments to buckle which decreases their effective elasticity [18]. These four mechanisms for mechanosensation are schematized in Figure 1.10. Three of these, namely the catch-bond mechanism of integrin, the reinforcement properties of talin and the rupture of actin filaments, have recently been integrated by Andreu et al into a comprehensive "molecular clutch model" of mechanosensation at focal adhesions [24].

It has to be noted, that this is not a comprehensive list of all possible mechanosensation mechanisms. Others include mechanosensitive ion channels for example, but those are beyond the scope of this work.

The research on how cells can sense forces and other mechanical properties is still ongoing and there is still much to discover. In order to understand how forces influence complex processes like differentiation, where the necessity of mechanical signals is not directly obvious, one has to study not only how forces are sensed, but also how these signals are integrated into the cells biochemical machinery. This process is called *mechanotransduction*.

1.1.4 Translating mechanical signals into behavior - Mechanotransduction

Mechanotransduction is the process by which mechanical signals get translated into behavioral changes. Signal transduction in its general definition denotes the

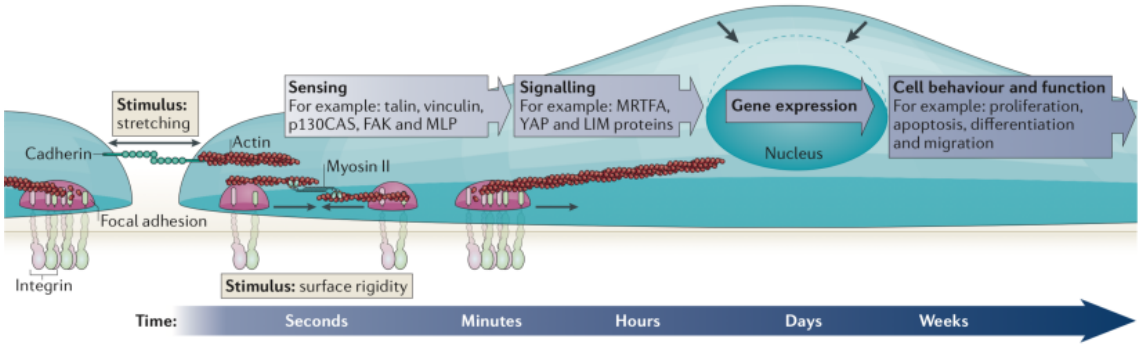

Figure 1.11: Mechanotransduction begins with a sensor that changes its properties in response to a mechanical stimulus. This change in property, generally a conformational change of a protein, triggers downstream signalling cascades that can ultimately alter gene expression and cell behavior. A major challenge in the study of mechanotransduction is the fact that it occurs over multiple time scales. Mechanical stimuli act on the order of less then a second, but the adaptation to (repeated) mechanical stimuli can happen within weeks or even months. Taken from [25]

transformation of the physical representation of a signal into a different physical representation. Mechanotransduction thus denotes the process of transforming a mechanical stimulus, which is picked up by a sensor sensitive to this stimulus, into a biochemical signal which then in turn alters cell behavior by e.g. altering gene expression. A classical mechanotransduction cascade in this manner is shown in Figure 1.11. One challenge in studying this process is its impact on processes on multiple time scales. Force changes can be picked up by the cell in matter of a fraction of a second, but tissue reorganisation in response to mechanical stimuli can take weeks or even months [25].

One of the most direct pieces of evidence for mechanotransduction is the fact that both focal adhesions as well as adherens junctions grow in response to externally applied forces. For focal adhesions this has been demonstrated by Riveline et al. in a study where they used a micropipette to directly push on the lamellipodia of an adhering fibroblast, which was sufficient to trigger focal adhesion growth [16]. For adherens junctions this was demonstrated by Liu et al. in a study where they plated endothelial cells on microneedle arrays that they functionalized in bow-tie-shape with microcontact printing. Cells formed doublets on those confined patterns and the microneedle arrays allowed for the measurement of cell-cell and cell-substrate forces. They found that pulling on one cell with a micropipette was sufficient to stimulate adherens junction growth in those doublets [17].

A less direct and more spectacular display of mechanotransduction has been

given by Engler et al. in a 2006 study, where they showed that substrate rigidity can strongly influence differentiation of naive mesenchymal stem cells (MSC) into neurons on soft ($\sim$1 kPa), myoblasts on intermediate ($\sim$10 kPa) or osteoblasts on rigid ($\sim$30 kPa) substrates [26]. The authors assessed both morphology and expression of differentiation markers of cells that have been grown on different rigidities but identical medium and found that cells start differentiating already a couple of hours after seeding. Additionally they found, that it is possible to reprogram cell differentiation by using soluble growth factors only in the first week in culture, before the cells commit completely to the differentiation path defined by the substrate rigidity. Pharmacological inhibition of myosin II through blebbistatin completely abolished the effect of substrate rigidity on differentiation, highlighting the fact that cells probe the rigidity of the environment by applying forces to it.

This study was highly influential in the field of mechanobiology, as it showed that mechanical stimuli not only affect the structures that are directly involved, such as the actin network or focal adhesions, but that they can also have a significant and far-reaching impact on cellular behavior. In fact, the study implies that there is a signalling pathway that somehow connects external mechanical stimuli to the regulation of gene transcription. This has since been confirmed by Dupont et al. who identified the transcriptional regulators YAP and TAZ to be an essential downstream element in the mechanotransduction chain that induce rigidity mediated differentiation in MSC [27].

The exact mechanisms by which mechanotransduction affect cell behavior are numerous and are still subject of intense research. For a more comprehensive review of mechanotransduction see [28–30]. Here I will focus on the pathways that are most relevant for this work, namely mechanotransduction at cell-cell and cell-matrix adhesions as well as the regulation of cell contractility.

A simplified signalling pathway for integrin and cadherin mediated mechanotransduction is shown in Figure 1.12. Upon force exertion, the cadherins in the adherens junction activate Abelson tyrosine kinase which phosphorylates vinculin, which then in turn triggers a signalling cascade including RhoA and ROCK, two prominent components of cell force and cytoskeleton regulation. In focal adhesions, integrins trigger two distinct signalling pathways including the Guanine Exchange Factors (GEF) GEF-H11 and LARG, ultimately triggering Rhoa and ROCK

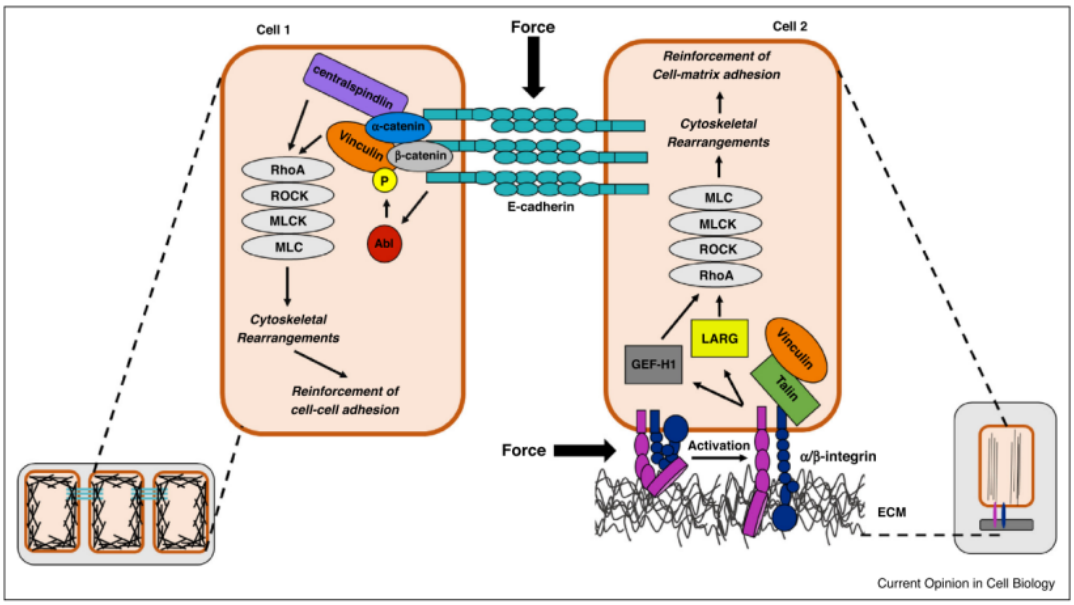

Figure 1.12: Force application on E-cadherins triggers the activation of Abelson tyrosine kinase which phosphorylates vinculin which then in turn triggers the RhoA signalling pathway. Similarly, force application on integrins activated the RhoA pathway, mediated by two distinct signalling pathways including the GEFs GEF-H11 and LARG. The RhoA pathway is known to play a major role in cell contractility and cytoskeletal rearrangements. Taken from [30]

as well [30].

Much of cell contractility and cytoskeletal rearrangements is coordinated by small GTPases such as RhoA, Rac1 or Cdc42. They are membrane-anchored proteins which's activity is regulated by it binding either GTP or GDP. If a GTP is bound to the GTPase, it is active until, after a certain amount of time or through the catalytic effect of a GTPase-activating proteins (GAP), it hydrolyzes the GTP to GDP. To reactivate the GTPase, a Guanine Exchange Factor (GEF) catalyses the exchange of GDP to GTP. An additional layer of regulation is achieved by sequestering inactive GTPases into the cytosol through Rho guanine nucleotide dissociation inhibitors (RhoGDI). Every GTPase has multiple effectors with varying affinities and every GEF and GAP activates and deactivates several different GTPases with varying efficiencies. This creates an enormously complex network of interactions, which allows it to regulate and coordinate the numerous complex processes and structures that are associated with the cytoskeleton [31]. This regulation mechanism is schematized in Figure 1.13.

Now that we covered the essential molecular mechanisms that build the foundation of this work, we can move on to see how these lead to cell and tissue scale mechanical properties

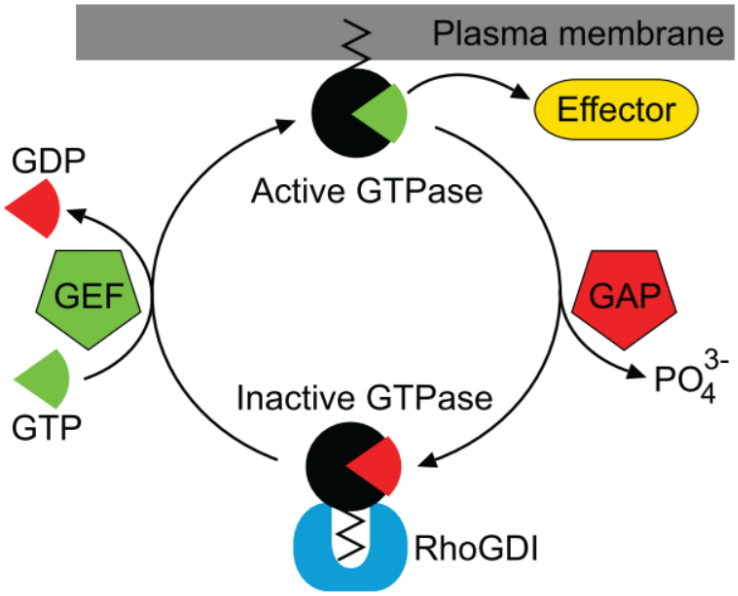

Figure 1.13: GTPases are membrane anchored signalling proteins which's activity is regulated by GTP/GDP. It is active while it is bound to GTP and after a certain time or when catalysed by a GAP, it hydrolyzes GTP to GDP which ends the signalling event. Inactive GTPases are kept in the cytosol by RhoGDIs and they get reactivated by GEFs, which catalyse the exchange of GTP for GDP. Taken from [31].

1.2 Building up scale: From single cells to simple multi-cellular assemblies

As stated in chapter 1, the question that we are interested in in our lab is: How are mechanical signals generated by cells and then transmitted to the surrounding environment and how do these signals influence their behavior and structure and that of surrounding cells?

As discussed previously, this question has to be addressed on multiple length scales, since living organisms are highly structured across multiple orders of magnitude of size and since they show emergent properties on several length scales, that are not easily understood through a reductionist approach. To get a complete picture, one would have to study life from the nanometer scale of biomolecules and their chemistry, up to the meter scale of whole organisms or even the kilometer scale of ecosystems. This is of course a daunting task for a single lab, so naturally one has to modestly chose a comparably narrow range of scales one wants to study.

In this work we are interested in intercellular communication on the smallest

scale possible; between one cell and another in cell doublets. In order to place the results of this work in a larger context, I want to review in the following chapters some of the main findings in our field right around this length scale: From single cells to simple multicellular assemblies.

Since we are interested in cell communication via mechanical forces, I will focus on the relationship between cell contractility and cell structure in varying extracellular environments. Most notably, that excludes studies that are concerned with measuring the passive mechanical properties of cells. For this subject I would refer the interested reader to [32].

1.2.1 The basic building block - single cells

As established in the previous chapters, cells exert forces on the extracellular matrix or on other cells. We established that these forces can be regarded as signals, that can potentially be perceived by other cells in their surrounding. The amplitude of cellular forces can vary over several orders of magnitude, depending mostly on cell type and the physical and biochemical properties of the surrounding environment. To characterize the contractile state, one also has to look at the spatial distribution of those forces and their orientation, which themselves vary largely, depending on the environment. Thus, in order to understand how force signals influence cellular behavior, we first need to establish some basic relationships between force generation, cell type and their environment.

In order to study the relationship between force generation of cells and environmental parameters, of course one needs tools to measure those forces. In the several decades since the emergence of mechanobiology, scientist developed a multitude of tools for this purpose. An extensive review of those tools can be found in [33, 34]. A prominent and nowadays standard tool for this purpose is called *Traction Force Microscopy (TFM)*, which is discussed extensively in section 2.1. In short, to do TFM, cells are plated on a continuous, elastic substrate in which fluorescent beads are embedded. When cells then spread on those substrates, they deform the gel and thus displace the beads. By measuring the displacement of those beads, one can then interpolate a deformation map and calculate a corresponding traction force map.

Using these force measurement tools, scientists found, that many structural

and mechanical parameters of cells and their environment are interdependent in an intricate way. For example, spreading surface correlates positively with traction force amplitude [35], traction force amplitude correlates positively with substrate rigidity [36], stress fiber formation correlates positively with traction force magnitude [37], cell geometry influences traction forces [38], and so on. To entangle this complicated web of correlations, one would like to vary these parameters individually and assess their influence on the other parameters. A prominent tool in mechanobiology that has proven quite useful for this purpose is micropatterning, which is discussed in section 2.3. Micropatterning is a tool, that allows for precise control of adhesion ligand geometry, which imposes the shape and spreading surface to the cell.

A study published by Oakes et al. combined micropatterning and TFM in an attempt to establish causal relationships between these correlations [39]. First they noticed that traction force does increase with substrate rigidity, but the substrate deformation decreases. The strain energy stored in the substrate, calculated by taking the dot product between deformation and traction force map, stayed relatively constant though when controlling for spreading size. Second they varied pattern geometry and thus cell shape and internal structure, but leaving the spreading surface constant and they still found the strain energy in the substrate to be conserved. Summarizing, their study suggests that the mechanical work a cell does on the substrate is independent of cell geometry, internal structure or substrate rigidity, but only depends linearly on spreading surface. Figure 1.14 a shows an actin fluorescence image and traction force maps for three different shapes with constant spreading size. Although actin organization and traction force distribution vary considerably between those three cases, the mechanical work done by the cell is similar in all three. According to this view, cells can thus be characterized by a single value for mechanical work done per unit of spreading area. This coefficient is dependent on cell type and varies greatly between cell types, as shown in Figure 1.14 (b) [40].

This view has since been challenged by Vignaud et al. in a study, where they plated epithelial cells on pill vs. dumbbell shaped micropatterns [41]. These two shapes aim at comparing a structure with two pronounced stress fibers to a structure with a more homogeneous actin structure, as shown in Figure 1.15. They found that the mechanical work performed by cells with pronounced stress fibers

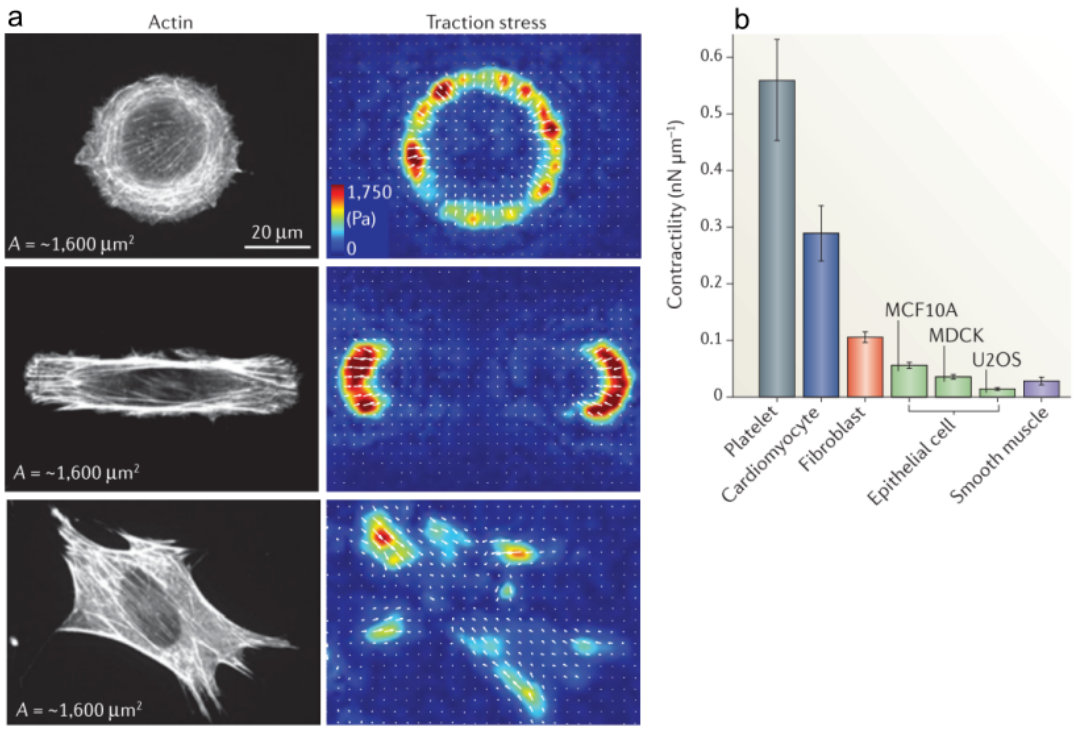

Figure 1.14: (a) Actin organisation and traction force maps for three fibroblast cells with different shape but similar spreading area. Although actin organization and traction force distributions vary considerably, the mechanical work between all three is similar. (b) Proportionality constant between spreading size and contractile energy for different cell types. Taken from [40].

was almost 10 times as high as for the cells with more homogeneous actin network. Although not explicitly discussed by the authors, I hypothesize that it is the strong stress fibers that span over a non-adhesive region that make the difference to the work of Oakes et al., who only looked at completely filled micropatterns. The different cell type used in both studies could also explain the difference. Oakes et al. used fibroblast cells, which are more contractile and generally form higher pronounced stress fibers than the epithelial cells used in the work of Vignaud et al.

So far we focused on the global force amplitude cells exert on the substrate. However, in order to fully describe the contractile state of a cell, we also have to look at the spatial distribution of traction forces, their orientation and their dynamic evolution in different contexts.

A study by Kalpana et al. looked at the relationship between adhesion geometry and traction force distribution [42]. In order to quantitatively compare two force maps that differ only in orientation, one needs to find a way to quantify it with a single value. One way of doing that, is by looking at the degree of polariza-

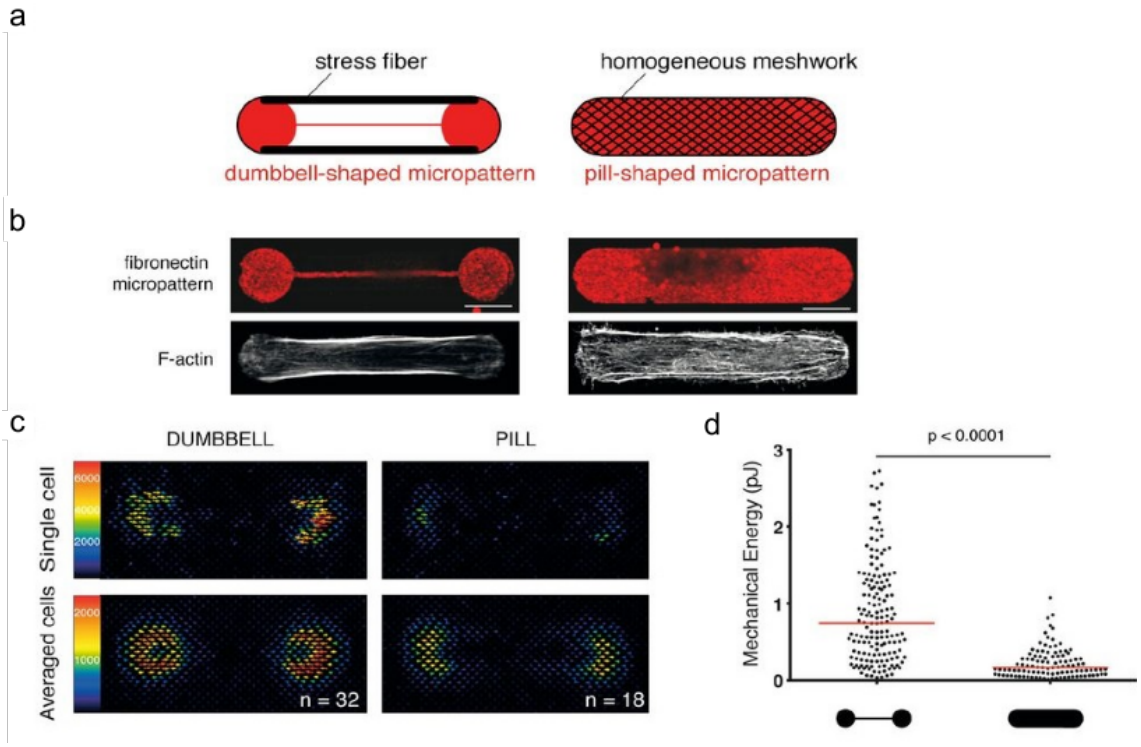

Figure 1.15: (a) Shape of the two different micropatterns used and the kind of actin organisation they induce. (b) Fluorescence image of the micropattern and the resulting actin organisation of cells plated on those patterns. (c) example (top) and average of traction force maps of cells for each pattern. (d) Contractile energy for cells on corresponding patterns. Taken and adapted from [41].

tion of the force field. The degree of polarization is a measure of how strongly the forces are pointed towards a single axis, with a value between 0 and 1. A value of 0 means, that all forces point towards the center and a value of 1 means that all forces point towards one axis. The authors found, that patterns with constant projected area but with varying subcellular geometry significantly alters traction field polarisation as well as the orientation of the main traction axis (Figure 1.16). This can be explained by the fact that the ECM geometry limits the possible points of adhesion, which in turn imposes a particular distribution of stress fibers, which then in turn determines the orientation of traction forces. This relationship between adhesion points, ECM geometry and stress fiber has been explored by Thery et al. in [43]. Furthermore, it has been discovered recently that also spreading history can influence stress fiber distribution and thus traction force distribution [44].

All studies discussed so far have in common that they look at steady-state contractile behavior of cells in different environmental conditions. In order to assess the dynamics of cell contractility, one needs tools that dynamically perturb the cell while at the same time measuring its contractile state. Some tools like AFM, opti-

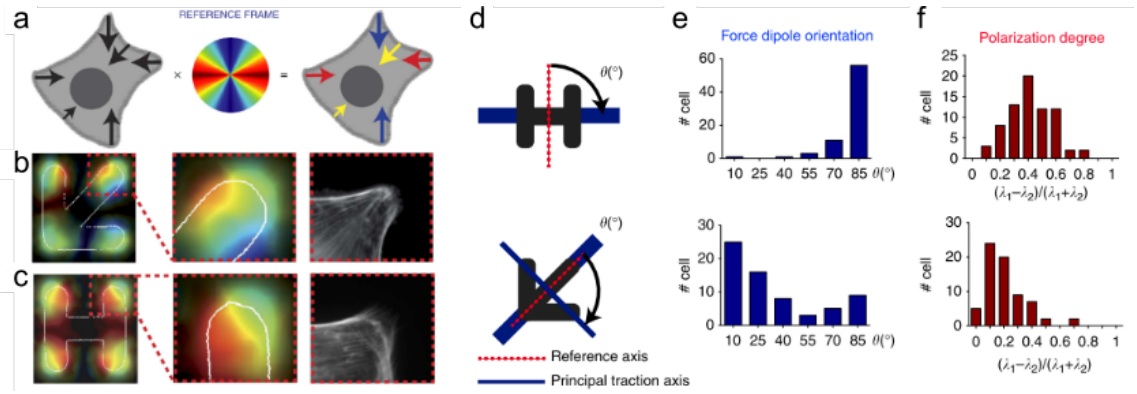

Figure 1.16: (a) shows a color code to visualize force orientation. (b) and (c) show the force orientation of example cells on two different micropatterns, leading to differing force orientation maps. (d) shows the principle traction axis for both patterns. (e) shows a histogram with the angles between principle traction axis and reference axis, as defined in (e). (f) shows a histogram with the degrees of polarization. Together, these data show that subcellular ECM geometry significantly influences force polarization and defines the orientation of the force dipole. Taken and adapted from [42]

cal or magnetic tweezers allow for dynamic stimulation as well as measurement, but they cannot be performed independently from each other. Pharmacological manipulation of cells allows for perturbation of its contractility while measuring it, but the spatio-temporal resolution is so limited, that it evokes rather a transition from one steady state to another, rather than than a dynamic evolution.

A tool that overcomes this limitation is laser ablation, which allows to severe the actin network in precise locations. By cutting stress fibers in adherent cells in specific locations, analysing the retraction dynamics and measuring traction forces at the same time, Kumar et al. showed that stress fibers behave like viscoelastic solids that are under active, cell generated tension [45]. By combining this approach with micropatterns, Kassianidou et al. managed to precisely control the length of severed fibers and establish a link between stress fiber mechanics, their length and the way they connect to the rest of the actin network [46].

Another tool to allow for dynamic perturbation of cell contractility is optogenetics, which is discussed in section 2.2. In short, optogenetics allows for the manipulation of biochemical pathways with the spatio-temporal precision of light, by transfecting cells with light-sensitive proteins. By using an optogenetic tool that induces the activation of RhoA, an upstream regulator of cell contractility, Andersen et al. showed in a yet to be published work from our lab, that the degree of alignment of stress fibers in fibroblast cells affects dynamic, but not the steady-state contractility.

1.2.2 The simplest multicellular assembly possible - Cell doublets

One major challenge in the study of intercellular communication via forces has been the difficulty to measure intercellular forces. Most cellular force measurements techniques rely on measuring the deformation of a soft substrate with known material properties and then calculating the corresponding forces and as such, they only measure cell-substrate forces. New tools are currently being developed to overcome this limitation, like FRET-based molecular tension sensors. With this tool, it is possible to measure the tension within a specific protein, like E-cadherin for example. However, at the current stage it is not possible to reliably infer tension distribution across a whole cell-cell junction with this tool without further assumptions. Additionally, the dynamic range of forces that can be measured is rather limited [47]. Despite their current limitations, these tools represent an exciting possibility to further our understanding in intercellular communication and many improvements in their capabilities are to be expected.

Another approach to measure cell-cell forces is based on cell-substrate force measurements and a simple force balance argument. Since the sum of all forces on a non-accelerating object are zero, one can measure the cell-substrate forces of a multicellular assembly, sum over all the cell-substrate forces for one cell and if the result is non-zero, this force has to be balanced at the cell-cell boundaries of this cell. This approach only yields a unique solution in very specific situations though, where a cell-cell boundary is only shared by two cells at a time and is thus best adapted for simple multicellular assemblies, such as cell doublets (see Figure 1.17).

Liu et al. used this method to study the relationship between adherens junction size and cell-cell force in endothelial cell doublets [17]. They used a micro-needle array of well defined rigidity for force measurement and they printed a bow-tie shape of adhesion ligand on top using micro-contact printing, which allowed the authors to control for cell doublet geometry. They found that the size of the adherens junction was tightly correlated with the cell-cell force, when they pharmacologically increased or decreased cell contractility. They also found, that the adherens junction grows when micro-injecting constitutively active RhoA in one of the cells or when directly pulling on one of the cells with a micro-pipette.

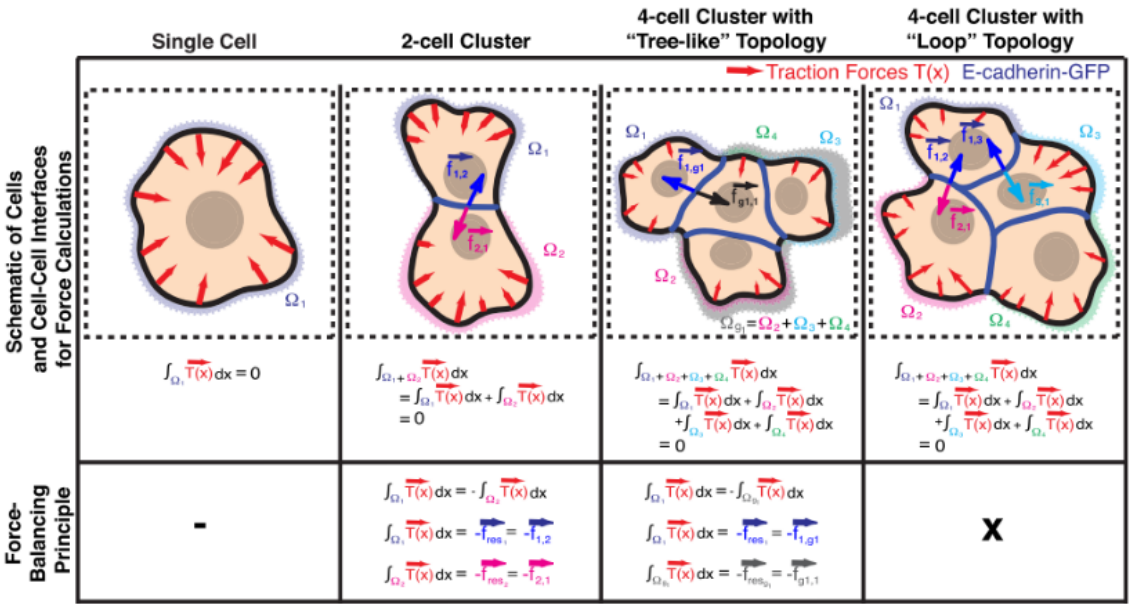

Figure 1.17: Force balance considerations allow for the calculation of intercellular forces in cases where each cell boundary is only shared by two cells at once. This is the case for any cell doublet and for multicellular assemblies with "tree-like" topology. Taken and adapted from [48]

A similar approach was used by Maruthamuthu et al. to measure cell-cell forces in epithelial cells, but instead of a micro-needle array they used TFM to measure cell-substrate forces [49]. They also did not impose a specific adhesion geometry on the cell, meaning that the cells could spread freely. By measuring both adherens junction size as well as cell-cell forces over time, they found, in contrast to Liu et al., cell-cell forces to be quite stable despite high variations of adherens junction length. The authors hypothesize that this difference can be attributed to the fact, that their cell doublet system were not confined to specific adhesion geometries. By disrupting the adherens junction through Ca^{2+} depletion, they found an abrupt decrease of cell-cell force right on the onset of junction disruption, leading the authors to conclude, that most of the intercellular stress is concentrated at the edges of the junction. Additionally, they found a strong correlation between cell-cell force and cell-substrate force when altering rigidity and when changing adhesion ligand from fibronectin to collagen I. When analysing cell-cell force and cell-substrate force in cell triplets forming a line, they found that the center cell showed much higher cell-cell forces, since it was pulling on two cells at the same time, but the sum of cell-cell and cell-substrate force was comparable between all three cells. Together, these results indicate, that cells regulate the overall forces they exert, whether they pull on other cells or on a substrate.

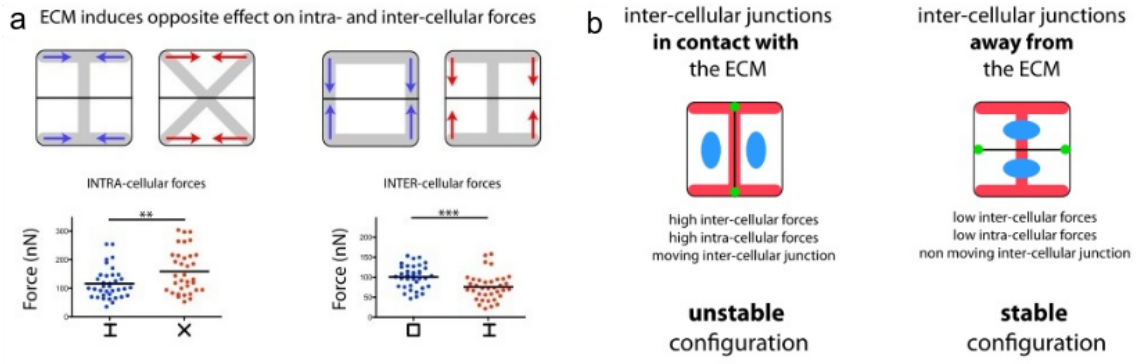

Figure 1.18: (a) ECM presence has an opposite effect on intra and intercellular forces when they are oriented either parallel or perpendicular to the cell-cell junction. (b) shows a summary of where the cell-cell junction positions itself in a given ECM configuration. Taken and adapted from [50]

The strong correlation between cell-cell force and cell-substrate force that was found by Maruthamutu et al. in unconfined doublet does not hold true when confining doublets on varying adhesion ligand (i.e. ECM) geometries. This was found by Tseng et al. in a study where they looked at how adhesion geometry influences cell-cell junction positioning in epithelial cell doublets and is confirmed in this work [50]. Tseng et al. found that the cell-cell junction positions itself in a way that maximizes the distance between the junction and potential cell-substrate adhesion points (Figure 1.18 b). They found that intercellular forces increase in the presence of ECM, whereas intracellular forces decrease (Figure 1.18 a). The authors show that this relationship is sufficient to drive junction positioning over areas that are devoid of ECM, assuming that the doublet minimizes its contractile energy.

Sim et al. took a closer look at the relationship between cell-cell and cell-substrate force on varying ligand geometries in epithelial cells [51]. They found that, similarly to single cells, cell forces scale with spreading surface in doublets. Interestingly, they also found that a cell, that is in contact with another cell, exerts more than twice as much force than a single cell with comparable spreading surface. They also looked at the molecular tension in E-cadherin in different conditions using a FRET sensor. Strikingly, they found the molecular tension to be constant and independent of cell-cell force. The favorite hypothesis of the authors to explain this observation, is that the increased tension is to be found somewhere else in the adhesive chain between actin and E-cadherin.

Another aspect of the contractile state, that has not been addressed by the

studies mentioned so far, is the degree of cooperativity in the contractile state of a doublet. In other words, how much do the cells contract individually vs. how much do they contract as a single unit. This question has been addressed by McCain et al. for cardiac myocytes [52] and by Polio et al. for airway smooth muscle cells [53]. Both groups looked at cell doublets on rectangular ECM patterns, on which the cells mostly contract along the long axis of the pattern. This allowed them to reduce the problem to a quasi 1D system and allowed them to define a coefficient of cooperativity. This coefficient of cooperativity is defined as the amount of force the cells exerts on their junction normalized by its contractile moment, which reflects the amount of force exerted on the substrate. With this experimental setup and this analysis, they found high cooperativity in cells on soft substrate, reflecting conditions in healthy tissues, and low cooperativity in cells on rigid substrate, which is associated to certain type of diseases. The authors conclude, that the lack of cooperative contraction in stiff environments is a major contributor to diseases like asthma or hypertension.

Vargas et al. used these results to develop a computational model that explains this substrate rigidity dependence as a result of mechanosensing events that happen at focal adhesions and the cell-cell junction [54]. Li et al. found similar results in 1D cell chains comprised of two to five cells [55]. They found higher cooperativity in epithelial vs. fibroblast cells, higher cooperativity on softer substrate, and lower cooperativity when disrupting the cell-cell junction with a Ca^{2+} chelating agent.

Similarly to the studies discussed in the previous chapter, all here mentioned studies have in common that they mostly study cell contractility that have reached mechanical equilibrium in varying conditions. This is most likely due to the lack of appropriate tools, which lack spatio-temporal resolution and do not allow for dynamic perturbation. I will discuss how we try to overcome this limitation with optogenetics in section 2.2.

1.2.3 Increasing complexity: 2D monolayers and small 3D tissues

Now that we established some basic properties of mechanical cell-cell interactions we can start looking at more complex multicellular assemblies. A popular *in vitro*

model for tissues are epithelial monolayers, which line most organs *in vivo* to form a barrier and interface to the outer environment. Here, the complexity of living systems becomes very obvious, as a lot of emergent behavior can be observed, which cannot readily be predicted from the findings derived from the more reductionist approaches discussed so far.

A major field of research on cells is concerned with cell migration, which is observed both in single cells and in multicellular assemblies. Both single cell migration and collective cell migration have been intensively studied in the past up until now, so here I will only give one example of emergent behavior on the tissue scale. A more extensive review on cell migration can be found in [56, 57].

It is known, that both single cell and collective cell migration can be guided by many different types of cues, including chemical gradients (chemotaxis) [58], adhesion ligand density (haptotaxis) [59], rigidity gradients (durotaxis) [60] and others. All these are examples, where findings on single cells could be translated to bigger tissues, highlighting the importance of simple models. However, some situations in complex systems do not have a pendant in their simpler counterpart and are thus emergent. One of these situations is the fact, that cells during collective cell migration tend to migrate along a direction that minimizes shear stress with the surrounding cells, which was discovered in a pioneering study by Tambe et al. [8] [61].

Another example of emergent behavior at the tissue scale was recently published by Luciano et al., where they demonstrate the capability of an epithelial monolayer to sense the curvature of a substrate that it is living on [62]. Although it is known, that single cells also sense local curvature and align, depending on the cell type, parallel or perpendicular to the axis of curvature [63], it was unclear, how this local curvature sensing translates to curvature sensing at scales larger than the size of a cell. Luciano et al. plated epithelial monolayers on corrugated hydrogels with wavelengths of 2-4 cell lengths and found, that cells were thicker on valleys than they were on crests. This thickness modulation affects nuclear positioning and shape, which in turn affects YAP nuclear localization and nuclear lamina expression, which in turn affects cell proliferation rate.

Epithelial monolayers are an excellent model to understand some fundamental

[8] This finding was enabled by the author's development of "monolayer stress microscopy" (MSM), a method to calculate intercellular stresses from substrate deformations. The method is explained shortly in subsection 2.1.3

emergent properties from cell-cell interaction, but they are still far away from the physiological situation of a real organ. First, most studies on monolayers are done on only one cell type, whereas most organs are comprised of a multitude of different cell types. Second, monolayers in culture are just a 2D, flat surface, whereas tissues *in vivo* generally have a 3D structure. Third, tissues are not only comprised of cells but also of extracellular matrix proteins, serving as a scaffold for cells.

Therefore, the logical next step in this bottom-up approach, is to reproduce *in vitro* some of those more complex aspects of tissues that we observe *in vivo*. The simplest 3D tissue model that includes bulk ECM, are so called spheroids. Spheorids are an assembly of hundreds of cells embedded in a 3D matrix of ECM, often collagen or matrigel [9]. Spheroids are widely used as a model for cancerous tissues, due to their stronger morphological similarity to real cancer tissues compared to 2D cultures [64, 65]. A spheroid is formed by mixing cells, generally cancer or fibroblast cells, with unpolymerized ECM solution and then culturing them in an anti-adhesive environment. The cells will then compact the ECM and form a spherical structure in the end. If the cell collection is presented with obstacles during its formation, the tissue will form around the obstacles, which will alter the shape and the mechanical properties of the tissue. Additionally, if elastic obstacles are used, the deflection of those can be used to measure the tension created by the tissue [66].

From here, the next step towards more physiological *in vitro* tissue models, is to incorporate more different cell types and to recreate the more complex structures that are found *in vivo*, such as the villi structures that can be found in the gut and in lungs. This is studied in the exciting and recent field of organoids and of organ-on-chip models. Many different type of organ models, such as brains, guts, lungs and kidneys are being worked on and represent many new opportunities for both fundamental and medical research [67–69].

[9] matrigel is an extract of the ECM proteins produced by cancerous tissues in mice. Its composition is rich in different types of ECM proteins, but not very well understood, nor controlled, due to its natural origin.

1.3 Basic idea of my PhD project

As stated in the chapter 1, the main question that we want to address in this work, is how cells use forces to communicate and coordinate their behavior. This is a very complex question, so for this project we decided to break it down to a much simpler question: If we put two cells next to each other and make one of them pull on the other, how does the other cell react? These two questions are represented schematically in Figure 1.19

To do this experiment, we need two main ingredients: We need a way to locally and transiently modulate cell contractility and we need a way to measure cell forces. For the measurement of cell forces we use a now classical tool called traction force microscopy, which is explained in detail in section 2.1. Local and transient modulation of cell behavior generally speaking is something, that was impossible to do until the advent of optogenetic tools some decades ago, and probably also the reason why this questions has not been addressed earlier. The basic principle of these tools rely on the transfection of genes that induce the expression of engineered, photosensitive proteins, which trigger some cell signalling pathway. More details on this tool are described in section 2.2. Last but not least, we have to make sure that the cell doublet is stable during the course of the experiment, i.e. that it doesn't start moving or migrating. To achieve this, we use micropatterns in H-form, which are know to stabilize cell doublet geometry [50]. Details about this tool are described in section 2.3

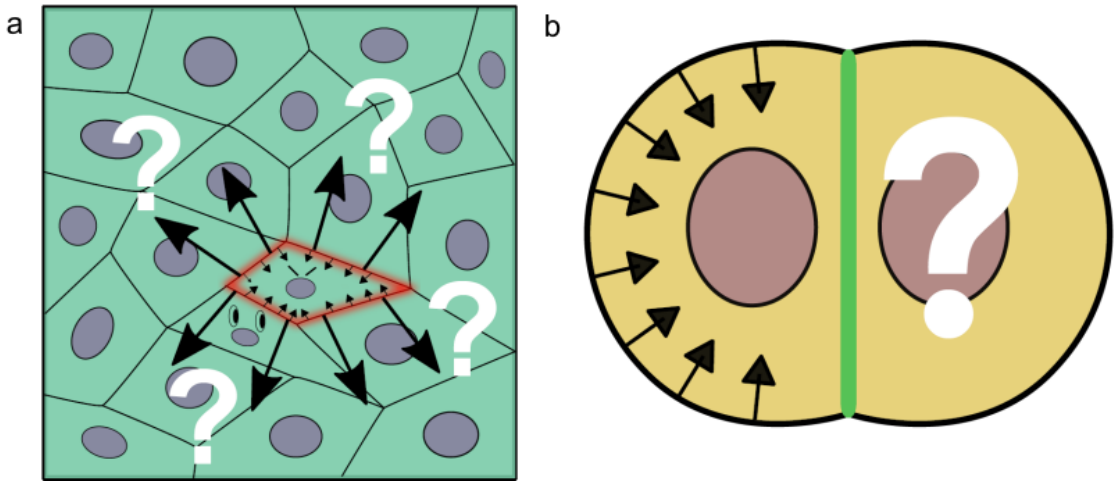

Figure 1.19: (a) Cartoon of one cell in an epithelial monolayer contracting and influencing the neighboring cells (b) Cartoon of one cell in a doublet pulling on the other one.

2. Tools to study intercellular communication through forces

All methods used throughout this work are described briefly in the draft for the article, in subsection 3.2.4. This chapter will go into much more detail about the three main methods I used in this work: Traction force microscopy to measure cell forces, optogenetics to generate cell force signals and micropatterning to control and modulate the shape of the cells. I will review and compare different methods and discuss what they have been used for in the past.

2.1 Traction force microscopy to measure mechanical activity of cells

In the early days of cell culture and still today, cells were generally observed on hard and flat substrates, like glass or plastic. Already in the 70's, people hypothesized that adherent, especially migrating cells, exert traction forces onto those substrates. In a pioneering study by Harris et al., published in 1980, they added a thin sheet of soft silicone on top of the culture dish and cultured cells on top of it [70]. Both individual cells and entire explants from chick hearts made visible wrinkles in the silicon substrate, as shown in Figure 2.1. Thus, for the first time in history, Harris et al. managed to visualize cell traction forces.

Despite the breakthrough this study represented, it only gave a qualitative visualization of the traction forces cells exert on the substrate. Several methods have since been developed, which use this basic principle of force visualization in a more quantitative manner. These methods are reviewed extensively in [34]. The two main methods being used widely today are shown in Figure 2.2.

The technique shown in Figure 2.2 (a) uses an array of micro-fabricated mi-

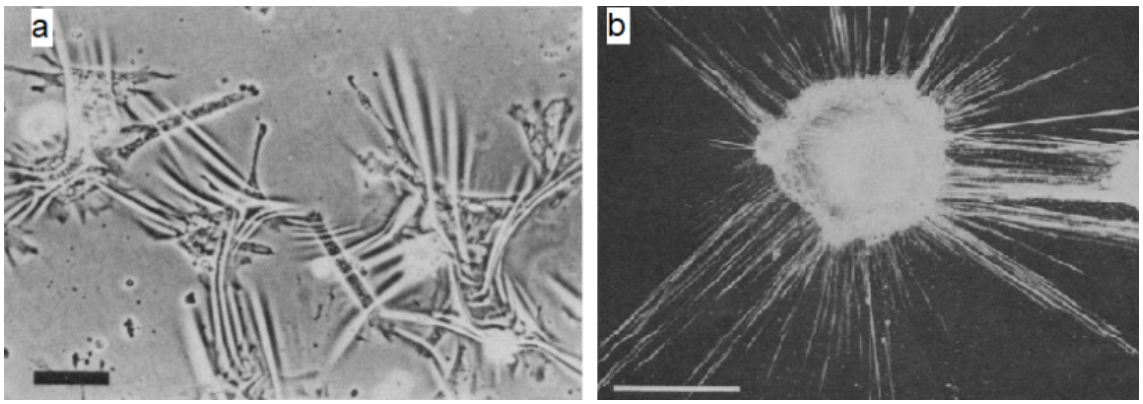

Figure 2.1: (a) A collection of chick fibroblast cells spreading on a thin silicone sheet, making visible wrinkles into the elastic substrate. Scale bar: 100 μm. (b) An explant of a chick heart after 48 h of spreading on a thin silicone sheet. The thin lines are wrinkles in the silicone substrate, visualising the deformation induced by the explant. Scale bar: 1 mm. Taken and adapted from [70]

cropillars with known elastic and geometric properties. When cells spread on these pillars, the pillars get deflected by the applied force and this deflection can then be measured with a microscope. The forces exerted on each of these pillars can be calculated from the known pillar properties. The main advantage of this technique is, that force calculation is straight forward and direct. The main disadvantage of this technique is, that the pillar array has a certain topography and cells can only adhere on the pillars and not in between. This by itself can influence the behavior of the cells and therefore it is impossible to study the effect of substrate topography independently from e.g. substrate rigidity.

Figure 2.2 (b) represents traction force microscopy, the method being reviewed here. Fluorescent markers, generally microbeads with 0.2 to 1 μm diameter, are embedded in a thick, elastic gel and by measuring the displacement of the beads, the deformation of the gel imposed by the cell can be measured accurately. Knowing the material properties of the gel, one can then calculate the traction forces applied to the substrate using elastic theory of continuous media. Both the deformation measurement and the force calculation is considerably more challenging and error prone than the method of the micropillar array. However, TFM substrates are generally much easier to fabricate and the topography can be defined independently from the substrate. For these reasons, TFM has established itself as most common cell-substrate force measurement method, which is also the chosen method for this work. The main challenge and some solutions for the displacement measurement and the force calculation are presented in subsection 2.1.1

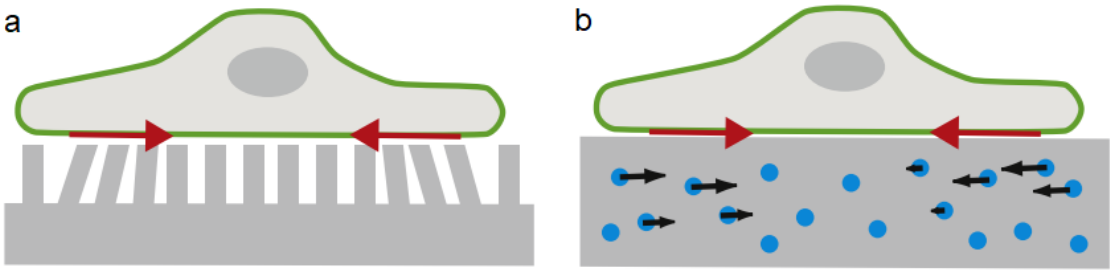

Figure 2.2: (a) A cartoon representing the principle of micropillar based force microscopy. The deflection of each pillar can be measured and forces can be calculated based on the geometrical and elastic properties of the pillars. (b) A cartoon showing the principle of traction force microscopy (TFM). Fluorescent beads are embedded in a thick elastic gel. The displacement of the beads can be tracked and a displacement field can be measured. The traction field can then be obtained by deconvolution of the displacement field. Taken and adapted from [71]

and subsection 2.1.2.

2.1.1 Displacement field measurement methods

A problem much older than traction force microscopy, but quite similar in its problematic, is the measurement of fluid flow. Fluid flow can be visualised by adding particles to a moving fluid and recording their movement with a camera. The problem then becomes essentially the same as when doing traction force microscopy: Measuring the movement of the particles between two images. From here, different possible solutions can be imagined: Either we track the movement of each particle over time, or we look at a specific spot in the image and we look in which spot of the other image we find the same features. Both of these approaches have been used in the past and go with the name of "particle tracking velocimetry" (PTV) for the former and "particle image velocimetry" (PIV) for the latter.

PTV will, in principle, give the most accurate solution for a given set of images, because every data point (i.e. every marker) is measured and used. In practice, this approach is very hard to implement in an algorithm, unless both marker density and marker displacement are low. If the density or displacements are too high, the algorithm will not be able to reliably associate the marker to the right reference marker. Additionally, the algorithm running time will scale with the number of markers in the image. Both these points are major limitations and effectively reduce the spatial resolution of the displacement field measurement one can achieve.

For these reasons, PIV has become the most prominent method both in fluid flow measurements as well as in TFM. Here, instead of looking at individual particles, we look at a specific spot in the moving image and then look in the reference image, where we find the same configuration of particles. In practice this is done by cutting the moving image into windows of a certain size [1], which are then cross-correlated to the reference image. The result of the cross correlation should then have a peak at a coordinate that corresponds to the displacement of this window. Often times, the performance of these algorithms can be enhanced by choosing large window sizes first and then gradually decreasing the size of the interrogation window. Here the final resolution of the displacement field will be determined by the smallest window size used. Thus, the resolution is fundamentally limited to window sizes that still contain a fair number of markers [2]. In practice, at least in our application, it is the algorithm run time that limits the final resolution though, as it increases exponentially with smaller window sizes. But, in contrast to PTV, the algorithm run time is independent of marker density and both the accuracy as well as the best possible resolution are improved by higher marker densities. More information and the history of the application of this technique in fluid flow can be found in [72]. Many publicly available implementations of PIV algorithms exist nowadays, including the MATLAB toolbox PIVlab [73], an ImageJ plugin [3] and the python package OpenPIV [4]

In order to overcome the limitations of both approaches, algorithms have been developed that combine both these methods [74, 75]. PIV is first used to estimate the displacement field and then this estimation is used to crop small windows in the moving image that correspond to the same position in the reference image and then PTV is performed on these small windows. This approach allows for sub-pixel resolution measurement of the displacement field, even with large marker displacements and high marker densities. It does come with a computational cost though, but runtime is still sufficiently low to do time resolved TFM analyses [5]. Therefore, this is the approach that has been used in the algorithm that was developed in our team and that I have been using for all the analyses in this work.

[1] should typically contain about 10 particles

[2] generally, the fewer markers in a window the more error prone the measurement

[3] https://sites.google.com/site/qingzongtseng/piv

[4] https://openpiv.readthedocs.io/en/latest/

[5] In our implementation, it takes about half an hour to analyse a 60 frame stack of 1000x1000 pixels

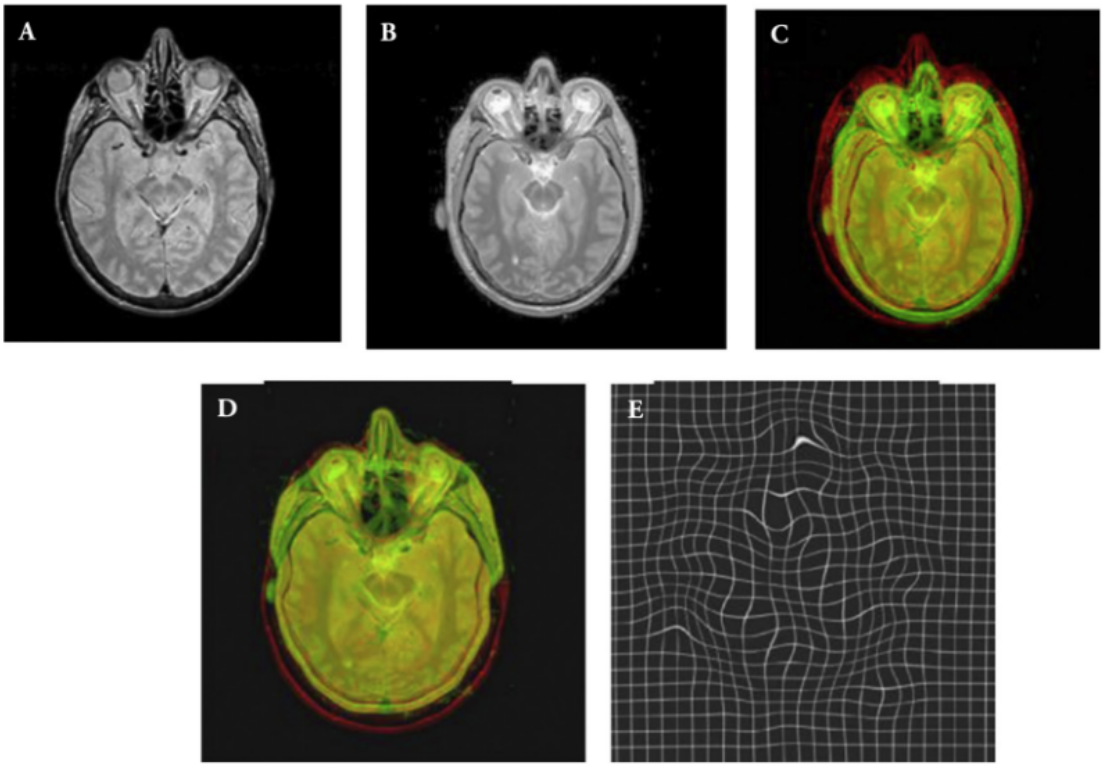

Figure 2.3: A) shows a brain MRI template and B shows the brain MRI image that has to be mapped to the template. C) shows an overlay of the two images and D) shows an overlay after deformation of the image in B). E) shows a visualization of the deformation by applying it to a regular grid. Taken from [76].

Other solutions to this problem exist from completely different fields. In medical imaging, image registration is a major problem, in which images from patients have to be aligned with a template in order to standardize the images and more easily extract certain features. In simple applications, the image is only translated and rotated to match the template, which is also called "rigid image registration". More sophisticated approaches exist too, where the image gets deformed locally in order to match the template, also called "non-rigid registration". An example of this application is shown in Figure 2.3. Many algorithms have been proposed to solve this problem for many specific applications. A review of this goes beyond the scope of this work, but can be found in [76]. Many of these algorithms are implemented in the popular, open-source toolbox "elastix" [77]. This approach has been used before in a TFM setting, and the authors claim to achieve better results as when using PIV on simulated data, but a comparison to a combined PIV+PTV approach is lacking [78].

Another field that has looked at a similar problem is the field of computer vision, where measuring the movement of an object from one frame to another also

Figure 2.4: An example of an optical flow algorithm applied in a computer vision setting. Left: The result of a sparse optical flow algorithm, with the lines representing the movement of the features over time. Right: The result of dense optical flow algorithm, with the intensity showing the magnitude of the displacement and the color showing the direction. Taken from: https://nanonets.com/blog/optical-flow/

is a major problem. In computer vision, the problem of measuring the apparent velocity of an object with respect to the observer, i.e. the camera, is framed as "optical flow". Many algorithms have been proposed to solve this problem and, again, a review of those algorithms is beyond the scope of this work, but can be found in [79]. Broadly, one can distinguish between sparse optical flow, where certain features in the moving image are detected and then mapped to the reference image, and dense optical flow, where each pixel gets assigned a displacement vector. An example output of both methods is shown in Figure 2.4. This method has also been applied successfully in a TFM setting and the authors claim that this method outperforms both PIV and PTV based methods [80]. However, to me it is unclear, if the increased performance is fundamental to the method, or more a result of the specific algorithms and parameters used in the study.

In conclusion, I think that PIV by itself is insufficient for most TFM applications, as one loses a lot of spatial resolution by averaging the displacement of many markers to a single value. Thus, tracking every single marker accurately with high marker density should be the goal of every TFM experiment, where achieving a good spatial resolution of forces is important. PTV by itself is insufficient to do that in most applications, unless one reduces the marker density, which then in turn reduces the final spatial resolution. Thus, the algorithm that was developed in our lab and that has been used for this work, uses a combined PIV and PTV approach, which seems to me to be an ideal solution that other methods have to be compared against. That being said, in practice this approach often comes with a high computational cost, especially in extreme situations where displacements

are large [6] and marker density is high. Thus, one often has to sacrifice precision and accuracy to get analysis time down to a reasonable level. Therefore, I think optical flow and non-rigid registration methods are very promising, alternative approaches that could yield results as accurate as PIV+PTV approaches, without the associated computational cost. This becomes particularly important in 2D+t, 3D and especially in 3D+t applications.

2.1.2 Traction force field calculation

In order to infer the traction force field from the displacement field, one needs to use elastic theory of continuum mechanics to relate the two with each other. A complete derivation of the required equations can be found in [71] and are summarized and slightly simplified in the following section.

In order to map forces to displacements, one needs to assume some constitutive relationships that characterize the material being looked at. These constitutive relationships generally relate the substrate strain with the substrate stress. Therefore, one first needs to define the strain in terms of the displacement field we obtained in the previous section. This strain is given by the Green-Lagrange tensor **E**:

$$\mathbf{E} = \frac{1}{2}[(\nabla \otimes \mathbf{u}) + (\nabla \otimes \mathbf{u})^\top + (\nabla \otimes \mathbf{u})(\nabla \otimes \mathbf{u})^\top] \tag{2.1}$$

Where **u** is the displacement field and $\nabla \otimes \mathbf{u}$ describes the Jacobian matrix of **u**. The third summand in this equation shows, that there is a non-linear relationship between strain and displacement. For small strains, this term can be neglected and the equation can be linearized to obtain the linear strain tensor ε:

$$\varepsilon = \frac{1}{2}[(\nabla \otimes \mathbf{u}) + (\nabla \otimes \mathbf{u})^\top] \tag{2.2}$$

Next, one needs to assume some constitutive equations for the material being used. For most biological materials, such as matrigel or collagen gels, the resulting equations are very complex to solve and often times the materials are not well enough characterized at the cell length scale. Therefore, in most TFM applications up to this day, linearly elastic and isotropic materials are used, such as

[6] For example more than 3 times the marker diameter

polyacrylamide gels. If these assumptions can be made, the constitutive equation corresponds to the generalized Hook law, which relates the stress components σ_{ij} to the strain components ε_{ij} as follows:

$$\sigma_{ij} = \frac{E}{1+\nu}(\varepsilon_{ij} + \frac{\nu}{1-2\nu}\varepsilon_{ll}\delta_{ij}) \tag{2.3}$$

With E describing the Young's modulus of the material and ν its Poisson ratio. The gradient of the stress is balanced by external forces at all time, i.e. $\nabla\sigma = \mathbf{f}$. Then, substituting ε_{ij} in Equation 2.3 by Equation 2.2 and calculating the gradient, one obtains the following second order differential equation, also called "Lamé equation":

$$\frac{E}{2(1+\nu)}\Delta\mathbf{u} + \frac{E}{2(1+\nu)(1-\nu)}\nabla(\nabla\cdot\mathbf{u}) = \mathbf{f} \tag{2.4}$$

This equation can be solved for point forces and those solutions are called "Green's functions". From those solutions, a general solution for the displacement field can be constructed by convoluting the Green's function **G(x)** with the traction force field $t(x)$, such as:

$$\mathbf{u(x)} = \int \mathbf{G(x,x')t(x')}\mathrm{d}\mathbf{x'} \tag{2.5}$$

This Green function is known for semi-infinite elastic substrates, but also for elastic layers of finite thickness. In many TFM applications, a semi-infinite substrate can be assumed, since the displacements induced by cell generated forces decay fast enough into the substrate. As a rule of thumb, the substrate should be thicker than the lateral dimensions of the cell or cell layer being looked at, in order to make this assumption.

Many different approaches exist to use these equations to obtain the traction force field from the displacement field. A detailed review is beyond the scope of this work, but can also be found in [71]. Generally speaking, these equations suggest two possible routes to obtain the traction force field from the displacement field. The first possibility is to calculate the stress directly with Equation 2.3, which involves taking the derivative of the displacement field to obtain the strain. With perfect data, this would be quite straight forward, but in practice, every displacement measurement will be noisy, due to tracking errors, Brownian motion

of the markers, camera noise, etc. Therefore, a more common and robust approach is to solve Equation 2.5 for **t(x)**.

Again, two main approaches exist to solve this equation. The first approach, called "boundary element method" (BEM), was initially proposed by Dembo et al. [81]. It solves the equation in real space by formulating it as a minimization problem. This involves discretization of Equation 2.5, estimating the traction field, calculating the displacement field from this estimated traction field, calculating the difference with the actual displacement field and then minimizing this difference [7]. This method is computationally very intensive, so the more common approach nowadays is to solve Equation 2.5 in Fourier space, where the convolution becomes a simple multiplication. This approach is called Fourier transform traction cytometry (FTTC), was initially suggested by Butler et al. [82] and is the chosen method for the algorithm used in this work. With this approach, one can then easily solve Equation 2.5 for **t(x)** as follows:

$$\tilde{\mathbf{t}}(\mathbf{k}) = \tilde{\mathbf{G}}(\mathbf{k})^{-1}\tilde{\mathbf{u}}(\mathbf{k}) \tag{2.6}$$

Here, the $\sim$ denotes the Fourier transformation and **k** denotes the wave vector of the Fourier transformation. Now we have an explicit equation for the traction force field. The last thing we need, to implement this equation in an algorithm, is the Fourier transformation of the Green function **G(k)**. For an incrompessible material (i.e. $\nu \simeq 0.5$), where only lateral forces are considered, this is given by:

$$\tilde{\mathbf{G}}(\mathbf{k}) = \frac{2(1+\nu)}{Ek^3}\begin{pmatrix} (1-\nu)k^2 + \nu k_y^2 & -\nu k_x k_y \\ -\nu k_x k_y & (1-\nu)k^2 + \nu k_x^2 \end{pmatrix} \tag{2.7}$$

Now, one only needs to calculate the 2D Fourier transformation of the displacement field, multiply by the inverse of Equation 2.7 and then calculate the inverse Fourier transformation of the result. In order to use the fast Fourier transformation (FFT) algorithm for these calculations, the displacement field has to be defined on a regular grid. If PIV or dense optical flow is used for the measurement of displacement field, this is already given. When PTV or sparse optical flow is used, the tracking data from the markers have to be interpolated onto a regular grid.

This is in principle sufficient to implement a TFM algorithm. In practice, one

[7] This is a simplification. The process also requires regularization to account for noisy data and requires measurement of the cell boundary. For more details, see [71]

still has to take care of noise in the displacement data. This can be done by applying noise filters [8] to either the displacement field or the resulting traction field or both. A more rigorous approach is to implement a regularization scheme into the force calculation, as proposed by Sabass et al. [75]:

$$\tilde{\mathbf{t}} = (\tilde{\mathbf{G}}^{\top}\tilde{\mathbf{G}} + \lambda^2\mathbf{H})^{-1}\tilde{\mathbf{u}} \tag{2.8}$$

H is called the "regularization kernel" and in the simplest case, this is just the identity matrix **1**. This regularization procedure leads to a 0th order regularization, which has been used throughout this work. λ^2 is the regularization parameter, which should be as small as possible. Generally speaking, the smaller λ^2, the more t corresponds to a true solution of Equation 2.5. In fact, for $\lambda^2 = 0$ one finds Equation 2.6 again. By increasing λ^2, the solution gets smoother, in disfavor of being close to the real solution, given the actual measurement.

2.1.3 Cell stress calculation

As discussed until this point, with traction force microscopy it is possible to measure the forces cells exert on their substrate, but it does not give any information about the stress inside and in between of cells. However, those can also be calculated by a simple force balance argument, that can be conceptually understood with the game "tug-of-war", as illustrated in Figure 2.5 (a). Basically, as cells pull on each other, this force has to be balanced in the substrate, exactly the same way the force that people transmit to the rope in a tug-of-war game has to be transmitted through the feet to the ground. In 1D, this can me modeled through a simple equation as presented in Figure 2.5 (b). In 2D, the equations become more complicated and can be written down as follows:

$$\frac{\partial \sigma_{xx}}{\partial x} + \frac{\partial \sigma_{xy}}{\partial y} = T_x, \frac{\partial \sigma_{xy}}{\partial x} + \frac{\partial \sigma_{yy}}{\partial y} = T_y \tag{2.9}$$

The definitions of the stresses and tractions in these equations are shown in Figure 2.5 (c). These equations have been solved in the context of collective cell migration in cell monolayers by Tambe et al., who dubbed this technique "monolayer stress microscopy" (MSM) [61].

[8] e.g. Gaussian or median filter

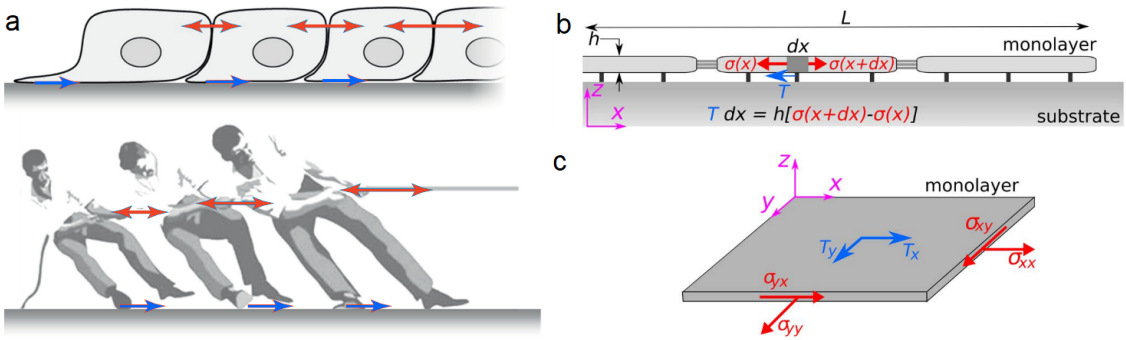

Figure 2.5: (a) A cartoon showing the analogy between cells in a monolayer, pulling on each other and on the substrate, with the game "tug-of-war". Taken from [83]. (b) 1D mathematical model of the force balance argument represented in (a). (c) Schematic representation of stresses and traction forces in a 2D monolayer. Taken from [84]

A complete discussion of this method can be found in [84]. Here I will discuss only shortly some important assumptions and limitations.

First, one needs to define some boundary conditions in order to solve Equation 2.9. In experiments where the whole monolayer is in the field of view, the boundary conditions are simply that the normal stresses at the edge are 0. This can be understood easily in the tug-of-war analogy, where, at the end of the rope, there is no other person to pull at. In experiments where the monolayer extends outside of the field of view, the boundary conditions are unknown. To overcome this, one has to assume that the monolayer inside the field of view can be extended symmetrically outside the field of view. We are not concerned with this here, since in our application the cells are always inside the field of view. Additionally, one has to assume certain material properties of the cell layer. In general, it is assumed to be a thin, elastic, homogeneous, isotropic and contractile sheet, but these assumptions are much less restrictive than they initially sound.

First, it is not required to assume a certain Young's modulus of the cell sheet. Intuitively this can be understood by the fact that elastic, passive stress that builds up during contraction and active stress that arises from the contraction itself, are interchangeable. Second, a Poisson ratio ν of the monolayer has to be assumed. Although the equations do depend on this parameter, the solution changes only slightly for big variations in ν. Tambe et al. compared results with $\nu = 0.5$ to results with $\nu = 0.3$ and they are virtually indistinguishable. Third, potential viscous properties of the monolayer would not have any influence on the recovered stress, as this technique does not give any information of the time dependence on the recovered stress, but only calculate them for the exact time point where

forces were recovered. Potential viscous properties would thus be reflected in the recovered traction forces, which can be measured over time and are thus implicitly being taken care of. Lastly, the homogeneity of the monolayer might be the biggest source of artifacts in this technique. Still, if one assumes a heterogeneous elastic modulus that is e.g. proportional to the internal normal stress, Tambe et al. found only marginal differences in the final recovered stress map, just with exaggerated peaks and valleys.

Although this technique has been developed already in 2010, only recently it has been democratized in a publicly available algorithm, published by Bauer et al. [85]. The software Bauer et al. published is called "pyTFM" and is a complete TFM toolbox implemented in python, which allows to do all the analyses discussed so far, i.e. measurement of the substrate deformation, calculation of the traction forces and calculation of the cell internal stresses. The module that calculates the cell stress from the traction forces has been used for this work.

2.1.4 Implementation of the whole analysis pipeline

During the whole duration of my PhD, I used the MATLAB script that was implemented by Irène Wang in our team, which uses a combined PIV+PTV approach for substrate displacement measurement and FTTC with a 0th order regularization scheme to calculate the traction forces. It is optimized for batch analysis of movies, which allowed for the necessary throughput to accomplish this work. During the end of my PhD, when Bauer et al. published their pyTFM, I developed an interface between the output of our TFM script and the MSM module of pyTFM. Although this worked pretty well, this analysis pipeline had some disadvantages.

First of all, the bead displacements in my experiments were quite large, in many cases over 5 times the diameter of the marker beads. I only managed to track them well with quite computationally intensive PIV parameters, i.e. with small window sizes of about 16 pixels, and after an implementation of a median and a threshold filter in order to remove badly tracked beads. In order to still be able to track entire movies in a reasonable amount of time, I had to use a version of the tracking algorithm that tracks the markers with reference to the previous time frame, instead of comparing every time frame to the reference image. This allowed me to use the very small PIV window sizes only for the first frame and then use big-

ger window sizes for all the other frames, where displacements are much smaller. This approach brought analysis time down to about half an hour per movie, but has the major disadvantage of accumulating noise with each frame, since every measurement depends on the previous measurement. This is particularly problematic, when looking at the strain energy stored in the substrate, because here the measurement gets effectively squared by multiplying the displacement with the traction field. The noise present in the displacement field generally has a mean of 0, but when taking the square of this noise, the mean shifts to a positive value proportional to the standard deviation of the noise. Thus, accumulating noise over time leads to a systematic increase of strain energy that is purely artifactual. In order to overcome this, I implemented a noise correction routine that measures the strain energy in an area outside of the cell where there should be 0 strain energy and then used this measurement to correct the strain energy measurement in the substrate under the cell. Second, maybe rather minor disadvantage, is that our TFM algorithm was implemented in MATLAB, a proprietary software, which hinders the democratization of this tool. Last but not least, the fact that the MSM part from pyTFM was implemented in python and our script was implemented in MATLAB made it impossible to have an integrated and smooth analysis workflow.

For these reasons, greatly inspired by the publication of pyTFM, I decided to implement my own TFM+MSM workflow. I did not aim at improving the accuracy or the resolution of the MATLAB script used for this work, but rather at improving usability, interface-ability with MSM and other practical aspects of the analysis. Therefore, I did not use it to reanalyze my previously obtained data. Based on this, I defined the following design criteria:

1. Batch analysis of movies should be automatic, fast and easy. It should be possible to load several movies into the pipeline, let the algorithm run e.g. over night and have all the results the next day. For this, I aimed at about half an hour to one hour analysis time per 1000x1000 pixel movie with 60 frames[9].

2. The whole pipeline should be fully automatic, from the image preprocessing, i.e. removing background and enhancing contrast, to the deformation measurement, the traction force and the cell stress calculation.

[9]Not including the MSM part, which takes about 1.5 hours per movie in my case

3. Every step of the analysis should be visualized and saved in a movie that is compressed, in order to save hard drive space, but can still be opened and manipulated in ImageJ.

4. It should be open source and as easy to use as possible. Ideally, it would have a graphical interface and does not require complicated installation of various packages in a python environment for example.

Based on these criteria, I made the following design choices:

1. Everything is implemented in python, in order to interface easily with pyTFM and to be completely open source

2. I use dense optical flow, which is quite slow, to get an estimation for the displacement field between first frame and reference image. Then this estimation is used to track individual beads in every frame with respect to the reference frame. This approach makes use of the small displacements during the movie without the disadvantage of accumulating noise over time

3. I use 0th order regularization FTTC to calculate traction forces, as implemented in our MATLAB script

4. I use the MSM module of pyTFM to calculate cell stresses.

So far I implemented a proof of principle and an example output of the script is shown in Figure 2.6 [10]. Future work will aim at rigorously testing the accuracy of the analyses on synthetic data and on data from other people, as well as implementing a graphical interface and an easy to install python distribution that improves the user-friendliness of the script.

Next, in order to validate both the analysis method of the MATLAB script used for this work and compare it with my own script, we decided to analyse a set of synthetic data, where the correct displacement field and traction force field are known. The focus of comparison here is on the choice of the bead tracking approach, since this is where I decided to use optical flow instead of PIV. For this, I used the simulated displacement field with the corresponding simulated traction stress field to create a test data set. The simulated data was kindly provided by Johannes Blumberg from Ulrich Schwarz's lab. I then used a reference image

[10] The actual outputs are movies in .gif format, but here only the last frame is shown

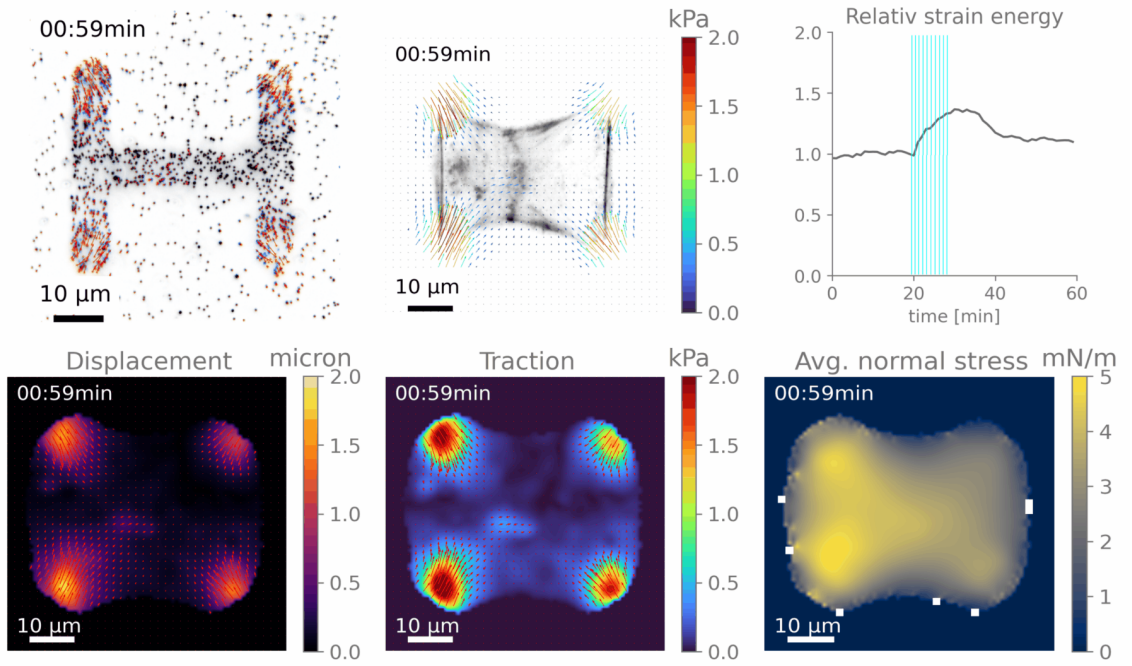

Figure 2.6: Top left: Tracking of beads between image of beads in relaxed and stressed gel. Bottom left: Displacement map obtained by interpolating measurements from top left on a regular grid. Middle column: Traction forces calculated from displacement fields, overlaid over actin images of the cells (top) and with a heat map of the substrate traction stress (bottom). Top right: Strain energy stored in the substrate over the course of the experiment, normalized by the initial strain energy value. Bottom right: Average normal stress in the cell, obtained by applying an MSM algorithm to the traction force maps.

from one of my experiments and used the simulated deformation field to deform the image. I then analyzed these two images with the different displacement field measurement methods discussed previously. Figure 2.7 (a) shows the result of this comparison, where I compared:

- PIV, implemented with openPIV in python
- PIV+PTV, as previously implemented in MATLAB by Irène Wang in the team, which is the implementation that was used throughout this work
- Dense optical flow, or more precisely, the Lucas-Kanade method
- Dense optical flow with subsequent PTV

For all the displacement fields I then calculated the traction stress field with FTTC and 0th order regularization (Figure 2.7 (b)) and calculated the strain energies for all the different situations (Figure 2.7 (c)). Qualitative comparison of the displacement field and traction stress maps with the simulated data show best results for optical flow and for PIV+PTV. Adding PTV to the optical flow in my

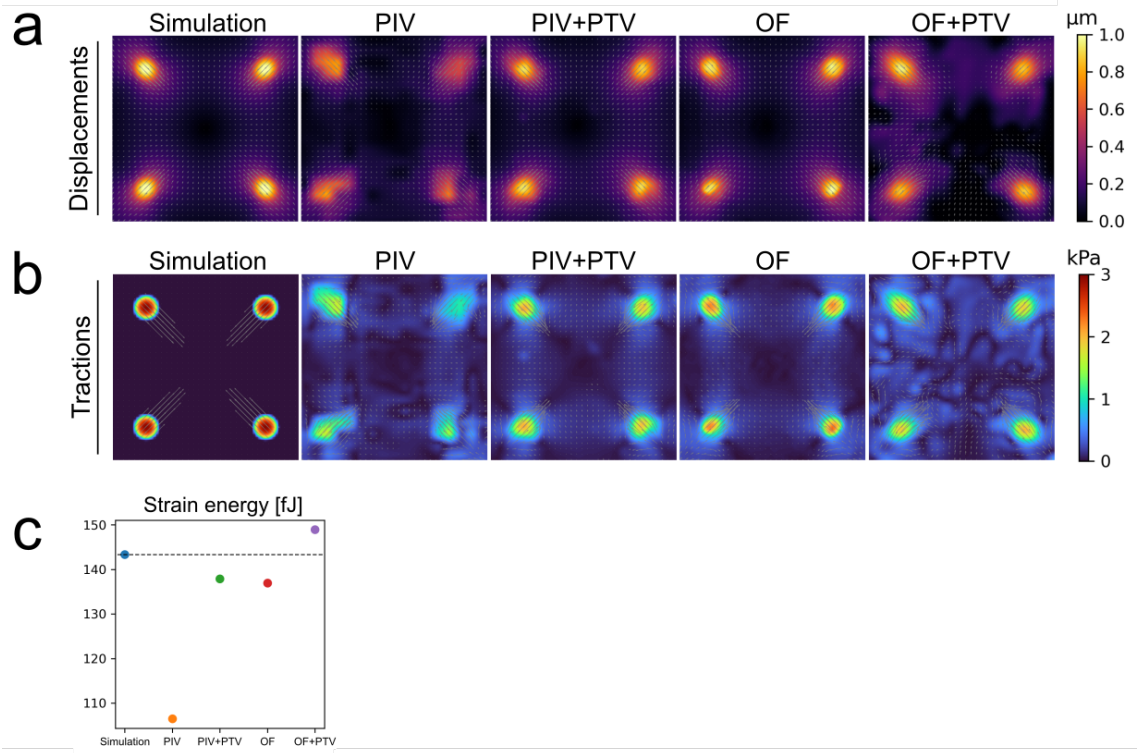

Figure 2.7: (a) The simulated displacement field on the left was used to deform an example image of beads and these two images were then used to test the different displacement measurement methods. This displacement field was then measured on the bead images with PIV, PIV+PTV, optical flow (OF) and with OF+PTV. (b) shows the correct traction stress field for the simulated data on the left, and the traction stress fields that were calculated from the displacement fields in (a). (c) shows the strain energy stored in the substrate for the different test conditions.

implementation, seemed to have introduced mostly noise and not improve the measurement. In my implementation, I crop a window slightly larger then the size of a bead around the locations where the beads are expected and measure their position by fitting a 2D Gauss-profile to the image. A possible improvement could be, to crop larger windows and detect several particles at once and associate them to the several particles in the reference image. This is also the approach used in the PIV+PTV approach implemented by Irène Wang. Another approach could be, to just use optical flow, which seems to yield results as good as PIV+PTV. This is also reflected in the comparison of strain energies shown in Figure 2.7 (c), where PIV+PTV yielded the most accurate result, closely followed by optical flow and optical flow+PTV. PIV by itself shows the least accurate results.

However, the results obtained by any of the different approaches depend strongly on the quality of the images, the density of the beads, the concrete implementation of the algorithm, the chosen parameters, the spatial distribution and magnitude of

the forces, etc. The framework here presented could be used to study the impact of all these different parameters to evaluate more precisely the performance of the different approaches, which could be the subject of a future project.

2.1.5 Strategies to improve certain aspects of TFM

TFM has become a standard tool to measure cellular forces and as such, many people keep developing this tool in order to improve spatial resolution, work on more complicated substrates or increase dimensionality from 2D to 3D. Here I will briefly discuss some of the strategies that have been developed to make these improvements.

One limitation of TFM compared to e.g. the micropillar approach, is that the cells have to be removed from the substrate after the experiment in order to record a reference image of the unstressed gel. In some experiments it would be interesting to fix the cells after the force measurement to stain for certain proteins, which is not possible with a classical TFM approach. To overcome this limitation, two solutions have been successfully employed. One solution is to create a periodic and homogeneous pattern in the substrate that can be tracked, instead of having marker beads being randomly distributed. This requires more sophisticated sample preparation methods and was successfully developed by Balaban et al. through micro-fabrication of fluorescent, regular patterns [86] (Figure 2.8 (a)) and further improved by Bergert et al. [87] (Figure 2.8 (b)), by embedding quantum dots in a regular grid with a nanodrip-printing method. Another solution is to add the fixation and immunostaining step in between the imaging of the stressed gel and the unstressed gel. This poses some practical challenges, as one has to get an image of the unstressed gel before seeding the cells. To do this, one needs to take high magnification images of the whole gel. Despite the practical challenges, this approach was successfully employed by Kollimada et al. [88].

In order to improve spatial resolution, one needs to increase the density of marker beads. At some point, the density will be so high, that the optical resolution limit will make it impossible to distinguish two beads close to each other. Therefore, one straightforward approach to improve spatial resolution, is to use a super-resolution technique to take the bead images. This has successfully been done with STED by Colin-York et al. [89], as shown in Figure 2.9 (b). Another

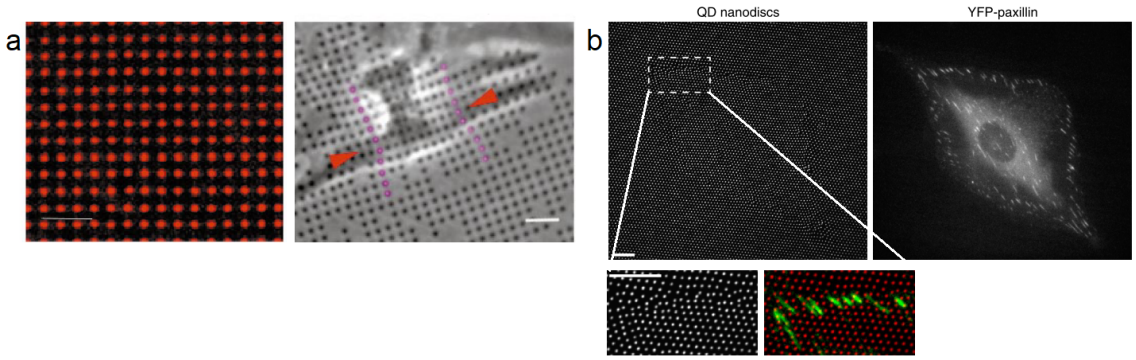

Figure 2.8: (a) Patterned elastomer without (left) and with (right) cardiac fibroblast for reference free TFM. Purple marked dots highlight the deformation of the regular grid induced by the cell. Scale bar is 6 μm. Taken from [86] (b) Regular grid of quantum dot nanodisc in a hydrogel (left) and paxilin staining of a rat fibroblast cell (right). The regular grid gets deformed by the cell, allowing for reference free measurement of traction forces. Scale bar is 10 μm. Taken from [87].

approach to effectively increase marker density, is to use beads of two different colors, as shown in Figure 2.9 (a). With that approach, one can obtain two independent measurements of the same substrate deformation, which can then be used together to get a more accurately resolved displacement field [75, 90]. In principle, this approach can be extended to three or even more different colors.

In order to increase dimensionality to 3D, the problems to overcome are mostly computational and theoretical and require a good 3D image data set, for example by using a confocal microscope. A discussion of the mathematical nuances is beyond the scope of this work, but 3D TFM has been successfully employed by measuring normal displacements, in addition to lateral displacements, of marker beads on a flat substrate [91], on cells fully embedded in a 3D matrix of an elastic hydrogel [92] (see Figure 2.10 (a)), of cells embedded in a 3D matrix of collagen [93] (see Figure 2.10 (b)) and of cell spheroids embedded in a 3D matrix of collagen, taking advantage of the radial symmetry of this setup [94].

2.1.6 Applications of TFM outside of cell biology

Traction force microscopy was developed in the context of cell biology, which is still by the far the most widespread application of this technique. However, the principle of TFM can be applied in any context, where an object applies forces onto an elastic substrate, on the condition that markers can be embedded into the elastic substrate.

For example, Rieu et al. used TFM to study the mechanism of propulsion of

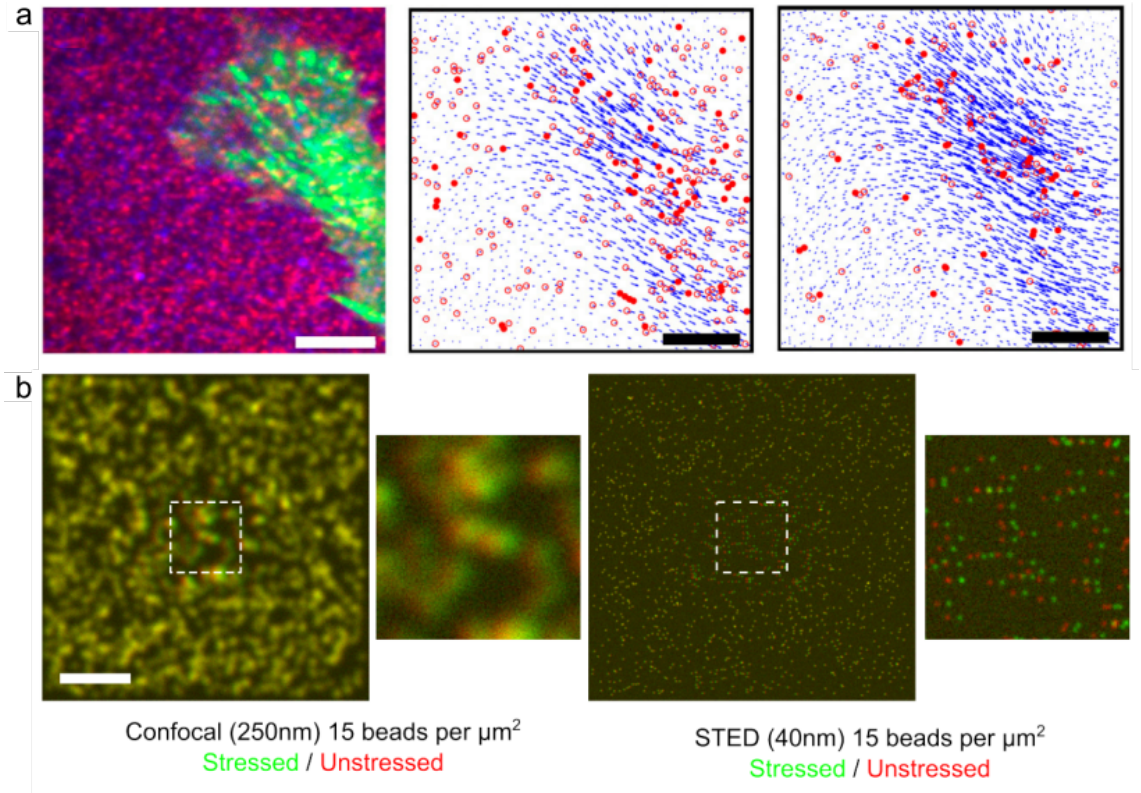

Figure 2.9: (a) The left image shows the two differently colored beads (red and blue) with a paxillin stained fibroblast cell on top of the gel. The center image shows the displacement field extracted from one color and the right image shows the displacement field extracted from both colors. Scale bar is 5 μm. Taken from [75]. (b) Confocal (left) and STED (right) images of beads in a hydrogel, before and after removing the cell. Taken from [89]

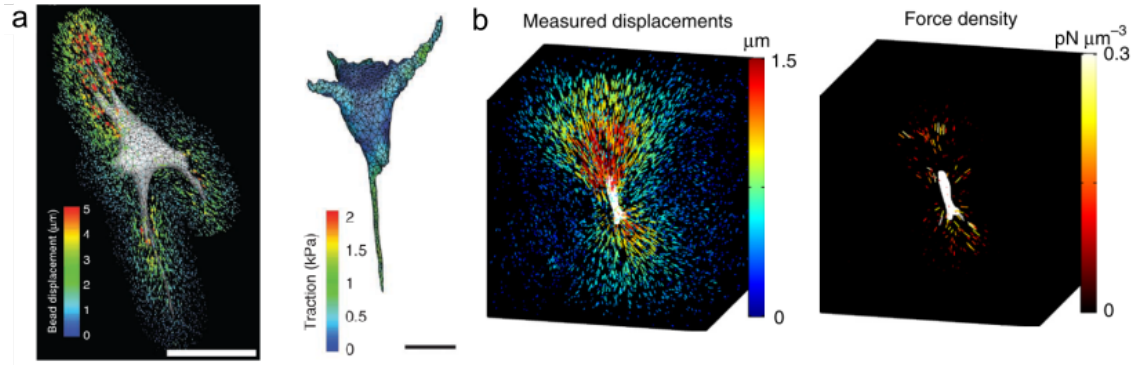

Figure 2.10: (a) Displacement field (left) and traction forces applied by a fibroblast cell in an elastic, PEG-hydrogel. Scale bar is 50 μm. Taken from [92]. (b) Displacement field (left) and traction forces applied by a breast cancer cell in a collagen gel. Taken from [93]

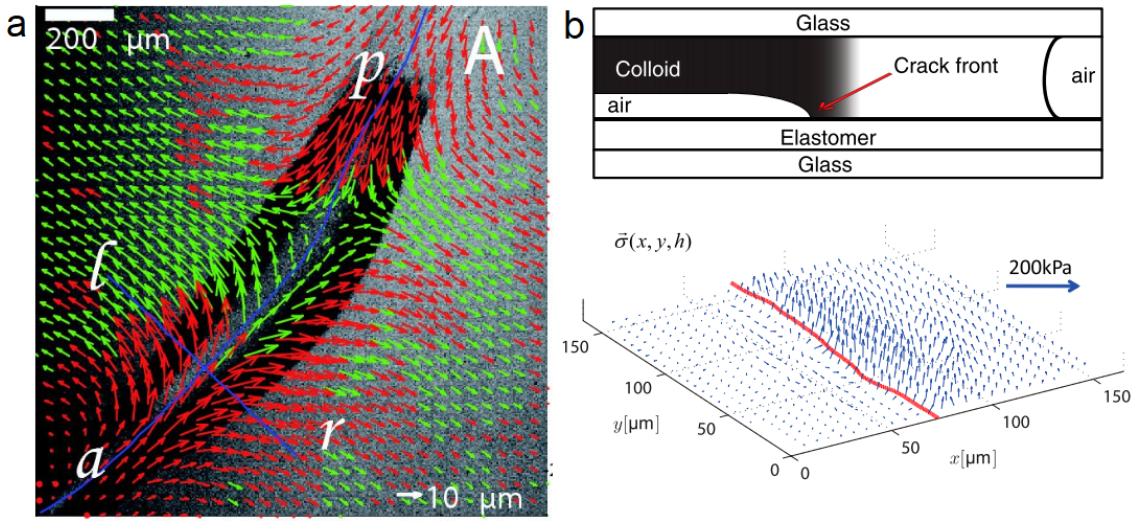

Figure 2.11: (a) Displacement field of a migrating *Dictyostelium* slug. Red arrows point out of the substrate and green arrows point into the substrate. Taken from [95]. (b) The schematic on top shows the experimental setup to perform TFM on drying paint, with the resulting 3D traction stresses shown below. Taken from [96].

the *Dictyostelium discoideum* slug [95]. *Dictyostelium discoideum* is a species of amoeba, which lives most of its life as a single, bacteria eating cell. When food supply is low, these cells can aggregate and form motile slugs of $\sim 10^5$ cells, which move towards light and finally form a fruiting body in order to disperse. How exactly these *Dictyostelium* slugs migrate is not completely understood and Rieu et al. shed some light on this question by performing 3D TFM experiments on these creatures. Figure 2.11 shows the resulting displacement map, where red arrows indicate displacements that point out of the substrate and green arrows point into the substrate. The displacements pointing away from the slug are caused by the internal pressure, similar to the turgor pressure in plant cells, of the slug. This internal pressure propels the slug forward, similarly to growing tips of fungi, where the growing/moving end is softer than the rest and gets pushed out by the internal pressure. Then the moving tip adheres to the substrate and pulls in the rest of the body.

Another example of TFM being applied to a completely different problematic was published by Xu et al., where they performed TFM experiments on drying colloidal coatings, such as paint [96]. With the experimental setup shown in Figure 2.11 (b) top, they were able to image the stresses in between an advancing crack front and the substrate over time, with black showing the already dried colloid. This represents a versatile and robust tool that can prove useful to study

when and how fractures in deposited films occur, which is important for many electronic or optical systems.

2.2 Optogenetics to modulate cell signalling pathways

Cells coordinate their behavior across length scales several orders of magnitude larger than their own size. This is particularly well observed during embryonic development, wound healing but also tissue homeostasis and when it goes awry during cancer development. For a cell, in order to coordinate their behavior in response to the surrounding cells and to the environment, it has to integrate a lot of different information from its environment, process it and ultimately translate it into behavior. This "algorithm of life" is implemented in cells in terms of a complex network of biochemical reactions, regulated by genes, their transcription into proteins and their feedback into gene transcription [97–99].

Classical approaches to study this network are loss or gain of function experiments, where some of the nodes in this network are enhanced, i.e. overexpressed, inhibited or completely removed through pharmacological or genetical intervention. This is a necessary first step to identify which nodes in this network inhibit or activate other nodes. However, this binary description of node interaction is not sufficient to fully capture the complexity of the network. Dynamic protein concentration patterns can have very different effects than continuous ones for example. Another aspect of these networks, which is difficult to capture with these kind of network diagrams, is their strong dependence on spatial organization. These spatial and dynamic dependencies are very difficult to analyse with pharmacological and genetical approaches [100].

Therefore, in order to decode the complex behaviour of each link in this network, we need new tools that allow for a more precise manipulation of those nodes. This is now possible with optogenetics, a tool that allows for powerful manipulation of protein activity through the use of light. The great advantage in using light over classical genetic and pharmacological methods, is the unprecedented sub-minute and sub-cellular spatiotemporal resolution of protein activity perturbation that is achievable. This ability allows the study of this complex sig-

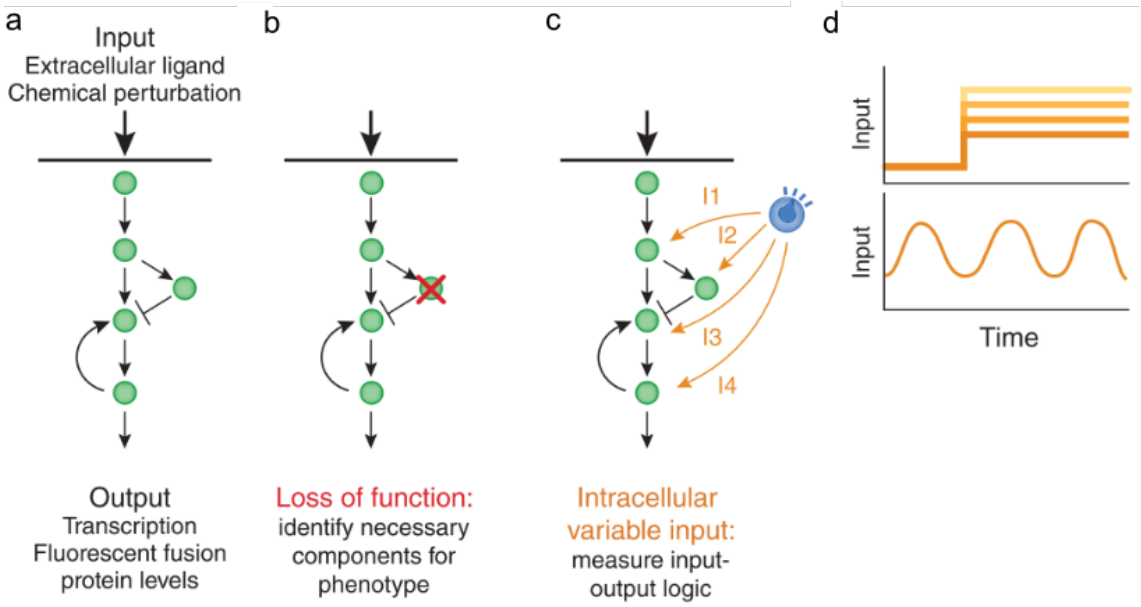

Figure 2.12: (a) Schematic of a signalling network that is chemically perturbed. The effect of the chemical perturbation can be assessed by measuring the expression levels of proteins, which are hypothesized to be affected by the perturbation. (b) Schematic of a loss of function experiment. One of the nodes can be taken out of the network by gene knock-out or silencing. The adaptation of the organism can give information about the remaining nodes in the network. (c) Schematic of an optogenetic approach to perturb this signalling network, where every link in the network can, in principle, be precisely manipulated. (d) Examples of activation functions one could apply to the signalling network. Taken from [101]

nalling network on a higher level of abstraction, seeing the network more as a black-box that transforms dynamical inputs to dynamical outputs, as illustrated in Figure 2.12 [101–103].

Different strategies exist to do this, some of which are shown in Figure 2.13. All of these strategies are based on photosensitive proteins, which were originally found in nature and then engineered to fulfill the specific functions of the desired application. A multitude of photosensitive proteins have been engineered, reacting to a wide range of wavelengths and with different response to the activation [104, 105]. Some change their confirmation and uncage a certain domain, which is then open for interaction. This can be used to directly attach a protein of interest, which can be uncaged through activation with light. Another approach, is to take a second binding partner, which binds only to the activated form of the photosensitve protein. A protein of interest can then be attached to both these proteins and then light can be used to bring these proteins together. Other light-sensitive proteins cluster into oligomers upon activation, which can be used to cluster a

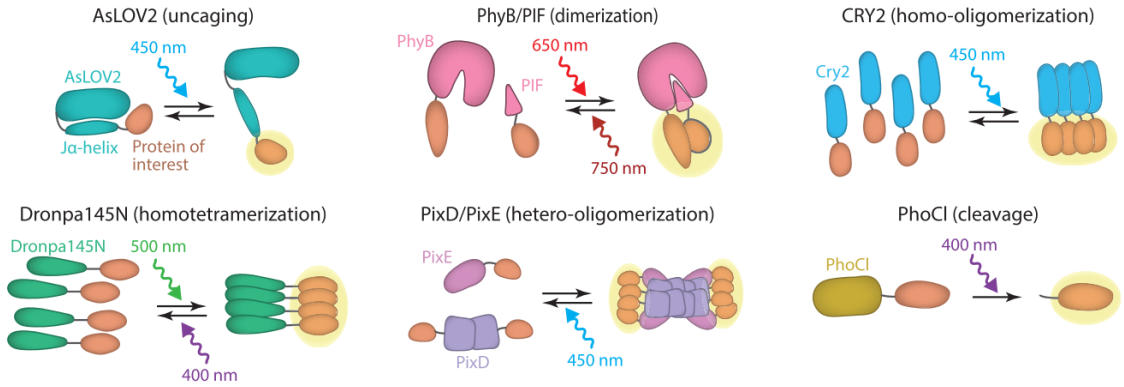

Figure 2.13: Different strategies to do optogenetics in cell signalling. Which of these approaches is adapted to a specific application strongly depends on the nature of the protein of interest. Taken from [105]

protein of interest. It is worth noting, that some of these proteins can also be inactivated by using a different wavelength. This allows for even more precise spatiotemporal control than just being able to activate and then being bound to the inactivation dynamics of the protein.

In our case we are interested in modulating the mechanical activity of cells and more particularly in their contractile state. A major regulator of cell contractility is RhoA, a small GTPase that controls both actin and myosin activity through different kinds of intermediate signalling proteins [31, 106]. RhoA is thus a great target to control with optogenetics.

2.2.1 Optogenetic manipulation of RhoA, major regulator of cell mechanical activity

Figure 2.14 shows a part of the network that RhoA is involved in. Its upstream activators are called GEFs and the upstream inhibtors are called GAPs. There are plenty of different GEFs and GAPs, which all have different activation and inhibition dynamics on RhoA. RhoA has different downstream effectors, which mostly control actin assembly and myosin activity. In order to address our research question, we need to increase cell contractility, so that we can make cells pull on each other. Therefore we need to increase myosin II activity, which is one of RhoA's downstream effectors, with ROCK being a major intermediate effector.

In order to find a way to control RhoA activity, first we need to understand how RhoA activity is regulated in nature. RhoA is a membrane bound protein, which binds GTP in its active form and GDP in its inactive form. RhoA passes from

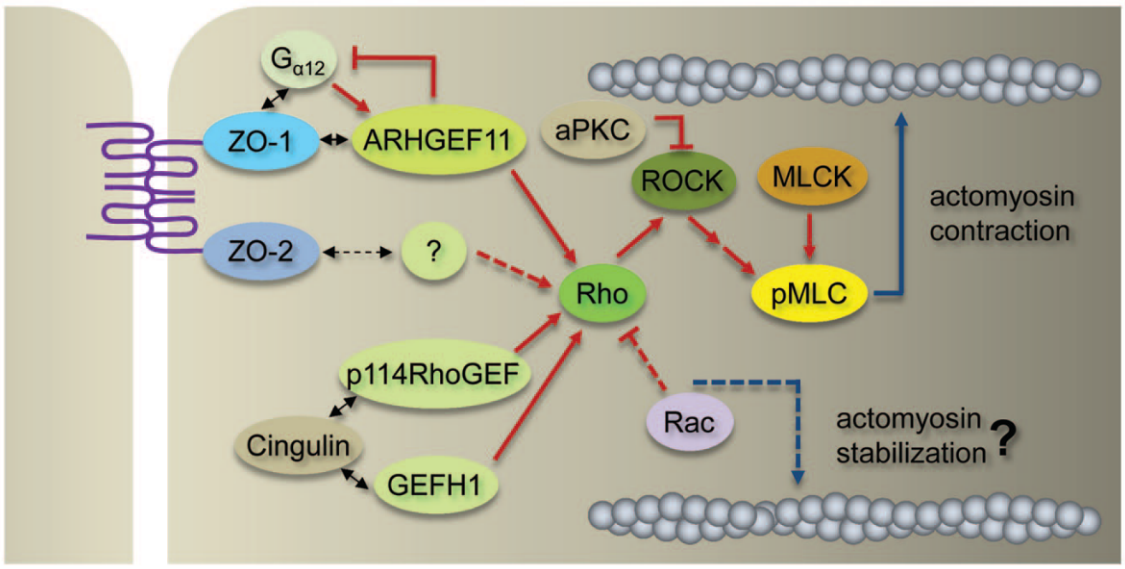

Figure 2.14: The RhoA network we want to manipulate via optogenetics. Taken from [107]

its active form to its inactive form when its GTP gets hydrolyzed to GDP, which RhoA will do by itself after a while and which can also be catalyzed by GAPs. To activate RhoA, a GEF catalyzes the exchange of GDP for GTP. Therefore, in order to activate RhoA, we either need to find a way to bring a GEF to the membrane or to remove a GAP from the membrane, the former strategy being the one that is used the most often.

In order to bring a GEF to the plasma membrane, a common strategy is to use a photosensitve protein which will form a heterodimer with another protein upon light illumination. One pair of protein that can do that is CRY2, the photosensitive one, and CIBN. The ability to recruit a protein of interest to the plasma membrane via the CRY2-CIBN system has been demonstrated by Kennedy et al. [108] and is illustrated in Figure 2.15. Upon activation with blue light, CRY2 changes its conformation and binds to CIBN, which is attached to the membrane through a CAAX linker. So in our case, in order to move a GEF to the plasma membrane, it needs to be attached to CRY2. In order to reduce the size of the protein, to facilitate its expression in cells, only the GEF domain that catalyses the activation of RhoA is attached to CRY2. A fluorescent tag is also added to both proteins, in order to verify that the recruitment of the protein works as expected.

The recruitment of CRY2 to the membrane in this construct in response to different light intensity values and activation durations has been characterized extensively by Valon et al. [109]. Valon et al. also published a proof of principle,

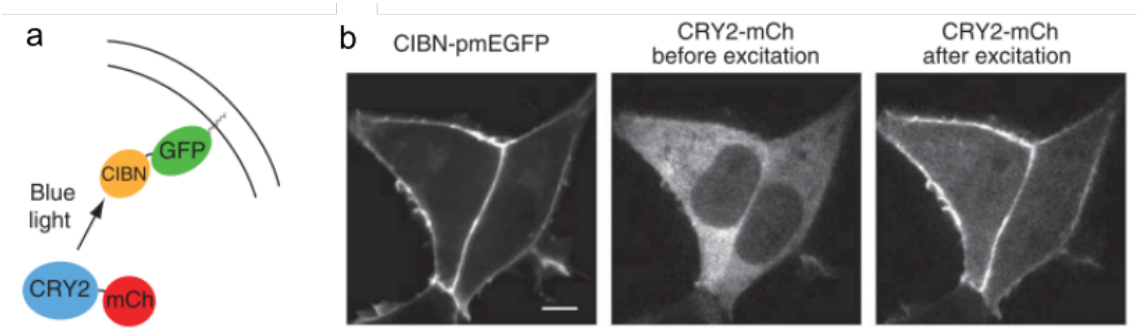

Figure 2.15: (a) A cartoon of the CRY2-CIBN system. CRY2 changes its conformation upon activation with blue light. This enables its association with CIBN, which is attached to the plasma membrane via a CAAX linker. (b) Left: A fluorescence image of CIBN, showing its localization on the plasma membrane. Center: A fluorescence image of CRY2 before photoactivation, showing its localization in the cytosol. Right: A fluorescence image of CRY2 after photoactivation, showing its localization on the plasma membrane. Taken from [108]

that this construct is able to induce cell contraction in small epithelial cell colonies [110]. Interestingly, a similar construct can also be used to reduce cell contractility, by targeting CIBN to the mitochondria, instead of the plasma membrane. This way, CRY2 get's recruited towards the mitochondria, away from the plasma membrane, reducing its activation of RhoA. Figure 2.16 (a) shows fluorescence image and the traction forces of a cell colony expressing the CRY2-CIBN system with CIBN targeted to the plasma membrane and Figure 2.16 (b) shows the same data for a cell colony expressing a CIBN that is targeted to the mitochondria. Cells in the top row were photoactivated and cells in the bottom row were not. Both the increase in traction forces and the recruitment to the plasma membrane can be seen in Figure 2.16 (a). Similarly, Figure 2.16 (b) demonstrates the recruitment of CRY2 to the mitochondria, as well as the decrease in traction forces. The control cells in the bottom row, located right next to the activated cells in the sample, do not show any response to the photoactivation, demonstrating the ability to only locally activate cells in a sample.

A similar construct has been used in *Drosophila* embryos to induce tissue invagination, as discussed in subsection 1.1.1, and in a cluster of *Xenopus* neural crest cells to induce or inhibit their collective migration [111]. A different approach, based on the same idea of heterodimerization, is used by the Gardel group to control RhoA activity. The construct is based on the LOV photosensitive protein and is schematized in Figure 2.17 (a). With this construct, Oakes et al. showed, that the elastic properties of stress fibers are mediated by a protein called "zyxin"

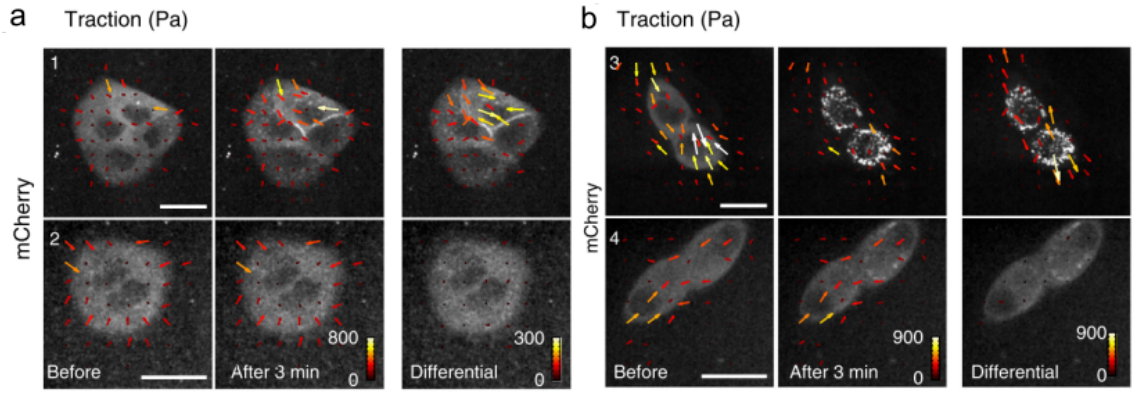

Figure 2.16: Cell colonies in the top row were photoactivated, cells in the bottom row were not. The fluorescence images show CRY2, which gets recruited to the plasma membrane in (a) and to the mitochondria in (b) after photoactivation. CRY2 fluorescence images are shown before and after activation. Traction forces are also shown before and after activation, as well as the difference between the two. Taken from [110]

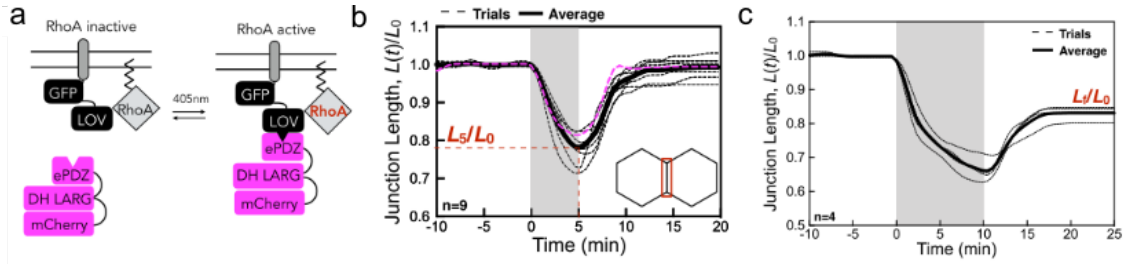

Figure 2.17: (a) A cartoon showing the optogenetic tool, based on LOV, used by the Gardel group. (b, c) The normalized junction length of a CACO2 cell pair in a monolayer over time, in response to photoactivation for 5 minutes (b) and 10 minutes (c). Taken from [113]

[112] and Cavanaugh et al. showed, that periodic RhoA activation cycles can mediate cell-cell junction shrinkage, depending on the duty cycle and the periodicity of activation [113]. They demonstrate this by photoactivating a single junction in a monolayer of CACO2 epithelial cells, cultured on a collagen gel, for different time periods. Figure 2.17 (b) shows, that photoactivation for 5 minutes leads to transient contraction of the junction, returning to its initial length, once RhoA activation is stopped. Figure 2.17 (c) shows that junctions that were continuously activated for 10 minutes did not return to the initial length, but were shortened permanently. By repeatedly applying this activation scheme, the authors showed that the junction continued to shrink in size in a ratchet-like manner.

For the project presented in this work, we wanted to modulate cell contractility with optogenetics. This can be done by using optogenetic constructs, that target RhoA, as presented in this section. To do this, we collaborate with Guillaume Charras' lab, who stably transfected MDCK cells with the CRY2/CIBN system here

presented. The advantage of this construct is, that an extensive characterization and a proof of principle is available for this tool [109, 110]. Optogenetics is still a quite young field and there are still many drawbacks in the tools being used and a lot of room for new developments. For example, it could be interesting to activate cell contractility more downstream of RhoA, since RhoA affects many other signalling pathways and not only myosin.

2.2.2 New optogenetic tools to modulate cell contractility

As a master regulator of the cytoskeleton, RhoA has been a popular target for optogenetic experiments that try to decipher the link between cell mechanics, structure and motility in many different contexts. This is due to the broad role RhoA plays in all these contexts and has been proven a fruitful approach. However, the main advantage of this approach is also the main disadvantage. By using GEFs to activate RhoA, the manipulation of the signalling network happens very far upstream of the whole signalling cascade, which gives the experiment a high chance of success to yield a clear phenotype. However, the fact that the signalling cascade is perturbed very far upstream, also means that it is not very clear, which mechanism exactly leads to the observed phenotype. For example, RhoA does not only activate myosin II contraction via ROCK, as shown in Figure 2.14, but also tends to stabilize actin filaments by activating profilin via mDia [114].

In addition to the fact that the downstream signalling of a given GEF is very complex, they also depend on the cellular and environmental context and are in general not very well known. Therefore, it could be desirable to develop new optogenetic tools, which perturb the actomyosin signalling network further downstream. Many studies, including my PhD project and the studies discussed in the previous chapter, try to address the role of myosin-mediated, cell-generated forces in different contexts, such as development and cancer. Therefore it would be interesting, to be able to modulate cell-generated forces further downstream the signalling cascade, to make sure that the observed effect is really due to the physical forces and not due to some unknown, biochemical signalling.

Figure 2.18 and [116] shows us some targets for such a construct. MLCK is a kinase that directly activates myosin and would be an excellent protein to be able to control with light. A study by Zhou et al., demonstrates a general

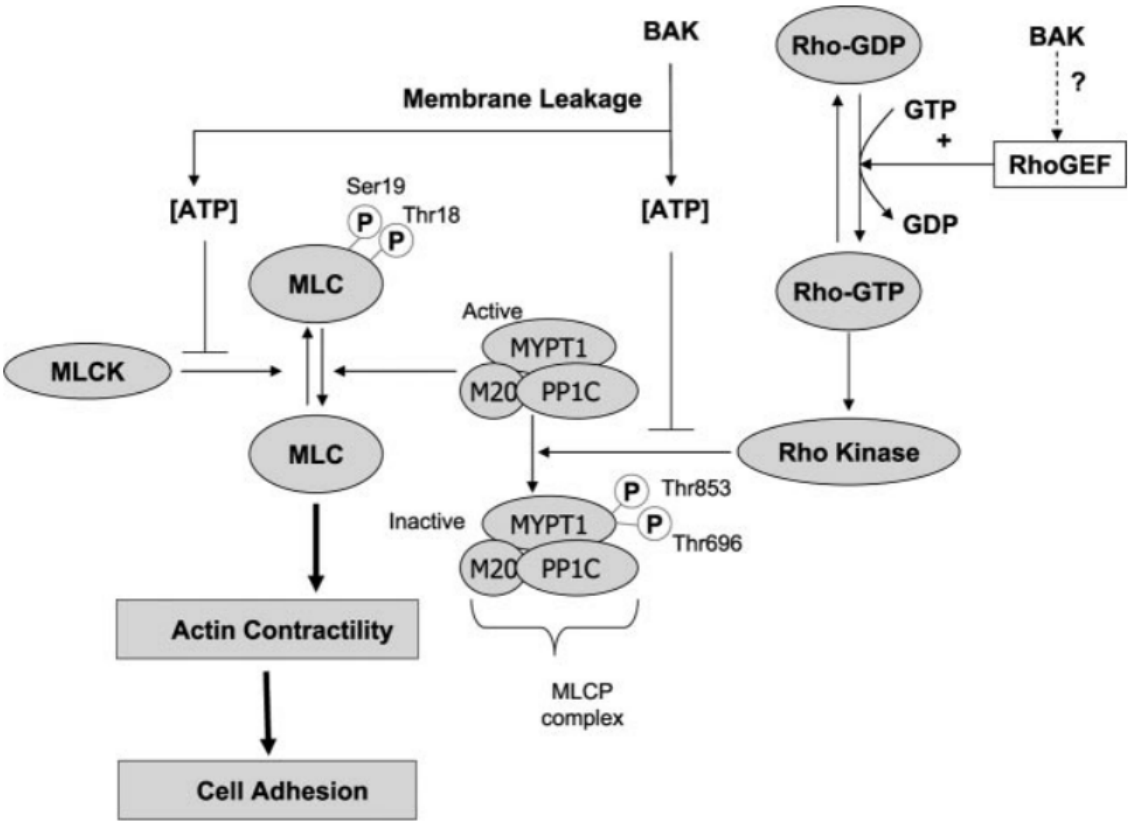

Figure 2.18: Network of regulatory proteins of myosin activity, here written as MLC (myosin light chain). [115]

approach of engineering photoswitchable kinases via the photosensitive protein Dronpa [117, 118]. Another interesting target would be MLCP, a phosphatase that deactivates myosin. A recently published study by Yamamoto et al. managed to control MLCP activity by recruiting its regulatory subunit MYPT1 to the plasma membrane via the iLID system [119]. With this system, the authors are able to directly reduce cell contractility, without passing through intermediate signalling proteins such as ROCK. A next step that would be interesting to test, is whether cell contractility could be increased with a similar construct, by targeting MLCP to the mitochondria, away from the plasma membrane and analogous to the approach by Valon et al. [110] shown in Figure 2.16.

2.2.3 Other applications of optogenetics

So far I discussed why optogenetic is such an interesting and powerful tool in the context of this work. However, optogenetics finds much wider application and enabled a multitude of new discoveries in various other fields. I find the research opportunities opened by optogenetics to be very exciting and therefore I would

like to spend some time mentioning its applications in other fields.

Optogenetics was first used in neuroscience to control the activity of certain ion channels with light [120, 121]. This represented a breakthrough for neuroscience research for similar reasons as I described in the previous section. With this approach, specific cells in an organism can be targeted and action potentials in those cells can be controlled at will, by using either activating or inhibiting ion channels. By allowing to pass either positive or negative ions, an action potential can either be triggered or inhibited. This was demonstrated in a pioneering study by Yizhar et al., where they used optogenetics to control neocortical activity in mice. They wanted to test the hypothesis, that the balance between excitation and inhibition in specific neural tissues can be the core cause of pathologies, such as schizophrenia and autism. They showed that shifting the balance towards excitation, either by increasing excitation or by decreasing inhibition, lead to significant impairment of social behavior in mice.

Optogenetics is now also used to control transcription in bacteria and yeast. This approach allows to implement feedback mechanisms and to use control theory concepts [122]. Whole metabolic circuits in bacteria could be engineered this way, representing exciting new opportunities for both industrial applications and academic research. For example, Benzinger et al managed to independently control the population wide variability of gene expression in yeast cells, by using a pulsating activation scheme with a fast-acting optogenetic tool [123]. More broadly, this demonstrates the possibility to reduce or increase intercellular variability, which could be used to test the robustness of multicellular processes, such as in development [124].

Controlling expression of genes by optogenetics is not only possible in bacteria and yeast, and has successfully been done *in vivo* in mouse neurons [125] and also to control expression of morphogens in a developing *Drosophila* embryo, as demonstrated by di Pietro et al [126]. With this new tool, the authors managed to induce gene expression in specific locations, during specific developmental stages and with varying intensity. With this approach, the authors could control the severity of a given phenotype by adjusting the light intensity of photoactivation, as shown in Figure 2.19 (a).

Another approach to study development with optogenetics was demonstrated by Johnson et al., in a study where they developed an optogenetic tool to control

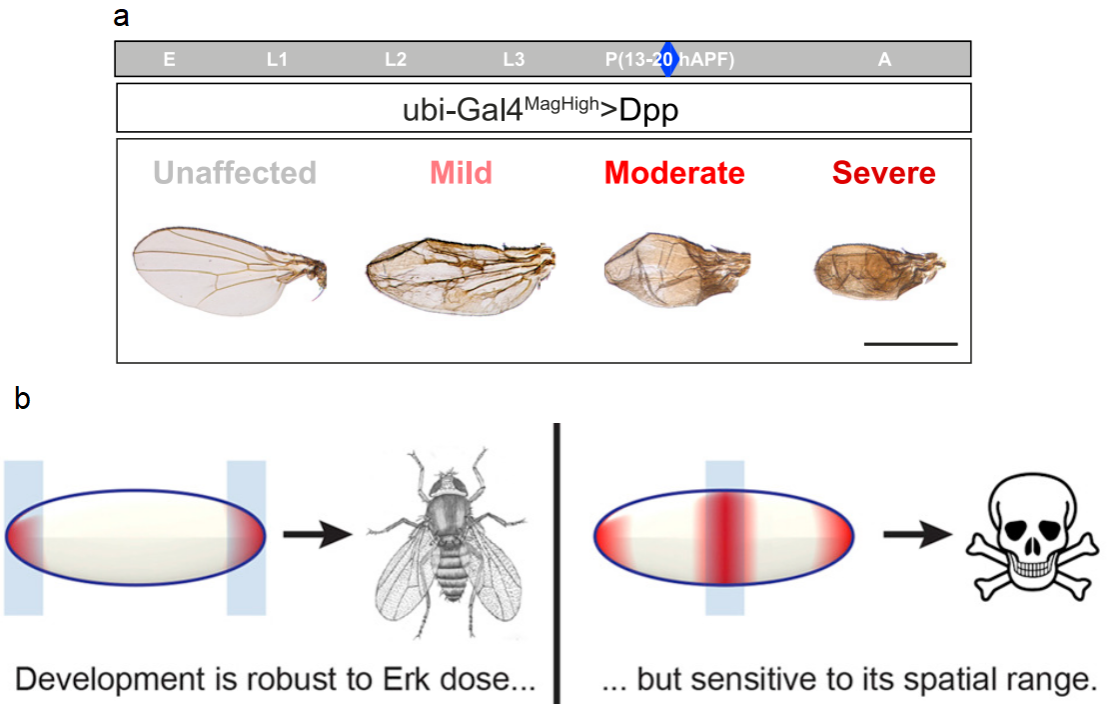

Figure 2.19: (a) Images of *Drosophila* wings with different activation intensities of Dpp overexpression, a gene that regulates ectopic vein formation in the wing. Taken from [126]. (b) Overactivation of ERK in places where it is usually active has little effect, whereas activation in other areas is lethal. Taken from [127].

ERK activity in a developing *Drosophila* embryo [127]. Taking advantage of the fact, that optogenetics allows for local photoactivation, the authors showed that increasing endogenous ERK activity at the tips of the embryo had little influence on its development, whereas activation in areas where it is not usually active was lethal, as illustrated in Figure 2.19 (b).

Taken together, these studies show the power of optogenetic tools to address important biological questions in many different fields, including neuroscience, microbiology and development.

2.3 Micropatterning to impose geometrical boundary conditions on cells

In multicellular systems, cells live in a highly structured and well defined micro-environment. The mechanical, geometrical and chemical properties of this micro-environment have a strong influence on the cell's behavior, which are in turn shaped by the cells as a collective as well. Together, from this constant feedback between cell behaviour and micro-environmental parameters emerge the highly

organized structures with very specialized functions that we see in multicellular systems.

In order to elucidate the effects of these different types of micro-environmental parameters, scientists deployed many different techniques to single out specific parameters and reconstitute them *in vitro*. This micro-engineering approach allows to vary the micro-environmental parameters over a wide, physiological and potentially pathological, range. Figure 2.20 shows different methods that can be used to modify some of the potentially relevant parameters, such as ligand density, ligand geometry, matrix stiffness or external stresses.

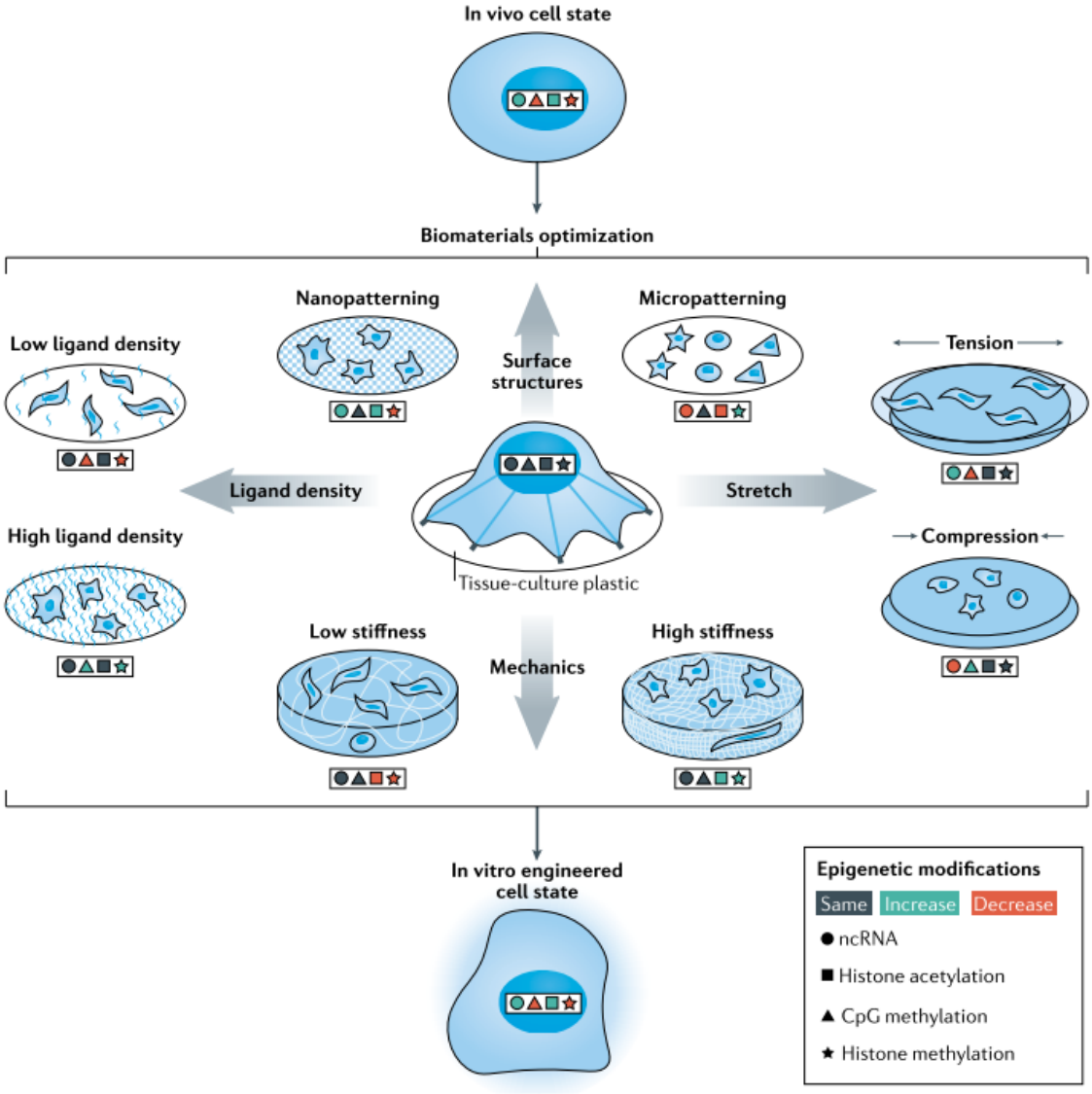

Figure 2.20: A cartoon reviewing how mechanical, geometrical and chemical boundary conditions influence gene expression in cells. The cartoon also schematizes how those influences can be studied *in vitro* through micro-engineering of the cellular environment. Taken from [128].

With this micro-engineering approach, scientists showed that cells are sensitive

to different kinds of physical parameters, such as the rigidity of the local environment [26], the shear stress induced by flowing liquids [129] or by other cells [83], or by the geometry of the extracellular matrix (ECM) the cells can adhere to [2].

Here I want to focus on the influence of ECM geometry on cell shape and mechanical properties. To study this, the cell is presented with a specific, generally 2D, geometry of adhesive island and then let spread freely on this pattern. This technique, called micropatterning, has proven to be a useful tool to elucidated how cells organize their cytoskeleton and adapt their tensional state to these geometrical conditions.

2.3.1 Micropatterning to study single cell morphogenesis

One important aspect of the micro-environment of cells is the spatial confinement cells generally experience due to surrounding cells. With micropatterns, the area that a cell can spread on can be limited to small islands. When cells are confined to small circle patterns, comparable to the *in vivo* situation, where cell spreading is limited by surrounding cells, cells establish apico-basal polarity, with the centrosome positioned on the apical surface and a primary cillium growing out of it [130]. On bigger patterns, cells are much flatter, more contractile and form stress fibers spanning across the cell [131].

When plated on patterns with edges, like a triangle, cells form focal adhesions at the most distal parts from the center, grow protrusions and form stress fibers in between the focal adhesions [132]. When presented with non-adhesive area in between adhesive regions, cells can spread over those areas by forming thick and highly contractile stress fibers to bridge the gap [43]. A cartoon summarizing all these findings is shown in Figure 2.21 (a). Planar cell polarity is also influenced by geometrical cues, as demonstrated by the crossbow shape in Figure 2.21 (b). Cells spreading across these patterns align their nucleus-centrosome-golgi complex axis with the symmetry axis of the pattern [133].

The fact that the ECM geometry influences cell planar polarity has important downstream effects on cell behavior. For example, when migrating on wide stripes, the cell migrates similarly to a cell on a flat, unpatterned substrate, with lamellipodial protrusions on its front and with the cetrosome oriented towards the front. In contrast, on thin lines cells migrate faster and with the centrosome in the back,

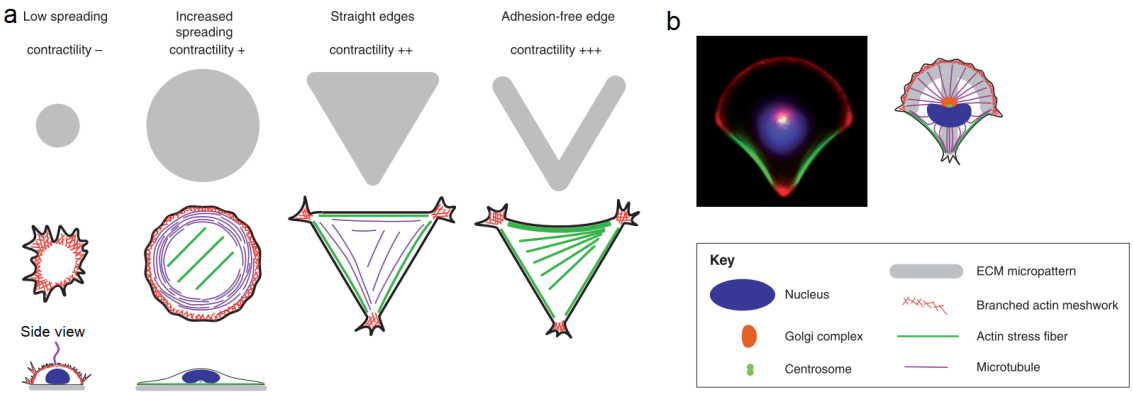

Figure 2.21: A cartoon summarizing some important finding on how cells adapt their morphology to the ECM geometry. On small, compared to big circle patterns, cells stay more round, are less contractile and grow a cillium with the centrosome being positioned closed to the apical surface. On bigger patterns, the centrosome is positioned at the basal surface, cells are flat, highly contractile an form stress fibers across the pattern. On patterns with edges, focal adhesions form at the most distal part in the corners and the cell forms stress fibers in between. If adhesive area is taken out in the center of the triangle, the cell spreads over the non-adhesive area and forms thick, highly contractile stress fibers that bridge the non-adhesive area. Taken and modified from [131].

which more closely resembles the migration mode observed when embedded in a 3D fibrillar ECM matrix (e.g. a collagen gel) [134]. Micropatterns in form of thin lines thus represent an interesting migration assay. Not only does it more closely resemble the *in vivo* situation, it also facilitates data analysis and statistics, since cells can only migrate in two directions and the spatial confinement also allows to observe more cells in a given field of view, without the risk of having them collide into each other.

2.3.2 Micropatterning to study collective cell behavior

Micropatterning approaches have also been employed successfully to study multicellular assemblies. The simplest multicellular assembly of just two cells has been reviewed extensively in subsection 1.2.2 and many of the highlighted studies use micropatterns. Segerer et al. looked at slightly bigger tissues of 2 to 8 cells on circular patterns [135]. They found that those small tissues start to rotate around each other, akin to vortex formation in monolayers, which is a common pattern observed in all kinds of systems of self-propelled, active matter. In their study on small micropatterns, the authors found that the persistence of the rotational movement increases with the number of cells, but dips at a 5-cell configuration. This is due to the fact that the cells geometrically rearrange in a way as to con-

tain one cell in the center. In this configuration, the outer cells are polarized and move into one direction, but the center cell is only weakly polarized and resists the movement of the surrounding cells.

Similar circular movement patterns have been observed by Peyret et al. on bigger tissues, plated on square micropatterns of about 500 μm width [136]. Here, the authors found that the spatial and temporal frequency is mostly determined by the smallest dimension of the pattern. These oscillatory movements were completely abolished, when cell-cell adhesion was perturbed through an α-actinin knockout, demonstrating the fact that these emergent dynamic patterns are dependent on cell-cell interactions. Additionally, the authors found, that the observed, oscillatory collective movements are correlated with oscillatory, nuclear translocation of YAP, a well known transcription factor known to be mechanosensitive.

Another study by Vedula et al. looked at collective cell migration of keratinocyte cells on finger-like, small stripes with a width of about 10 μm and separated by about 120 μm [137]. In their barrier function in the skin *in vivo*, these cells have to be able to collectively migrate over heterogeneously adhesive matrix without losing cohesiveness, in order to maintain tissue integrity. In their micropattern, migration assay, the authors found, that the tissue could collectively migrate over these widely spaced, thin lines, by forming supracellular bridges, suspended over the non-adhesive areas.

All these examples have in common, that the cells on those patterns were highly dynamic and did not show exact positioning of the cells. To our knowledge, so far this has only been demonstrated by Tseng et al. in cell doublets, where they showed that cell doublets on square patterns rotate around each other, whereas on H-patterns they stay stable with a well defined position of the cell-cell junction [50]. Finding a pattern that stabilizes more complicated structures of more than two cells could be an important advance to understand how cells organize themselves, especially for tissue engineering applications. In this work, we present some preliminary results of stable cell quadruplets, which could also be an interesting, minimal model to study the mechanics of T1 transition. This is discussed in more detail in chapter 4.

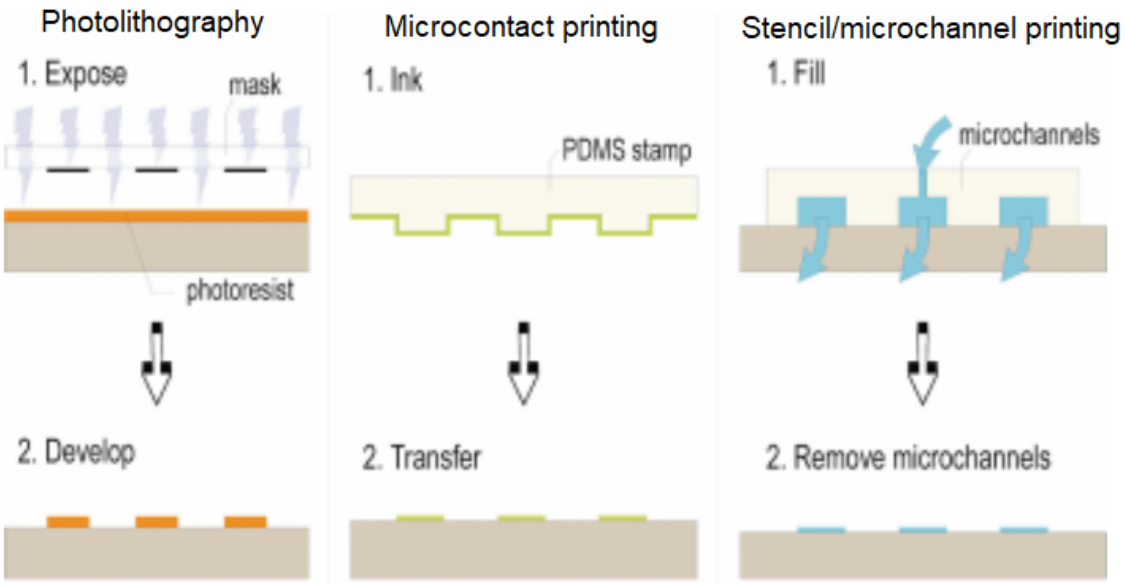

Figure 2.22: A cartoon describing the different approaches to fabricate micropatterns. Taken and adapted from [142]

2.3.3 Micropattern fabrication methods

Since their first use in cell biology, micropatterns have now become a widely spread tool to control and modify the shape of both single cells and small tissues. As such, many different protocols and methods have been developed [138–141], which can be categorised into three main approaches: Photolithography based, micro-contact printing and stencil based. A cartoon showing the principle of these different approaches is shown in Figure 2.22.

These methods all result in a glass coverslip with patterned adhesive islands that cells can adhere to. If one wishes to do TFM in addition to using micropatterns, the underlying substrate needs to be soft, so the protocols have to be adapted to work on soft substrates. There are protocols that make the patterns directly on polyacrylamide gels, but the most common approach is to make the patterns on glass and then transfer them onto a polyacrylamide gel.

The method used in this work is based on photolithography on glass with subsequent transfer to a gel. For the photolithography part, a photomask containing the micropatterns is required, which means that one needs to design and buy a new photomask every time one wishes to use a new type of pattern. To overcome this limitation, a company called "Alvéole" recently developed a product called "PRIMO", which allows to make micropatterns without photomask by using something similar to a videoprojector.

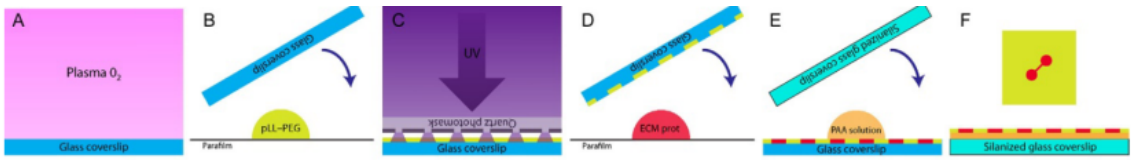

Figure 2.23: A cartoon describing the method to fabricate micropatterns on polyacrylamide gels that was used in this work. Taken from [141].

The procedure using a photomask is sketched out in Figure 2.23. In short, first a glass coverslip is cleaned with Isopropanol and then activated in an oxygen or air plasma. Then, a drop of pLL-PEG is deposited on parafilm and the activated surface of the coverslip is placed on the drop. The pLL-PEG will self-assemble a dense polymer brush on the coverslip which is highly hydrophobic. This will ensure that neither cells nor proteins can adhere to unwanted areas of the coverslip. Next, a droplet of water is placed on a quartz photomask which has holes in the form of the desired patterns. The water will make sure that the coverslip sticks to the photomask. Both the mask and the coverslip are then placed in a deep UV oven for 5 minutes, which will burn away the passivisation layer at places where the photomask has holes in form of the pattern. Then, this patterned coverslip is placed on top of a drop of ECM protein[11]. Last but not least, a drop of unpolymerized polycrylamide mixed with catalyzers is placed in between the patterned coverslip and a second, silanized coverslip. The polyacrylamide then polymerizes and the silanization of the top coverslip ensures that the gel adheres to it. Then, when polymerization is finished, the silanized coverslip can be peeled off and will rip off the patterns from the lower coverslip.

The protocol that I used during my PhD is described and discussed in great detail in [141]. The exact protocol that I followed is found in section 5.2, but differs only slightly from the process described in [141].

A second method is described in [141], where the pLL-PEG layer is deposited directly on the photomask, instead of using a coverslip. This method achieves better spatial resolution, but it will leave traces on the photomask which are very difficult to remove. It is thus not recommended, unless one wishes to print very fine features.

The PRIMO system has the great advantage of being able to quickly test any new ideas of patterns, without having to go through the whole process of design-

[11]The most common ones used are fibronectin and monomeric collagen I, but in principle any protein can be used, provided it will adhere to glass.

ing and buying a photomask. The same protocol as just described can be applied here, with the exeption of the UV burning step. Here, instead of a photomask, PRIMO uses a UV lamp and a digital micro-mirror device (DMD) that is attached to the microscope. A DMD is a dense array of micro-mirrors, which can be individually controlled to either shine light onto or away from the sample. This DMD is connected on one side to a UV lamp and to an objective of a microscope on the other side. This allows for the projection of arbitrary (pixelated) shapes through the objective onto the sample. Different grey levels, which translate to different protein concentrations, can be achieved by flipping the corresponding micro-mirror on and off at a certain frequency.

This process requires serial printing of micropatterns, one microscope field of view at a time. Therefore it would be unacceptable if that process took 5 minutes for every field of view, as is the case for the classical method with photomask. For this reason, Alvéole developed a photocatalyzer, accelerating the process 10-fold. Even with this improvement, it is still orders of magnitude slower than classical methods. The common approach in our team is thus to do rapid prototyping with the PRIMO, and once a pattern is found that works well for whatever research question we want to study, we design and order a photomask with these patterns.

3. Results & discussion

In this chapter, I will discuss the results I obtained during my PhD. In the first section I will talk about how we established the experimental conditions that we then used to address our main research question of force propagation in cell doublets and small monolayers. When I arrived in the lab, our collaborators from Guillaume Charras' lab were still in the process of creating the cell line that I later used for this work [1]. Additionally, there was only one publication demonstrating contraction of an equivalent cell line via TFM, but on small cell colonies and always activating many cells at once. Therefore, I was one of the first people using these cells and establishing an experimental protocol turned out to be quite challenging. There are two main issues that I had to find a solution to: First, the contraction induced by photoactivation in single cells is extremely variable from one cell to another. Part of this variability comes from the variability in expression of the optogenetic construct. Another big contribution to variability comes from the cells itself, which form different actin structures, which might express different levels of myosin, different levels of RhoA, etc. The second issue is, that the contractile state of these cells is in many occasions highly dynamic already without photoactivation. Many cells display an increase or a decrease of contractility before photoactivation and these dynamic trends are then superposed to the contraction induced by photoactivation. These baseline instabilities are in many cases of the some order of magnitude than the optogenetically induced contraction, especially when I used only single photoactivation pulses. This is mostly a problem when doing experiments in a few cells, since in bigger collections of cells, the variabilities tend to average out and the resulting amplitude of contraction is much less variable. For these reasons, I spent a lot of time in the first and part of the second year of my PhD into optimizing the experimental conditions and trying

[1] As a reminder, these are MDCK (epithelial) cells, transfected with an optogenetic system based on CRY2 and CIBN, allowing to activate RhoA with high spatiotemporal resolution

to maximize the contraction that we can induce in our system.

In the second section, I will present the main result of my PhD, where I address the research question raised in the introduction: How does one cell pulling on another cell influence that other cell? The results here are presented in the form of a paper draft, which we are in the process of finalizing.

In the third section, I will present results from two of the collaborations, that I had the chance to work on during my PhD. In these collaborations, our collaborators were interested in quantifying cell-cell and cell-substrate adhesion strength in mesodermic stem cells from the *Xenopus* embryo in one case and in breast cancer epithelial cells in the other case. Both these parameters are highly relevant for regulating embryonic developmental processes and also for cancer development and progression. We used H micropatterns to induce doublet formation in these cells and TFM to quantify cell-substrate and cell-cell forces, which are indirect indicators of cell-cell and cell-substrate adhesion strength.

3.1 Optimizing the experimental conditions

The experiment we want to do, is to optogenetically activate contractility of one in two cells in a cell doublet. To do this experiment, first we have to optimize the experimental conditions. There are many parameters to consider, the most important ones being listed below:

- Pattern size
- Substrate rigidity
- Seeding density
- Incubation time
- Activation pulse duration
- Activation pulse frequency
- Activation pulse power
- Activation area
- Pattern geometry

There was no experience in the lab with those cells by the time I joined and only two articles with these cells were published at that point: One characterizing the recruitment dynamics in response to different types of optical inputs [109] and one showing optogenetically induced contraction of MDCK colonies measured with TFM. Two former PhD students in the lab used 3t3 cells with the same optogenetic construct and therefore, preliminary experiments were oriented towards the typical parameters they used for their experiments. This chapter focuses on how we determined those parameters, partly by reviewing the literature, partly through practical considerations and partly through preliminary experiments.

3.1.1 Substrate rigidity and pattern size

One of the first parameters one has to fix is the size of the pattern to be used and the rigidity of the gel, since they both influence the very first step of doublet formation. They both are chosen right at the beginning of every experiment when preparing the samples.

In vivo, cells encounter a wide range of rigidities, depending on the surrounding tissue. This ranges from about 0.1 kPa in brain tissue to about 100 kPa in bone tissue [26]. A widely used substrate with well-defined, elastic properties is polyacrylamide. It is crucial for TFM applications, that the substrate behaves purely elastically and no stress is dissipated into the gel, since this is one of the assumptions when calculating the traction stresses from the substrate displacements. Polyacrylamide gels fulfil this property and its rigidity can be tuned over a wide range of about 0.1 kPa to 40 kPa, by adapting the ratio of acrylamide to bis-acrylamide, which tunes the amount of cross-linking during polymerization [143].

The rigidity of the substrate has a strong influence on cell spreading and force generation. Generally speaking, the higher the rigidity, the more the cell will spread, if no confinement is imposed. More rigid substrate also lead to higher higher tensions, but smaller displacements [39]. This has important implications for doing TFM: Substrate displacement should not be too high, because then the bead tracking becomes difficult and prone to errors, but also not too low, because then the resolution of the image acquisition will limit the precision of the measurement. On low rigidities, when cells tend to spread less and stay more round,

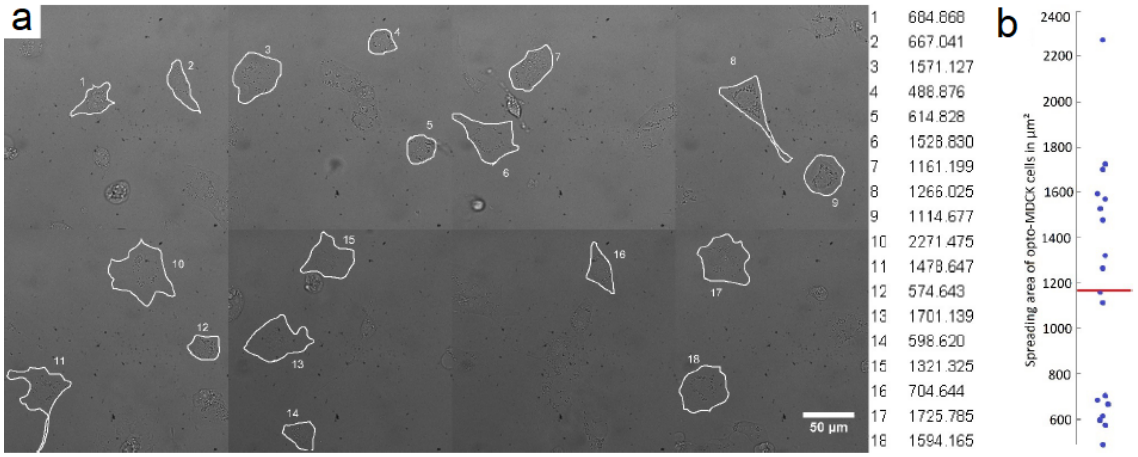

Figure 3.1: (a) A brightfield image of opto-MDCK cells spreading freely on a 20 kPa polyacrylamide gel. The contour of the cells is drawn in white. (b) A scatter plot of the measured spreading sizes of single cells.

the cells also tend to exert more out-of-plane tractions, which are neglected in our TFM routine. Random bead movements due to thermal noise also tend to be higher on soft substrates.

Typical rigidities used for TFM on epithelial cells range from 5 kPa to 20 kPa. The cells used in this work overexpress a GEF, which increases the baseline contractility and we want to stimulate contractility even more in our experiments. Additionally, we want to measure small changes in contractility with high accuracy. Preliminary experiments on 5 kPa and 10 kPa showed displacements of over 1.5 μm, or almost 8 bead diameters, which lead to many tracking mistakes. Therefore, we used 20 kPa for all but preliminary experiments in this work.

In order to determine the pattern size, I let single cells spread freely on a gel of the chosen rigidity of 20 kPa and measured their spreading size. The result of this experiment is shown in Figure 3.1. The average spreading size for a single cell was measured to be around 1200 μm^2, but varied over a wide range from 500 μm^2 to 2300 μm^2. Therefore it is likely, that a wide range of pattern sizes will lead to stable and reproducible doublet formation. Indeed, preliminary experiments on H-patterns showed reproducible doublet morphology on both 1000 μm^2 and 2000 μm^2. Some example brightfield images of those doublets are shown in Figure 3.2. In this work, we oriented our choice on the measurements shown in Figure 3.1 and chose 2000 μm^2 for all but preliminary experiments.

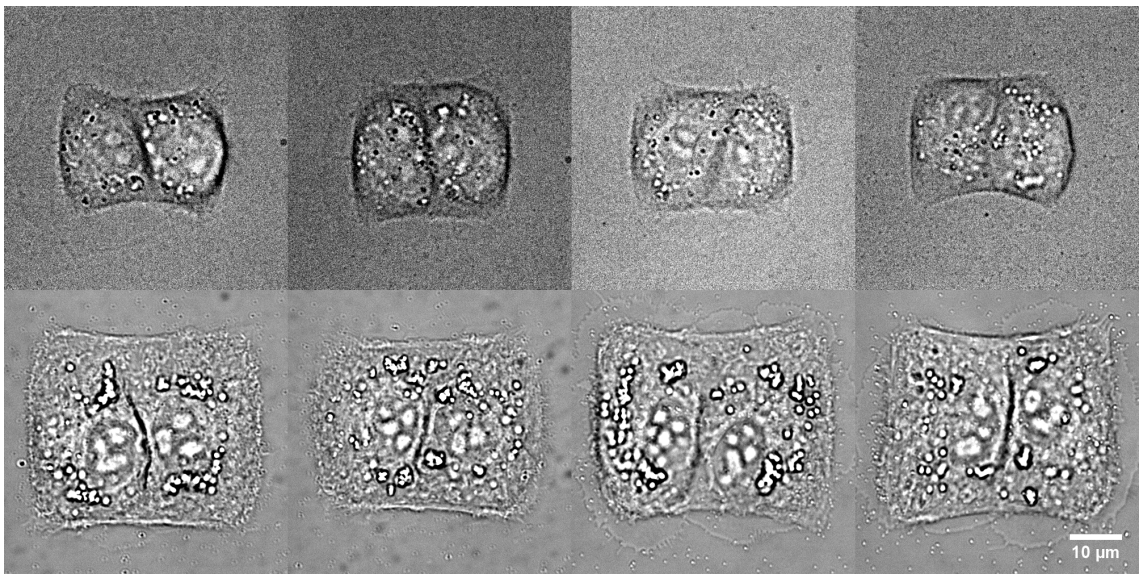

Figure 3.2: Top row: Brightfield images of opto-MDCK doublets on H-patterns of $1000\,\mu m^2$. Bottom row: Brightfield images of opto-MDCK doublets on H-patterns of $2000\,\mu m^2$

3.1.2 Seeding density and incubation time

In order to obtain cell doublets on micropatterns, two different strategies can be considered: The first strategy is to choose a seeding density, where on average two cells fall on a given pattern. Then, incubation time needs to be long enough to ensure good cell spreading and short enough to avoid cell division. The second strategy is to chose a seeding density, where on average just one cell occupies a given pattern. In that case, incubation time is optimized such that most of those single cells will have divided by the time the experiment starts.

We chose the latter strategy, because that way we reduce variability of cells within the doublet, since both of them started from the same mother cell. This is also the strategy that has been used by Tseng et al. in the article where they studied junction positioning of doublets on different kind of patterns. The optimal seeding density for this strategy can be calculated by dividing the number of patterns on the sample by its surface area. This calculation amounted to a seeding density of $7000\,\text{cells}\,\text{cm}^{-2}$. Next, I seeded samples with this density and made a brightfield timelapse experiment for 40 h. For every frame, I counted how many stable doublets are found in the sample and plotted this over time. The result of this experiment is shown in Figure 3.3. The graph shows, that there is a large time window with a large number of doublets on the sample, approximately between 18 h to 28 h. Therefore, samples can be prepared the day before the experiment,

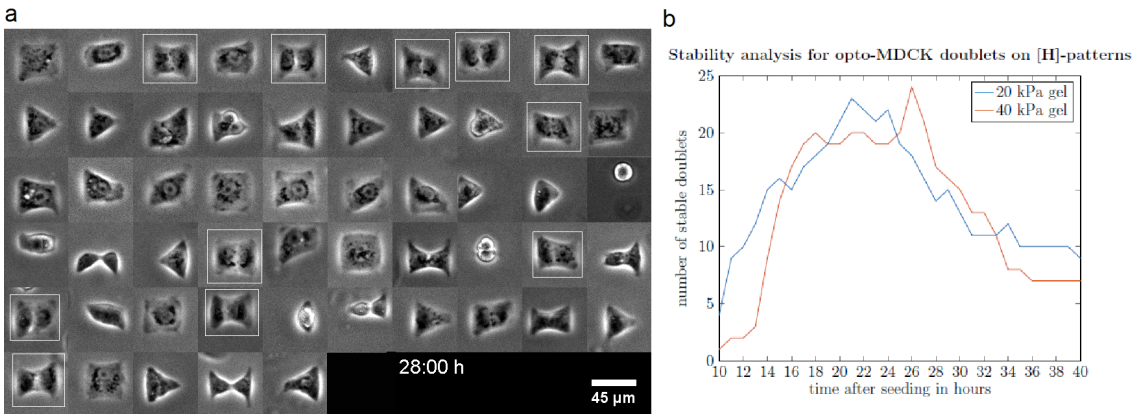

Figure 3.3: (a) Composite brightfield image of opto-MDCK cells spreading on H-patterns. Fully spread doublets are marked with a white frame. (b) Graph showing number of fully spread doublets over time from one experiment on 20 kPa and one experiment on 40 kPa polyacrylamide gels.

incubated over night and then imaged during the whole next day.

3.1.3 Activation pulse duration and frequency

In order to study force transmission from one cell to another, first we have to find an experimental protocol that reliably leads to significant contraction of the cells. Previous work in the lab used single 3t3 cells with the exact same optogenetic construction on circular patterns with sizes varying from 500 μm^2 to 1500 μm^2. Here we want to use a different cell type and two, instead of one cell. One of the first experiments we conducted aimed at comparing the contraction induced in 3t3 cells vs MDCK cells. To this end, we activated one of the two cells in a doublet with the typical activation parameters used by previous students in the lab. The photomask with the 2000 μm^2 patterns hadn't arrived at that point, so I had to use the only available photomask with 1000 μm^2 sized patterns. Our readout parameter for activation strength is the strain energy stored in the substrate, which is obtained by multiplying the displacement field and the traction field, dividing by two and then integrating over the whole surface. We normalize all curves by their baseline value, in order to evaluate the relative increase of strain energy induced through optogenetic activation. The results of this experiment are shown in Figure 3.4, where the red curve shows the average and the grey curves the individual cell doublets. The experiment shows, that 3t3 cells respond much stronger than MDCK cells to a given activation pulse, with an increase in relative strain energy of more than 60 % in 3t3 compared to around 10 % in MDCK. Furthermore, we

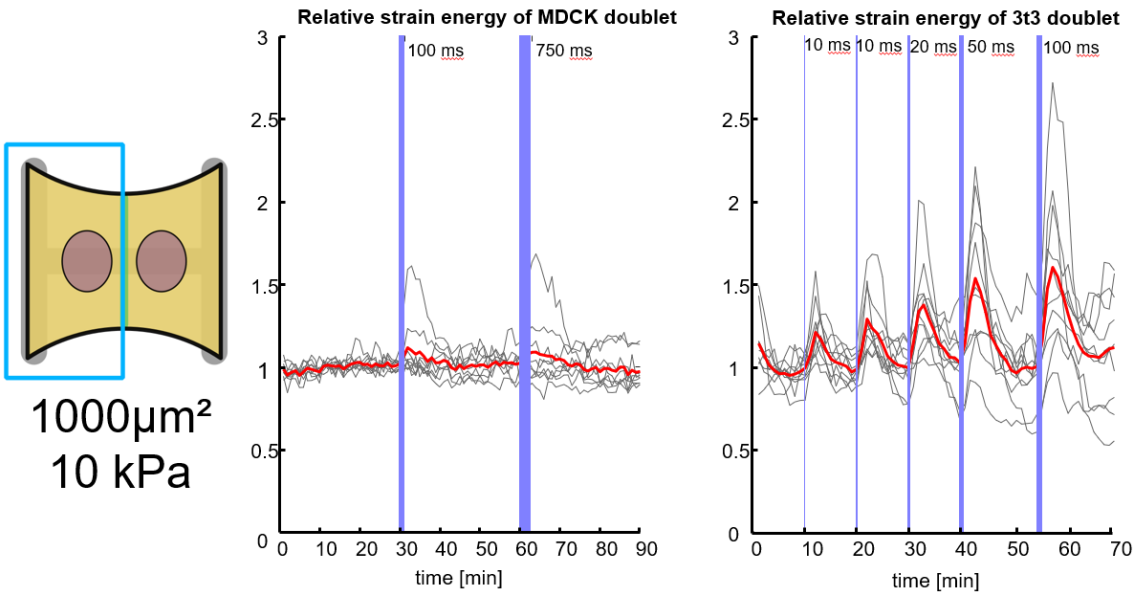

Figure 3.4: Single pulse experiments comparing 3t3 with MDCK. In both 3t3 and MDCK doublets, the left cell was activated with activation pulses of increasing pulse duration. Graphs show the strain energy stored in the substrate over time, normalized by the strain energy before activation. The red curves show the average and the grey curves the individual doublets.

can see from the left graph in Figure 3.4, that increasing the pulse duration from 100 ms to 750 ms had no effect on the amplitude of contraction, meaning that a single pulse of 100 ms already saturates the optogenetic system. The measurement is not very precise though and was not repeated many times, therefore we set the pulse duration to 200 ms, to make sure that each pulse saturates the optogenetic system well.

Next we tried to achieve stronger contractions than shown in Figure 3.4 by activating the cells with repeated pulses, in order to counteract the unbinding of CRY2 from the membrane. This was demonstrated both experimentally and theoretically by Valon et al. for both recruitment dynamics, as well as cell contraction [109, 110]. Therefore, in the next experiment we activated the cells with one pulse per minute for 10 min, similarly to the activation protocols from [110]. The results of this experiment is shown in Figure 3.5. With this approach, the measured contraction in response to the activation increased from around 10% to around 33%. We can see, that the relaxation is not yet finished in the 10 minutes after release of the activation. Furthermore, many cells show an instable baseline and already increase or decrease their contractility before the photoactivation. This makes it difficult to quantify the impact of the activation, since this trend superposes over

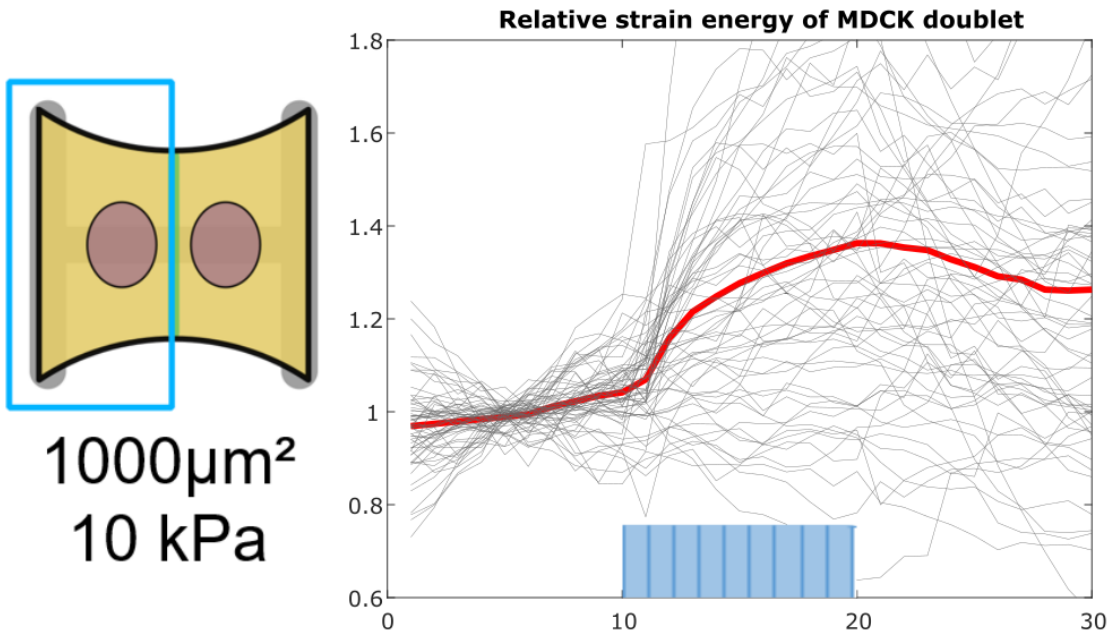

Figure 3.5: Multiple pulse experiments on MDCK doublets. The left cell was activated with one activation pulse per minute for 10 minutes. Graphs show the strain energy stored in the substrate over time, normalized by the strain energy before activation. The red curves show the average and the grey curves the individual doublets.

the contraction from the activation. For this reason, in future experiments we added 10 more minutes of imaging before and 20 more minutes after the activation routine. This way, the baseline trend can be more accurately estimated and potentially used to filter out cells that are too unstable.

3.1.4 Activation pulse power and activation area

All experiments described so far aimed at maximizing the cell contracting in response to photoactivation. Therefore, the illumination power was always set to a value well above saturation point, as determined through estimations from [109]. However, we want to activate only one of the cells in the doublet and not accidentally activate the other one through stray light from the DMD, which is used to activate the cells. Thus, ideally we want to activate the cells just below saturation point, as to maximize activation of one cell and minimize stray light activation of the other cell.

Therefore, first we need to know, at which power the optogenetic system saturates at the set pulse duration of 200 ms. To this end, we set up an experiment, where we activate only the left cell with one activation pulse every 30 min and image the CRY2 distribution in the cells in response to that activation. Figure 3.6 (a)

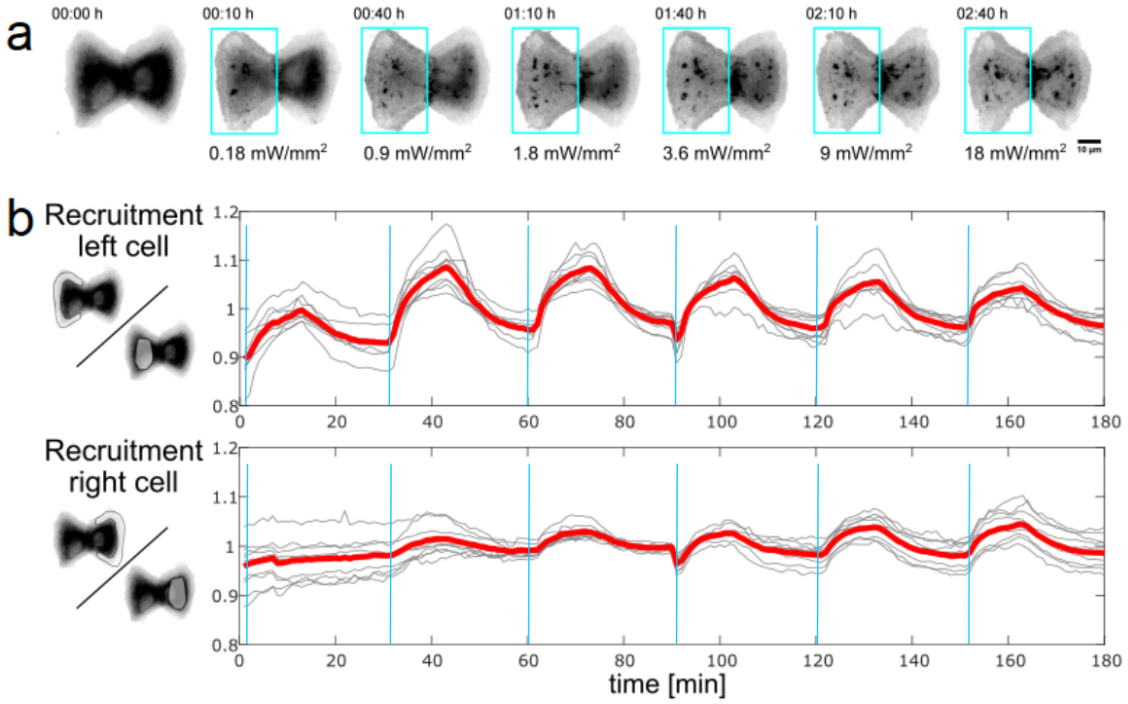

Figure 3.6: (a) Fluorescence images of CRY2 in MDCK cell doublets in response to photoactivation pulse of increasing power. (b) CRY2 recruitment from the cytosol to the plasma membrane, quantified by measuring the ratio of intensities in the lamellipodium vs the cytosol.

shows fluorescence images of CRY2 before photoactivation, and in response to the different activation powers. We then sought to quantify the recruitment of CRY2 to the plasma membrane. To do this with high accuracy, generally it is advisable to do either confocal or TIRF microscopy, so that the plasma membrane clearly separates from the cytosol in the image. Here, we needed to do the experiments on a classical epifluorescence microscope, because that is where all the TFM experiments were conducted. Despite this drawback, we can still see a clear recruitment of CRY2 from the cell body to the lamellipodium. Therefore, we quantified the CRY2 recruitment by measuring the ratio of intensity in the lamellipodium vs. the cell body, both for the left and for the right cell. This quantification is shown in Figure 3.6 (b). This experiment shows, that recruitment saturates somewhere below $0.9\,\mathrm{mW\,mm^{-2}}$, and that there is already some recruitment visible in the right cell at this activation power.

Next we need to know the optical characteristics of the DMD, with which we activate the cells. Particularly we need to know the steepness with which the light intensity decreases near the border of the activation zone, so that we know how far from the center we should place the activation region in order to avoid stray light

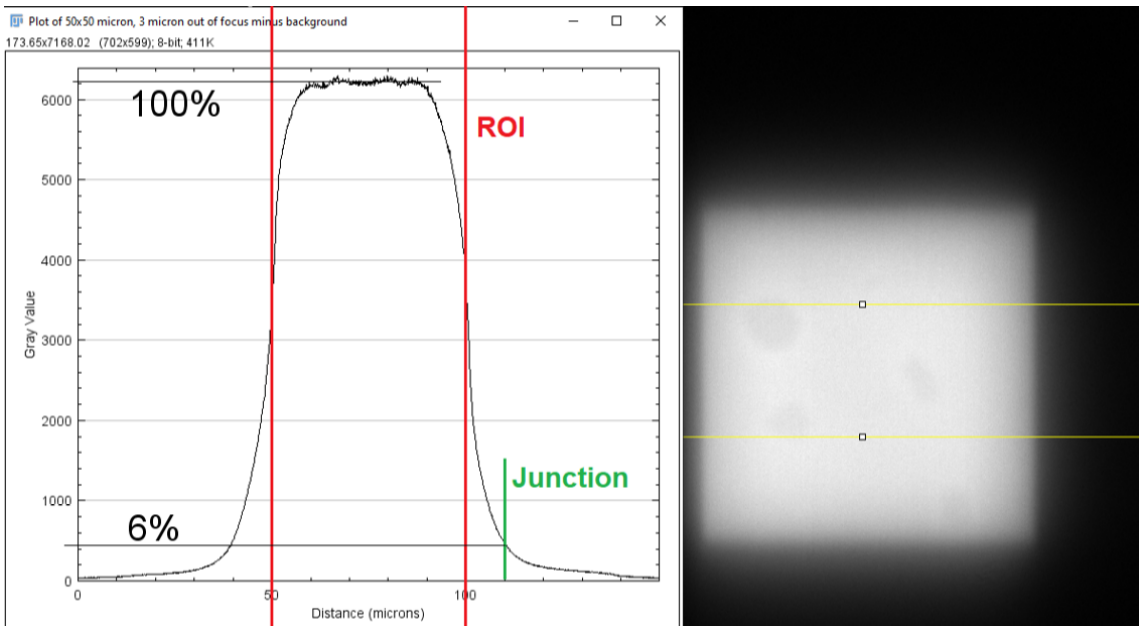

Figure 3.7: Fluorescence image of a homogeneously coated coverslip, illuminated on a rectangular zone with a DMD and the horizontal intensity profile. The background was subtracted from the image before making the measurements.

activation of the right cell. This can be measured by illuminating a rectangular zone of a homogeneously coated, fluorescent coverslip, taking an image and then measuring the intensity profile of the activated zone. This is shown in Figure 3.7, where we can see that the intensity drops to 6 % of it's peak value over a distance of about 10 μm. Therefore, in all but preliminary experiments on doublets, I placed the activation area 10 μm away from the junction. By doing this, the non-activated cell receives only 6 % of the light energy that the activated cell receives.

Next, we wanted to verify that the small amount of stray light the right cell receives does not lead to a contraction of the doublet. Therefore, we conducted an experiment, where we first activate the whole doublet at 6 % of 0.9 mW mm^{-2}, i.e. at 0.054 mW mm^{-2}. It should be noted, that this activation power corresponds to the stray light intensity right at the junction and that the stray light intensity received by the right cell continues to decrease towards the right edge. The results of this experiment are shown in Figure 3.8, with a cartoon describing the experiment in (a) and the relative strain energies stored in the substrate under the left and under the right cell. We can see, that the contraction from activating the whole doublet at the "stray light intensity" is negligible compared to the contraction induced by activating only the left cell at 0.9 mW mm^{-2}. Interestingly, the strain energy also increases under the right, non-activated cell. The activation at

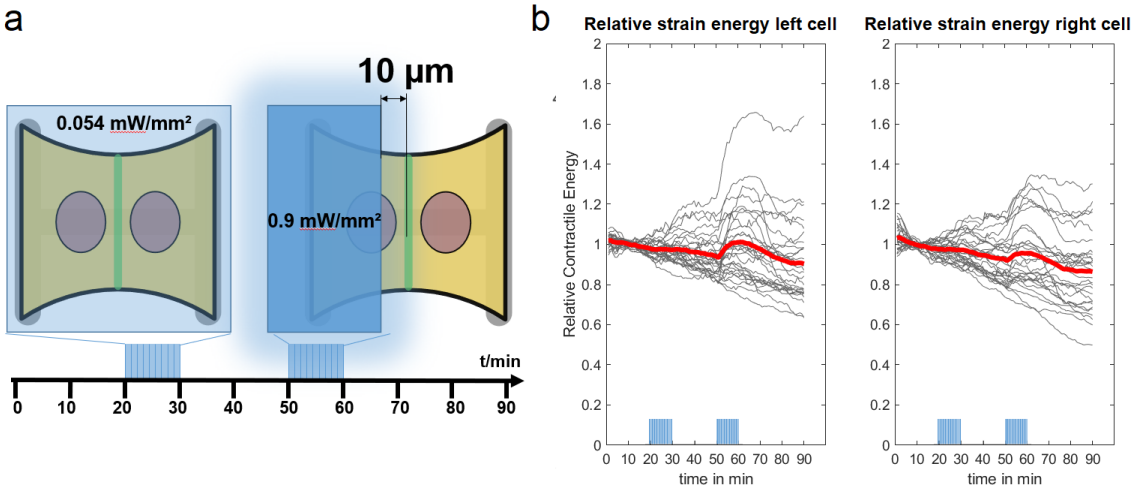

Figure 3.8: (a) A cartoon describing the experiment. First, the whole doublet is activated at low light intensity and then only the left cell is activated with higher intensity. The intensity of the first activation routine corresponds to the intensity right at the junction from the second activation routine. (b) Curves showing the strain energy stored in the substrate under the left cell (left) and under the right cell (right). The strain energy curves were normalized by the strain energy level before photoactivation. Red curves show the average and grey curves show the individual doublets.

low light intensity shows, that this increase is not due to activation through stray light. This is one of the main results of this work and is discussed in detail in the article in section 3.2.

3.1.5 Pattern geometry

All experiments presented so far were conducted on H-shaped micropatterns, because they are well studied and known to induce stable and reproducible doublet morphology [50, 51]. However, cells can also form stable doublets on other kind of shapes. Exploiting the fact that we had received a PRIMO system [2] in the meantime, we decided to test two other shapes in addition to the H: An X shape and an hourglass shape. A drawing of the patterns is shown in Figure 3.9, together with a representative fluorescence image of the actin structure of doublets formed on these patterns. We can see, that the pattern geometry has an influence on the orientation of the inner stress fibers. This could have an influence on how forces get transmitted from one cell to the other, which we could study with our optogenetic setup.

Therefore, next we activated these three type of doublets with the experimental parameters established in the previous sections:, 2000 μm^2 pattern size, 20 kPa

[2] See subsection 2.3.3 for more information on the PRIMO system

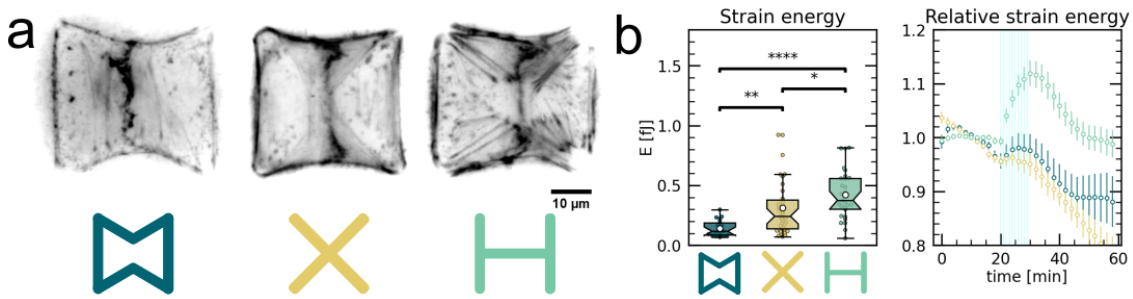

Figure 3.9: (a) A Cartoon of the different shapes used to form doublets and a representative fluorescence image of their actin structure. (b) Left: A boxplot comparing the baseline contractility of doublets on these different shapes. The innerquartile range is shown by the boxes and the whiskers extend to 1.5 times the innerquartile range. The notches show the 95 % confidence interval for the median and the white dot shows the sample mean. The Mann-Whitney-Wilcoxon U test was used to test for differences between singlets and doublets, with ns: $p > 0.05$, *: $p < 0.05$, **: $p < 0.01$,***: $p < 0.001$ and ****: $p < 0.0001$. Right: The relative strain energy during the course of the experiment is shown, with circles representing every other data point and the lines extending to $\pm$ s.e.m.

gel rigidity, 1 pulse per minute, 200 ms and 0.9 mW mm^{-2} per pulse, 10 μm distance from the center. Figure 3.9 (b) shows a boxplot of the strain energy of the three different conditions before activation, as well as the relative strain energy in response to the activation. We can see that there are big differences in both the baseline contractility and the response to the photoactivation: The baseline contractility on H patterns is almost 5 times higher on average than on the hourglass shapes, the baseline is much more stable and the optogenetic response is also much stronger.

For these reasons, more complicated analyses of force transmission from one cell to the other would be very difficult on these data and the different conditions would be very difficult to compare with each other. Therefore, we decided to not pursue this idea much further and used H-patterns for all the main experiments on force transmission.

3.1.6 Discussion

In this section, I tried to highlight all the important aspects to consider when setting up an optogenetic experiment of force propagation. Especially for the optogenetic part, many technical aspects need to be taken into account. The optics used for photoactivation need to be characterized, particularly the sharpness of the light intensity profile and light power density, and locality of photoactivation

needs to be validated on the biological system used. Defining these experimental conditions is particularly difficult, because there is no common approach in characterizing the photoactivation optics in the optogenetics community and the subject is often times little discussed in the publications that use these systems. I think, that the optogenetics community could profit from a more open discussion about these issues and a more detailed and standardized description of the experimental setups.

Another major issue in optimizing these experiments, was the high variability in the data. Despite all efforts in reducing variability, such as using micropatterns to standardize morphology, FACSing the cells to homogenize CRY2 and CIBN expression and increasing incubation time in order to have doublets coming from a single cell, the variability in response to photoactivation was still huge. A lot of this variability comes from the cells themselves and can hardly be reduced, but a big part of variability also comes from variable expression levels, despite the cells being FACSed. This seems to be due to the difficulty of transfecting these protein constructions into cells, since the proteins are quite large and cells do not readily express these proteins. Therefore, a given cell culture tends to lose expression levels over time, which in turn increases data variability.

Another, somewhat related issue, is the generally low contractile response of these cells induced by photoactivation. Both the variability and the low amplitude make it difficult to vary the amplitude of contraction, which would allow for more sophisticated experiments. For example, it could be interesting to study, if over a given threshold of contraction of the left cell, the other cell starts to react differently, e.g. by releasing tension through its focal adhesions. This problem is exacerbated by the fact, that these cells have a higher baseline contractility than wildtype cells, which is probably due to some dark-state activity of the CRY2/GEF construct.

These are all issues, that are actively being worked on, so major improvements are to be expected in the near future. This could e.g. be achieved by using different GEFs, different optogenetic carrier system, by removing endogenous GEFs through CRISPR or by using different promoters for the expression of these constructs.

3.2 Force propagation across cell boundaries depends on actin organization

Here I will present the main result of my PhD, where we address the question raised in the introduction, of how cell-generated force signals propagate from one cell to another. As discussed in the introduction, we used cell doublets on H formed micropatterns and we vary key morphological parameters, such as the length of the junction and the organisation of actin by changing the form of the underlying pattern.

We compare this system of cell doublets to single cells of similar geometry, where we do the same kind of photoactivation as in the doublets. This experiment showed us, that the presence of the junction fundamentally changes the mechanical properties of the system: Single cells with the same spreading area, which we impose with the micropattern, are surprisingly slightly more contractile and they show much stronger actin polarization. The dynamic contractile properties are also very different: Activating half of a single cell does not lead to efficient transmission of force from the stress fibers to the substrate, but rather leads to a flow of actin from the non-activated to the activated region. When activating half of a doublet, i.e. one cell, this flow cannot happen due to the cell-cell junction in the center presenting a barrier. That's why in this case, we see an increase in cell-substrate force instead.

We then compare doublets on H patterns of different aspect ratios, which significantly changes both mechanical and structural polarity and size of the cell-cell junction. Repeating the same experiment in these doublets showed us, that the non-activated cell responds by contracting itself, which we call "active coupling". We quantify this degree of active coupling by comparing cell stresses calculated from the TFM measurements to an analogous FEM model, which was developed by our collaborators Ulrich Schwarz and his PhD student Dennis Wörthmüller. This quantification showed, that the degree of active coupling is highest, when the actin structure is organized perpendicularly to the direction of signal propagation, or in other words, if it is parallel to the border of the photactivation area.

Lastly, we investigated in collaboration with a new PhD student from the team, Vladimir Misiak, if this finding can be generalized to larger structures, i.e. to

small monolayers. We use rectangular micropatterns to induce mechanical and structural polarity in the tissue and then photoactivate either the top or the left half. We find that, also in this case, the degree of active coupling is strongest, when actin is organized parallel to the photoactivation border.

The full documentation of these results is presented in the following pages in form of a paper draft. The supplemental document, describing in detail the theory can be found in section 5.1.

Efficiency of force propagation across cell boundaries depends on mechano-structural polarization: An optogenetic study of minimal models of epithelial tissues

Artur Ruppel[1, *], Dennis Wörthmüller[2, 3, *], Vladimir Misiak[1], Manasi Kelkar[4], Irène Wang[1], Philippe Moreau[1], Adrien Méry[1], Jean Révilloud[1], Guillaume Charras[4,5,6], Giovanni Cappello[1], Thomas Boudou[1], Ulrich S. Schwarz[2, 3, **], and Martial Balland[1, **]

[*]*These authors contributed equally to this work*

[1]*Laboratoire Interdisciplinaire de Physique, Grenoble Alpes University, Saint Martin d'Heres, France.*

[2]*Institute for Theoretical Physics, Heidelberg University, Heidelberg, Germany*

[3]*BioQuant–Center for Quantitative Biology, Heidelberg University, Heidelberg, Germany*

[4]*London Centre for Nanotechnology, University College London, London, United Kingdom*

[5]*Department of Cell and Developmental Biology, University College London, London, United Kingdom*

[6]*Institute for the Physics of Living Systems, University College London, London, United Kingdom*

[**]*Corresponding authors. Contact at martial.balland@univ-grenoble-alpes.fr and schwarz@thphys.uni-heidelberg.de*

3.2.1 Introduction

Cell generated forces are the essential element of tissue morphodynamics, when eukaryotic cells change number, shape and positions to build a multi-cellular tissue. This process is most impressive during development, but also occurs in adult physiology and disease. During development, a genetically encoded program of

cell growth, division, shape changes and migration leads to a tissue with robust function [144, 145]. In addition to the role of cell forces in driving cell shape change and movement, the cell also uses forces to probe the mechanical and geometrical properties of its environment [62, 146], which can feed back on major cellular processes, such as differentiation [3, 26, 147, 148], fate [2] or migration [60, 149, 150].

There are two main mechanisms for force generation. One is a pushing force, generated by the polymerisation of actin filaments against a load, and the other is a pulling force, generated by molecular motors, such as myosin II, acting on actin filaments [40]. These force patterns are both of biochemical origin, since high level regulators like the small GTPases from the Rho-family are used to control these processes in space and time [31, 106].

Given the complexity of these underlying processes, it is quite remarkable that tissues always develop to roughly the same final shape, which is orders of magnitude larger than the individual cell. Recent work has shown, that this robustness is partly due to a high level of feedback between the different layers of organization [4, 6]. Not only do biochemical patterns lead to force patterns which lead to shape change [151], but cells also sense their shape and their surrounding mechanical environment and transduce this information into biochemical signals, thus closing the mechanochemical feedback loop [11, 152, 153].

While much work has focused on the regulation of force generation, it is less clear how force is propagated through tissues and how this process is shaped by mechanochemical feedback loops. Such force propagation suffers the same challenge as any other information propagation through a passive medium, e.g. the electrical signal on a telegraph line or the action potential propagating along neurons: the signal typically attenuates and finally will die out. The main measure to counteract this attenuation are active processes that restore signal strength, like the pumping of ions for action potentials. Long-range velocity waves have been observed in expanding and in confined epithelial tissues, which implies that cells respond actively to external forces in order to keep up such signalling as they propagate through the tissue [136, 154, 155]. Additionally, it has been shown that passive cells in an epithelial tissue act as obstacle for the force transmission chain [48]. Altogether, it remains poorly understood how far locally produced force signals propagate and how signal propagation efficiency depends on tissue orga-

nization. What is needed to address this important question, is an experimental system in which one can control force generation and then follow its propagation through cell-cell junctions to neighboring cells.

Here we introduce a minimal system that allows us to perform exactly this research program. We use micropatterning to generate cell doublets and small cell aggregates of reproducible shape [17, 50]. A further advantage of this technique is that the aspect ratio of the pattern allows to control the orientation of stress fibres within cells [42, 133]. Thus we can control the arrangement of cells and their subcellular organisation. We use an optogonetic tool based on CRY2/CIBN to control RhoA activity, which enables local and transient activation of force production in cells with light [8, 110, 111]. Creating a local force signal then allows us to study how this signal propagates within a model tissue. Finally, we use Traction Force Microscopy (TFM) and Monolayer Stress Microscopy (MSM) to read out the response of the receiving cell.

Our work aims at demonstrating and quantifying the active responses of cells to the contraction of neighbouring cells, which we call their "degree of active coupling", in a minimal setup, i.e. in cell doublets. Furthermore we demonstrate how this degree of active coupling varies with key morphological parameters, such as junction length and the degree and orientation of mechanical polarization, which we vary by changing the aspect ratio of the underlying micropattern. Finally we verify, that our findings in doublets can be generalized to larger systems, i.e. to small cell clusters. Overall we show that active response to incoming forces can maintain signal strength and leads to the emergence of elasticity, which means that signals are not dissipated like in a viscous system, but can propagate over large distances, like in an elastic system.

3.2.2 Results

The cell-cell junction leads to a decrease in mechanical polarization

First, we wanted to understand how the presence of a junction influences structural elements and the force patterns generated by cells on H micropatterns (Figure 3.10 A) by comparing TFM measurements and actin and vinculin stainings of single cells ("singlets") and doublets. We found that both singlets and doublets form pronounced stress fibers around the cell contour, as well as some internal

stress fibers (Figure 3.10 B-C). In both cases, most focal adhesions were located in the corners of the pattern, although some were present on the middle bar of the H-pattern, which is required for the cells to spread over the whole pattern. As previosly demonstrated by Tseng et al. [50], the junction in the doublets formed in the center of the H-pattern, parallel to the lateral bars of the H (Figure 3.10 B).

By quantifying cell-generated forces using TFM, we found that the magnitude of traction forces is surprisingly similar between singlets and doublets, despite having twice as many cells in the doublet (Figure 3.10 D). We quantified this overall contractility by calculating the strain energy stored in the substrate and found, that it is slightly higher for singlets than for doublets, despite spreading over a the same surface area (Figure 3.10 F). This can be attributed to the fact that the singlet has to spread a smaller volume over the same surface as the doublet, which leads to stronger tension in the system.

Next we applied an MSM algorithm to the traction force maps to calculate cell internal stresses (Figure 3.10 E). In doublets, the normal stress in x-direction, $\sigma_{\mathbf{xx}}$, is comparable to the normal stress in y-direction, $\sigma_{\mathbf{yy}}$, whereas in singlets $\sigma_{\mathbf{xx}}$ is much larger than $\sigma_{\mathbf{yy}}$ (Figure 3.10 F).

The normalized difference $(\sigma_{\mathbf{xx}} - \sigma_{\mathbf{yy}})/(\sigma_{\mathbf{xx}} + \sigma_{\mathbf{yy}})$ is related to the mechanical polarization of the system and ranges from -1 to 1, with -1 being completely polarized vertically, 0 being completely unpolarized and 1 being completely polarized horizontally. We found that doublets are unpolarized with an average degree of polarization of 0, whereas singlets have an average degree of polarization of almost 0.5. Altogether, our results thus demonstrate that the junction acts as a barrier preventing the horizontal organization of stress fibers that exist in singlets, thus strongly altering the mechanical polarization of the system.

The cell-cell junction leads to a redistribution of tension from free to adherent peripheral stress fiber

An inherent limitation of TFM, is that only tension that is transmitted to the substrate can be measured. In both doublets and singlets there are two stress fibers on the top and bottom, which are only attached to the substrate on the endpoints. Any tension acting perpendicular on that fiber would not be transmitted to the substrate but rather lead to a change of curvature and a change of distance be-

tween the two free fibers. For this reason we decided to also analyze the shape of the doublets and singlets in an effort to characterize more fully the mechanics that govern their behavior.

Previous work has shown that the shape of a free stress fiber can be described with a circle, which is the result of an equilibrium between an isotropic surface tension pulling the arc into the cell and a line tension acting across the fiber, tending to straighten those fibers [156, 157]. The radius of this circle is then given by the ratio of line and surface tension. The line tension can be calculated from the TFM data, which means that it is possible to fit circles to the arc contour, and to infer the surface tension from the circle radius and the line tension.

However, we showed that it is not correct to assume isotropy of surface tensions for single cells (Figure 3.10 F). In order to quantify surface tension, we thus used a generalization of this circle model to anisotropic systems [158], which infers surface tensions in x- and y- direction by fitting an ellipse to the fiber. We developed a mathematical model based on this approach to describe the mechanics of our cells (Figure 3.11 A). A more detailed description of the model can be found in section 5.1. We solved the equations describing this model numerically and two examples for highly anisotropic contours (Figure 3.11 B) highlight the elliptical shape of the resulting contour. A visualisation of this combined contour tracking, fitting and TFM analysis is shown in Figure 3.11 C.

Next we compared the measurements obtained through MSM and through the application of the contour model (Figure 3.11 D). Although these two measurements describe similar characteristics of the cell, they are not the same, because the underlying mechanical assumptions are very different. In MSM the cell is described as a linearly elastic, continuous material with homogeneous bulk properties whereas in the contour model the cell is described as a network of fibers with non-linear elastic properties (i.e. non-zero elasticity only in extension, like a cable or a rubber band). In other words: MSM describes only the bulk but ignores stress fibers, whereas the contour model describes only stress fibers, but ignores the bulk.

In the previous section we showed, that the cell-cell junction leads to a change in mechanical polarization of cell stress. Here we show, that the stress fibers also pull differently. The line tension, which corresponds to the force applied by the free stress fiber, is higher in singlets than in doublets. For the force of the adherent

fiber the opposite is the case: It is higher in doublets than in singlets (Figure 3.11 E).

Therefore we conclude, that the cell-cell junction leads to a redistribution of tension from the free to adherent peripheral stress fiber. This is consistent with the MSM analysis, where σ_{xx} (corresponds roughly to the free stress fiber, since it is approximately parallel to the x-axis) is higher in singlets and σ_{yy} (corresponds roughly to the adherent stress fiber, since it is parallel to the y-axis) is higher in doublets.

Local activation of RhoA leads to stable force increase in both the activated and the non-activated cell in doublets, but destabilizes force homeostasis in singlets

Next we addressed the question of how locally produced stresses propagate in doublets compared to singlets. To this end, we activated RhoA, a major regulator of cell contractility, with an optogenetic tool. This optogenetic tool is comprised of two proteins: CIBN, which is anchored to the membrane and Cry2, which is present in the cytosol. Upon illumination with cyan light, Cry2 changes conformation and binds to CIBN at the membrane. The catalytic domain of ArhGEF11, which is attached to Cry2, then activates RhoA (Figure 3.12 A). This tool was first used and characterised by Valon et al. [109] and later demonstrated to induce contraction in MDCK cell colonies [110].

We then used this tool to locally activate the left half of singlets and doublets. We activate a region 10 μm to the left of the center, to avoid accidentally activating the right cell in the doublet. In doublets, the forces on the substrate increased both in the activated and the non-activated region. In the singlets on the other hand, it increases slightly and very locally in the activated region, but decreases in the non-activated region (Figure 3.12 C-D).

In order to understand if this behavior can be explained by a passive response of the non-activated region, we developed an FEM model and compared it to the experimental results. It is composed of a network of Kelvin-Voigt elements that are connected to an elastic substrate. Every Kelvin-Voigt element also has an active element, which describes the contractility increase induced by photoactivation (Figure 3.12 B).

We activated the model with an activation profile corresponding to the light intensity profile that we used to activate the cells (see supplement section 5.1 for details). When comparing the results of the model with the experiment, we saw that the behavior of the non-activated region cannot be reproduced with a purely passive reaction, at least not in the frame of this model. In order to qualitatively reproduce the TFM maps seen in Figure 3.12 C we thus added an active coupling term between the left and the right half. This coupling is positive in doublets, meaning the right half contracts in response to the contraction of the left half and negative in singlets, meaning the right half relaxes in response to the contraction of the left half.

From this result we hypothesized that we might see some evidence for this active reaction of the non-activated part by assessing the behavior of the actin cytoskeleton during the light stimulation. To this end, we tracked the fluorescence intensity of LifeAct inside the cells, which increased both in the left cell and in the right cell of the doublets with similar magnitude, whereas in the singlets it increases strongly in the activated region and decreases similarly in the non-activated region (Figure 3.12 E-F).

From this we conclude that the cells in the doublet are actively coupled, i.e. the right cell responds to the contraction of the left cell by contracting itself. This conclusion is in good agreement with results from previous work [17, 159]. Furthermore, the doublets show a homeostatic force response to this transient increase of RhoA activity, i.e. the increase in tension is released as soon as the activation is stopped and goes back to it's initial level. On the singlets on the other hand, transient and local RhoA activation has a destabilizing effect. The local increase of stress and the local accumulation of actin in the photoactivated region is compensated with a decrease of stress and a release of actin in the non-activated region and the stress keeps decreasing even after the activation is stopped. We hypothesized, that this is because the actin structures acutely fluidizes in response to the local stress increase, which has been described in the literature before [24, 160]. Since there is no junction and thus no diffusion barrier in singlets, this would lead to a flow of actin from the non-activated to the activated region, which is consistent with our LifeAct intensity measurements (Figure 3.12 E-F). Qualitative study of an FEM model, where we exchange the Kelvin-Voigt elements in the cell body to Maxwell elements after photoactivation confirmed the plausibility of this

hypothesis (Figure 3.16).

Stress and contour modelling show strong active coupling of actin cortices in doublets

We showed that the right cell in doublets reacts actively to the contraction of the left cell by contracting itself. Next we wanted to quantify the strength of this active response. To this end, we compare our experimental data to the results obtained with our theoretical model (Figure 3.13 A-C). To do this, we made simulations, where the left half is always activated and where the level of contraction of the right half is gradually increased. The relative level of activation of the right half compared to the left half then corresponds to their degree of active coupling, where an active coupling of 0 means no contraction of the right half, an active coupling of 1 means contraction of the right half with same magnitude as the left half and an active coupling of -1 means relaxation of the right half with same magnitude as contraction of the left half. In order to understand which level of active coupling in the simulation corresponds to the experiment, we normalize the stress increase of the right cell by the total stress increase for both the experiment and the simulations (Figure 3.13 C).

Interestingly, the analysis showed stronger degree of active coupling in y-direction (about 0.2) then in x-direction (about -0.05). This could be related to the fact that all forces in y-direction are balanced within the cell and the substrate, but not in between cells. This means the cells can more or less contract independently from one another in this direction. The forces in x-direction on the other hand are always balanced in between both cells and the substrate, similarly to a "tug of war".

Next, we tracked the position of the free stress fibers over time and measured the distance between the fibers for every position in x-direction (Figure 3.13 D) in order to get a readout for cortical tensions which are not transmitted to the substrate. By dividing this distance after photoactivation to the distance before photoactivation, we can define a contour strain as a function of the position in x-direction (Figure 3.13 E). We compared this contour strain to the contour strain of a simulated contour, in which we again progressively activated the right half of the contour (Figure 3.13 D-E). Then we repeated the same analysis as in Figure 3.13

C and we saw that the measured contour strain is most consistent with a global contraction, i.e. an active coupling of almost 1 (Figure 3.13 F). This is consistent with the result shown in Figure 3.13 C, since it is mostly forces in y-direction that deform the contour.

In conclusion, traction forces, as measured by TFM, show weaker active coupling between activated and non-activated region than cortical tensions, as inferred by measurement of contour strain. The traction forces are dominated by the activity of the stress fibers, both internal and on the periphery. The contour of the free fiber on the other hand is determined by the activity of the actin cortex and the free stress fiber. Thus, the strong active coupling in the contour suggests strong active coupling of the cortices and the comparatively weak active coupling of the forces suggests a weak active coupling of the stress fibers (Figure 3.13 G).

Mechanical stresses transmit most efficiently perpendicularly to the axis of mechanical and structural polarization in doublets

We showed that active coupling in y-direction compared to the x-direction is much higher in our doublets, so we hypothesized that the mechanical polarization of the cells modulate their degree of active coupling. Therefore we sought out to vary the structural and mechanical polarization of the doublets. We did this by changing the aspect ratio of the underlying micropattern, height to width from 1to2 to 1to1 to 2to1 at constant spreading area. We performed TFM and MSM experiments on these doublets and quantified the degree of mechanical polarization on these doublets. Additionally, we quantified the degree of structural polarization on the actin images using the structure tensor (see methods section for details). We found, that both structural and mechanical polarization are tightly linked to each other and vary greatly in between the three different aspect ratios (Figure 3.14 A-C).

Next we activate the left half of the doublets and measured their traction forces over time and calculate the stress difference in the doublet before and after photoactivation with MSM. Comparing the experiment to the model, we see that the degree of active coupling increases greatly with increasing degree of mechanical polarization (Figure 3.14 D-F). In the 1to2 doublets, where the cells are polarized along the direction of stress transmission, the right cell reacts by relaxation to the contraction of the left cell, whereas in 2to1 doublets, where the cells are polar-

ized perpendicular to the direction of stress transmission, the right cell contracts almost as strongly as the left cell

We performed measurements of contour strain in order to get a readout for cortical tensions which are not transmitted to the substrate. Here we saw, in agreement with Figure 3.13 E, that the contour deformation is completely symmetrical in both the 1to1 and the 2to1 doublets, but much less in the 1to2 doublets, where the degree of active coupling is lower (Figure 3.17).

Altogether, we conclude that mechanical stresses transmit most efficiently perpendicularly to the axis of mechanical and structural polarization in doublets (Figure 3.14 G).

Mechanical stresses transmit most efficiently perpendicularly to the axis of mechanical and structural polarization in small cell clusters

Next we sought out to investigate, whether this conclusion is generalizable to larger systems, i.e. to small monolayers. To this end, we confined about 10-20 cells on 150 μmx40 μm rectangular micropatterns. We again performed TFM and MSM experiments in combination with live actin imaging and quantified the mechanical and structural polarization. This quantification showed, that the tissue is mechanically and structurally polarized along the long axis of the pattern (Figure 3.15 A-C).

Next, we wanted to compare the efficiency of stress propagation in these tissues parallel and perpendicular to the axis of polarization. To do this, we changed the region of optogenetic stimulation and then photoactivated either the top half or the left half of the tissues with the same frequency and duration as the doublets. We compared this to our FEM model, analogous to the analysis on doublets, and found that the degree of active coupling is higher, when the direction of stress propagation is perpendicular to the axis of polarization. Additionally, we measured the distance over which the maximum stress attenuates to 20%, and found that it is, on average, about three times as long, when the direction of stress propagation is perpendicular to the axis of polarization (Figure 3.15 D-F).

Therefore, the correlation between mechano-structural polarization and active coupling observed at the doublet level is also present in larger groups of cells. In summary, the degree of active coupling is correlatd with mechanical and structural

polarization across the 5 conditions tested in this article. In addition, the degree of active coupling is correlated with junction length in doublets (Figure 3.18).

Figures

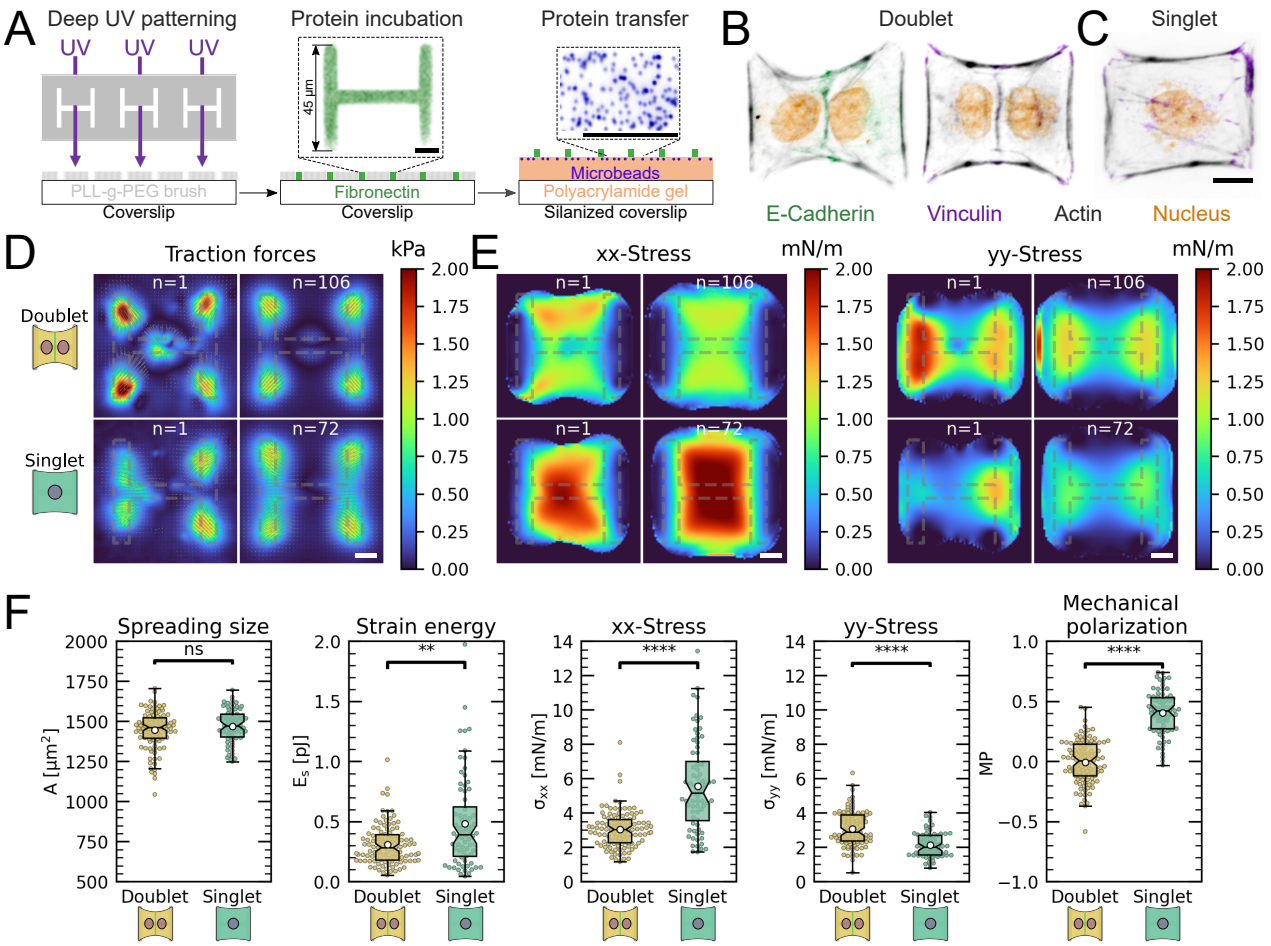

Figure 3.10: **The cell-cell junction leads to a decrease in mechanical polarization.** **A** Cartoon of the micropatterning process on soft substrates, allowing to control cell shape and to measure forces at the same time by embedding fluorescent microbeads into the gel and measuring their displacement. The middle panel shows the used pattern geometry, an H with dimensions of 45 μmx45 μm. **B, C** Immunostaining of opto-MDCK cells plated on H-patterns and incubated for 24 h before fixing. Actin is shown in black, E-Cadherin in green, Vinculin in violet and the nucleus in orange. **B** The left and right images show a representative example of a doublet **C** A representative example of a singlet. **D** Traction stress and force maps of doublets (top) and singlets (bottom) with a representative example on the left and an average on the right. **E** Cell stress maps calculated by applying a monolayer stress microscopy algorithm to the traction stress maps, with a representative example on the left and an average on the right. **F** From left to right: Boxplots of: Spreading size, measured within the boundary defined by the stress fibers. Strain energy, calculated by summing up the squared scalar product of traction force and displacement field divided by two. xx-Stress and yy-stress calculated by averaging the stress maps obtained with monolayer stress microscopy. Degree of polarization, defined as the difference of the average xx- and yy-stress normalized by their sum. Doublets are shown in yellow and singlets are shown in green. The figure shows data from n=106 doublets from N=10 samples and n=72 singlets from N=12 samples. All scale bars are 10 μm long.

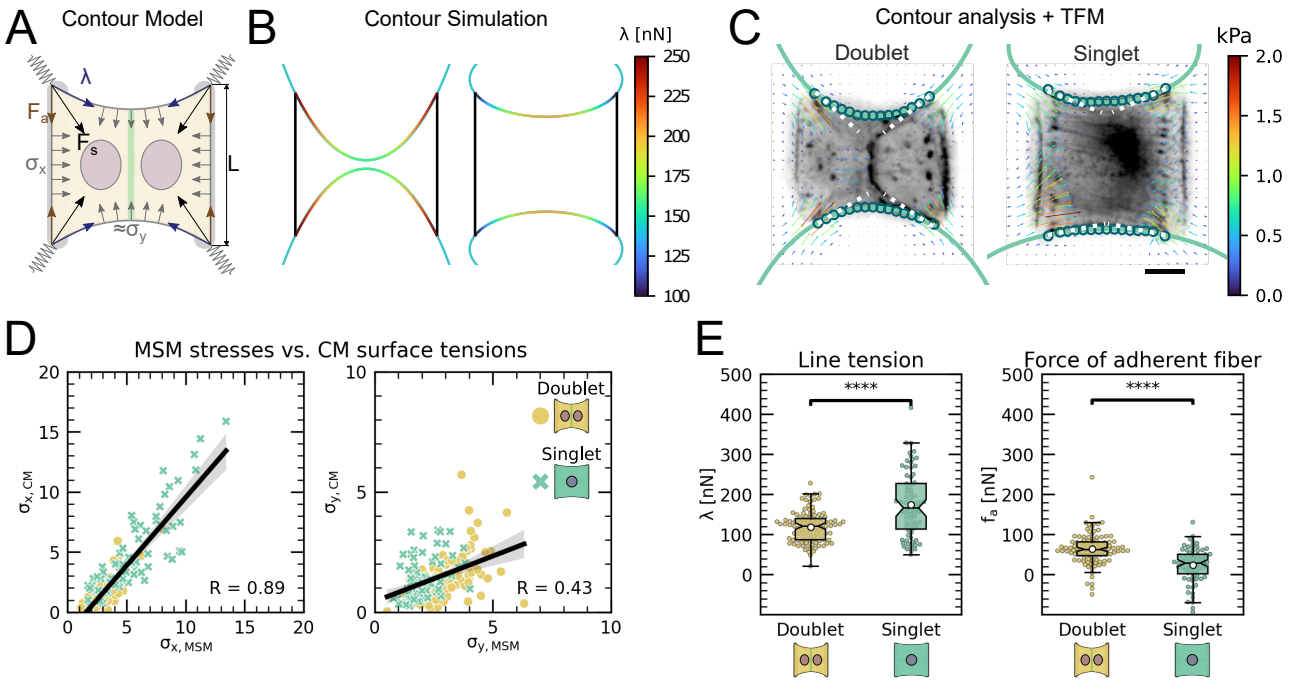

Figure 3.11: **The cell-cell junction leads to a redistribution of tension from free to adherent peripheral stress fiber.** **A** Cartoon of the contour model used to analyze the shape of the doublets and singlets. **B** FEM simulation of the contour with $\sigma_y > \sigma_x$ left and $\sigma_x > \sigma_y$ right. **C** Actin images of doublets (left) and singlets (right) with traction stresses (arrows), tracking of the free fiber (blue circles), elliptical contour fitted to the fiber tracks (green line) and tangents to the contour at adhesion point (white dashed line). The scale bar is 10 μm long. **D** Correlation plot of MSM stresses and CM surface tensions. MSM stresses were calculated by averaging the stress maps obtained with monolayer stress microscopy and the surface tensions were obtained by the contour model analysis, where σ_x was measured on the TFM maps by summing up the x-traction stresses in a window around the center of the vertical fiber and σ_y was determined by fitting the resulting ellipse to the tracking data of the free fiber. Doublets are shown as yellow dots and singlets are shown as green crosses. The black line shows the linear regression of the data and the shaded are shows the 95% confidence interval for this regression. The R-value shown corresponds to the pearson correlation coefficient. **E** Boxplots of line tension λ (left) and force of adherent fiber $\mathrm{F_a}$ (right) as defined in panel A. Both values were calculated by first calculating the force in each corner by summing up all forces in a radius of 12 μm around the peak value and then projecting the resulting force onto the tangent of the contour for the line tension and onto the y-axis for the force of adherent fiber. Doublets are shown in yellow and singlets are shown in green. The figure shows data from n=106 doublets from N=10 samples and n=72 singlets from N=12 samples. All scale bars are 10 μm long.

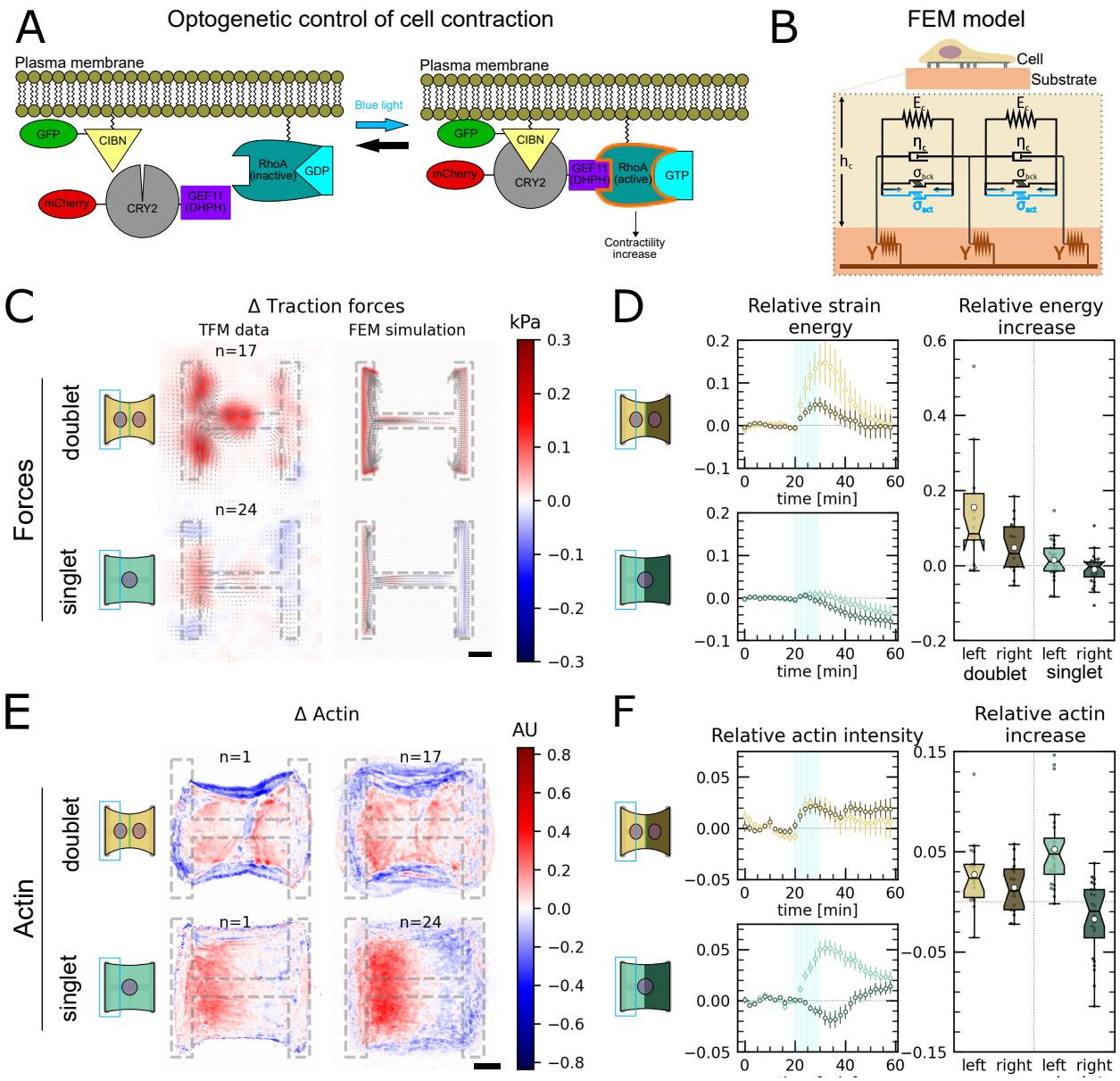

Figure 3.12: **Local activation of RhoA leads to stable force increase in both the activated and the non-activated cell in doublets, but destabilizes force homeostasis in singlets A** Cartoon of the optogenetic CIBN/CRY2 construction used to locally activate RhoA. **B** Cartoon of the FEM model used to explain optogenetic experiments. **C** Difference of average traction force maps after and before photoactivation of cell doublets (top) and singlets (bottom). Maps on the left show the TFM data and maps on the right show the result of the FEM simulations. **D** Relative strain energies of doublets (top) and singlets (bottom) with local photoactivation, divided in left half (bright) and right half (dark). One frame per minute was acquired for 60 minutes and cells were photoactivated with one pulse per minute for 10 minutes between minute 20 and minute 30. Strain energy curves were normalized by first substracting the individual baseline energies (average of the first 20 minutes) and then dividing by the average baseline energy of all cell doublets/singlets in the corresponding datasets. Data is shown as circles with the mean $\pm$ s.e.m. Boxplots on the right show the value of the relative strain energy curves 2 minutes after photoactivation, i.e. at minute 32. **E** Difference of actin images after and before photoactivation of doublets (top) and singlets (bottom), with an example on the left and the average on the bottom. All scale bars are 10 μm long. **E** LifeAct intensity measurement over time (left) of left half (bright) vs right half (dark) of doublets (top) and singlets (bottom) after local photoactivation. Boxplots on the right show the relative actin intensity value after 2 minutes after photoactivation of activated vs non-activated half

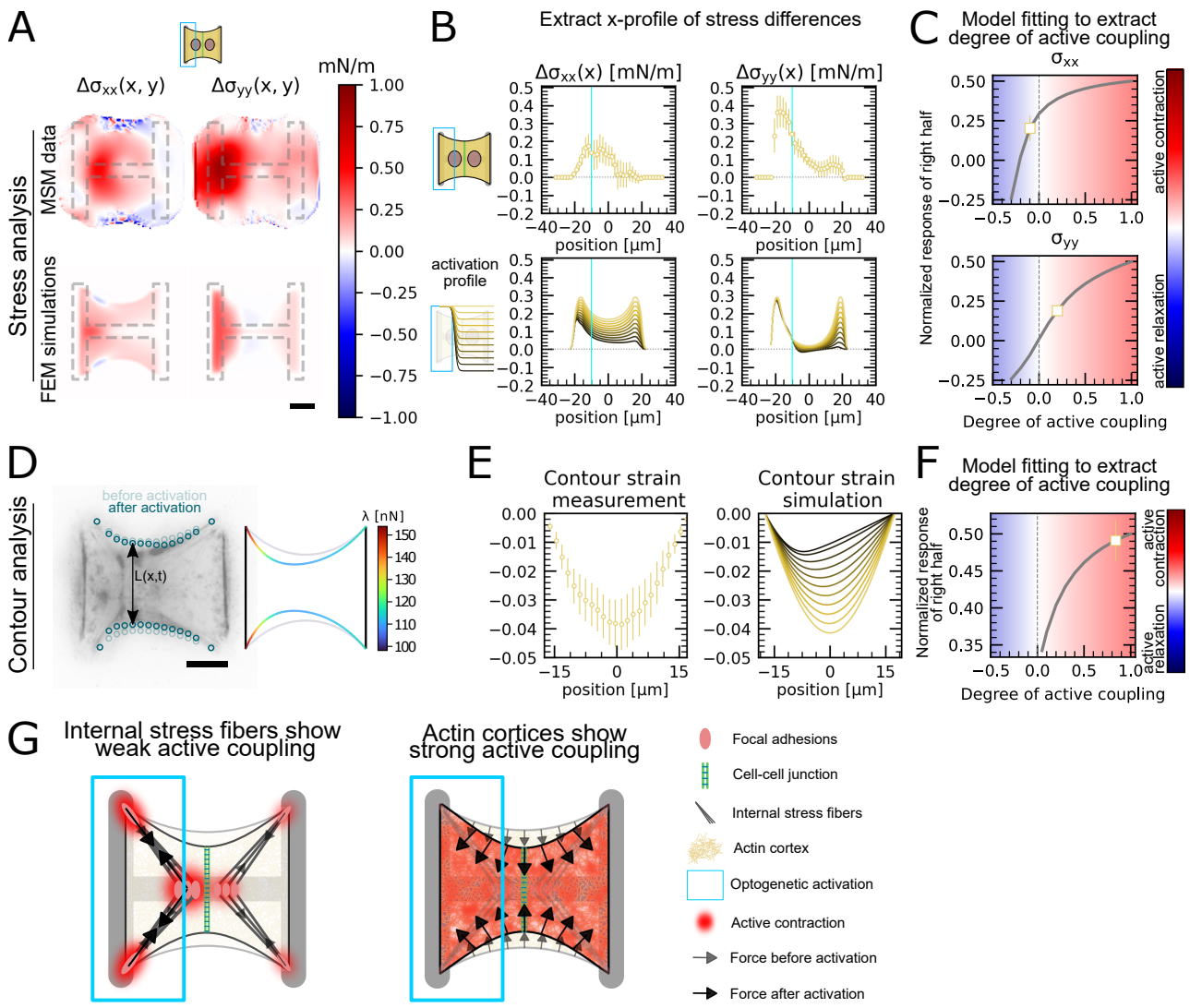

Figure 3.13: **Stress and contour modelling show strong active coupling of actin cortices in doublets.** **A** Difference of average cell stress maps after and before photoactivation of cell doublets, calculated with MSM (top) and simulated in an FEM model (bottom) Stress in x direction is shown on the left and stress in y direction is shown on the right. **B** Average over the y-axis of the maps in D. Data is shown as circles with the mean ± s.e.m. In the simulation, the right half of the cell was progressively activated to obtain the family of curves shown in the bottom. **C** Response of the right half (normalized by the total response), obtained from the model (grey line), as a function of the degree of active coupling. The experimental MSM value is placed on the curve to extract the degree of active response of the right cell in the experiment. **D** Contour analysis of the free stress fiber. In the experiment, the distance between the free fibers as a function of x is measured, as shown in the image on the left. An example for a contour model simulations is shown in the right. **E** The contour strain after photoactivation is calculated from the distance measurements shown in D, by dividing the distance between the free stress fibers for each point in x-direction after and before photoactivation. Similarly to the FEM simulation, in the contour simulation, the right half of the contour is progressively activated to obtain the curve family shown in the right plot. **F** Response of the right half (normalized by the total response), obtained from the model (grey line), as a function of the degree of active coupling. The experimental strain value is placed on the curve to extract the degree of active response of the right cell in the experiment. **G** A cartoon showing our interpretation of the results shown in panel A to F. The traction force analysis only sees forces that are transmitted to the substrate, which are dominated by the activity of the stress fibers. The contour of the free fiber is determined by the activity of the actin cortex and the free stress fiber. Thus, the strong active coupling in the contour suggests strong active coupling of the cortices and the comparatively weak active coupling of the forces suggests a weak active coupling of the stress fibers.

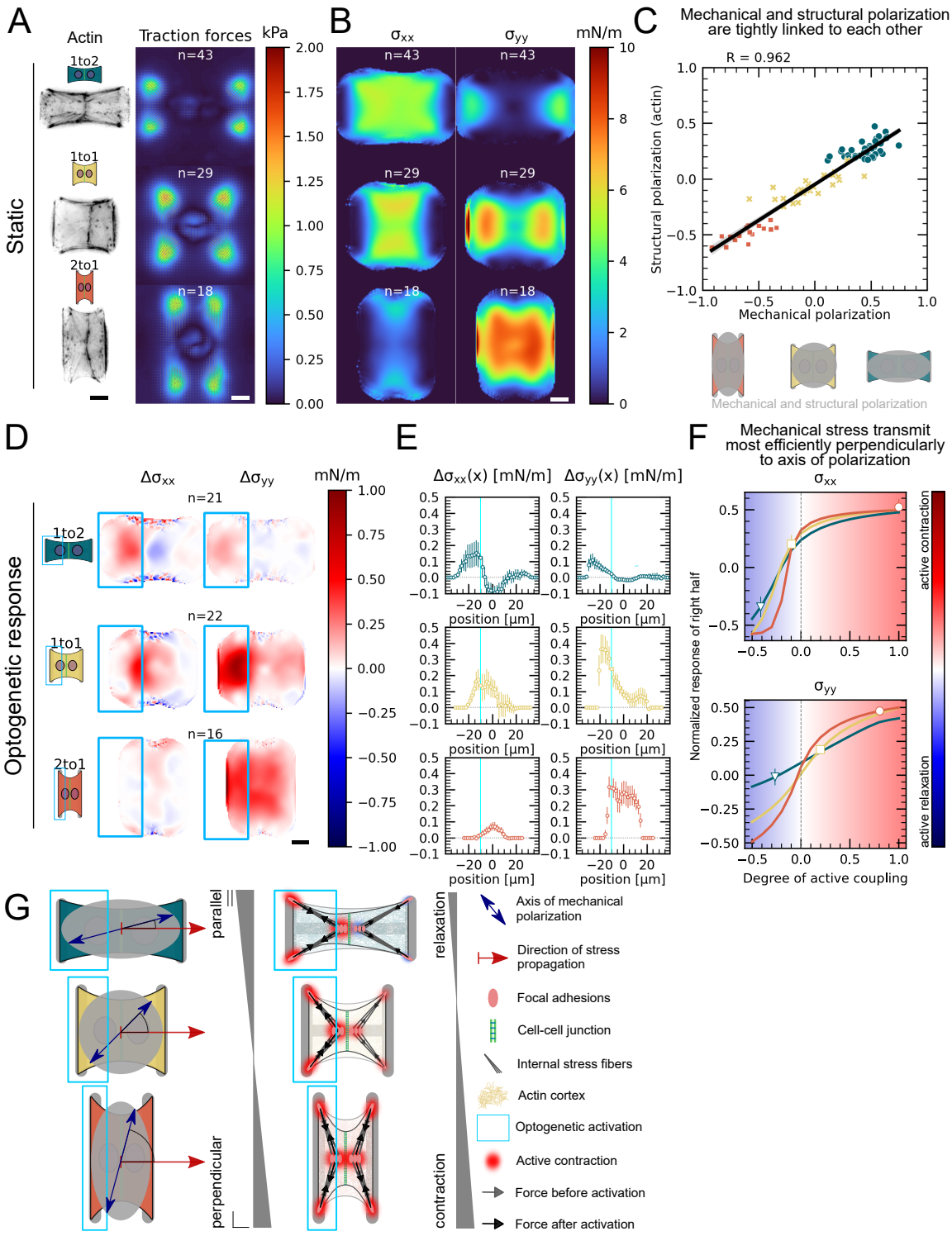

Figure 3.14: **Mechanical stresses transmit most efficiently perpendicularly to the axis of mechanical and structural polarization in doublets.** **A** Actin images (left) and average traction stress and force maps (right) of cell doublets on H-patterns with different aspect ratios (1to2, 1to1 and 2to1). **B** Average cell stress maps calculated by applying a monolayer stress microscopy algorithm to the traction stress maps. **C** Correlation plot of average actin angle and anisotropy coefficient. The black line shows the linear regression of the data and the shaded are shows the 95% confidence interval for this regression. The R-value shown corresponds to the pearson correlation coefficient. **D** Stress maps of the difference of xx-stress (left) and yy-stress (right) before and after photoactivation. **E** Average over the y-axis of the maps in D. Data is shown as circles with the mean ± s.e.m. **F** Response of the right half (normalized by the total response), obtained from the model (grey line), as a function of the degree of active coupling. The experimental MSM value is placed on the curve to extract the degree of active response of the right cell in the experiment. All scale bars are 10 μm long. **G** A cartoon showing our interpretation of the data shown in panel A to F. The relative response of the right cell in response to the activation of the left cell varies strongly in the different aspect ratios. In the 1to2 doublet, where polarization and transmission direction are aligned, the right cell relaxes, whereas in the 2to1 doublet, where the polarization axis is perpendicular to the transmission direction, the right cell contracts almost as strongly as the left cell.

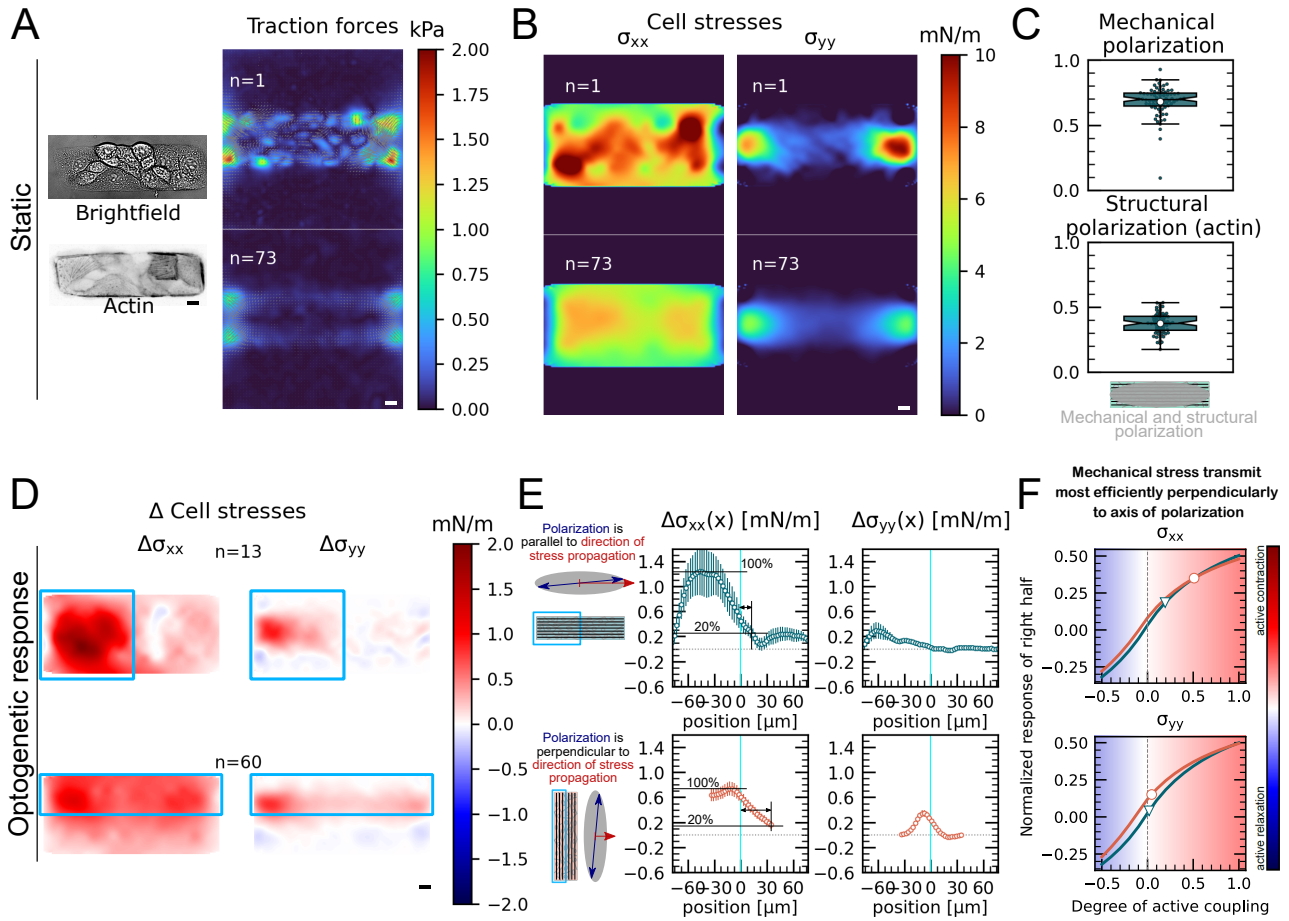

Figure 3.15: **Mechanical stresses transmit most efficiently perpendicularly to the axis of mechanical and structural polarization in small monolayers. A** An actin and a brightfield image of a representative monolayer on rectangular micropattern (left) and a representative traction stress and force map, as well as an average traction stress and force maps (right) of a small monolayer on rectangular micropattern. **B** Representative example and average cell stress maps calculated by applying a monolayer stress microscopy algorithm to the traction stress maps. **C** Box plots of average actin angle and anisotropy coefficient. **D** Stress maps of the difference of xx-stress (left) and yy-stress (right) before and after photoactivation. **E** Average over the y-axis of the maps in D. Data is shown as circles with the mean ± s.e.m. **F** Response of the right half (normalized by the total response), obtained from the model (grey line), as a function of the degree of active coupling. The experimental MSM value is placed on the curve to extract the degree of active response of the right cell in the experiment. All scale bars are 10 μm long.

Supplementary figures

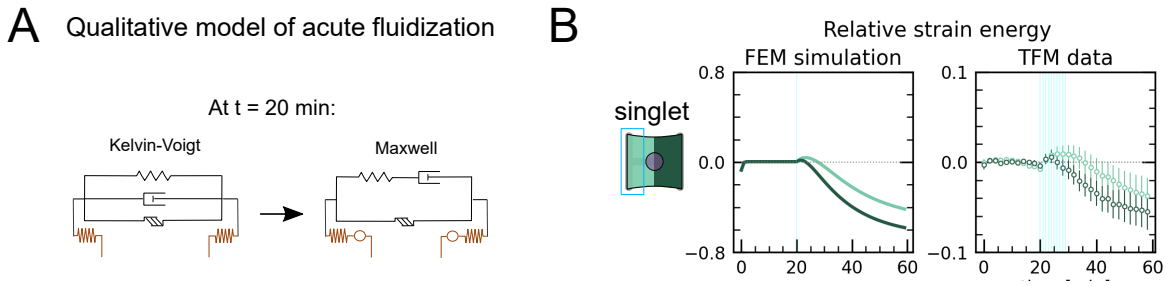

Figure 3.16: **A** A cartoon showing the basic elements of the FEM simulation. Acute fluidization is modeled as a switch from Kelvin-Voigt to Maxwell elements. **B** Relative strain energies of singlets with local photoactivation, divided in left half (bright) and right half (dark). One frame per minute was acquired for 60 minutes and cells were photoactivated with one pulse per minute for 10 minutes between minute 20 and minute 30. Strain energy curves were normalized by first substracting the individual baseline energies (average of the first 20 minutes) and then dividing by the average baseline energy of all cell doublets/singlets in the corresponding datasets. Data is shown as circles with the mean ± s.e.m and the result of an FEM simulation is shown as a solid line.

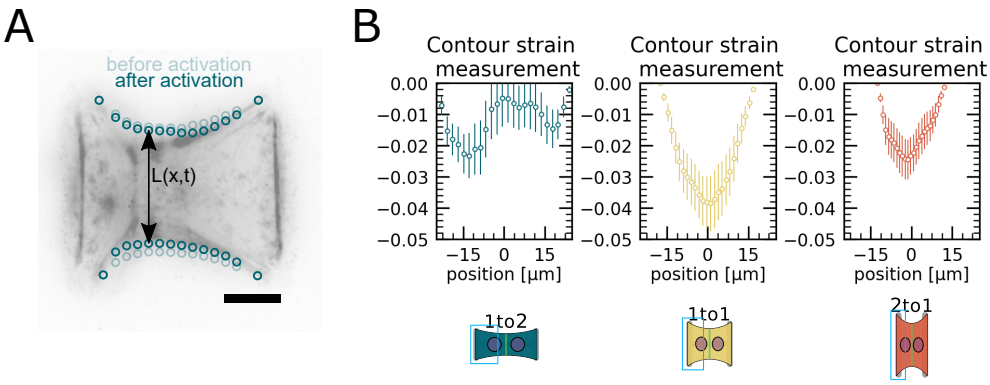

Figure 3.17: **A** Contour analysis of the free stress fiber. In the experiment, the distance between the free fibers as a function of x is measured, as shown in the image on the left. **B** The contour strain after photoactivation is calculated from the distance measurements shown in A, by dividing the distance between the free stress fibers for each point in x-direction after and before photoactivation.

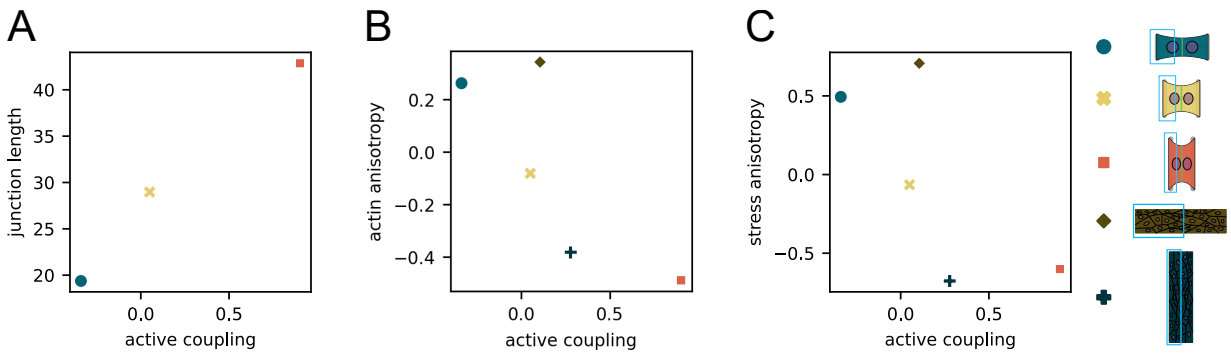

Figure 3.18: The degree of active coupling vs. junction length (**A**), degree of actin anisotropy (**B**) and degree of stress anisotropy (**C**)

3.2.3 Discussion

Intercellular forces play a major role in regulating and coordinating tissue morphogenesis. As such, these forces have signalling properties that can be sent by cells, propagate a certain distance and finally be received by another cell. Direct measurement of intercellular forces and cell internal stresses within embryos is very challenging and most of our knowledge of the distribution of these forces is inferred from theoretical models [7, 161–163]. Experimental tools, i.e. laser ablation and FRET tensional sensors have also been developed [164–166], but they have substantial disadvantages: Laser ablation relies on destroying the corresponding structures and FRET sensors measure only tension within a molecule and it is still unclear, how to infer cell and tissue scale tension from these measurements. In this paper, we aim at completing those approaches at another scale. We follow a bottom up approach, where we interrogate force propagation in the simplistic tissue model made of two interacting cells.

By performing mechanical and molecular manipulations via the combination of an optogenetic tool controlling RhoA activity, micropatterning and force imaging, we show that force signal propagation within cellular assemblies depends on the supracellular actin organization. We show, that forces propagate more efficiently in a direction perpendicular to the mechanostructural polarity of the tissue itself. This is supported by the following findings:

First, we found that cells are actively coupled. By photoactivation of specifically one of the two cells in our minimal tissue doublet, this cell contracts and sends a force signal to the other cell. We found that the non stimulated cell, the receiver cell, reacts to this contraction with an active contractile response. Interestingly, the sub-cellular stimulation of a single cell does not display the same behavior. Here, the reaction of the non-activated region is more accurately described by acute fluidization of the actin structure. This leads to actin flow instead of the stress buildup which we see in doublets, where flow is suppressed by the junction acting as a barrier.

Second, the intercellular active force coupling strongly depends on the anisotropy of actin organisation and force distribution. However, as this system is evolving in a complex phase diagram where both force readouts and structural elements are coupled via dynamic mechanotransduction feedback loops, it is barely possi-

ble to uncouple the respective contribution of each elements, such as actin fiber orientation, force distribution, cell/substrate and cell/cell adhesion strength or cell junction length. Therefore, it is not possible to set the mechanostructural anisotropy at the causal origin of the more efficient force propagation we observe, but should rather be seen as emerging in parallel due to the boundary conditions imposed by the surrounding environment.

Finally, aside from those complex biomechanical couplings, our findings on force propagation in monolayers show that the supracellular organization of actin is a major regulator of force propagation within tissues. We found, that forces are transmitted more efficiently in a direction perpendicular to the axis of actin polarity at two different scales, i.e. on cell doublets and small monolayers. To our knowledge this mode of propagation highlights the two following points:

First, recent studies have proposed that group of cells behave as a "supracellular unit", which share many of the characteristics of the cells that it consists of [111, 167]. Some emerging mesoscale phenomena, such as collective gradient sensing, might be explained by common principles, such as supracellular polarity and supracellular force transmission [61, 137, 168–170]. Our findings complement those papers, as we show that intercellular force transmission is an active process and we present a new mode of force propagation.

Second, at a much larger scale we would like to speculate on the potential impact of such force propagation mode. In developing drosophila embryos, anisotropic distribution of tension has been proposed to guide convergent extension [171]. Our results suggest, that active cell tension propagates preferentially perpendicular to the axis of polarization. This could lead to a reduction of structural anisotropy in an anisotropic tissue, which is observed e.g. in the developing drosophila imaginal disk [172], if these tensions are converted to plastic cell deformations.

To further understand this active force propagation process, future work could focus on identifying the molecular mechanisms by which active contraction of the receiver cell depends on its own mechanostructural polarization and that of the sender cell. Another angle of future work could aim at identifying exactly which physical properties the receiver cell reacts to, e.g. strain or stress on the cell-cell junction or strain or stress of the supracellular stress fibers. On the modelling side, future work could focus on coupling the here presented mechanical model

with the underlying biochemistry of GEFs, GAPs, RhoA, actin and myosin. Ideally, this active mode of force propagation would emerge from this model, instead of being added ad hoc as an analysis and quantification tool, such as presented here. Both the just mentioned experimental and theoretical work would need to be developed in parallel, as they both require information from each other: For example, the model could suggest physical properties the receiver cell senses and responds too and then experiments need to find the molecule that can do the suggested measurement and confirm the validity of the hypothesis through e.g. knock-down experiments.

3.2.4 Materials & Methods

Cell Culture Opto-MDCK and opto-MDCK LifeAct cells have been kindly provided by Manasi Kelkar and Guillaume Charras. Both cell lines were cultured at 37 °C and in 5% CO_2 atmosphere in DMEM (Life Technologies) medium containing 10% heat-inactivated FBS (Life Technologies) and 1% penicillin/streptomycin (Sigma-Aldrich). Between 20.000 and 50.000 cells were plated on the micropatterned hydrogels. After 1 h, cells were checked for their adhesion to the hydrogels. In case of excessive amount of cells the sample was rinsed with fresh medium to wash off the non-adhered cells. Cells were let spread on patterns for 16 h to 28 h, so that on average most doublets have started as single cells and divided on the pattern to form a doublet.

Cell fixing and immunostaining First, cells were fixed for 10 min with 4% PFA diluted in PBS. Next, the cell membrane was permeabilized with 0.5% Triton X-100 for 5 min. Cells were then washed twice with TBS and blocked at room temperature for 1 h with a blocking buffer solution containing TBS, 1% bovine serum albumin (BSA, Sigma-Aldrich) and 50 mM Glycine (Sigma-Aldrich). Then, cells were incubated for 2 h in a dilution of primary antibodies with blocking buffer. For E-Cadherin stainings a 1:200 dilution of DECMA-1 (ThermoFisher 14-3249-82) was used and for Vinculin stainings a 1:400 dilution of hVIN-1 (Sigma-Aldrich V9131) was used. Cells were then washed three times with TBS for 10 min each. Then cells were incubated in a dilution of secondary antibodies, 555-fluorescently labeled-phalloidin and DAPI in blocking buffer. For E-Cadherin stainings a 1:1000 dilution of 647anti-rat (Sigma-Aldrich SAB4600186) was used, for Vinculin stain-

ings a 1:1000 dilution of 647anti-mouse (ThermoFisher A-21235) and a 1:1000 dilution for phalloidin and DAPI. Fixed cells were then mounted with Mowiol 4-88 (Polysciences, Inc.) onto glass slides and kept at 4 °C until imaging.

Preparation of micropatterned polyacrylamide gels Patterned PAA hydrogels were prepared according to the glass method described previously in [141]. In short, 32 mm coverslips were first plasma cleaned for 60 s and then incubated with a drop of PLL-PEG 0.1 mg mL^{-1} in HEPES 10 mM, ph 7.4 for 30 min at room temperature. Then, coverslips were rinsed with a squirt bottle of MilliQ water and carefully dried with a nitrogen gun. The coverslips were then placed on a quartz photomask (Toppan) on a 10 μL drop of MilliQ water. Excess water was removed by placing a kimwipe on the coverslips, a flat surface on top (e.g. the lid of a petridish) and then pressing gently. The coverslips on the photomask were then exposed to deep-UV for 5 min. After recovery from the photomasks, the coverslips are incubated with 20 μg mL^{-1} fibronectin (Sigma-Aldrich) and 20 μg mL^{-1} Alexa488-conjugated fibrinogen (Invitrogen) in 100 mM Sodium Bicarbonate buffer for 30 min at room temperature. To prepare the gels, a 47 μL drop of 20 kPa mix of polyacrylamide and bis-acrylamide (Sigma-Aldrich) was prepared (see [143] for the proportions). To perform Traction Force Microscopy, carboxylate-modified polystyrene fluorescent microbeads (Invitrogen F-8807) were added to the polyacrylamide premix and sonicated for 3 min to break bead aggregates. A second coverslip of the same size is then placed on top, after previous silanization with a solution of 5 mL 100% ethanol, 18.5 μL Bind Silane (GE Healthcare Life Science) and 161 μL 10% acetic acid (Sigma-Aldrich) for 5 min. During the polymerization process, the hydrogel adheres to the silanized coverslip and fibronectin proteins are trapped within the polyacrylamide mesh. The silanized coverslip is finally detached by wetting it with MilliQ water, letting the gel rehydrate for 5 min and lifting it up with a scalpel. Hydrogels were stored in 100 mM Sodium Bicarbonate buffer at 4 °C for maximum 2 days before cell seeding.

Imaging and optogenetic photoactivation All experiments were conducted 16 h to 28 h after seeding the cells on the sample. Then the cells were observed on an inverted Nikon Ti-E2 microscope with an Orca Flash 4.0 sCMOS camera (Hama-

matsu), a temperature control system set at 37 °C, a humidifier and a CO_2 controller. For the opto-experiments on cell doublets and singlets a Nikon 60x oil objective was used and for the opto-experiments on tissues a Nikon 40x air objective was used. The E-cadherin and vinculin staining images were taken with an Eclipse Ti inverted confocal microscope (Nikon France Instruments, Champigny sur Marne, France), equipped with sCMOS prime camera (Photometrics), a 60× objective, and a CSU X1 spinning disk (Yokogawa, Roper Scientific, Lisses, France). MetaMorph software was used for controlling the microscope (Universal Imaging Corporation, Roper Scientific, Lisses, France). Unless otherwise stated, all photoactivations were done with 1 pulse per min for 10 min and each pulse had a duration of 200 ms, a power density of 0.9 mW mm^{-2} and a wavelength of 470 nm. The power density was measured with a power meter right after the objective by shining light on a surface of a given size and dividing the measured power by this size.

Traction Force Microscopy and Monolayer Stress Microscopy Force measurements were performed using a method described previously [173]. In short, fluorescent beads were embedded in a polyacrylamide substrate with 20 kPa rigidity and images of those beads were taken before, during and after photoactivation. At the end of the experiment, cells were removed with 2.5% Trypsin and an unstressed reference image of the beads was taken. The displacement field analysis was done using a homemade algorithm based on the combination of particle image velocimetry and single-particle tracking. After correcting for experimental drift, bead images were divided into smaller subimages of 13.8 μm width. The displacement between corresponding bead sub-images was obtained by cross-correlation. After shifting the stressed sub-images to correct for this displacements, the window size is divided by 2 and new displacement values are determined by cross-correlations on the smaller sub-images. This procedure is repeated twice. On the final sub-images, single-particle tracking was performed: this ensures that the displacement measurement has the best possible spatial resolution at a given bead density. Erroneous vectors were detected by calculating the vector difference of each vector with the surrounding vectors. If the vector magnitude was higher than 2.5 μm or the vector difference higher than 1 μm, the vector was discarded and replaced by the mean value of the neighbouring vectors. Only the first frame

of each movie was compared to the unstressed reference image. All subsequent frames were compared to their predecessor. This leads to more precise measurements because the displacements are much smaller. From the bead displacement measurements a displacement field was then interpolated on a regular grid with 1.3 μm spacing. Cellular traction forces were calculated using Fourier transform traction cytometry with zero-order regularization [174] [75], under the assumption that the substrate is a linear elastic half-space and considering only displacement and stress tangential to the substrate. To calculate the strain energy stored in the substrate, the scalar product of the stress and displacement vector fields was integrated over the surface of the whole cell. The algorithm was implemented in MATLAB. Cell internal stresses were calculated from the traction stress with the code from Bauer et al. [85]. To do this calculation, the cell is assumed to behave like a thin, elastic sheet that is attached to a substrate and then contracts. Equilibrium shape is reached, when the active stress that leads to the contraction is balanced by the elastic stress that builds up within the sheet and in the substrate. The resulting stress is the sum of the active and the passive stress in the elastic sheet and is independent of its elastic modulus.

Fiber Tracking A semi-automatic procedure was used to detect and track the actin fibers at the cell contour over time. First the operator clicks on the endpoints of each fiber on the first image of a time lapse. The adherent fibers are very static and straight, so, in this case, we just draw a straight line between the two end points. The free fibers are curved and move over time. To follow the shape of a given fiber over time, we used a custom script: on each image, parallel line profiles are drawn at regular intervals in between the two defined endpoints, in a direction perpendicular to the overall fiber direction; each profile is analyzed to detect the point where it intersects the fiber, using intensity variation as criterion. The line linking these points describes the actin fiber position at each time point. In order to filter out badly detected points, the consistency of the resulting positions is analyzed over both time and space. Temporal filtering consists of first a median filter over 5 time points and the removal of outliers. Within a moving time window of 10 time points, positions distant from the average value by more than 2 times the standard deviation are deleted. Spatial filtering includes also removal of outliers, defined as being distant from the spatial average position by more than

3 times the standard deviation. Then the angle of lines joining adjacent points are computed at each position and badly tracked points are excluded by ensuring that these angles stay below 15°. Finally, we use this tracking data to create a stack of masks for each cell which accurately describes the complete contour of the cell. The algorithm was implemented in MATLAB.

Actin polarization analysis To measure the average polarization of the internal actin network, we analyze the orientation of the internal actin network using the structure tensor formalism. For each pixel with intensity $I(x, y)$, the structure tensor J is calculated over a Gaussian local neighborhood $w(x, y)$ with a waist of 3 pixels, according to equation (3.1).

$$\begin{aligned} J_{11} &= \iint w(x,y) \left(\frac{\partial I(x,y)}{\partial x}\right)^2 dx\, dy \\ J_{22} &= \iint w(x,y) \left(\frac{\partial I(x,y)}{\partial y}\right)^2 dx\, dy \\ J_{12} = J_{21} &= \iint w(x,y) \left(\frac{\partial I(x,y)}{\partial x}\right) \left(\frac{\partial I(x,y)}{\partial y}\right) dx\, dy \end{aligned} \tag{3.1}$$

The orientation angle θ on this local neighborhood corresponds to the direction of the main eigenvector of the structure tensor and is obtained by equation (3.2).

$$\tan(2\theta) = \frac{2J_{12}}{J_{22} - J_{11}} \tag{3.2}$$

This angle is only meaningful if the image shows oriented structures in this neighborhood. This confidence can be estimated from the coherency, which quantifies the degree of anisotropy and is calculated from the structure tensor according to equation (3.3). Values with a coherency value under 0.4 were excluded before averaging the orientation angles over the cell to obtain the mean direction of the actin network. The degree of polarization is then obtained according to (3.4) The algorithm was implemented in MATLAB.

$$Coherency = \frac{\sqrt{(J_{22} - J_{11})^2 + 4J_{12}^2}}{J_{11} + J_{22}} \tag{3.3}$$

$$Polarization = < \cos(2(\theta - \theta_{mean})) > \tag{3.4}$$

Actin Intensity Measurement To measure the actin intensity in the left and the right half of the doublet/singlet, we first segment the cells using the masks obtained from the fiber tracking. We reduce its size a little bit to exclude the external stress fibers from the measurement. We then divide the doublet/singlet vertically in two halves and sum up all the intensity values within the region of interest, yielding one intensity value per frame and per half. This intensity over time is then normalized by the intensity value of the average over the first 20 frames before photoactivation.

Statistical analysis and boxplots All boxplots show the inner quartile range as boxes and the whiskers extend to 1.5 times the inner quartile range. The notches show the 95 % confidence interval for the median and the white dot shows the sample mean. The Mann-Whitney-Wilcoxon U test was used to test for differences between singlets and doublets, with ns: $p > 0.05$, *: $p < 0.05$, **: $p < 0.01$,***: $p < 0.001$ and ****: $p < 0.0001$.

Data exclusion for optogenetic experiments Many of the cells showed an unstable baseline energy level, which made it difficult to judge the impact of the optogenetic activation. Thus, we quantified the baseline stability of each cell by applying a linear regression to the relative strain energy curve before photoactivation and excluded all cells with a slope larger in absolute value than a threshold value. For figure 3, this process excluded 16 globally activated doublets, 7 globally activated singlets, 12 locally activated doublets and 17 locally activated singlets. For figure 5 D to F, this process excluded 22 1to2 doublets, 7 1to1 doublets and 2 2to1 doublets.

3.2.5 Author contributions

A.R. performed experiments from figures 1 to 5, a large part of the data analysis and writing the manuscript under the supervision of M.B. and T.B.. D.W. developed the contour model, the network model and developed the algorithms for the circle and ellipse fitting under the supervision of U.S.. V.M. performed the experiments and data analysis from figure 6 under the supervision of M.B.. M.K. developed the optogenetic cell line expressing LifeAct under the supervision of G.Ch.. I.W. developed the TFM algorithm, the algorithm for measuring the orien-

tation of the actin network and the algorithm for tracking the actin fibers. P.M. designed the photomasks used to make the micropatterns and, together with J.R., provided technical assistance and maintenance for the technical facilities. All authors contributed with editing the manuscript and providing fruitful discussions and feedback.

3.2.6 Acknowledgements

M.B. acknowledges financial support from the French Agence Nationale de la Recherche (ANR) MechanoSwitch project, grant ANR-17-CE30–0032-01. U.S.S. acknowledges funding through a joint ANR-DFG grant, project number SCHW 834/2-1. T.B. acknowledges fundings through CNRS grants (Actions Interdisciplinaires 2017, DEFI Instrumentation aux limites 2017, Tremplin@INP 2021, PEPS CNRS-INSIS 2021). G.Ca. acknowledges financial support from the ANR SupraWaves project, grant ANR-19-CE13-0028. This work was supported by the Center of Excellence of Multifunctional Architectured Materials "CEMAM" (n° AN-10-LABX-44-01).

We would like to thank Luis Vigetti and Isabelle Tardieux for providing access to their spinning disc confocal microscope that was used to take the immunofluorescence images. We would like to thank Simon de Beco, Laurent Blanchoin and the whole MicroTiss team for useful discussions and feedback.

3.3 Cell doublets to understand cell-matrix vs. cell-cell adhesion in other contexts

In the results described so far, we used cell doublets on micropatterns as a minimal tissue model to study dynamic force transmission from one cell to the other. We used different pattern geometries to modify the actin architecture and the junction length, optogenetics to stimulate contraction in one of the cells and TFM to measure these contractions. What is interesting about doing TFM on cell doublets in general, is that it is possible to calculate both cell-cell and cell-substrate forces, which can then give clues about cell-cell and cell-matrix adhesive properties. Both cell-cell and cell-matrix adhesion, how they are regulated and how they cross talk are of major interest in development and in cancer research, due to their major

role in regulating collective cell migration, cell intercalation, cancer metastasis, cell sorting, etc. Concretely, cell doublets can be used to study the effect of all kinds of pharmacological or genetical interventions on cell-cell and cell-matrix adhesion or to compare different cell types. The additional benefit of using micropatterns, is that they impose a certain geometry and size to the system, which reduces variability in morphology within and in between different conditions and facilitates quantification and interpretation of the data.

Here I will present results that we obtained in collaboration with François Fagotto, a researcher who is interested in early embryonic development, particularly the process of gastrulation, in *Xenopus* and who also currently leads a research project on breast cancer cells. François Fagotto is particularly interested in how basic biophysical cell properties regulate large scale tissue behavior and our doublet approach seemed well suited to characterize those. In our collaboration so far, we contributed to two questions they are working on:

The first is related to gastrulation in *Xenopus*, where cells started to differentiate into three germband layers: ectoderm, mesoderm and endoderm. During gastrulation, the embryo undergoes dramatic shape change as the mesoderm layer involutes and migrates alongside the ectoderm layer from the inside of the embryo. For this process, the mesoderm layer becomes very motile and fluid-like, in contrast to the ectoderm layer which is stationary and solid-like. To understand how these tissue mechanical properties arise from cell mechanical properties, we need to measure those cell mechanical properties. To this end, we performed TFM measurements, together with with Guillaume Desgarceaux and David Rozema, on doublets of mesodermic stem cells, which they isolated from *Xenopus* gastrula. The results of this experiment is shown in subsection 3.3.1

The second question is related to the role of EpCAM, a protein that plays a major role in regulating tissue plasticity during gastrulation and it is also overexpressed in a majority of carcinomas and is correlated with poor prognosis [175]. It is known, that EpCAM is implicated in the regulation of cell-cell adhesion, but it is not well understood how it does so. Therefore, deciphering the role of EpCAM in cancer development and progression was the goal of Azam Aslemarz, who recently finished her PhD on the role of EpCAM in cancer cells. In our collaboration, we used the TFM + cell doublet approach in breast cancer cells with and without inhibition of EpCAM to understand its effect on cell contractility and cell-cell

forces, which are related to cell-cell adhesion. The results of these experiments are shown in subsection 3.3.2

3.3.1 Cell doublets of mesodermic *Xenopus* stem cells

In these exploratory experiments we aimed at evaluating their feasibility. It was unclear, if these cells will even form doublets on H-patterns, how big the pattern needs to be and if the forces they exert on the substrate are sufficiently large to be easily measured with TFM. In Figure 3.19, we show a proof of concept that mesodermic stem cells also form doublets on H-patterns and that it is possible to do TFM in this system. It is worth noting that the overall traction stress exerted by these cells is only about a tenth of what I observed in opto-MDCK cells and that the H-pattern is about twice as large in terms of surface area. This is coherent with the high motility of these cells, which is generally correlated with low contractility and high spreading surface [176]. Future work will use this system in combination with gene knock-down experiments, to study the effect of proteins which are known to be essential regulators of gastrulation. The system could also be used to compare doublets of meso-, ecto- and endodermic stem cells to understand how cell-cell and cell-matrix adhesion differs in these different kind of stem cells. This could give some insight into how these differences in cell biophysical properties lead to the different kind of tissue behaviors we see during gastrulation.

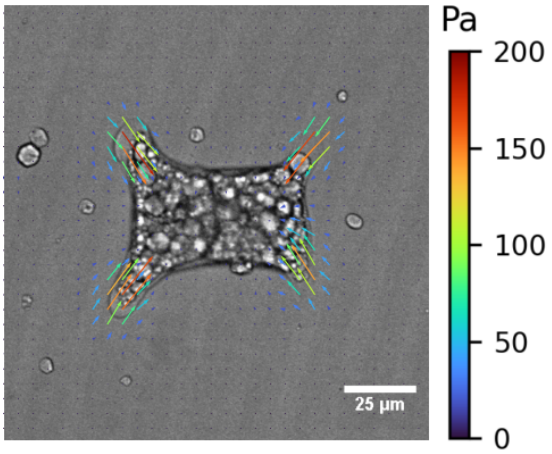

Figure 3.19: Brightfield image of *Xenopus* mesodermic stem cell doublet from a *Xenopus* embryo, right after onset of gastrulation, spreading on an H-pattern. Superposed arrows show traction stresses the doublet exerts on the substrate.

3.3.2 Cell doublets to decipher the role of EpCAM in breast cancer cells

EpCAM (Epithelial Cell Adhesion Molecule) is a protein that has been associated with the majority of human carcinomas including breast cancer [177] and is being used as a cancer marker. Early experiments proposed, that EpCAM is a homophilic cell-cell adhesion protein, similarly to cadherins, since expressing EpCAM in cells without cell-cell adhesion proteins tended to induce aggregation [178]. However, when EpCAM was co-expressed with E-cadherin, it negatively affected cell aggregation and adhesion [179]. EpCAM also tends to increase single cell migration but decrease collective cell migration, which suggests that EpCAM might rather have a regulating role in cell-cell and cell-ECM adhesion [175]. In order to clarify the role of EpCAM and its close relative Trop2, Azam performed a variety of migration and cell-cell adhesion assays on the epithelial breast cancer cell line MCF7, which overexpresses both EpCAM and Trop2 compared to healthy epithelial cells. To investigate the effect of EpCAM and Trop2, she used siRNA in order to reduce the overexpression of these proteins back to more physiological levels. The results of her work are documented in her recently published thesis, where she showed that EpCAM up-regulates single cell migration but down-regulated collective cell migration through down-regulation of global cell contractility and down-regulation of cadherin mediated cell-cell adhesion [180].

In the experiment that Azam and I performed together, we used TFM and H micropatterns to compare cell-cell forces in wildttype and in EpCAM knockdown cells. Figure 3.20 (a) shows brightfield images of representative doublets for the four different conditions: siCtrl, siEpCAM, siTrop2 and the double knockdown dKD. An average traction force map of the different conditions is shown in Figure 3.20 (b). We quantified the overall contractility of the doublet by calculating the strain energy stored in the substrate, which can be obtained by multiplying traction stress and displacement field, dividing by two and then integrating over the surface of the doublet. This quantification, shown in Figure 3.20 (c), shows that both siEpCAM and siTrop2 doublets have significantly increased contractility, which suggests that both EpCAM and Trop2 downregulate myosin activity.

Next we calculated the intercellular force between the cells, which is an indirect indicator for cell-cell adhesion strength. This can be calculated, as proposed

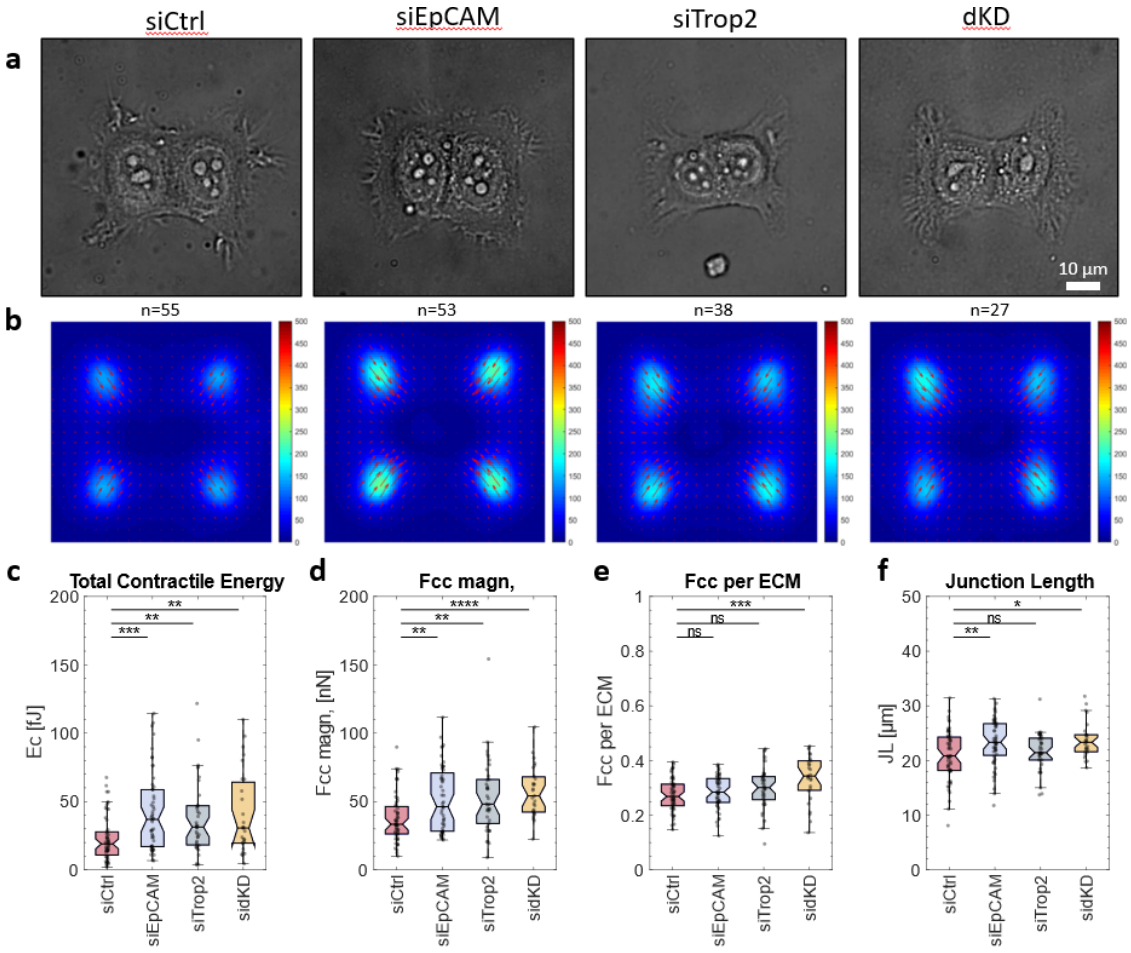

Figure 3.20: (a) A representative bright field image of a MCF7 doublet on an H-micropattern for the different siRNA conditions. (b) Average traction stress maps for the four different conditions. (c) Boxplots of the contractile energy stored in the substrate, which serves as indicator for overall cell contractility. This is calculated by multiplying traction stress and displacement maps, dividing by two and integrating over the whole doublet surface. (d) Boxplots of intercellular forces, obtained by summing up the force vectors enclosed by the cell-cell boundary and the edge of one of the cells. (e) Boxplots of intercellular forces normalized by the total force exerted by the doublet. The total force is calculated by integrating the absolute values of the traction stresses over the whole cell doublet. (f) Boxplots of the junction lengths. In all boxplots, the innerquartile range is shown by the boxes and the whiskers extend to 1.5 times the innerquartile range. The notches show the 95 % confidence interval for the median. The Mann-Whitney-Wilcoxon U test was used to test for differences between the different conditions, with ns: $p > 0.05$, *: $p < 0.05$, **: $p < 0.01$,***: $p < 0.001$ and ****: $p < 0.0001$.

in [17, 49], by calculating the vector sum of all forces enclosed by the cell-cell junction and the boundary of one of the cells. The resulting force then has to be balanced at the junction. The result of this quantification is shown in Figure 3.20 (d), which shows that cell-cell forces are also significantly higher in both siEpCAM and siTrop2. In Figure 3.20 (e) we then normalize this cell-cell force by the total force exerted by the doublet, which we obtain by integrating the absolute values of the traction stresses over the surface of the doublet. This value is an indicator of how much of the cell-generated forces are oriented towards the cell-cell vs the cell-matrix adhesions. Here we observe no effect on siEpCAM and siTrop2, but on the dKD, where forces are more oriented towards the junction. We hypothesize, that EpCAM and Trop2 can compensate for each other to a certain extent and that the phenotype here only becomes visible, when both proteins are downregulated.

Last but not least, we approximated the length of the junction, another indirect indicator for cell-cell adhesion strength, by measuring the shortest distance between the upper and lower cell boundary on the brightfield images. Here we observed a significant increase in junction length in siEpCAM and dKD, but not in siTrop2.

Together, these results suggest that EpCAM and Trop2 downregulate cell-cell adhesion by downregulating myosin II activity. Both cadherins and integrins are known to have catch-bond properties, as discussed in subsection 1.1.3, so less conractility should à priori lead to less cell-cell, but also less cell-substrate adhesion. The results also indicate that both proteins together have a stronger effect on cell-cell than on cell-matrix adhesion. Altogether, these results are in line with the main conclusion of Azam's work, that EpCAM favors single cell migration over collective cell migration through down-regulation of cell contractility and cell-cell adhesion, which could favor detachment of cells from a tumor and induce cancer metastasis.

3.3.3 Discussion

In this section I showed, how the tools I used throughout my PhD can be applied to answer important biological questions. Cell contractility, cell-cell adhesion and cell-substrate adhesion are central biophysical properties that play a huge role in development, cancer development and progression but also in tissue homeostasis

or wound healing. How exactly these cell biophysical properties regulate tissue scale behavior is still a much discussed, open question. For example during development, regulation of cell-cell and cell-substrate adhesion is thought to regulate tissue separation in between tissues and tissue cohesiveness within a tissue. Tissue motility, which is essential to drive morphogenetic processes, is also regulated through both cell contractility and cell-substrate adhesion. Characterizing and comparing these properties in different cell types and in different biological contexts is therefore essential to understand tissue scale behavior. The TFM and H micropattern cell doublet approach for characterizing these properties has numerous unique advantages:

First, the morphology of the doublet is standardized and the spreading surface, which correlates with cell contractility, is limited. In other words, we can asses cell contractility for a given spreading size instead of having to measure and compare both. This makes it easier to compare different conditions.

Second, the symmetry of the system makes it easy to calculate cell-cell and cell-substrate forces from the TFM data, which facilitates high throughput in order to get good statistics.

Third, the fact that the doublets are fixed in space makes dynamical measurements in response to e.g. mechanical or pharmacological perturbation much easier. This was not exploited in the projects just presented, but was essential for my own project.

Last but not least, the system can be even further exploited by combining morphometrics, such as junction length and free stress fiber curvature, with force measurements and mechanical modelling to calculate further interesting quantities, such as cortical stress and tension in the stress fibers. Again, this was not fully exploited here, but was demonstrated in my project.

In the future, this approach can be used to characterize basic biophysical properties of different cell types and different combination of cells. In addition with biochemical perturbation of molecules implicated in cell-cell adhesion and/or cell-substrate adhesion, such as cadherins or integrins, this is a powerful tool to decipher the cross-talk between these different molecules and how they regulate basic cell-cell interactions.

4. Future perspectives

Many of the concrete questions we are trying to address in the team are inspired by the beautiful and complex processes that happen during the development of an organism. As physicists, we try to reduce the complexity of these systems as much as possible in order to make precise measurements and develop models. Our goal here is to start with something as simple as possible, such as single cells or cell doublets and try to find underlying principles that can predict the complex tissue scale behavior that we see *in vivo*. In the paper draft presented in section 3.2, we propose a novel mode of force propagation, where we suggest that cells amplify mechanical signals coming from their surrounding, preferentially so if their mechano-structural, planar polarization axis is perpendicular to the direction of the signal transmission direction. In line with our bottom-up approach, we first found this property in epithelial cell doublets and subsequently confirmed, that a similar principle is at work in small epithelial cell clusters comprised of about 10 to 20 cells. Going forward, I suggest three different ideas to expand on this finding:

First, it is important to better understand the role of the cell-cell junction in this mode of force signal propagation, particularly with respect to the different molecules involved in cell-cell adhesion. We know, that cell-cell junctions are signalling hubs and that, among others, mechanical signals get transduced here into biochemical signals which can then in turn lead to complex, downstream cell behavior. Addressing this question would require combining the experiment on cell doublets with biochemical perturbations of cell-cell adhesion. Concretely, it would be interesting to disrupt the junction somehow and then repeat the optogenetic perturbation of one of the cells, in order to see how this affects the efficiency of force signal propagation. We discussed three main ideas to perform this experiment: First, interchalating calcium with e.g. EGTA would disrupt the junction, but

calcium has many roles in regulating cell mechanics, far beyond the regulation of cell-cell junctions, and therefore we deemed this experiment to be too unspecific. Second, one could perturb the junction with antibodies, which I think would be a challenging but potentially feasible experiment. However, it is unclear how one would go on about doing this experiment. It is unlikely, that the junction can be disrupted with this approach after it is already formed, so comparison of force propagation in the same doublet with and without junction seems impossible and one would have to rely on statistical comparison. The third option, which to me is the most exciting one, would be to combine the optogenetic tool used in my work with LInDA, an optochemical tool developed in the group of Elisabetta Ada Cavalcanti-Adam, that allows for the disruption of adherens junctions with a short pulse of UV light [181]. Combining these two tools would certainly be challenging as well, but a successful implementation would allow to study force signal propagation with and without adherens junction in the same system, e.g. in doublets or in small cell clusters.

Second, the next logical step after studying single cells and cell doublets would be to increase the complexity of the system. Most studies that can be found in the literature look at either single cells or cell doublets, where morphology can be controlled with micropatterns, or self-organized cell clusters, where only the shape of the cluster, but not the shape nor the position of the cells is precisely controlled. I think it would be interesting to try to find patterns that stabilize more complex structures with more then two cells. In fact, some preliminary experiments I did during my PhD showed, that it is possible to form reproducible quadruplet structures by extending the idea of the H pattern (which works because junctions tend to position themselves over regions that are devoid of ECM) to a four cell pattern (Figure 4.1). These quadruplet structures form interesting t-junctions, where two of the cells have only two neighbors, whereas the other two cells have three neighbors. This means, that there are two possible configurations of this system: One, where the t-junction is vertical and one where it is horizontal. During development, one can observe the same kind of t-junction patterns and transitioning from one of these configurations to the other, called a T1 transition, is a major process that cells use to release tissue mechanical stress during e.g. convergent extension of a tissue [165, 182]. This model system therefore represents a minimalistic *in vitro* model that could be used to study the mechanics of T1 transitions, particu-

larly interesting when combined with optogenetics and TFM. The dream experiment here would be, to induce a T1 transition on these patterns with optogenetics and map the cell-substrate forces that lead to that transition.

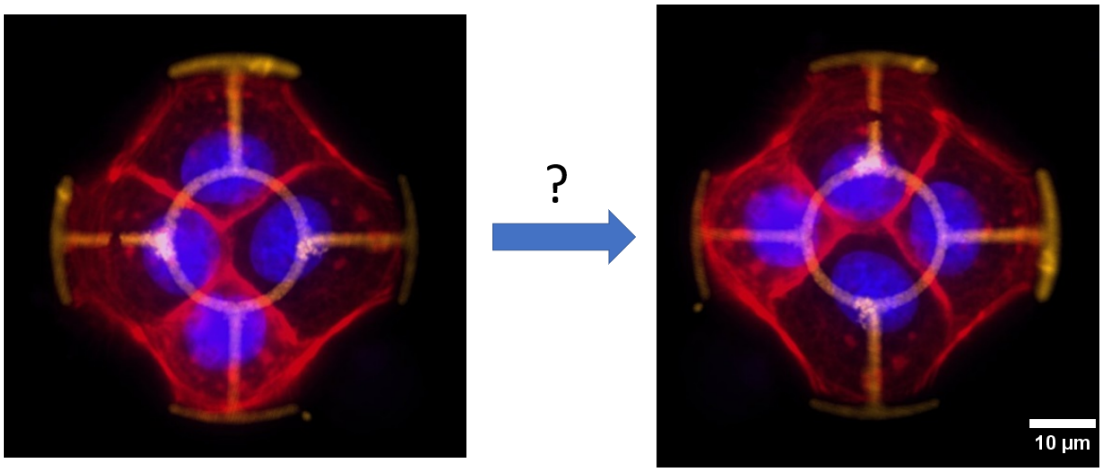

Figure 4.1: opto-MDCK cells forming quadruplets on micropatterns.

Third, I think it is important to move towards more physiologically relevant model systems in order to gain more biological insight. Despite being a classical epithelial cell model, MDCK cells, specifically in combination with the optogenetic construct and the use of micropatterns, are quite artificial. There are many advantages in using these systems, especially because they allow for detailed and extensive mechanical characterization and modelling, but it is important to translate the findings from these *in vitro* models into more physiological situations. Since much of our work is inspired by morphogenetic processes during development, it would be interesting to combine the ideas and methods from this and previous studies from our lab with embryonic stem cells. In fact, this and the previously mentioned idea are at the basis of an ANR grant proposal coordinated by François Fagotto in collaboration with us, using the preliminary data shown in Figure 3.19 and Figure 4.1. At the core of this project is the idea of reconstituting fundamental morphogenetic processes *in vitro* and then validate and translate those findings *in vivo*, as sketched out in Figure 4.2. I am happy to say, that this grant proposal has been successful and that I will be able to continue developing these ideas as a postdoc in François Fagotto's lab.

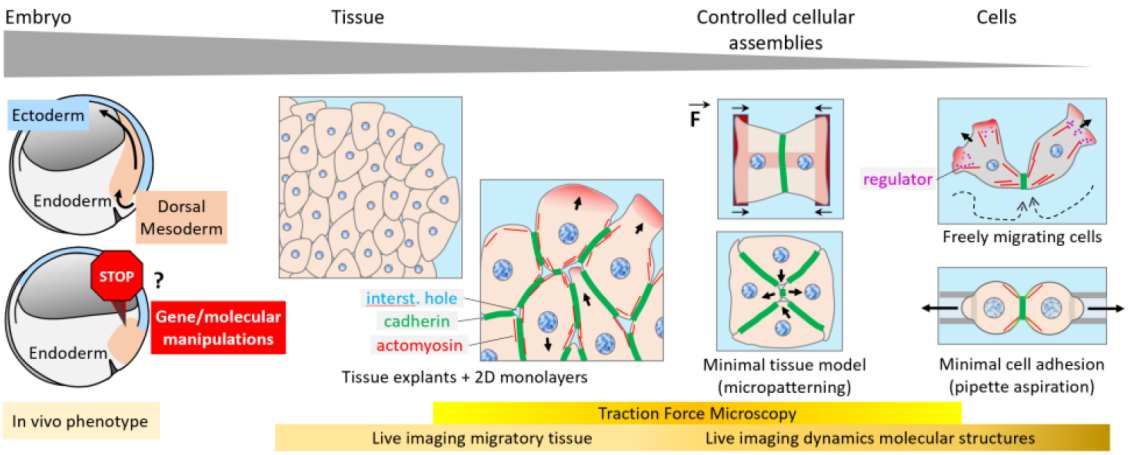

Figure 4.2: How can mesoderm be so motile yet remain so coherent? A multi-scale dissection of tissue plasticity. Made by François Fagotto for the Inter-s-cal ANR pre-proposal in collaboration with Martial Balland.

Bibliography

[1] Jarosław Kwapień and Stanisław Drozdz. Physical approach to complex systems. *Physics Reports*, 515(3-4):115–226, 2012.

[2] Christopher S. Chen, Milan Mrksich, Sui Huang, George M Whitesides, and Donald E. Ingber. Geometric Control of Cell Life and Death. *Science*, 276(5317):1425–1428, 1997.

[3] R McBeath, D M Pirone, C M Nelson, K Bhadriraju, and C S Chen. Cell shape, cytoskeletal tension, and RhoA regulate stemm cell lineage commitment. *Developmental Cell*, 6:483–495, 2004.

[4] Edouard Hannezo and Carl Philipp Heisenberg. Mechanochemical Feedback Loops in Development and Disease, jun 2019.

[5] Thomas Boudou, Tomas Andersen, and Martial Balland. On the spatiotemporal regulation of cell tensional state. *Experimental Cell Research*, In press, 2019.

[6] Claudio Collinet and Thomas Lecuit. Programmed and self-organized flow of information during morphogenesis, 2021.

[7] G. W. Brodland, V. Conte, P. G. Cranston, J. Veldhuis, S. Narasimhan, M. S. Hutson, A. Jacinto, F. Ulrich, B. Baum, and M. Miodownik. Video force microscopy reveals the mechanics of ventral furrow invagination in Drosophila. *Proceedings of the National Academy of Sciences*, 107(51):22111–22116, 2010.

[8] Emiliano Izquierdo, Theresa Quinkler, and Stefano De Renzis. Guided morphogenesis through optogenetic activation of Rho signalling during early Drosophila embryogenesis. *Nature Communications*, 9(1):1–13, 2018.

[9] A. M. Turing. The Chemical Basis of Morphogenesis. *Philosophical transactions of the Royal Society of London. Series B, Biological sciences*,

237(641):37–72, aug 1952.

[10] Jonathon Howard, Stephan W. Grill, and Justin S. Bois. Turing's next steps: The mechanochemical basis of morphogenesis. *Nature Reviews Molecular Cell Biology*, 12(6):400–406, 2011.

[11] Nicolas Desprat, Willy Supatto, Philippe Alexandre Pouille, Emmanuel Beaurepaire, and Emmanuel Farge. Tissue Deformation Modulates Twist Expression to Determine Anterior Midgut Differentiation in Drosophila Embryos. *Developmental Cell*, 15(3):470–477, 2008.

[12] Daniel A. Fletcher and R. Dyche Mullins. Cell mechanics and the cytoskeleton. *Nature*, 463(7280):485–492, 2010.

[13] Lisa Urry, Michael Cain, Steven Wasserman, Peter Minorsky, Jane Reece, and Neil Campbell. *Campbell Biology 11th Edition*. Pearson, 2016.

[14] Romain Levayer and Thomas Lecuit. Biomechanical regulation of contractility: Spatial control and dynamics, feb 2012.

[15] Laurent Blanchoin, Rajaa Boujemaa-Paterski, Cécile Sykes, and Julie Plastino. Actin Dynamics, Architecture, and Mechanics in Cell Motility. *Physiological Reviews*, 94(1):235–263, jan 2014.

[16] Daniel Riveline, Eli Zamir, Nathalie Q. Balaban, Ulrich S. Schwarz, Toshimasa Ishizaki, Shuh Narumiya, Zvi Kam, Benjamin Geiger, and Alexander D. Bershadsky. Focal contacts as mechanosensors: Externally applied local mechanical force induces growth of focal contacts by an mDia1-dependent and ROCK-independent mechanism. *Journal of Cell Biology*, 153(6):1175–1185, 2001.

[17] Z. Liu, J. L. Tan, D. M. Cohen, M. T. Yang, N. J. Sniadecki, S. A. Ruiz, C. M. Nelson, and C. S. Chen. Mechanical tugging force regulates the size of cell-cell junctions. *Proceedings of the National Academy of Sciences*, 107(22):9944–9949, 2010.

[18] Ulrich S Schwarz and Margaret L Gardel. United we stand – integrating the actin cytoskeleton and cell – matrix adhesions in cellular mechanotransduction. *Journal of Cell Science*, 13(125):3051–3060, 2012.

[19] Joshua A. Broussard, Avinash Jaiganesh, Hoda Zarkoob, Daniel E. Conway, Alexander R. Dunn, Horacio D. Espinosa, Paul A. Janmey, and Kathleen J.

Green. Scaling up single-cell mechanics to multicellular tissues - the role of the intermediate filament-desmosome network. *Journal of cell science*, 133(6), 2020.

[20] Fang Kong, Andrés J. García, A. Paul Mould, Martin J. Humphries, and Cheng Zhu. Demonstration of catch bonds between an integrin and its ligand. *Journal of Cell Biology*, 185(7):1275–1284, 2009.

[21] Kristine Manibog, Hui Li, Sabyasachi Rakshit, and Sanjeevi Sivasankar. Resolving the molecular mechanism of cadherin catch bond formation. *Nature Communications*, 5:1–11, 2014.

[22] Armando Rio, Raul Perez-jimenez, Ruchuan Liu, Pere Roca-cusachs, Julio M Fernandez, and Michael P Sheetz. Stretching Single Talin Rod. *Science*, 323(January):638–641, 2009.

[23] Mingxi Yao, Wu Qiu, Ruchuan Liu, Artem K. Efremov, Peiwen Cong, Rima Seddiki, Manon Payre, Chwee Teck Lim, Benoit Ladoux, René Marc Mège, and Jie Yan. Force-dependent conformational switch of α -catenin controls vinculin binding. *Nature Communications*, 5, 2014.

[24] Ion Andreu, Bryan Falcones, Sebastian Hurst, Nimesh Chahare, Xarxa Quiroga, Anabel Lise Le Roux, Zanetta Kechagia, Amy E.M. Beedle, Alberto Elosegui-Artola, Xavier Trepat, Ramon Farré, Timo Betz, Isaac Almendros, and Pere Roca-Cusachs. The force loading rate drives cell mechanosensing through both reinforcement and cytoskeletal softening. *Nature Communications*, 12(1):1–12, 2021.

[25] Thomas Iskratsch, Haguy Wolfenson, and Michael P. Sheetz. Appreciating force and shape-the rise of mechanotransduction in cell biology. *Nature Reviews Molecular Cell Biology*, 15(12):825–833, 2014.

[26] Adam J. Engler, Shamik Sen, H. Lee Sweeney, and Dennis E. Discher. Matrix Elasticity Directs Stem Cell Lineage Specification. *Cell*, 126(4):677–689, 2006.

[27] Sirio Dupont, Leonardo Morsut, Mariaceleste Aragona, Elena Enzo, Stefano Giulitti, Michelangelo Cordenonsi, Francesca Zanconato, Jimmy Le Digabel, Mattia Forcato, Silvio Bicciato, Nicola Elvassore, and Stefano Piccolo. Role of YAP/TAZ in mechanotransduction. *Nature*, 474(7350):179–184,

2011.

[28] A. Wayne Orr, Brian P. Helmke, Brett R. Blackman, and Martin A. Schwartz. Mechanisms of mechanotransduction. *Developmental Cell*, 10(1):11–20, 2006.

[29] Christopher C. Dufort, Matthew J. Paszek, and Valerie M. Weaver. Balancing forces: Architectural control of mechanotransduction. *Nature Reviews Molecular Cell Biology*, 12(5):308–319, 2011.

[30] Alicia M. Salvi and Kris A. DeMali. Mechanisms linking mechanotransduction and cell metabolism. *Current Opinion in Cell Biology*, 54(Figure 1):114–120, 2018.

[31] Rafael Dominik Fritz and Olivier Pertz. The dynamics of spatio-temporal Rho GTPase signaling: formation of signaling patterns. *F1000Research*, 5(0):749, 2016.

[32] Pei Hsun Wu, Dikla Raz Ben Aroush, Atef Asnacios, Wei Chiang Chen, Maxim E. Dokukin, Bryant L. Doss, Pauline Durand-Smet, Andrew Ekpenyong, Jochen Guck, Nataliia V. Guz, Paul A. Janmey, Jerry S.H. Lee, Nicole M. Moore, Albrecht Ott, Yeh Chuin Poh, Robert Ros, Mathias Sander, Igor Sokolov, Jack R. Staunton, Ning Wang, Graeme Whyte, and Denis Wirtz. A comparison of methods to assess cell mechanical properties. *Nature Methods*, 15(July):1–8, 2018.

[33] Pere Roca-Cusachs, Vito Conte, and Xavier Trepat. Quantifying forces in cell biology. *Nature Cell Biology*, 19(7):742–751, 2017.

[34] William J. Polacheck and Christopher S. Chen. Measuring cell-generated forces: A guide to the available tools. *Nature Methods*, 13(5):415–423, 2016.

[35] Louise K. Wrobel, Tim R. Fray, Justin E. Molloy, Julian J. Adams, Mark P. Armitage, and John C. Sparrow. Micropatterning tractional forces in living cells. *Cell Motility and the Cytoskeleton*, 52(2):97–106, 2002.

[36] Joseph P. Califano and Cynthia A. Reinhart-King. Substrate stiffness and cell area predict cellular traction stresses in single cells and cells in contact. *Cellular and Molecular Bioengineering*, 3(1):68–75, 2010.

[37] Tony Yeung, Penelope C. Georges, Lisa A. Flanagan, Beatrice Marg,

Miguelina Ortiz, Makoto Funaki, Nastaran Zahir, Wenyu Ming, Valerie Weaver, and Paul A. Janmey. Effects of substrate stiffness on cell morphology, cytoskeletal structure, and adhesion. *Cell Motility and the Cytoskeleton*, 60(1):24–34, 2005.

[38] Andrew D. Rape, Wei Hui Guo, and Yu Li Wang. The regulation of traction force in relation to cell shape and focal adhesions. *Biomaterials*, 32(8):2043–2051, 2011.

[39] Patrick W. Oakes, Shiladitya Banerjee, M. Cristina Marchetti, and Margaret L. Gardel. Geometry regulates traction stresses in adherent cells. *Biophysical Journal*, 107(4):825–833, 2014.

[40] Michael Murrell, Patrick W Oakes, Martin Lenz, and Margaret L Gardel. Forcing cells into shape: the mechanics of actomyosin contractility. *Nature Publishing Group*, 16(July):486—-498, 2015.

[41] Timothée Vignaud, Calina Copos, Christophe Leterrier, Mauricio Toro-Nahuelpan, Qingzong Tseng, Julia Mahamid, Laurent Blanchoin, Alex Mogilner, Manuel Théry, and Laetitia Kurzawa. Stress fibres are embedded in a contractile cortical network. *Nature Materials*, 20(3):410–420, 2021.

[42] Kalpana Mandal, Irène Wang, Elisa Vitiello, Laura Andreina Chacòn Orellana, and Martial Balland. Cell dipole behaviour revealed by ECM subcellular geometry. *Nature Communications*, 5, 2014.

[43] Manuel Théry, Anne Pépin, Emilie Dressaire, Yong Chen, and Michel Bornens. Cell distribution of stress fibres in response to the geometry of the adhesive environment. *Cell Motility and the Cytoskeleton*, 63(6):341–355, 2006.

[44] Elena Kassianidou, Dimitri Probst, Julia Jäger, Stacey Lee, Anne Lou Roguet, Ulrich Sebastian Schwarz, and Sanjay Kumar. Extracellular Matrix Geometry and Initial Adhesive Position Determine Stress Fiber Network Organization during Cell Spreading. *Cell Reports*, pages 1897–1909, 2019.

[45] Sanjay Kumar, Iva Z Maxwell, Alexander Heisterkamp, Thomas R Polte, Tanmay P Lele, Matthew Salanga, Eric Mazur, and Donald E Ingber. Viscoelastic Retraction of Single Living Stress Fibers and Its Impact on Cell

Shape , Cytoskeletal Organization , and Extracellular Matrix Mechanics. *Biophysical Journal*, 90(10):3762–3773, 2006.

[46] Elena Kassianidou, Christoph A. Brand, Ulrich S. Schwarz, and Sanjay Kumar. Geometry and network connectivity govern the mechanics of stress fibers. *Proceedings of the National Academy of Sciences*, 114(10):2622–2627, 2017.

[47] Charlène Gayrard and Nicolas Borghi. FRET-based Molecular Tension Microscopy. *Methods*, 94:33–42, 2016.

[48] Mei Rosa Ng, Achim Besser, Joan S. Brugge, and Gaudenz Danuser. Mapping the dynamics of force transduction at cell-cell junctions of epithelial clusters. *eLife*, 3:e03282, 2014.

[49] V. Maruthamuthu, B. Sabass, U. S. Schwarz, and M. L. Gardel. Cell-ECM traction force modulates endogenous tension at cell-cell contacts. *Proceedings of the National Academy of Sciences*, 108(12):4708–4713, 2011.

[50] Q. Tseng, E. Duchemin-Pelletier, A. Deshiere, M. Balland, H. Guillou, O. Filhol, and M. Thery. Spatial organization of the extracellular matrix regulates cell-cell junction positioning. *Proceedings of the National Academy of Sciences*, 109(5):1506–1511, 2012.

[51] J. Y. Sim, J. Moeller, K. C. Hart, D. Ramallo, V. Vogel, A. R. Dunn, W. J. Nelson, and B. L. Pruitt. Spatial distribution of cell-cell and cell-ECM adhesions regulates force balance while main taining E-cadherin molecular tension in cell pairs. *Molecular Biology of the Cell*, 26(13):2456–2465, 2015.

[52] M. L. McCain, H. Lee, Y. Aratyn-Schaus, A. G. Kleber, and K. K. Parker. Cooperative coupling of cell-matrix and cell-cell adhesions in cardiac muscle. *Proceedings of the National Academy of Sciences*, 109(25):9881–9886, 2012.

[53] Samuel R. Polio, Suzanne E. Stasiak, Ryan R. Jamieson, Jenna L. Balestrini, Ramaswamy Krishnan, and Harikrishnan Parameswaran. Extracellular matrix stiffness regulates human airway smooth muscle contraction by altering the cell-cell coupling. *Scientific Reports*, 9(1):1–12, 2019.

[54] Diego A. Vargas, Tommy Heck, Bart Smeets, Herman Ramon, Harikrishnan Parameswaran, and Hans Van Oosterwyck. Intercellular Adhesion Stiffness Moderates Cell Decoupling as a Function of Substrate Stiffness. *Biophysical*

Journal, 119(2):243–257, 2020.

[55] Xiaojun Li, Shijie He, Jiayi Xu, Peiliu Li, and Baohua Ji. Cooperative Contraction Behaviors of a One-Dimensional Cell Chain. *Biophysical Journal*, 2018.

[56] Anne J. Ridley, Martin A. Schwartz, Keith Burridge, Richard A. Firtel, Mark H. Ginsberg, Gary Borisy, J. Thomas Parsons, and Alan Rick Horwitz. Cell Migration: Integrating Signals from Front to Back. *Science*, 302(5651):1704–1709, 2003.

[57] Xavier Trepat, Zaozao Chen, and Ken Jacobson. Cell migration. *Comprehensive Physiology*, 2(4):2369–2392, 2012.

[58] P. N. Devreotes and S. H. Zigmond. Chemotaxis in eukaryotic cells: A focus on leukocytes and Dictyostelium. *Annual Review of Cell Biology*, 4:649–686, 1988.

[59] S. B. Carter. Haptotaxis and the mechanism of cell motility. *Nature*, 213(5073):256–260, 1967.

[60] Raimon Sunyer and Xavier Trepat. Durotaxis. *Current Biology*, 30(9):R383–R387, 2020.

[61] Dhananjay T. Tambe, C. Corey Hardin, Thomas E. Angelini, Kavitha Rajendran, Chan Young Park, Xavier Serra-Picamal, Enhua H. Zhou, Muhammad H. Zaman, James P. Butler, David A. Weitz, Jeffrey J. Fredberg, and Xavier Trepat. Collective cell guidance by cooperative intercellular forces. *Nature Materials*, 10(6):469–475, 2011.

[62] Marine Luciano, Shi-Lei Xue, Winnok H. De Vos, Lorena Redondo-Morata, Mathieu Surin, Frank Lafont, Edouard Hannezo, and Sylvain Gabriele. Cell monolayers sense curvature by exploiting active mechanics and nuclear mechanoadaptation. *Nature Physics*, 2021.

[63] Sebastien J.P. Callens, Rafael J.C. Uyttendaele, Lidy E. Fratila-Apachitei, and Amir A. Zadpoor. Substrate curvature as a cue to guide spatiotemporal cell and tissue organization. *Biomaterials*, 232(December 2019):119739, 2020.

[64] Juergen Friedrich, Claudia Seidel, Reinhard Ebner, and Leoni A. Kunz-Schughart. Spheroid-based drug screen: Considerations and practical ap-

proach. *Nature Protocols*, 4(3):309–324, 2009.

[65] Eelco Fennema, Nicolas Rivron, Jeroen Rouwkema, Clemens van Blitterswijk, and Jan De Boer. Spheroid culture as a tool for creating 3D complex tissues. *Trends in Biotechnology*, 31(2):108–115, 2013.

[66] W. R. Legant, A. Pathak, M. T. Yang, V. S. Deshpande, R. M. McMeeking, and C. S. Chen. Microfabricated tissue gauges to measure and manipulate forces from 3D microtissues. *Proceedings of the National Academy of Sciences*, 106(25):10097–10102, 2009.

[67] Jarno Drost and Hans Clevers. Organoids in cancer research. *Nature Reviews Cancer*, 18(7):407–418, 2018.

[68] Sunghee Estelle Park, Andrei Georgescu, and Dongeun Huh. Organoids-on-a-chip. *Science*, 364(6444):960–965, 2019.

[69] Hsih Yin Tan, Hansang Cho, and Luke P. Lee. Human mini-brain models. *Nature Biomedical Engineering*, 5(1):11–25, 2021.

[70] Albert K. Harris, Patricia Wild, and David Stopak. Silicone Rubber Substrata: A New Wrinkle in the Study of Cell Locomotion. *Science*, 208(4440):177–179, apr 1980.

[71] Ulrich S. Schwarz and Jérôme R.D. Soiné. Traction force microscopy on soft elastic substrates: A guide to recent computational advances. *Biochimica et Biophysica Acta - Molecular Cell Research*, 1853(11):3095–3104, 2015.

[72] R. J. Adrian. Twenty years of particle image velocimetry. *Experiments in Fluids*, 39(2):159–169, July 2005.

[73] William Thielicke and René Sonntag. Particle image velocimetry for MATLAB: Accuracy and enhanced algorithms in PIVlab. *Journal of Open Research Software*, 9, 2021.

[74] Irène Wang. Développements en microscopie optique pour le vivant : imagerie, mesures de mobilité et forces. *unpublished*, 2013.

[75] Benedikt Sabass, Margaret L. Gardel, Clare M. Waterman, and Ulrich S. Schwarz. High resolution traction force microscopy based on experimental and computational advances. *Biophysical Journal*, 94(1):207–220, 2008.

[76] Fakhre Alam, Sami Ur Rahman, Shah Khusro, Sehat Ullah, and Adnan Khalil. Evaluation of medical image registration techniques based on na-

ture and domain of the transformation. *Journal of Medical Imaging and Radiation Sciences*, 47(2):178–193, June 2016.

[77] S. Klein, M. Staring, K. Murphy, M.A. Viergever, and J. Pluim. elastix: A toolbox for intensity-based medical image registration. *IEEE Transactions on Medical Imaging*, 29(1):196–205, January 2010.

[78] Alvaro Jorge-Peñas, Alicia Izquierdo-Alvarez, Rocio Aguilar-Cuenca, Miguel Vicente-Manzanares, José Manuel Garcia-Aznar, Hans Van Oosterwyck, Elena M. De-Juan-Pardo, Carlos Ortiz-De-Solorzano, and Arrate Muñoz-Barrutia. Free form deformation-based image registration improves accuracy of traction force microscopy. *PLoS ONE*, 10(12):1–22, 2015.

[79] Ibrahim Kajo, Aamir Saeed Malik, and Nidal Kamel. Motion estimation of crowd flow using optical flow techniques: A review. In *2015 9th International Conference on Signal Processing and Communication Systems (ICSPCS)*. IEEE, December 2015.

[80] Claude N. Holenstein, Unai Silvan, and Jess G. Snedeker. High-resolution traction force microscopy on small focal adhesions-Improved accuracy through optimal marker distribution and optical flow tracking. *Scientific Reports*, 7, 2017.

[81] M Dembo, T Oliver, A. Ishihara, and K. Jacobson. Imaging the traction stresses exerted by locomoting cells with the elastic substratum method. *Biophysical Journal*, 70(4):2008–2022, 1996.

[82] James P Butler, Iva Marija Toli-Nørrelykke, Ben Fabry, and Jeffrey J Fredberg. Traction fields, moments, and strain energy that cells exert on their surroundings. *American Journal of Physiology - Cell Physiology*, 282(3 51-3):595–605, 2002.

[83] Xavier Trepat and Jeffrey J Fredberg. Plithotaxis and emergent dynamics in collective cellular migration, 2011.

[84] Dhananjay T Tambe, Ugo Croutelle, Xavier Trepat, Chan Young Park, Jae Hun Kim, Emil Millet, James P Butler, and Jeffrey J Fredberg. Monolayer Stress Microscopy: Limitations, Artifacts, and Accuracy of Recovered Intercellular Stresses. *PLoS ONE*, 8(2), 2013.

[85] Andreas Bauer, Magdalena Prechová, Lena Fischer, Ingo Thievessen, Martin

Gregor, and Ben Fabry. pyTFM: A tool for traction force and monolayer stress microscopy. *PLOS Computational Biology*, 17(6):e1008364, 2021.

[86] Nathalie Q. Balaban, Ulrich S. Schwarz, Daniel Riveline, Polina Goichberg, Gila Tzur, Ilana Sabanay, Diana Mahalu, Sam Safran, Alexander Bershadsky, Lia Addadi, and Benjamin Geiger. Force and focal adhesion assembly: A close relationship studied using elastic micropatterned substrates. *Nature Cell Biology*, 3(5):466–472, may 2001.

[87] Martin Bergert, Tobias Lendenmann, Manuel Zündel, Alexander E. Ehret, Daniele Panozzo, Patrizia Richner, David K. Kim, Stephan J.P. Kress, David J. Norris, Olga Sorkine-Hornung, Edoardo Mazza, Dimos Poulikakos, and Aldo Ferrari. Confocal reference free traction force microscopy. *Nature Communications*, 7, 2016.

[88] Somanna Kollimada, Fabrice Senger, Timothée Vignaud, Manuel Théry, Laurent Blanchoin, and Laëtitia Kurzawa. The biochemical composition of the actomyosin network sets the magnitude of cellular traction forces, 2021.

[89] Huw Colin-York, Dilip Shrestha, James H. Felce, Dominic Waithe, Emad Moeendarbary, Simon J. Davis, Christian Eggeling, and Marco Fritzsche. Super-Resolved Traction Force Microscopy (STFM). *Nano Letters*, 16(4):2633–2638, 2016.

[90] Sergey V. Plotnikov, Benedikt Sabass, Ulrich S. Schwarz, and Clare M. Waterman. *High-Resolution Traction Force Microscopy*, volume 123. Elsevier Inc., 1 edition, 2014.

[91] Jennet Toyjanova, Eyal Bar-Kochba, Cristina López-Fagundo, Jonathan Reichner, Diane Hoffman-Kim, and Christian Franck. High resolution, large deformation 3D traction force microscopy. *PLoS ONE*, 9(4):1–12, 2014.

[92] Wesley R. Legant, Jordan S. Miller, Brandon L. Blakely, Daniel M. Cohen, Guy M. Genin, and Christopher S. Chen. Measurement of mechanical tractions exerted by cells in three-dimensional matrices. *Nature Methods*, 7(12):969–971, 2010.

[93] Julian Steinwachs, Claus Metzner, Kai Skodzek, Nadine Lang, Ingo Thievessen, Christoph Mark, Stefan Münster, Katerina E. Aifantis, and Ben

Fabry. Three-dimensional force microscopy of cells in biopolymer networks. *Nature Methods*, 13(2):171–176, 2016.

[94] Christoph Mark, Thomas J. Grundy, Pamela L. Strissel, David Böhringer, Nadine Grummel, Richard Gerum, Julian Steinwachs, Carolin C. Hack, Matthias W. Beckmann, Markus Eckstein, Reiner Strick, Geraldine M. O'neill, and Ben Fabry. Collective forces of tumor spheroids in three-dimensional biopolymer networks. *eLife*, 9:2–9, 2020.

[95] Jean Paul Rieu and Hélène Delanoë-Ayari. Shell tension forces propel Dictyostelium slugs forward. *Physical Biology*, 9(6), 2012.

[96] Ye Xu, Wilfried C. Engl, Elizabeth R. Jerison, Kevin J. Wallenstein, Callen Hyland, Larry A. Wilen, and Eric R. Dufresne. Imaging in-plane and normal stresses near an interface crack using traction force microscopy. *Proceedings of the National Academy of Sciences of the United States of America*, 107(34):14964–14967, 2010.

[97] Ben Zion Shilo. Regulating the dynamics of EGF receptor signaling in space and time. *Development*, 132(18):4017–4027, 2005.

[98] Xaralabos Varelas, Bryan W. Miller, Richelle Sopko, Siyuan Song, Alex Gregorieff, Frederic A. Fellouse, Rui Sakuma, Tony Pawson, Walter Hunziker, Helen McNeill, Jeffrey L. Wrana, and Liliana Attisano. The Hippo Pathway Regulates Wnt/β-Catenin Signaling. *Developmental Cell*, 18(4):579–591, 2010.

[99] Norbert Perrimon, Chrysoula Pitsouli, and Ben Zion Shilo. Signaling mechanisms controlling cell fate and embryonic patterning. *Cold Spring Harbor Perspectives in Biology*, 4(8), 2012.

[100] Benjamin E. Housden and Norbert Perrimon. Spatial and temporal organization of signaling pathways. *Trends in Biochemical Sciences*, 39(10):457–464, 2014.

[101] Jared E. Toettcher, Christopher A. Voigt, Orion D. Weiner, and Wendell A. Lim. The promise of optogenetics in cell biology: Interrogating molecular circuits in space and time. *Nature Methods*, 8(1):35–38, 2011.

[102] Mark Shaaya, Jordan Fauser, and Andrei V. Karginov. Optogenetics: The art of illuminating complex signaling pathways. *Physiology*, 36(1):52–60,

2021.

[103] Akarawin Hongdusit, Evan T. Liechty, and Jerome M. Fox. Optogenetic interrogation and control of cell signaling. *Current Opinion in Biotechnology*, 66:195–206, 2020.

[104] Doug Tischer and Orion D. Weiner. Illuminating cell signalling with optogenetic tools. *Nature Reviews Molecular Cell Biology*, 15(8):551–558, 2014.

[105] Payam E. Farahani, Ellen H. Reed, Evan J. Underhill, Kazuhiro Aoki, and Jared E. Toettcher. Signaling, Deconstructed: Using Optogenetics to Dissect and Direct Information Flow in Biological Systems. *Annual Review of Biomedical Engineering*, 23:61–87, 2021.

[106] Sandrine Etienne-Manneville and Alan Hall. Rho GTPases in cell biology. *Nature*, 420(6916):629–635, 2002.

[107] Masahiko Itoh. ARHGEF11, a regulator of junction-associated actomyosin in epithelial cells. *Tissue barriers*, 1(June):1–5, 2013.

[108] Matthew J. Kennedy, Robert M. Hughes, Leslie A. Peteya, Joel W. Schwartz, Michael D. Ehlers, and Chandra L. Tucker. Rapid blue-light-mediated induction of protein interactions in living cells. *Nature Methods*, 7(12):973–975, 2010.

[109] Leo Valon, Fred Etoc, Amanda Remorino, Florencia Di Pietro, Xavier Morin, Maxime Dahan, and Mathieu Coppey. Predictive Spatiotemporal Manipulation of Signaling Perturbations Using Optogenetics. *Biophysical Journal*, 109(9):1785–1797, 2015.

[110] Léo Valon, Ariadna Marín-Llauradó, Thomas Wyatt, Guillaume Charras, and Xavier Trepat. Optogenetic control of cellular forces and mechanotransduction. *Nature Communications*, 8:14396, 2017.

[111] Adam Shellard, András Szabó, Xavier Trepat, and Roberto Mayor. Supracellular contraction at the rear of neural crest cell groups drives collective chemotaxis. *Science*, 362(6412):339–343, 2018.

[112] Patrick W. Oakes, Elizabeth Wagner, Christoph A. Brand, Dimitri Probst, Marco Linke, Ulrich S. Schwarz, Michael Glotzer, and Margaret L. Gardel. Optogenetic control of RhoA reveals zyxin-mediated elasticity of stress fibres. *Nature Communications*, 8, 2017.

[113] Kate E. Cavanaugh, Michael F. Staddon, Shiladitya Banerjee, and Margaret L. Gardel. Adaptive viscoelasticity of epithelial cell junctions: from models to methods. *Current Opinion in Genetics and Development*, 63:86–94, 2020.

[114] Bros, Haas, Moll, and Grabbe. RhoA as a Key Regulator of Innate and Adaptive Immunity. *Cells*, 8(7):733, 2019.

[115] Ying Guo, Minati Satpathy, Graeme Wilson, and Sangly P. Srinivas. Benzalkonium chloride induces dephosphorylation of myosin light chain in cultured corneal epithelial cells. *Investigative Ophthalmology and Visual Science*, 48(5):2001–2008, 2007.

[116] Miguel Vicente-Manzanares, Xuefei Ma, Robert S. Adelstein, and Alan Rick Horwitz. Non-muscle myosin II takes centre stage in cell adhesion and migration. *Nature Reviews Molecular Cell Biology*, 10(11):778–790, 2009.

[117] Xin X. Zhou, Hokyung K. Chung, Amy J. Lam, and Michael Z. Lin. Optical control of protein activity by fluorescent protein domains. *Science*, 338(6108):810–814, 2012.

[118] Xin X. Zhou, Linlin Z. Fan, Pengpeng Li, Kang Shen, and Michael Z. Lin. Optical control of cell signaling by single-chain photoswitchable kinases. *Science*, 355(6327):836–842, 2017.

[119] Kei Yamamoto, Haruko Miura, Motohiko Ishida, Yusuke Mii, Noriyuki Kinoshita, Shinji Takada, Naoto Ueno, Satoshi Sawai, Yohei Kondo, and Kazuhiro Aoki. Optogenetic relaxation of actomyosin contractility uncovers mechanistic roles of cortical tension during cytokinesis. *Nature Communications*, 12(1):1–13, 2021.

[120] Ofer Yizhar, Lief E. Fenno, Thomas J. Davidson, Murtaza Mogri, and Karl Deisseroth. Optogenetics in Neural Systems. *Neuron*, 71(1):9–34, 2011.

[121] Lief Fenno, Ofer Yizhar, and Karl Deisseroth. The Development and Application of Optogenetics. *Annual Review of Neuroscience*, 34(1):389–412, 2011.

[122] Armin Baumschlager and Mustafa Khammash. Synthetic Biological Approaches for Optogenetics and Tools for Transcriptional Light-Control in Bacteria. *Advanced Biology*, 5(5), 2021.

[123] Dirk Benzinger and Mustafa Khammash. Pulsatile inputs achieve tunable attenuation of gene expression variability and graded multi-gene regulation. *Nature Communications*, 9(1), 2018.

[124] Jonas Hartmann, Daniel Krueger, and Stefano De Renzis. Using optogenetics to tackle systems-level questions of multicellular morphogenesis. *Current Opinion in Cell Biology*, 66:19–27, 2020.

[125] Silvana Konermann, Mark D. Brigham, Alexandro E. Trevino, Patrick D. Hsu, Matthias Heidenreich, Le Cong, Randall J. Platt, David A. Scott, George M. Church, and Feng Zhang. Optical control of mammalian endogenous transcription and epigenetic states. *Nature*, 500(7463):472–476, 2013.

[126] Florencia di Pietro, Sophie Herszterg, Anqi Huang, Floris Bosveld, Cyrille Alexandre, Lucas Sancéré, Stéphane Pelletier, Amina Joudat, Varun Kapoor, Jean-Paul Vincent, and Yohanns Bellaïche. Rapid and robust optogenetic control of gene expression in Drosophila. *Developmental Cell*, pages 3393–3404, 2021.

[127] Heath E. Johnson, Yogesh Goyal, Nicole L. Pannucci, Trudi Schüpbach, Stanislav Y. Shvartsman, and Jared E. Toettcher. The Spatiotemporal Limits of Developmental Erk Signaling. *Developmental Cell*, 40(2):185–192, 2017.

[128] Stephanie Nemec and Kristopher A. Kilian. Materials control of the epigenetics underlying cell plasticity. *Nature Reviews Materials*, 6(1):69–83, 2021.

[129] Masafumi Takahashi, Takafumi Ishida, Oren Traub, Marshall A. Coron, and Bradford C. Berk. Mechanotransduction in endothelial cells: Temporal signaling events in response to shear stress. *Journal of Vascular Research*, 34(3):212–219, 1997.

[130] Amandine Pitaval, Qingzong Tseng, Michel Bornens, and Manuel Théry. Cell shape and contractility regulate ciliogenesis in cell cycle-arrested cells. *Journal of Cell Biology*, 191(2):303–312, 2010.

[131] M. Thery. Micropatterning as a tool to decipher cell morphogenesis and functions. *Journal of Cell Science*, 123(24):4201–4213, 2010.

[132] Amy Brock, Eric Chang, Chia Chi Ho, Philip LeDuc, Xingyu Jiang, George M.

Whitesides, and Donald E. Ingber. Geometric determinants of directional cell motility revealed using microcontact printing. *Langmuir*, 19(5):1611–1617, 2003.

[133] M. Thery, V. Racine, M. Piel, A. Pepin, A. Dimitrov, Y. Chen, J.-B. Sibarita, and M. Bornens. Anisotropy of cell adhesive microenvironment governs cell internal organization and orientation of polarity. *Proceedings of the National Academy of Sciences*, 103(52):19771–19776, 2006.

[134] François Pouthas, Philippe Girard, Virginie Lecaudey, Thi Bach Nga Ly, Darren Gilmour, Christian Boulin, Rainer Pepperkok, and Emmanuel G. Reynaud. In migrating cells, the Golgi complex and the position of the centrosome depend on geometrical constraints of the substratum. *Journal of Cell Science*, 121(14):2406–2414, 2008.

[135] Felix J. Segerer, Florian Thüroff, Alicia Piera Alberola, Erwin Frey, and Joachim O. Rädler. Emergence and persistence of collective cell migration on small circular micropatterns. *Physical Review Letters*, 114(22):1–5, 2015.

[136] Grégoire Peyret, Romain Mueller, Joseph D'Alessandro, Simon Begnaud, Philippe Marcq, René Marc Mège, Julia M. Yeomans, Amin Doostmohammadi, and Benoît Ladoux. Sustained Oscillations of Epithelial Cell Sheets. *Biophysical Journal*, 117(3):464–478, 2019.

[137] Sri Ram Krishna Vedula, Hiroaki Hirata, Mui Hoon Nai, Agustí Brugués, Yusuke Toyama, Xavier Trepat, Chwee Teck Lim, and Benoit Ladoux. Epithelial bridges maintain tissue integrity during collective cell migration. *Nature Materials*, 13(1):87–96, 2014.

[138] Ammar Azioune, Marko Storch, Michel Bornens, Manuel Théry, and Matthieu Piel. Simple and rapid process for single cell micro-patterning. *Lab on a Chip*, 9(11):1640, 2009.

[139] George M Whitesides, Emanuele Ostuni, Shuichi Takayama, Xingyu Jiang, and Donald E. Ingber. Soft Lithography in Biology and Biochemistry. *Annual Review of Biomedical Engineering*, 3(1):335–373, aug 2001.

[140] Kalpana Mandal, Martial Balland, and Lionel Bureau. Thermoresponsive micropatterned substrates for single cell studies. *PLoS ONE*, 7(5):1–7,

2012.

[141] Timothée Vignaud, Hajer Ennomani, and Manuel Théry. Polyacrylamide Hydrogel Micropatterning. *Methods in Cell Biology*, 120:93–116, 2014.

[142] Albert Folch and Mehmet Toner. Microengineering of Cellular Interactions. *Annual Review of Biomedical Engineering*, 2(1):227–256, aug 2000.

[143] Justin R. Tse and Adam J. Engler. Preparation of hydrogel substrates with tunable mechanical properties. *Current Protocols in Cell Biology*, (SUPPL. 47):1–16, 2010.

[144] Adam C. Martin. Pulsation and stabilization: Contractile forces that underlie morphogenesis. *Developmental Biology*, 341(1):114–125, may 2010.

[145] Carl-Philipp Heisenberg and Yohanns Bellaïche. Forces in Tissue Morphogenesis and Patterning. *Cell*, 153(5):948–962, may 2013.

[146] Dennis E. Discher, Paul Janmey, and Yu-li Wang. Tissue Cells Feel and Respond to the Stiffness of Their Substrate. *American Association for the Advancement of Science (AAAS)*, 310(NOVEMBER):1139–1144, 2005.

[147] Jessica H. Wen, Ludovic G. Vincent, Alexander Fuhrmann, Yu Suk Choi, Kolin C. Hribar, Hermes Taylor-Weiner, Shaochen Chen, and Adam J. Engler. Interplay of matrix stiffness and protein tethering in stem cell differentiation. *Nature Materials*, 13(10):979–987, 2014.

[148] Kristopher A. Kilian, Branimir Bugarija, Bruce T. Lahn, and Milan Mrksich. Geometric cues for directing the differentiation of mesenchymal stem cells. *Proceedings of the National Academy of Sciences of the United States of America*, 107(11):4872–4877, 2010.

[149] Amit Pathak and Sanjay Kumar. Independent regulation of tumor cell migration by matrix stiffness and confinement. *Proceedings of the National Academy of Sciences*, 109(26):10334—-10339, 2012.

[150] A Shellard and R Mayor. Collective durotaxis along a self-generated stiffness gradient in vivo. *Nature*, 2021.

[151] Thomas Lecuit and Pierre François Lenne. Cell surface mechanics and the control of cell shape, tissue patterns and morphogenesis. *Nature Reviews Molecular Cell Biology*, 8(8):633–644, 2007.

[152] Michele A. Wozniak and Christopher S. Chen. Mechanotransduction in de-

velopment: A growing role for contractility. *Nature Reviews Molecular Cell Biology*, 10(1):34–43, 2009.

[153] William K. W. Ho, Lucy Freem, Debiao Zhao, Kevin J. Painter, Thomas E. Woolley, Eamonn A. Gaffney, Michael J. McGrew, Athanasia Tzika, Michel C. Milinkovitch, Pascal Schneider, Armin Drusko, Franziska Matthäus, James D. Glover, Kirsty L. Wells, Jeanette A. Johansson, Megan G. Davey, Helen M. Sang, Michael Clinton, and Denis J. Headon. Feather arrays are patterned by interacting signalling and cell density waves. *PLOS Biology*, 17(2):e3000132, 2019.

[154] Xavier Serra-Picamal, Vito Conte, Romaric Vincent, Ester Anon, Dhananjay T. Tambe, Elsa Bazellieres, James P. Butler, Jeffrey J. Fredberg, and Xavier Trepat. Mechanical waves during tissue expansion. *Nature Physics*, 8(8):628–634, 2012.

[155] Vanni Petrolli, Magali Le Goff, Monika Tadrous, Kirsten Martens, Cédric Allier, Ondrej Mandula, Lionel Hervé, Silke Henkes, Rastko Sknepnek, Thomas Boudou, Giovanni Cappello, and Martial Balland. Confinement-Induced Transition between Wavelike Collective Cell Migration Modes. *Physical Review Letters*, 122(16):1–5, 2019.

[156] Ilka B Bischofs, Franziska Klein, Dirk Lehnert, Martin Bastmeyer, and Ulrich S Schwarz. Filamentous Network Mechanics and Active Contractility Determine Cell and Tissue Shape. *Biophysical Journal*, 95(7):3488–3496, 2008.

[157] Ilka B Bischofs, Sebastian S Schmidt, and Ulrich S Schwarz. Effect of Adhesion Geometry and Rigidity on Cellular Force Distributions. *Physical Review Letters*, 048101(JULY):1–4, 2009.

[158] Wim Pomp, Koen Schakenraad, Hayri E. Balcloğlu, Hedde Van Hoorn, Erik H.J. Danen, Roeland M.H. Merks, Thomas Schmidt, and Luca Giomi. Cytoskeletal Anisotropy Controls Geometry and Forces of Adherent Cells. *Physical Review Letters*, 121(17):1–5, 2018.

[159] Naoya Hino, Leone Rossetti, Ariadna Marín-Llauradó, Kazuhiro Aoki, Xavier Trepat, Michiyuki Matsuda, and Tsuyoshi Hirashima. ERK-Mediated Mechanochemical Waves Direct Collective Cell Polarization. *Developmental Cell*, 53(6):646–660.e8, 2020.

[160] Ramaswamy Krishnan, Chan Young Park, Yu Chun Lin, Jere Mead, Richard T. Jaspers, Xavier Trepat, Guillaume Lenormand, Dhananjay Tambe, Alexander V. Smolensky, Andrew H. Knoll, James P. Butler, and Jeffrey J. Fredberg. Reinforcement versus fluidization in cytoskeletal mechanoresponsiveness. *PLoS ONE*, 4(5), 2009.

[161] Chloé Roffay, Chii J. Chan, Boris Guirao, Takashi Hiiragi, and François Graner. Inferring cell junction tension and pressure from cell geometry. *Development*, 148(18):dev192773, sep 2021.

[162] Xingbo Yang, Dapeng Bi, Michael Czajkowski, Matthias Merkel, M. Lisa Manning, and M. Cristina Marchetti. Correlating cell shape and cellular stress in motile confluent tissues. *Proceedings of the National Academy of Sciences of the United States of America*, 114(48):12663–12668, 2017.

[163] Laure Saias, Jim Swoger, Arturo D'Angelo, Peran Hayes, Julien Colombelli, James Sharpe, Guillaume Salbreux, and Jérôme Solon. Decrease in Cell Volume Generates Contractile Forces Driving Dorsal Closure. *Developmental Cell*, 33(5):611–621, 2015.

[164] Satoshi Yamashita, Takashi Tsuboi, Nanako Ishinabe, Tetsuya Kitaguchi, and Tatsuo Michiue. Wide and high resolution tension measurement using FRET in embryo. *Scientific Reports*, 6(November 2015):1–8, 2016.

[165] Raphaël Etournay, Marko Popović, Matthias Merkel, Amitabha Nandi, Corinna Blasse, Benoît Aigouy, Holger Brandl, Gene Myers, Guillaume Salbreux, Frank Jülicher, and Suzanne Eaton. Interplay of cell dynamics and epithelial tension during morphogenesis of the Drosophila pupal wing. *eLife*, 4(JUNE2015):1–51, 2015.

[166] Mirjam Mayer, Martin Depken, Justin S. Bois, Frank Jülicher, and Stephan W. Grill. Anisotropies in cortical tension reveal the physical basis of polarizing cortical flows. *Nature*, 467(7315):617–621, 2010.

[167] Nargess Khalilgharibi, Jonathan Fouchard, Nina Asadipour, Ricardo Barrientos, Maria Duda, Alessandra Bonfanti, Amina Yonis, Andrew Harris, Payman Mosaffa, Yasuyuki Fujita, Alexandre Kabla, Yanlan Mao, Buzz Baum, José J Muñoz, Mark Miodownik, and Guillaume Charras. Stress relaxation in epithelial monolayers is controlled by the actomyosin cortex. *Nature Physics*, 2019.

[168] Raimon Sunyer, Vito Conte, Jorge Escribano, Alberto Elosegui-Artola, Anna Labernadie, Léo Valon, Daniel Navajas, José Manuel García-Aznar, José J. Muñoz, Pere Roca-Cusachs, and Xavier Trepat. Collective cell durotaxis emerges from long-range intercellular force transmission. *Science*, 353(6304):1157–1161, sep 2016.

[169] Xavier Trepat, Michael R. Wasserman, Thomas E. Angelini, Emil Millet, David A. Weitz, James P. Butler, and Jeffrey J. Fredberg. Physical forces during collective cell migration. *Nature Physics*, 5(6):426–430, 2009.

[170] Sjoerd van Helvert, Cornelis Storm, and Peter Friedl. Mechanoreciprocity in cell migration. *Nature Cell Biology*, 20(1):8–20, December 2017.

[171] Matteo Rauzi, Pascale Verant, Thomas Lecuit, and Pierre François Lenne. Nature and anisotropy of cortical forces orienting Drosophila tissue morphogenesis. *Nature Cell Biology*, 10(12):1401–1410, 2008.

[172] Kaoru Sugimura and Shuji Ishihara. The mechanical anisotropy in a tissue promotes ordering in hexagonal cell packing. *Development (Cambridge)*, 140(19):4091–4101, 2013.

[173] Qingzong Tseng, Irene Wang, Eve Duchemin-Pelletier, Ammar Azioune, Nicolas Carpi, Jie Gao, Odile Filhol, Matthieu Piel, Manuel Théry, and Martial Balland. A new micropatterning method of soft substrates reveals that different tumorigenic signals can promote or reduce cell contraction levels. *Lab on a Chip*, 11(13):2231–2240, 2011.

[174] Rachel Milloud, Olivier Destaing, Richard de Mets, Ingrid Bourrin-Reynard, Christiane Oddou, Antoine Delon, Irène Wang, Corinne Albigès-Rizo, and Martial Balland. αv β3 integrins negatively regulate cellular forces by phosphorylation of its distal NPXY site. *Biology of the Cell*, 109(3):127–137, December 2016.

[175] François Fagotto. EpCAM as Modulator of Tissue Plasticity. *Cells*, 9(9):1–15, 2020.

[176] Leily Kashkooli, David Rozema, Lina Espejo-Ramirez, Paul Lasko, and François Fagotto. Ectoderm to mesoderm transition by down-regulation of actomyosin contractility. *PLoS Biology*, 9(1):1–33, 2021.

[177] Dean P. Edwards, Kathleen T. Grzyb, Lynn G. Dressler, Robert E. Mansel,

David T. Zava, George W. Sledge, and William L. McGuire. Monoclonal antibody identification and characterization of a mr 43,000 membrane glycoprotein associated with human breast cancer. *Cancer Research*, 46(3):1306–1317, 1986.

[178] S V Litvinov, M P Velders, H A Bakker, G J Fleuren, and S O Warnaar. Ep-CAM: a human epithelial antigen is a homophilic cell-cell adhesion molecule. *Journal of Cell Biology*, 125(2):437–446, April 1994.

[179] Sergey V. Litvinov, Maarten Balzar, Manon J. Winter, Hellen A.M. Bakker, Inge H. Briaire de Bruijn, Frans Prins, Gert Jan Fleuren, and Sven O. Warnaar. Epithelial cell adhesion molecule (ep-CAM) modulates cell–cell interactions mediated by classic cadherins. *Journal of Cell Biology*, 139(5):1337–1348, December 1997.

[180] Azam Aslemarz. Epcam differentially regulates individual and collective migration of human carcinoma cells. *McGill university*, 2022.

[181] Dirk Ollech, Tim Pflästerer, Adam Shellard, Chiara Zambarda, Joachim Pius Spatz, Philippe Marcq, Roberto Mayor, Richard Wombacher, and Elisabetta Ada Cavalcanti-Adam. An optochemical tool for light-induced dissociation of adherens junctions to control mechanical coupling between cells. *Nature Communications*, 11(1), 2020.

[182] Robert J. Huebner and John B. Wallingford. Coming to Consensus: A Unifying Model Emerges for Convergent Extension. *Developmental Cell*, 46(4):389–396, 2018.

5. Annex

5.1 Theory supplement

- Theory supplement -

March 2, 2022

Contents

1 Two-dimensional continuum modelling of cellular contractility **2**

1.1 Thin-layer approximation 2

1.2 Plane stress 2

1.3 Active Kelvin-Voigt model 3

1.4 Cell - substrate coupling 4

1.5 Parametrization 4

1.6 Finite Element Simulation 5

1.7 Modelling Procedure for the 2D finite element simulation 6

2 Contour model **7**

2.1 Anisotropic surface tension 8

2.2 Shape analysis 9

2.2.1 Ellipse shape fitting 10

2.3 Contour Strain FEM-method 10

2.4 Modelling procedure for the contour finite element simulation 11

3 Supplement Figures and Tables **12**

1 Two-dimensional continuum modelling of cellular contractility

This model approximates the cell as an elastic continuum. The general constitutive relation can be written as

$$\sigma_{ij}^{\mathrm{3D}} = C_{ijkl}\epsilon_{kl} + \sigma_{ij}^{\mathrm{m,3D}} \,, \tag{1}$$

with stiffness tensor C_{ijkl}, motor stress tensor σ_{ij}^{m} and strain tensor ϵ_{kl}. Further, the force balance equation

$$\partial_j \sigma_{ij}^{\mathrm{3D}} - b_i = \rho a_i \approx 0 \tag{2}$$

is used to calculate the deformation of the cell where b_i is the so called external body force acting on the cell. For cells or tissues we always assume the inertial term to be zero.

1.1 Thin-layer approximation

Another assumption that we make is that the cell height is much smaller than the overall extent of the cell $h_c \ll L_c$. Thus, variations along the z-direction are assumed to be small and it is sufficient to consider a thickness-averaged stress tensor given by

$$\tilde{\sigma}^{\mathrm{3D}}(x,y) = \frac{1}{h_c}\int_0^{h_c} \mathsf{d}z\, \sigma^{\mathrm{3D}}(x,y,z)\,. \tag{3}$$

Averaging the force balance equation leads to a two dimensional force balance equation in which the thickness-averaged body force is now acting as a traction

$$\frac{1}{h_c}\int_0^{h_c} \mathsf{d}z\, \partial_j \sigma_{ij}^{\mathrm{3D}} = \frac{1}{h_c}\int_0^{h_c} \mathsf{d}z\, b_i \tag{4}$$

$$h_c \partial_j \tilde{\sigma}_{ij} = \int_0^{h_c} \mathsf{d}z\, b_i \tag{5}$$

$$\partial_j \sigma_{ij}^{\mathrm{2D}} = t_i(x,y)\,. \tag{6}$$

The cell height is the conversion factor between three-dimensional and two-dimensional quantities $q^{\mathrm{2D}} = q^{\mathrm{3D}} h_c$.

1.2 Plane stress

Under plane stress assumption we set $\sigma_{zz} = \sigma_{xz} = \sigma_{zx} = \sigma_{yz} = \sigma_{zy} = 0$ and further neglect out-of-plane strain ϵ_{zz}. Hooke's law under plane stress conditions can be written in Voigt notation as

$$\begin{bmatrix}\sigma_{xx}\\ \sigma_{yy}\\ \sigma_{xy}\end{bmatrix} = \frac{h_c E_c^{\mathrm{3D}}}{1-\nu_c^2}\begin{bmatrix}1 & \nu_c & 0\\ \nu_c & 1 & 0\\ 0 & 0 & \frac{1-\nu_c}{2}\end{bmatrix}\begin{bmatrix}\epsilon_{xx}\\ \epsilon_{yy}\\ \epsilon_{xy}\end{bmatrix}\,. \tag{7}$$

Together with the general version of Hooke's law

$$\sigma_{ij} = \lambda \epsilon_{kk} \delta_{ij} + 2\mu \epsilon_{ij} \tag{8}$$

we determine the 2D Lamé parameter as

$$\lambda = \frac{\nu_c h_c E_c^{\mathrm{3D}}}{1-\nu_c^2}, \quad \mu = \frac{h_c E_c^{\mathrm{3D}}}{2(1+\nu_c)} \,. \tag{9}$$

1.3 Active Kelvin-Voigt model

The constitutive relation of an active Kelvin-Voigt model in index notation is given by

$$\sigma_{ij} = (1 + \tau_c \frac{\partial}{\partial t})(\lambda \epsilon_{kk} \delta_{ij} + 2\mu \epsilon_{ij}) + \sigma_{ij}^{\mathrm{m}} \,, \tag{10}$$

with stress tensor σ_{ij}, strain tensor ϵ_{ij} and the 2D Lamé coefficients as defined in equation (9). The material relaxation time is defined as $\tau_c = \eta_c / E_c$ with η_c denoting the cell viscosity. The linearized strain tensor is defined as

$$\epsilon_{ij} = \frac{1}{2}(\partial_i u_j + \partial_j u_i) \,, \tag{11}$$

where u_j is the j^{th} component of the displacement field vector $\mathbf{u}(\mathbf{x})$. The overall active contraction is described by the anisotropic motor stress tensor σ_{ij}^{m} which is split into

$$\sigma_{ij}^{\mathrm{m}} = \sigma_{ij}^{\mathrm{bck}} + \sigma_{ij}^{\mathrm{opto}} \,, \tag{12}$$

i.e. a time-independent background stress to account for the cellular energy baseline level and a time dependent photo-activation stress tensor describing the stress increase during photo activation (PA).

Based on experimental observations and verification with the MSM analysis of the TFM data, the anisotropy of the cytoskeleton enters the stress tensor for the background stress through the stress anisotropy coefficient which is defined as

$$\mathrm{AIC} = \frac{\sigma_{\mathrm{xx}} - \sigma_{\mathrm{yy}}}{\sigma_{\mathrm{xx}} + \sigma_{\mathrm{yy}}} \,. \tag{13}$$

This leads to

$$\boldsymbol{\sigma}^{\mathrm{bck}} = \begin{pmatrix} \sigma_{xx} & 0 \\ 0 & \sigma_{yy} \end{pmatrix} = \sigma_{xx} \begin{pmatrix} 1 & 0 \\ 0 & \frac{1-\mathrm{AIC}}{1+\mathrm{AIC}} \end{pmatrix} \,. \tag{14}$$

Upon photo-activation we assume a time dependent stress contribution given by

$$\boldsymbol{\sigma}_{\mathrm{opto}} = \sigma_{\mathrm{act}} \left(1 - e^{-\frac{t-t_{\mathrm{act}}}{\tau_{\mathrm{act}}}}\right) \left(1 - \frac{1}{1 + e^{-\frac{t-\tilde{t}}{\tau_{\mathrm{rel}}}}}\right) \,, \tag{15}$$

which is a combination of an increasing saturating exponential and a sigmoidal shaped decrease (Fig. 1AS).

1.4 Cell - substrate coupling

The cell substrate coupling is described by equation (6) where the traction is formulated as

$$\mathbf{t}(\mathbf{x}) = Y(\mathbf{x})\mathbf{u}(\mathbf{x}) \tag{16}$$

which yields

$$\partial_j \sigma_{ij} = Y u_i \,. \tag{17}$$

Y denotes the position-dependent spring stiffness density. Combining equation (10) and (17) one can show that the interplay of cellular and substrate elasticity defines a natural length scale

$$l_p^2 = \frac{h_c E_c^{3\mathrm{D}}}{Y(1-\nu_c^2)} \,, \tag{18}$$

known as the force-localization length which describes how far a point force is transmitted in the elastically coupled isotropic material. We note that Y is a combined (effective) representation of the stiffness of focal adhesion bonds and the substrate stiffness. The effective spring stiffness density Y can be calculated via

$$\frac{1}{Y} = \frac{1}{Y_s} + \frac{1}{Y_a} \,, \tag{19}$$

assuming that the focal adhesion bonds and the substrate are connected in series. The stiffness of the substrate can be estimated via

$$Y_s = \frac{\pi E_s}{h_{\mathrm{eff}}} \,, \tag{20}$$

in which the effective substrate height is given by an interpolation formula

$$h_{\mathrm{eff}}^{-1} = \frac{1}{h_s 2\pi(1+\nu_s)} + \frac{1}{L_c} \,, \tag{21}$$

where h_s and L_c denote the substrate height and cell layer size, respectively. E_s and ν_s are the Young's modulus and Poisson's ratio of the substrate. Two main assumptions are necessary to adapt our theory as close as possible to the traction force computation of the experiments. Firstly, we assume that the substrate is infinitely thick and therefore we have $h_{\mathrm{eff}} \approx L_c$. Secondly, we neglect the contribution of the focal adhesions in equation (19) leading to $Y \approx Y_s = \pi E_s / L_c$. The traction forces are then given by

$$\mathbf{T} = T\mathbf{u} = Y_s \mathbf{u}_s \,. \tag{22}$$

The elastic energy stored in the substrate is calculated via

$$U_s = \frac{1}{2}\int_\Omega \mathbf{T}\mathbf{u}_s \mathrm{d}\Omega = \frac{1}{2}\int_\Omega Y \mathbf{u}_s^2 \mathrm{d}\Omega = \frac{1}{2}\int_\Omega Y \mathbf{u}^2 \mathrm{d}\Omega \,. \tag{23}$$

1.5 Parametrization

Although in principle it is possible to use a downhill-simplex method to find the set of parameters which minimizes the theoretically computed substrate energy against the experimentally measured curve, we

nevertheless decide to fix some of the parameters to avoid overfitting. All fixed parameters are listed in Tab. 1. While the substrate parameters are known, we fix the parameters for Young's modulus and viscosity of the cell to typically reported values from the literature [1, 2, 3, 4, 5]. The fixed substrate parameters yield a spring stiffness density of $Y_s = 1.257 \times 10^9\,\mathrm{N\,m^{-3}}$ and a force-localization length of $l_p = 3.25\,\mu\mathrm{m}$. Simulations with these parameters lead to a very good agreement of theoretically computed and experimentally measured stress and traction maps. Although the traction and stress maps as computed with the FEM-model show all characteristic features of the experimental maps, latter seem to be blurred. The blurring can be traced back to the TFM and MSM analysis methods.

1.6 Finite Element Simulation

We solve the combination of equations (10) and (17) for the displacement vector $\mathbf{u}$ of the cell by means of a finite element simulation using the open source software package FEniCS [6]. This approach has been used in several other works [1, 2, 7, 8, 3, 4, 9]. The full problem statement is given by: Find the displacement field vector $\mathbf{u}(\mathbf{x})$ with initial conditions $\mathbf{u}_0 = \mathbf{u}(\mathbf{x}, 0) = 0$ such that together with $\boldsymbol{\sigma} = (1 + \tau_c \frac{\partial}{\partial t})(\lambda \mathrm{tr}\,(\boldsymbol{\epsilon}) 1 + 2\mu\boldsymbol{\epsilon}) + \boldsymbol{\sigma}^{\mathrm{m}}$

$$\nabla \cdot \boldsymbol{\sigma} = Y\mathbf{u} \quad \text{in } \Omega \times (0, T] \tag{24}$$

$$\boldsymbol{\sigma} = 0 \quad \text{on } \partial\Omega \times (0, T] \tag{25}$$

Therefore, we derive the weak form of equation (17) by multiplying with a vector-valued test function $\mathbf{v} \in \mathcal{D}(\Omega)$ over the simulation domain Ω. Multiplying equation (24) with the test function and integrating over the whole simulation domain leads to

$$\int_\Omega (\nabla \cdot \boldsymbol{\sigma}) \cdot \mathbf{v}\,\mathrm{d}\Omega = \int_\Omega Y\mathbf{u} \cdot \mathbf{v}\,\mathrm{d}\Omega\,. \tag{26}$$

The left hand side can be integrated using integration by parts i.e. using the following identity

$$\nabla \cdot (\boldsymbol{\sigma}^{\mathrm{T}} \cdot \mathbf{v}) = (\nabla \cdot \boldsymbol{\sigma}) \cdot \mathbf{v} + \boldsymbol{\sigma} : \nabla\mathbf{v}\,, \tag{27}$$

where we use the standard notation for the inner product between tensors (double contraction) and $\nabla\mathbf{v} = \partial_i(v_j\mathbf{e}_j) \otimes \mathbf{e}_i$ being the vector gradient. Equation (26) can be simplified to

$$\int_\Omega \boldsymbol{\sigma} : \nabla\mathbf{v}\,\mathrm{d}\Omega - \int_{\partial\Omega} (\boldsymbol{\sigma} \cdot \mathbf{n}) \cdot \mathbf{v}\,\mathrm{d}\Gamma + \int_\Omega Y\mathbf{u} \cdot \mathbf{v}\,\mathrm{d}\Omega = 0\,. \tag{28}$$

$\boldsymbol{\sigma} \cdot \mathbf{n}$ is the traction vector at the boundary $\Gamma = \partial\Omega$ which is set to zero in case of stress free boundaries. We further use that $\boldsymbol{\sigma}$ is symmetric and thus, the double contraction with the antisymmetric part $\mathbf{a}(\mathbf{v}) = \frac{1}{2}(\nabla\mathbf{v} - \nabla\mathbf{v}^{\mathrm{T}})$ of $\nabla\mathbf{v}$ is zero i.e. $\boldsymbol{\sigma} : \mathbf{a}(\mathbf{v}) = 0$. This allows us to replace $\nabla\mathbf{v}$ by its symmetric part $\mathbf{s}(\mathbf{v}) = \frac{1}{2}(\nabla\mathbf{v} + \nabla\mathbf{v}^{\mathrm{T}})$ and leads to the final weak form statement

$$\int_\Omega \boldsymbol{\sigma} : \mathbf{s}(\mathbf{v})\,\mathrm{d}\Omega + \int_\Omega Y\mathbf{u} \cdot \mathbf{v}\,\mathrm{d}\Omega = 0\,. \tag{29}$$

Since we are aiming at solving for the displacment vector $\mathbf{u}$ we have to express all terms in the constitutive relation in terms of $\mathbf{u}$

$$\boldsymbol{\sigma} = (1 + \tau_c \frac{\partial}{\partial t})(\lambda \mathrm{tr}\,(\boldsymbol{\epsilon}) 1 + 2\mu\boldsymbol{\epsilon}) + \boldsymbol{\sigma}^{\mathrm{m}} \tag{30}$$

$$= \lambda(\nabla \cdot \mathbf{u})\mathbf{I} + \mu(\nabla\mathbf{u} + \nabla\mathbf{u}^{\mathrm{T}}) + \tau_c\lambda(\nabla \cdot \dot{\mathbf{u}})\mathbf{I} + \tau_c\mu(\nabla\dot{\mathbf{u}} + \nabla\dot{\mathbf{u}}^{\mathrm{T}}) + \boldsymbol{\sigma}^{\mathrm{m}} \tag{31}$$

$$= \boldsymbol{\Sigma_E} + \boldsymbol{\Sigma_\eta} + \boldsymbol{\sigma}^{\mathrm{m}}\ . \tag{32}$$

For the time derivatives we use a backward Euler discretization scheme which is numerically stable even for larger time steps. We set

$$\dot{\mathbf{u}}^{(n+1)} = \frac{\mathbf{u}^{(n+1)} - \mathbf{u}^{(n)}}{\Delta t} \tag{33}$$

and since we are dealing with linear equations the discretization scheme translates directly to

$$\dot{\boldsymbol{\Sigma}}_{E,\eta}^{(n+1)} = \frac{\boldsymbol{\Sigma}_{E,\eta}^{(n+1)} - \boldsymbol{\Sigma}_{E,\eta}^{(n)}}{\Delta t} \tag{34}$$

which enables us to define

$$a(\mathbf{u}^{(n+1)}, \mathbf{v}) = \int_\Omega \boldsymbol{\Sigma}_E^{(n+1)} : \mathbf{s}(\mathbf{v})\Delta t\ \mathrm{d}\Omega + \int_\Omega \boldsymbol{\Sigma}_\eta^{(n+1)} : \mathbf{s}(\mathbf{v})\ \mathrm{d}\Omega + \int_\Omega Y\mathbf{u}^{(n+1)} \cdot \mathbf{v}\Delta t\ \mathrm{d}\Omega \tag{35}$$

and

$$L^{(n+1)}(\mathbf{v}) = \int_\Omega \boldsymbol{\Sigma}_\eta^{(n)} : \mathbf{s}(\mathbf{v})\ \mathrm{d}\Omega - \int_\Omega \boldsymbol{\sigma}_{\mathrm{m}} : \mathbf{s}(\mathbf{v})\Delta t\ \mathrm{d}\Omega \tag{36}$$

after inserting the time discretized version of equation (32) in equation (29). Our initial problem statement now reduces to solving

$$a(\mathbf{u}^{(n+1)}, \mathbf{v}) = L^{(n+1)}(\mathbf{v}) \quad \forall \mathbf{v} \in \mathcal{D}(\Omega) \tag{37}$$

Equation (37) can be directly handed to the FE solver.

1.7 Modelling Procedure for the 2D finite element simulation

To obtain the final theoretical result by means of our finite element simulation (Fig.4C), several steps were necessary. We used the open source meshing software GMSH [10] to create a finite element mesh as depicted in Fig. 1BS. Then we fixed all known parameters in order to match the experimental setup to our simulations. All fixed parameters are gathered in Tab. 1 and were fixed throughout the simulations. Next we mathematically defined the pattern geometry of the H-pattern which determines the portion of the simulation domain on which the cell is assumed to establish a connection to the elastic foundation (Fig.1CS)

$$(x, y)_{Y\neq 0} = \left\{ x, y \,\middle|\, x \leq w - \frac{d}{2} \vee x \geq \frac{d}{2} - w \vee -\frac{w}{2} \leq y \leq \frac{w}{2} \right\}. \tag{38}$$

We first determined the active background stress by fitting the baseline of simulated strain energy curve (Eq. 23) to the given experimental substrate strain energy. In a second step we fitted the temporal evolution of the strain energy by optimizing the free parameters $\sigma_{\mathrm{act}}, \tau_{\mathrm{act}}, t_{\mathrm{act}}$ and $\tilde{t}$ in Eq. 15.

The obtained parameters for all fitted conditions are summarized in Tab. 2. The fit results of the doublet and singlet strain energy curves can be see in Fig. 4D.

In the final step, we simulated the photo-activation on only the left half of the pattern. For this we measured the spatial intensity profile and fitted a function of the form

$$I(x) = 1 - \frac{1}{1 + e^{-a(x-b)}} \tag{39}$$

to obtain the right shape given by parameters $a = 0.6497$ and $b = 13.186$. Subsequently we modified the intensity profile such that it reaches a constant level f as $x \to \infty$

$$\tilde{I}(x) = (1 - f)\left(1 - \frac{1}{1 + e^{-a(x-b)}}\right) + f \ . \tag{40}$$

The parameter $f \in [-1, 1]$ controls an active stress level on the non-activated side and is referred to as the *degree of active coupling*. Positive and negative values for f correspond to active contraction and active relaxation, respectively. The intensity profile and corresponding fit are shown in Fig. 1DS, while the activation profile $\tilde{I}(x)$ for different values of f can be seen in Fig.4B. The time-dependent opto-stress tensor is modified by the spatial distribution of the intensity profile[1] by multiplication

$$\tilde{\boldsymbol{\sigma}}_{\mathrm{opto}}(x, t) = \boldsymbol{\sigma}_{\mathrm{opto}}(t)\tilde{I}(x) \ . \tag{41}$$

Finally, fixing all parameters as obtained by the baseline and full stimulation strain energy fits, we varied the degree of active coupling f as a free parameter ranging from -1 to 1 in steps of $\Delta f = 0.1$, in other words, we increased the active response on the non-activated side in steps of 10%. For each value of f, the stress difference $\Delta\sigma_{xx}(x, y)$ and $\Delta\sigma_{yy}(x, y)$ between baseline and maximum strain energy were then averaged over the y-axis (Fig.4B). After that, the resulting x-profiles were normalized by integrating the right half of the curves and dividing that by the integral of the whole curve. This procedure allowed us to translate the family of curves (Fig.4B) into a relationship between the normalized stress response for σ_{xx} and σ_{yy} and the degree of active coupling f (Fig.4C).

2 Contour model

The observed invaginated arcs in strongly adherent cells (Fig.1A,2B) can be geometrically explained by the interplay between a surface tension σ associated with the contractile cortex and the resisting line tension λ in the strong peripheral actin bundle. In case of a homogeneous cortex one may assume the surface tension to be isotropic which yields a Laplace law predicting a constant radius of curvature

[1] To keep the activation profile static in the lab-frame (eulerian frame) we incorporate the, although in many cases negligible, deformation by shifting the activation profile according to the displacement field of the previous time step such that $I(x) = \hat{I}(X + u_x)$. Here, the coordinate X is fixed in the material.

$R = \lambda/\sigma$ [11, 12]. Moreover, the observed dependence of the curvature of the arc on the spanning distance d of the two endpoints can be explained by assuming an elastic contribution to the line tension [11]. This modification of the simple tension model (STM) is known as the tension elasticity model (TEM) and yields a relationship $\lambda(d)$ which in turn leads to an increasing R-d-relationship. However, in some cases the assumption of a homogeneous isotropic cortex fails in the presence of strongly embedded internal stress fibers. In this scenario the isotropic surface tension is modified by a directional component aligned with the direction of the internal stress fibers. This so called anisotropic tension model predicts elliptical arcs and a position dependent line tension in the fiber [13]. A comprehensive summary of the different types of existing contour models can be found in [14].

2.1 Anisotropic surface tension

Like all contour models, the anisotropic tension model (ATM) is based on a very general force balance equation for a slender fiber which we will motivate very briefly. The fiber is assumed to be restitant to tension only such that bending and shearing are neglected. Further we assume the fiber to start and end at discrete fixed points which resemble the focal adhesions. Each fiber has a reference shape (unstrained, stress free) and a current configuration (strained). All quantities associated with the reference shape are denoted by a $\wedge$-symbol (Fig. 1F).

The resulting surface tension acting on the edge bundle is given by the difference of the interior and exterior stress tensors (Fig. 1E). Since the micropattern in all our experiments has two symmetry axes, we assume an anisotropic surface tension tensor of the form

$$\Sigma_{\text{out}} - \Sigma_{\text{in}} = \begin{pmatrix} \sigma_x & 0 \\ 0 & \sigma_y \end{pmatrix} . \tag{42}$$

By introducing a Frenet-Serret frame as a local basis to the current configuration of the fiber

$$\frac{\mathrm{d}\mathbf{x}}{\mathrm{d}s} = \mathbf{T} \tag{43}$$

$$\frac{\mathrm{d}\mathbf{T}}{\mathrm{d}s} = \kappa\mathbf{N} , \tag{44}$$

where s denotes the arc-length parameter along the current state, x the shape of the current state and κ the local curvature (Fig. 1F), one can derive the force balance equation by considering an infinitesimal line element in the current configuration as illustrated in Fig. 1G. For such a line element the force balance reads

$$\frac{\mathrm{d}}{\mathrm{d}s}\mathbf{F}(s) + \begin{pmatrix} \sigma_x & 0 \\ 0 & \sigma_y \end{pmatrix} \mathbf{N}(s) = 0 , \tag{45}$$

where $\mathbf{F}(s) = \lambda(s)\mathbf{T}(s)$ always points tangential to the fiber with line tension $\lambda(s)$. Finally, it can be shown that Eq. 45 leads to the equation of an ellipse

$$\frac{y^2}{C\sigma_y} + \frac{x^2}{C\sigma_x} = 1 , \tag{46}$$

with semi-axes given by $a = \sqrt{C\sigma_x}$ and $b = \sqrt{C\sigma_y}$. In the isotropic case, for which $\sigma_x = \sigma_y$, the ellipse attains circular shape consistent with the results of the STM and TEM.

The line tension is now a complicated function of the turning angle $\theta(s)$ given by

$$\lambda(\theta) = \sigma_x \sqrt{\sigma_y C} \sqrt{\frac{1 + \tan^2\theta}{1 + \frac{\sigma_x}{\sigma_y}\tan^2\theta}} \, . \tag{47}$$

By taking derivative of this expression with respect to the turning angle θ one can show that the line tension has an extremum at $\theta = \theta_0 = 0$ given by

$$\lim_{\theta \to 0} \lambda(\theta) = \sigma_x \sqrt{\sigma_y C} \, . \tag{48}$$

Depending on the ratio, this extremum is either a maximum for $\sigma_x/\sigma_y > 1$ or a minimum for $\sigma_x/\sigma_y < 1$. In case of $\sigma_x = \sigma_y$ we obtain a constant line tension independent of the turning angle. Plots of the line tension and its derivative are shown in Fig. 2.

2.2 Shape analysis

Analysing cell shape is equivalent to quantifying the minimal number of key parameters like line and surface tension based on the shape of the free spanning fiber. Our goal was to apply the ATM to the TFM and fiber tracking data.

By means of our analysis we assume that all traction contribution stems from the combined action of the free spanning arc and the vertical "adherent" fiber of length L and add up at the intersection

$$\mathbf{F}_{\mathrm{s}} = F_{\mathrm{ad}}\mathbf{e}_y + \sigma_x \frac{L}{2}\mathbf{e}_x + \lambda \mathbf{T}(\theta_{\mathrm{fa}}) \, , \tag{49}$$

Where $\mathbf{F}_s$ is the force measured in the substrate, θ_{fa} denotes the tangent angle at the focal adhesion and the second term is a possible contribution of the surface tension which only has an x-component due to the fact that the adherent fiber is straight and aligned in y-direction (Fig.2A-C). Splitting up Eq. 49 into the respective x-and y-components yields a system of two equations in the unknowns F_{ad} and λ. The force $\mathbf{F}_{\mathrm{s}}$ was obtained by dividing the traction map into four quadrants and calculating the sum for each quadrant. A similar procedure as presented in [15]. The contribution of the surface tension along the vertical fiber was estimated on TFM data as well. For the two unknowns we have

$$\lambda = \frac{1}{T_x}\left(F_{\mathrm{s},x} - \sigma_x \frac{L}{2}\right) \tag{50}$$

$$F_{\mathrm{ad}} = F_{\mathrm{s},y} - \frac{T_y}{T_x}\left(F_{\mathrm{s},x} - \sigma_x \frac{L}{2}\right) \, , \tag{51}$$

such that λ and F_{ad} can be calculated in terms of the tangent angle of the free spanning fiber at the focal adhesion.

2.2.1 Ellipse shape fitting

It turned out, that fitting ellipses directly to "short" arcs is very unstable and highly depends on the initialization of the fit parameters. This is because one can find a wide range of ellipses that fit equally well. Due to large data sets of 10 to 40 cells per condition, where each cell data set consists of 60 time frames, it was not feasible to fit ellipses by hand. Therefore, we decided to use a very stable and fast circle fitting algorithm to obtain an estimate for the tangent vector at the adhesion point[2]. For the circle fitting we exploited a *Hyper least squares* algorithm presented in [16] based on algebraic distance minimization. The already determined parameters from TFM data and circle fitting are $\sigma_x, \theta_{\mathrm{fa}}, \mathbf{T}(\theta_{\mathrm{fa}}), \lambda(\theta_{\mathrm{fa}})$. The remaining unknowns are the y-component of the surface tension tensor σ_y as well as the center of the ellipse $\mathbf{x}_{\mathrm{c}}$. Using Eq. 47 evaluated at θ_{fa} this yields

$$a = \frac{\lambda(\theta_{\mathrm{fa}})}{\sqrt{\sigma_x \sigma_y}} \sqrt{\frac{1 + \frac{\sigma_x}{\sigma_y} \tan^2(\theta_{\mathrm{fa}})}{1 + \tan^2(\theta_{\mathrm{fa}})}} \tag{52}$$

$$b = \frac{\lambda(\theta_{\mathrm{fa}})}{\sigma_x} \sqrt{\frac{1 + \frac{\sigma_x}{\sigma_y} \tan^2(\theta_{\mathrm{fa}})}{1 + \tan^2(\theta_{\mathrm{fa}})}} \tag{53}$$

such that the shape of the ellipse purely depends on σ_y. The fit was carried out by minimizing the squared distance of all tracking points along the fiber to the ellipse. The distance of those points to the ellipse was obtained by an elegant way to calculate the minimal distance of a point to the ellipse. Fig. 2C compares the standard deviations for the two fits for all conditions. In all cases, the ellipse fit yield a smaller standard deviation, although the differences vary for the different aspect ratios. The results of this analysis are summarized in Fig.2C-E.

2.3 Contour Strain FEM-method

In order to study the effect of photo-activation on the contour and to quantify the degree of active coupling purely based on the shape of the contour we developed a discretized FEM-version of the force balance equation Eq. 45. In this context we re-formulate Eq. 45 as a function of the reference arc length parameter $\hat{s}$ (Fig. 1F) in the reference state. The relationship between the two arc length parameters is given by stretch

$$\nu(\hat{s}) \coloneqq \left| \frac{\partial \mathbf{x}}{\partial \hat{s}} \right| = \frac{\mathrm{d}s}{\mathrm{d}\hat{s}} = \sqrt{(\partial_{\hat{s}} x)^2 + (\partial_{\hat{s}} y)^2} \, . \tag{54}$$

This allows to express the equation of mechanical equilibrium as

$$\frac{\mathrm{d}}{\mathrm{d}\hat{s}} \left(\lambda(\hat{s}) \frac{1}{\nu(\hat{s})} \frac{\mathrm{d}\mathbf{x}}{\mathrm{d}\hat{s}} \right) + \begin{pmatrix} \sigma_x & 0 \\ 0 & \sigma_y \end{pmatrix} \left(\frac{\mathrm{d}\mathbf{x}}{\mathrm{d}\hat{s}} \right)_{\perp} = 0 \, , \tag{55}$$

where $(\mathrm{d}\mathbf{x}/\mathrm{d}\hat{s})_{\perp} = (\mathrm{d}y/\mathrm{d}\hat{s}, -\mathrm{d}x/\mathrm{d}\hat{s}) = \nu(\hat{s})\mathbf{N}(s(\hat{s}))$. This coupled system of equations can be solved by means of a finite element implementation with mixed elements on a one-dimensional mesh. Let

[2]Although it is also possible to obtain the tangent vector directly from the fiber tracking data, we found through trial and error that this method is prone to large fluctuations.

$w_1, w_2 \in D([0,d])$ be two test functions over the interval $[0,d]$ representing the spanning distance of the unstretched straight fiber. Following the standard procedure by multiplying Eq. 55 with the test functions (one test function for each equation) and integrating it over the simulation domain yields

$$-\int_0^d \lambda(\hat{s})\frac{1}{\nu(\hat{s})}\frac{\mathrm{d}x}{\mathrm{d}\hat{s}}\frac{\mathrm{d}w_1}{\mathrm{d}\hat{s}}\,\mathrm{d}\hat{s} + \int_0^d \sigma_x \frac{1}{\nu(\hat{s})}\frac{\mathrm{d}x}{\mathrm{d}\hat{s}} w_1\,\mathrm{d}\hat{s} = 0 \tag{56}$$

$$-\int_0^d \lambda(\hat{s})\frac{1}{\nu(\hat{s})}\frac{\mathrm{d}y}{\mathrm{d}\hat{s}}\frac{\mathrm{d}w_2}{\mathrm{d}\hat{s}}\,\mathrm{d}\hat{s} - \int_0^d \sigma_y \frac{1}{\nu(\hat{s})}\frac{\mathrm{d}x}{\mathrm{d}\hat{s}} w_2\,\mathrm{d}\hat{s} = 0\,. \tag{57}$$

Here we used partial integration

$$\int_0^d \frac{\mathrm{d}}{\mathrm{d}\hat{s}}(.)w_i\,\mathrm{d}\hat{s} = (.)w_i\Big|_0^d - \int_0^d (.)\frac{\mathrm{d}w_i}{\mathrm{d}\hat{s}}\,\mathrm{d}\hat{s}\,, \tag{58}$$

and that by construction $w_i = 0$ on the boundary. Further we impose Dirichlet boundary conditions $x(0) = 0$, $x(d) = d$, $y(0) = y(d) = 0$ such that the endpoints of the fiber are fixed.

2.4 Modelling procedure for the contour finite element simulation

The modelling procedure for the contour simulation is very similar to the 2D version explained above. The aim was to quantify the active coupling between activated and non-activated part of the cell doublet. The results of the contour analysis allowed us to obtain an average ellipse by averaging the results for a,b,σ_x,σ_y. Based on actin images the spanning distance of the fiber was estimated to a value of $d = 35\,\mu\mathrm{m}$. An average ellipse contour was created by fixing σ_x and σ_y as well as the semi-axis a. From those values we then computed $b = a\sqrt{\sigma_y/\sigma_x}$. This was necessary since we averaged all those quantities independently of each other such that the averages of the single quantities not necessarily describe an elliptical arc.

In the spirit of the TEM and inspired by the work of [15] we split the line tension into an active and elastic contribution where the first accounts for the elastic properties of the cross-linking proteins within the actin bundle and the latter is an active contribution from myosin II motors such that

$$\lambda = \lambda_{\mathrm{el}} + \lambda_{\mathrm{act}}\,. \tag{59}$$

We further assumed a linear constitutive relationship between stress and strain for the elastic component

$$\lambda\mathrm{el} = EA\epsilon = EA(\nu(\hat{s}) - 1)\,, \tag{60}$$

which is directly connected to the stretch as defined in Eq. 54. The rest length of the fiber is set to the spanning distance $\hat{L} = d$. here, EA denotes the one-dimensional modulus of the fiber as a product of Young's modulus E and the crosssectional area A. This value is typically around $EA = 50\,\mathrm{nN} - 350\,\mathrm{nN}$ [17, 15, 18]. By means of our contour simulation we set this value to $EA = 300\,\mathrm{nN}$. All other fixed values for this simulation can be found in Tab. 3. Next, we minimized the simulated contour against the average contour from the contour analysis treating λ_{act} as a free parameter (Fig. 2D)). Subsequently, we introduced full optogenetic stimulation by defining

$$\sigma_i^{\mathrm{PA,max}} = \sigma_i + \sigma_i \cdot \mathrm{RSI}_i^{\mathrm{max}}\,, \tag{61}$$

where $\sigma_i^{\mathrm{PA,max}}$ denotes the respective surface tension component at maximum strain energy, RSI_i^{max} is the maximal relative surface tension increase and $i = x, y$. We optimized the values $\mathrm{RSI}_x^{\max}, \mathrm{RSI}_y^{\max}$ to fit the measured contour strain to the one computed with the contour FEM at maximum strain energy by additionally making sure that the values for the RSI do not exceed the from statistics experimentally obtained bounds for these values. The result of this optimization can is depicted in Fig.(2E). Local photo-activation was introduced analogously to the two-dimensional case (Eq. 40) by

$$\sigma_i^{\mathrm{PA,max}}(\hat{s}) = \sigma_i + \sigma_i \cdot \mathrm{RSI}_i^{\max} \cdot \tilde{I}(\hat{s}) \,, \tag{62}$$

For different values of the degree of active coupling f we simulated the contour strain leading to the family of curves as depicted in Fig.4E. The response of the non-activated side as a function of the degree of active coupling was then obtained by the integral of the right half of the curve divided by the integral of the whole curve (Fig.4F).

3 Supplement Figures and Tables

Fixed parameter	Value
Substrate	
Young's modulus of the substrate E_s	$20\,\mathrm{kPa}$
Poisson's ratio of the substrate ν_s	0.5
Thickness of the substrate h_s	$50\,\mu\mathrm{m}$
Cell	
Young's modulus of cell E_c	$10\,\mathrm{kPa}$
Viscosity of the cell η_c	$100\,\mathrm{kPa\,s}$
Thickness of the cell h_c	$1\,\mu\mathrm{m}$
Poisson's ratio of the cell ν_c	0.5
Length of the cell L_c	$50\,\mu\mathrm{m}$

Table 1: Fixed parameters for the two-dimensional finite element simulation.

Fit parameter	Singlet	Doublet
Baseline		
Background stress component $\sigma_{xx}^{\mathrm{bck}}$	$6.59\,\mathrm{kPa}$	$5.73\,\mathrm{kPa}$
Background stress component $\sigma_{yy}^{\mathrm{bck}}$	$2.78\,\mathrm{kPa}$	$5.73\,\mathrm{kPa}$
Full opto-stimulation		
Active stress σ_{act}	$0.287\,\mathrm{kPa}$	$0.618\,\mathrm{kPa}$
Activation time scale τ_{act}	$133\,\mathrm{s}$	$227\,\mathrm{s}$
Relaxation time scale τ_{rel}	$113\,\mathrm{s}$	$236\,\mathrm{s}$
Centroid $\tilde{t}$	$1057\,\mathrm{s}$	$1117\,\mathrm{s}$

Table 2: Fit parameter as obtained by the two-dimensional finite element simulation.

Parameter	Value
Fixed	
Surface tension component σ_x	$0.92\,\mathrm{nN\,\mu m^{-1}}$
Surface tension component σ_y	$1.12\,\mathrm{nN\,\mu m^{-1}}$
Semi-axis a	$61.94\,\mathrm{\mu m}$
Semi-axis b	$68.34\,\mathrm{\mu m}$
One-dimensional elastic modulus EA	$300\,\mathrm{nN}$
Contour fit	
Active line tension λ_{act}	$58.1\,\mathrm{nN}$
Strain fit	
Relative surface tension increase $\mathrm{RSI}_x^{\mathrm{max}}$	$0.11\,\mathrm{nN\,\mu m^{-1}}$
Relative surface tension increase $\mathrm{RSI}_y^{\mathrm{max}}$	$0.24\,\mathrm{nN\,\mu m^{-1}}$

Table 3: Fixed and opitimized parameter for the contour shape analysis by means of the contour finite element simulation.

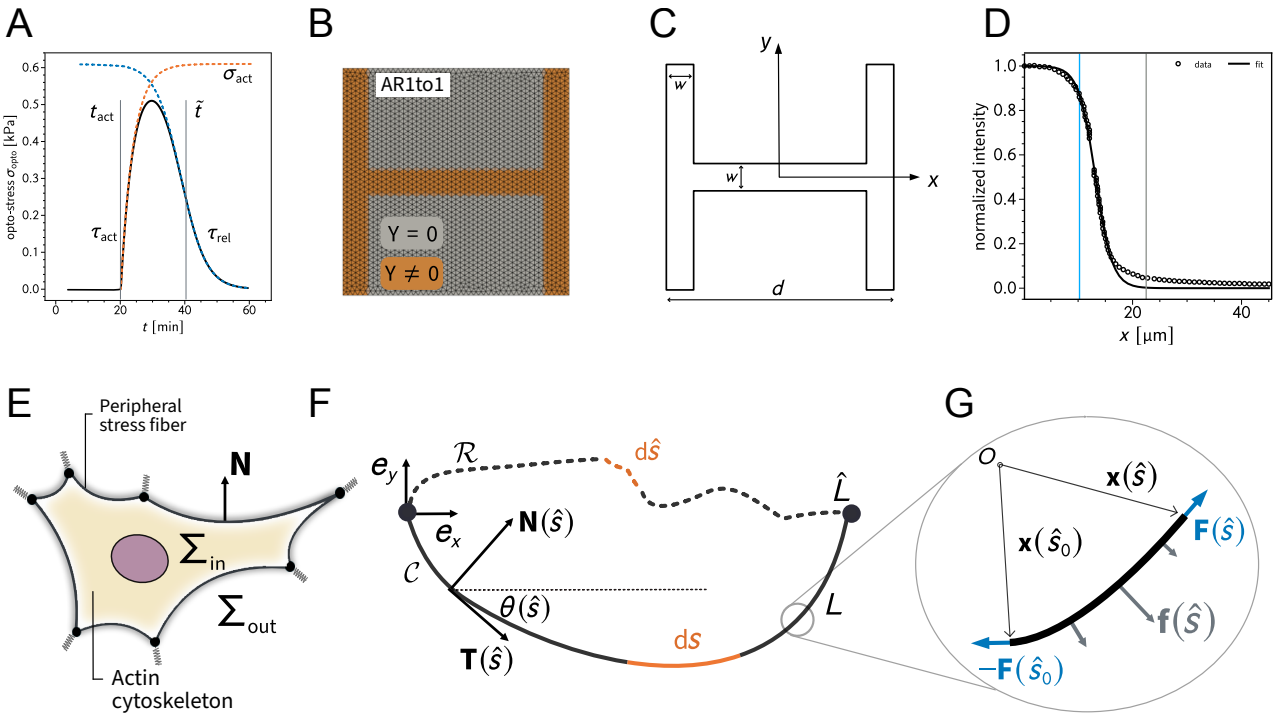

Figure 1: **A** shows the shape of the by optogenetic induced time dependent stress.**B** depicts the finite element mesh created with gmsh. The spring stiffness density is non-zero on the brown part of the domain. **C** is a schematic illustration of the relevant parameters to define the adhesion geometry. **D** shows the experimentally measured intensity profile of the light pulse used for photo-activation. The gray line indicates the center of the pattern (measured from left to right) while the blue line marks the inflection point of the sigmoidal fit function. **E** is a schematic illustration of the relevant quantities in the contour based description of cellular adhesion. **G,F** explain the relevant mathematical quantities to describe the equilibrium shape of a fiber subject to external loads.

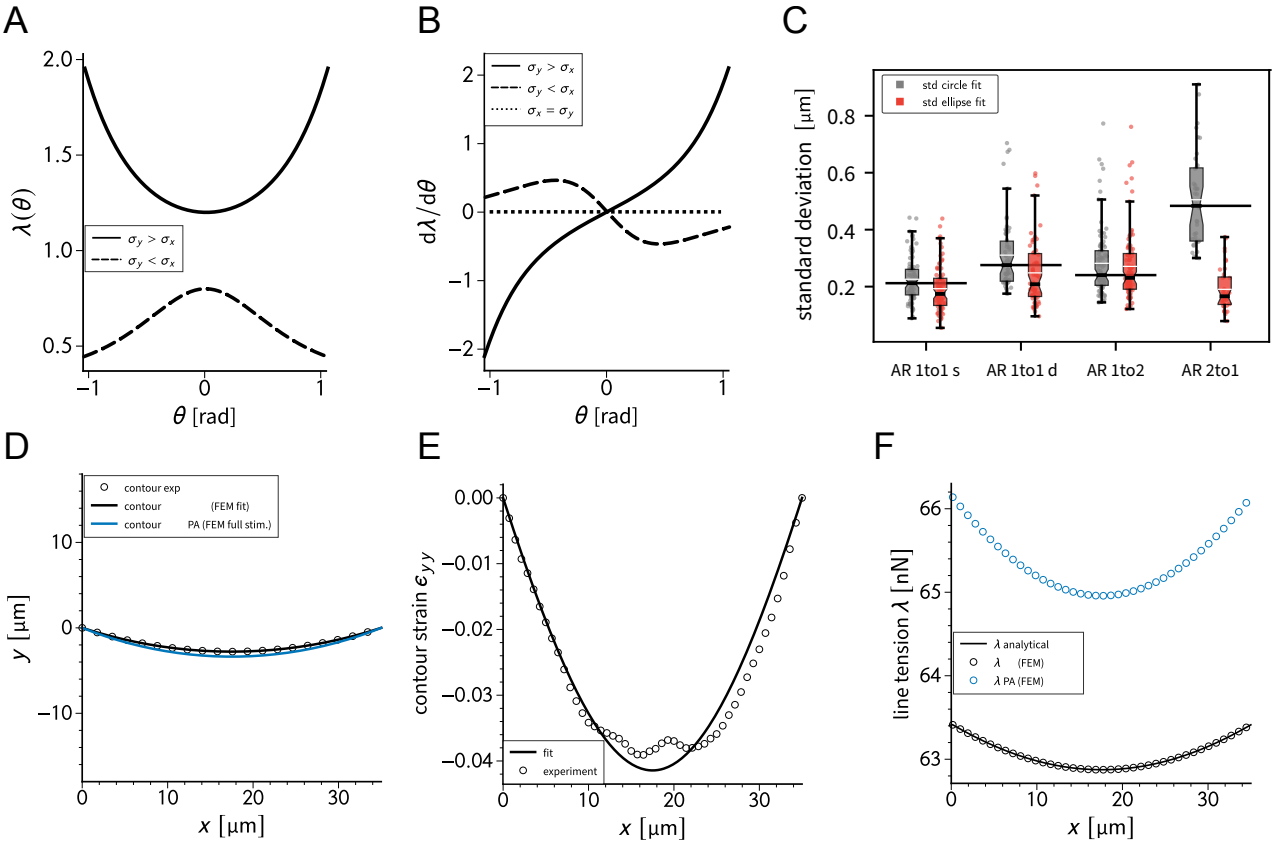

Figure 2: **A,B** show the predicted line tensions and the derivative with respect to the turning angle based on the analytical solution for different values of σ_x and σ_y. **C** compares the circle and ellipse fit of the contour of the cells for different pattern aspect ratios. **D** shows a generic cell contour for the doublet before and during photo-activation. The experimentally contour strain in y-direction with the respective fit from simulations and the corresponding line tensions are shown in **E** and **F**, respectively.

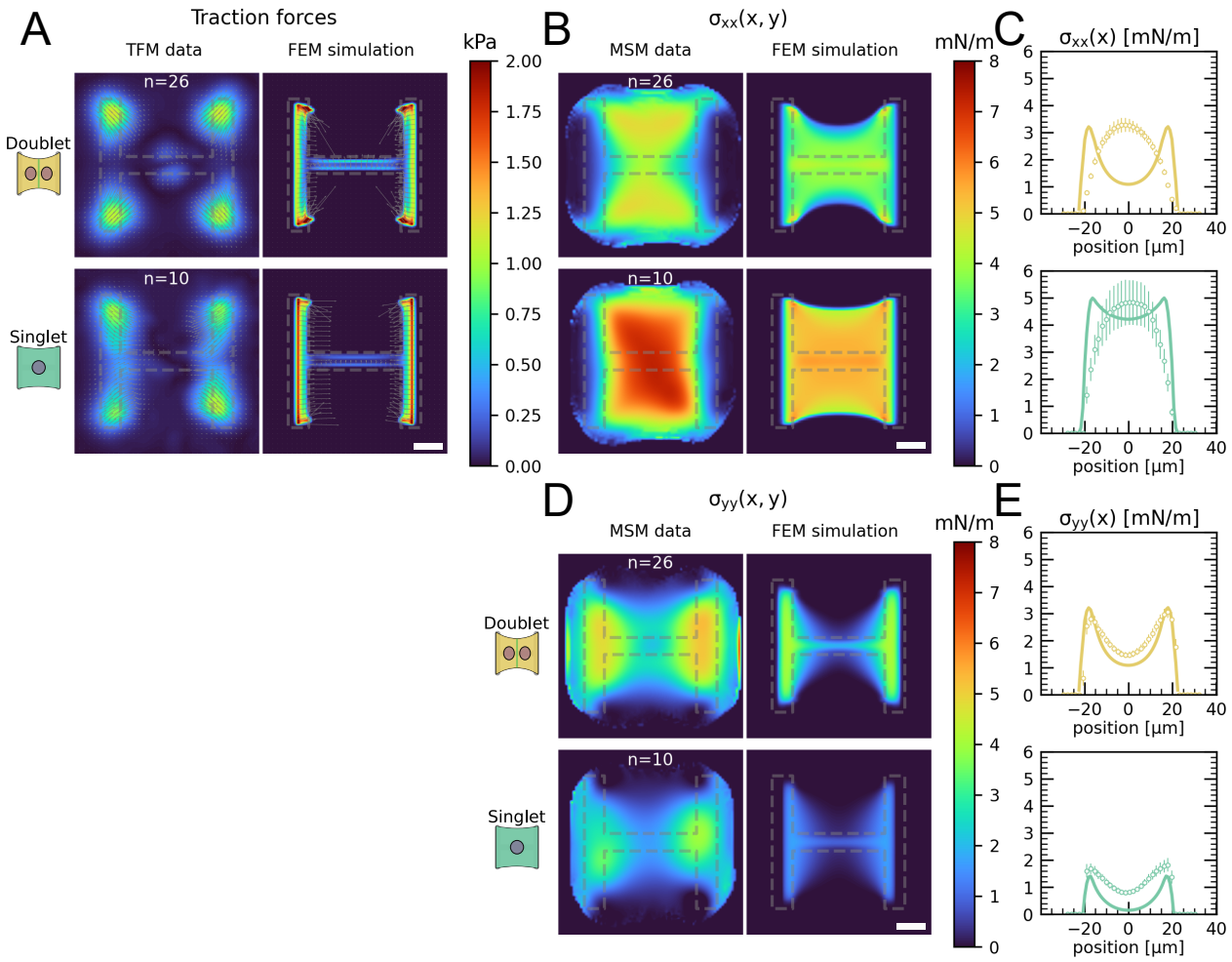

Figure 3: **A** Average traction stress and force maps of cell doublets (top) and singlets (bottom) on H-patterns on the left and corresponding traction stress and force maps from the FEM simulation. **B, D** Average cell stress maps of cell doublets (top) and singlets (bottom) on H-patterns on the left and corresponding cell stress maps from the FEM simulation. **C, E** Average over the y-axis of the maps in B and D. Data is shown as circles with the mean $\pm$ s.e.m., the solid line corresponds to the FEM simulations. All scale bars are $10\,\mu\mathrm{m}$ long.

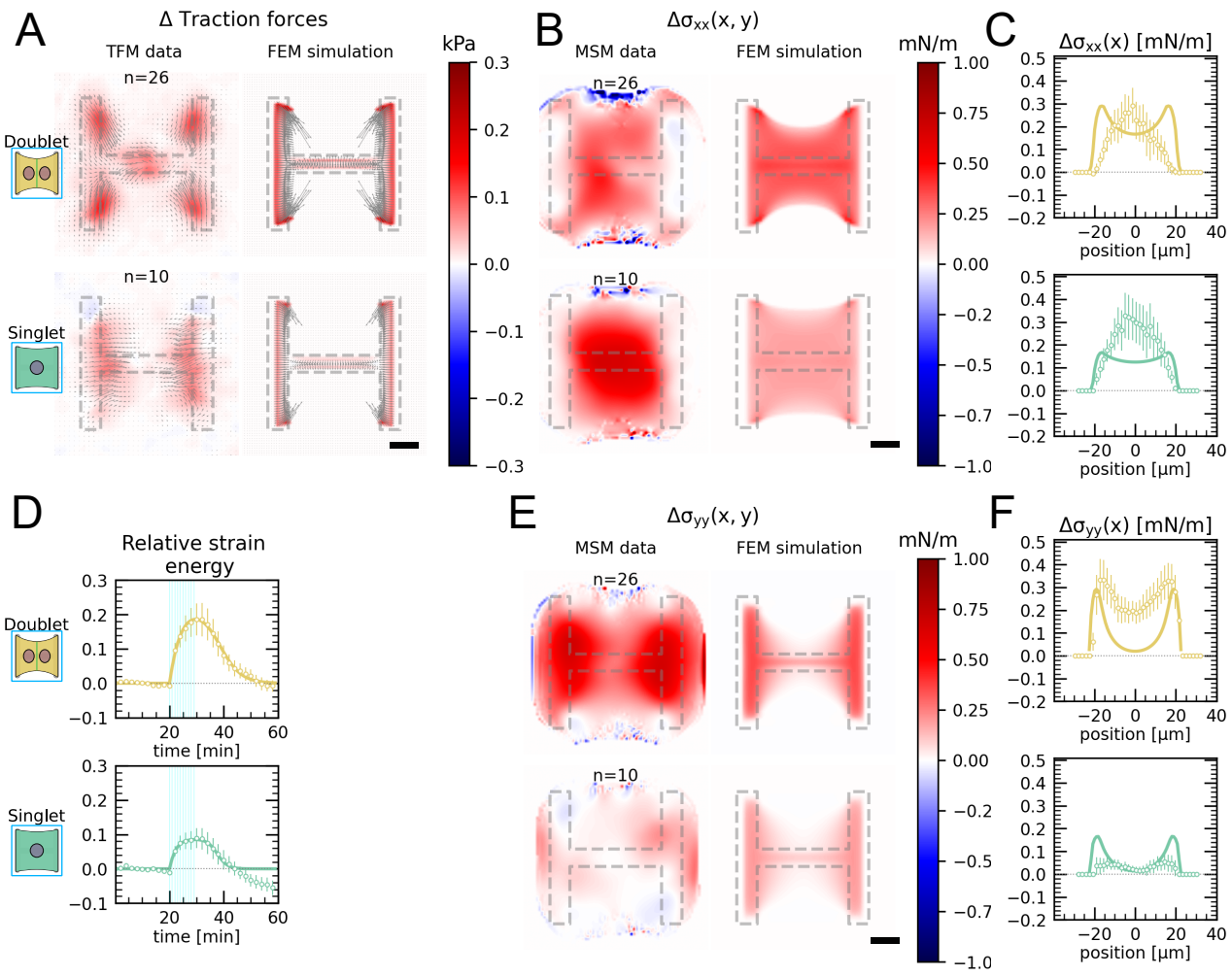

Figure 4: **A** Average traction stress and force map difference before and after photoactivation of cell doublets (top) and singlets (bottom) on H-patterns on the left and corresponding traction stress and force maps from the FEM simulation. **B, E** Average cell stress map difference before and after photoactivation of cell doublets (top) and singlets (bottom) on H-patterns on the left and corresponding cell stress maps from the FEM simulation. **C, F** Average over the y-axis of the maps in B and D. Data is shown as circles with the mean $\pm$ s.e.m., the solid line corresponds to the FEM simulations. **D** Relative strain energies of doublets (top) and singlets (bottom) with global photoactivation. One frame per minute was acquired for 60 minutes and cells were photoactivated with one pulse per minute for 10 minutes between minute 20 and minute 30. Strain energy curves were normalized by first substracting the individual baseline energies (average of the first 20 minutes) and then dividing by the average baseline energy of all cell doublets/singlets in the corresponding datasets. Data is shown as circles with the mean $\pm$ s.e.m and the result of an FEM simulation is shown as a solid line. All scale bars are $10\,\mu\mathrm{m}$ long.

References

[1] C.M. Edwards and U.S. Schwarz. Force localization in contracting cell layers. *Physical review letters*, 107(12):128101, 2011.

[2] S. Banerjee and M.C. Marchetti. Contractile stresses in cohesive cell layers on finite-thickness substrates. *Physical review letters*, 109(10):108101, 2012.

[3] Medhavi Vishwakarma, Jacopo Di Russo, Dimitri Probst, Ulrich S Schwarz, Tamal Das, and Joachim P Spatz. Mechanical interactions among followers determine the emergence of leaders in migrating epithelial cell collectives. *Nature communications*, 9(1):1–12, 2018.

[4] Jana Hanke, Dimitri Probst, Assaf Zemel, Ulrich S Schwarz, and Sarah Köster. Dynamics of force generation by spreading platelets. *Soft Matter*, 14(31):6571–6581, 2018.

[5] Arnab Saha, Masatoshi Nishikawa, Martin Behrndt, Carl Philipp Heisenberg, Frank Jülicher, and Stephan W. Grill. Determining Physical Properties of the Cell Cortex. *Biophysical Journal*, 110(6):1421–1429, 2016.

[6] M.S. Alnaes, J. Blechta, J. Hake, J. Johansson, B. Kehlet, A. Logg, C. Richardson, J. Ring, M.E. Rognes, and G.N. Wells. The fenics project version 1.5. *Archive of Numerical Software*, 3(100):9–23, 2015.

[7] Aaron F Mertz, Shiladitya Banerjee, Yonglu Che, Guy K German, Ye Xu, Callen Hyland, M Cristina Marchetti, Valerie Horsley, Eric R Dufresne, et al. Scaling of traction forces with the size of cohesive cell colonies. *Physical review letters*, 108(19):198101, 2012.

[8] P.W. Oakes, S. Banerjee, M.C. Marchetti, and M.L. Gardel. Geometry regulates traction stresses in adherent cells. *Biophysical journal*, 107(4):825–833, 2014.

[9] Josephine Solowiej-Wedderburn and Carina Dunlop. Sticking around: Optimal cell adhesion patterning for energy minimization and substrate mechanosensing. *bioRxiv*, 2020.

[10] Christophe Geuzaine and Jean-François Remacle. Gmsh: A 3-d finite element mesh generator with built-in pre-and post-processing facilities. *International journal for numerical methods in engineering*, 79(11):1309–1331, 2009.

[11] Ilka B. Bischofs, Franziska Klein, Dirk Lehnert, Martin Bastmeyer, and Ulrich S. Schwarz. Filamentous network mechanics and active contractility determine cell and tissue shape. *Biophysical Journal*, 95(7):3488–3496, 2008.

[12] Roy Bar-Ziv, Tsvi Tlusty, Elisha Moses, Samuel A. Safran, and Alexander Bershadsky. Pearling in cells: A clue to understanding cell shape. *Proceedings of the National Academy of Sciences of the United States of America*, 96(18):10140–10145, 1999.

[13] Wim Pomp, Koen Schakenraad, Hayri E. Balcloğlu, Hedde Van Hoorn, Erik H.J. Danen, Roeland M.H. Merks, Thomas Schmidt, and Luca Giomi. Cytoskeletal Anisotropy Controls Geometry and Forces of Adherent Cells. *Physical Review Letters*, 121(17):1–5, 2018.

[14] Luca Giomi. Contour Models of Cellular Adhesion. *Advances in Experimental Medicine and Biology*, 1146:13–29, 2019.

[15] Céline Labouesse, Alexander B. Verkhovsky, Jean Jacques Meister, Chiara Gabella, and Benoît Vianay. Cell shape dynamics reveal balance of elasticity and contractility in peripheral arcs. *Biophysical Journal*, 108(10):2437–2447, 2015.

[16] Kenichi Kanatani and Prasanna Rangarajan. Hyper least squares fitting of circles and ellipses. *Computational Statistics & Data Analysis*, 55(6):2197–2208, 2011.

[17] P. Guthardt Torres, I. B. Bischofs, and U. S. Schwarz. Contractile network models for adherent cells. *Physical Review E - Statistical, Nonlinear, and Soft Matter Physics*, 85(1):1–13, 2012.

[18] Shinji Deguchi, Toshiro Ohashi, and Masaaki Sato. Tensile properties of single stress fibers isolated from cultured vascular smooth muscle cells. *Journal of biomechanics*, 39(14):2603–2610, 2006.

5.2 Protocols

Alvéole patterning protocol

1. Clean coverslip with nitrogen gun and plasma clean it in air atmosphere for 1 min
2. Incubate on parafilm in 70 µL of 0.05 – 0.1% PLL for 30-60 min (I did 0.1% and 60 min last time)
3. Rinse with deionized water (with a squirt bottle) and either let it dry on a kimwipe or dry with a nitrogen gun (I generally use the nitrogen gun because it's faster)
4. Make a solution of PEG-SVA in HEPES 8<pH< 8,5 at 50 mg/mL. The solution has to be prepared right before use, since the half-life of the SVA ester in that pH is only about 10 min. Also always check the pH of the HEPES, since it drifts over time. Adjust the pH with NaOH or HCl if needed.
5. Incubate on parafilm in 70 µL of the PEG-SVA solution.
6. Rinse with deionized water (with the squirt bottle) and either let it dry on a kimwipe or dry with a nitrogen gun (I generally use the nitrogen gun because it's faster).
7. These coverslips can now be stored dry and should be stable for at least a week (no personal experience with that)
8. Mix 3 µL of PLPP-gel in 57 µL of 96% ethanol and let it dry for around 10 minutes on a shaker. The actual drying time depends on the temperature, humidity, air flow etc. If the gel is not dry, generally you can see it moving when you hold it against the light
9. Calibrate your PRIMO if necessary, focus on the coverslip, place your patterns and start the patterning process. The dose for illumination should be between 20 and 30 mJ/mm²
10. Rinse with deionized water (with the squirt bottle) and either let it dry on a kimwipe or dry with a nitrogen gun (I generally use the nitrogen gun because it's faster)
11. Prepare a dilution of your favourite protein. I generally use 20 µg/mL fibronectin with 20 µg/mL fluorescent fibrinogen dissolved in 100 mM Sodium Bicarbonate
12. Incubate your coverslip in 70 µL of protein solution on parafilm for 30 min
13. To remove the coverslip after incubation, pour a bunch of deionized water on top of the coverslips. The coverslips should not dewet with the protein solution, as this might deposit a thin layer of protein outside of the patterns.
14. Rinse with deionized water (with the squirt bottle) and either let it dry on a kimwipe or dry with a nitrogen gun (I generally use the nitrogen gun because it's faster).
15. Store in buffer solution for up to 48 h (the shorter the better).

MICROPATTERNING AND TFM GEL PREPARATION

Created by Artur Ruppel (artur.ruppel@univ-grenoble-alpes.fr) **on February 2, 2021**
Edited by Martial Balland (martial.balland@univ-grenoble-alpes.fr) on February 2, 2021

Last edit December 7, 2021

Protocol purpose:
This protocol describes how to make cell adhesive micropatterns on polyacrylamide gels for TFM experiments.

PROTOCOL

This protocol has been adapted from Vignaud, Ennomani, and Théry 2014.

Step 1 [Time required 0.5 h]

Preparation of aliquots

- Prepare PLL-g-PEG aliquots of 0.1 mg/mL in HEPES buffer of 10 mM and pH adjusted to 7.1. Filter through 200 nm filter and store in 500 µL aliquots at -20 °C. A thawed aliquot can be kept at 4° C for up to a week.
- Prepare a premix of acrylamide and bis-acrylamide. See Tse and Engler 2010 for the proportions needed to achieve the desired gel rigidity. Store it at 4°C for up to a year or even two.
- Prepare aliquots of a couple of mg Ammonium phosphate sulfate (APS). Ideally you store the aliquots as powder in a desiccator at 4°C, as APS is very hygroscopic. It is also possible to store them as a 10% w/v solution in water at -20°C though, if a desiccator is not available. APS is extremely unstable in solution and should be used in the half hour after thawing/preparing and been thrown away after.
- Prepare a 100 mM Sodium Bicarbonate solution (e.g. 0.42 g in 50 mL deionized water) to dilute the fibronectin and fluorescent fibrinogen in. You can also use this as an alternative to PBS to store your gels in for a short while (2 or 3 days max.).

Step 2 [Time required 0.5 h]

Preparation of silanized coverslips

- This glass treatment is necessary to ensure a good attachment between the polyacrylamide (PAA) gel and the underlying coverslip.
- As silane solutions are very toxic, this process should be performed under a chemical hood with appropriate user protection, at least the silane solution should not leave the hood outside of a hermetically closed container.
- Mix in a 15 ml tube: 5ml of 100 % alcohol, 161 µl of 10 % acetic acid and 18,5 µl of bind silane.
- Put 100-200 µl of silane solution on each coverslip.
- After 3-4 minutes wipe each coverslip with a kimwipe. (Do not let the coverslip dry before wiping it).

EQUIPMENT

Fume hood | Terahertz plasma | Deep UV oven | Ultrasonicator | Nitrogen gun (optional) | Photomask | 32 mm Coverslips | Coverslip holder | Petri dishes | Fluorescent nanobeads

CHEMICALS

Acrylamide | Bis-Acrylamide | Ammonium Phosphate Sulfate (APS) | Tetramethylethylenediamine (TEMED) | PLL-g-PEG | DPBS | 99 % Ethanol | 10 % Acetic acid | Bind Silane | 100 mM Sodium Bicarbonate | 10 mM, pH 7.4 HEPES | (Fluorescent) protein of interest

DANGERS

Chemicals
Physical
Environmental

PROTECTIVE GEAR

Laboratory Coat | Gloves

- Leave for 10 minutes to make sure the coverslips are dry and store them at room temperature in a petri dish. Seal the petri dish with parafilm to avoid air dust from getting in.
- This treatment is quite stable over few weeks so you can do many coverslips at the same time.
- Alternatively you can prepare a beaker with 50 mL silane solution, load a bunch of coverslips in a coverslip rack and dip them in the beaker. After taking them out, let the coverslips incubate for a few minutes, rinse them in a beaker full of 70% ethanol and then dry carefully with a nitrogen gun.

Step 3 [Time required 0.75 h]

Passivation of coverslip with PLL-g-PEG

- Clean 32x0,17mm coverslip with isopropanol. Use a nitrogen air gun to dry before the plasma activation.
- Activate/clean the coverslip in a plasma cleaner at 0.4 mbar with air atmosphere for 1 min.
- Put a drop of PLL–g-PEG solution (25 mL/cm² - 70 µl) on parafilm.
- Take each coverslip with tweezers and flip it on the droplet in order to have the plasma-activated side of the coverslip facing the pLL–PEG solution and let incubate in the dark for 30 min.
- At the end of the incubation, lift the coverslips carefully without scratching the coating.
- Clean with a squirt bottle of deionized water. The PLL–g-PEG side should be very hydrophobic and the water should pearl down easily. That property allows you to distinguish the functionalized side from the other if necessary. Dry coverslip completely with the nitrogen gun or just let it dry on a kimwipe.

Step 4 [Time required 0.25 h]

Mask treatment

- It is of great importance for the quality of the micropatterns that the used photomask is very clean. The micropatterning protocol itself leaves resistent organic traces on the mask, so it is important to thoroughly clean it before and after use.
- Wash the mask with hot water and soap. Use your gloves gently rubbing on the surface.
- Rinse the mask with plenty of deionized water and dry the mask with nitrogen gun.
- Rest the mask on a kimwipe and pour isopropanol on it. Use another kimwipe to vigorously rub the surface of the mask and make sure it is clean.
- Rinse the mask with isopropanol and dry it thoroughly with a nitrogen gun.
- Put the mask in a plasma cleaner and pull a vacuum. If you didn't dry the mask properly, it might break when pulling the vacuum. F
- Flush the chamber with oxygen for 5 min..
- Pull a vacuum again and stabilize the pressure at 0.4 mbar.
- Activate the plasma for 10 min. The plasma should have a very faint white color.
- If no plasma cleaner sufficiently big is available, you can use electroscrub to clean the mask (http://electroscrub.com/)

Step 5 [Time required 0.75 h]

Deep UV burning and protein coating

- Heat up the UV lamp for at least 5 min to make sure the light intensity reached a stable level.

NOTES

- Rest the mask on a horizontal surface, chrome facing up
- Put 10 µl of water on the region of interest on the mask. Flip the coverslip on the drop of water, PLL-g-PEG side facing the water. Put a kimwipe on top and take a flat surface (e.g. a big petri dish) to press excess water out. The goal is to have the coverslip "glued" tightly to the mask without having any bubbles. Make sure the mask doesn't accumulate dust on it's surface between cleaning and this step.
- Put the entire setup in the warmed up UV lamp. Flip the mask to have the coated side away from the UV source. Expose to UV for 5 min.
- Prepare protein coating solution: We use a solution of 20 µg/mL of fibronectin diluted in 100 mM Sodium Bicarbonate.
- After 5 min UV-light exposition, pour deionized water to help detaching the coverslips from the mask.
- You can use a scalpel or tweezers (ideally with teflon tips) When detaching the coverslips from the photomask, but be very careful (!) to not damage the mask.
- Put a drop of protein solution on parafilm (70 µl for 32 mm coverslips) and put the functionalized side of the coverslip on the droplet. Protect from light and let it incubate for 30 min.

Step 6 [Time required 0.75 h]

Transfer of micropatterns to PAA gel

- TEMED, APS, Acrylamide and Bisacrylamide are harmful to your health. Handle with care under a chemical hood wearing personal protective equipment (lab coat and gloves).
- Put 165 µl of Acrylamide + Bisacrylamide premix of your desired rigidity in a vial and add nanobeads. 165 µl is good for three coverslips. If you need more, just make multiples of this. It is not advised to do more then three coverslips at a time, since the PAA mix can polymerize very quickly and you might have trouble finishing the process in time. The quantity of beads has to be adapted to your experiment and depends mostly on the used magnification. 0.5 µl are good for 60x. You can prepare a 1:10 dilution of your beads in deionized water to make pipetting easier. Vortex the bead aliquot before using it and after mixing it with the PAA.
- Sonicate for 3 min to destroy any bead aggregates that could have formed during the storage.
- Prepare the TEMED and APS and silanized coverslips under the hood.
- Take a petri dish and put parafilm on top. Add 10 µl of water for each of your coverslips and put your coverslips on top with the functionalized surface facing UP. Transport to the hood.
- You will add TEMED and APS solution to the acrylamide with the following proportions: 1 µL of TEMED and 1 µL of APS 10 % for 165 µL of acrylamide solution. You should proceed as fast as possible in the next steps, so make sure that the pipettes are already adjusted to the needed volumes and that the TEMED, APS and silanized coverslips are readily available.
- First, add TEMED to the acrylamide solution, briefly but vigorously mix.
- Second, add APS solution to the acrylamide solution, briefly but vigorously mix.
- Put a drop of 47 µl of the acrylamide polymerization mix on coverlips (stuck on parafilm thanks to the water).
- Slowly place the silanized coverslip on top while taking care to avoid bubbles (place silanized side on polyacrylamide).
- Let polymerization proceed for 30 min. You can turn the hood off.
- After incubation time is over, pour deionized water on the coverlips and wait for 5 minutes. This will make the coverslips a little easier to detach since water will enter in between the two coverslips.

NOTES

- Detach the two coverslips using a scalpel. Be extremely careful here, it is very easy to break the coverslips and ruining all your work. Find the edge of your coverslip sandwich with the side of the scalpel, not with the tip and patiently go around the sandwich to let water flow in. Don't try to lever the coverslips apart and don't try to shear them against each other. Also stay very close to the border of the coverslip as to not damage the gel. If you're having a hard time doing this, you can use two different sizes of coverslips to make it easier to find the edge.
- Store in PBS or Sodium Bicarbonate for 2-3 days.

References

- Vignaud, Timothée, Hajer Ennomani, and Manuel Théry (2014). "Polyacrylamide Hydrogel Micropatterning". In: *Methods in Cell Biology* 120, pp. 93–116. ISSN: 0091679X. DOI: 10.1016/B978-0-12-417136-7.00006-9.
- Tse, Justin R. and Adam J. Engler (2010). "Preparation of hydrogel substrates with tunable mechanical properties". In: *Current Protocols in Cell Biology* SUPPL. 47, pp. 1–16. ISSN: 19342500. DOI: 10.1002/0471143030.cb1016s47.

NOTES

IMMUNOFLUORESCENCE STAINING

Created by Artur Ruppel (artur.ruppel@univ-grenoble-alpes.fr) **on January 6, 2021**
Edited by Martial Balland (martial.balland@univ-grenoble-alpes.fr) on January 6, 2021

Last edit December 7, 2021

Protocol purpose:
This protocol describes how to fix cells and stain for your favorite proteins via immunofluorescence staining.

PROTOCOL

Step 1 [Time required 0.5 h]

Preparation

- Prepare a sample that you want to stain.
- Prepare Blocking Buffer. I use 1% BSA + 50 mM Glycin in TBS.
- Prepare TBS.

Step 2 [Time required 0.5 h]

Fixing and permeabilizing the cells

- Wash your cells with TBS.
- Add 1 mL of PFA (for 32 mm petri dishes), incubate for 10 minutes. This will fix the cells. This step should be performed under a fume hood, as PFA is volatile and harmful for your health.
- Remove PFA and discard in the proper trash container. Add Trition, incubate for 5 minutes. This will permeabilize the cell membrane.
- Wash 2 times with TBS.

Step 3 [Time required 3.5 h]

Incubation of first antibody

- Add blocking buffer, incubate for 1h. This will saturate nonspecific binding sites to increase specificity of primary antibody binding.
- Prepare the proper dilution of your primary antibody in blocking buffer. I used 1:200 for E-Cadherin (Ref: 14-3249-82) staining and 1:400 for Vinculin (Ref: V9131).
- (Optional) Centrifuge antibodies for 5 minutes at 5000 rpm or filter through 200 nm filter to remove aggregates. Careful! Some volume always gets lost when filtering (100 µL).
- Remove the blocking buffer and replace with antibody solution. Incubate (upside down on parafilm to save material) for 2 h. You can also incubate over night at 4° C to achieve potentially better results.
- Wash 3 times with TBS for 10 minutes each.

EQUIPMENT

Fume hood | Cell culture dish | Ultracentrifuge (optional) | Syringe and 200 nM filter (optional) | Glass slides | Mounting medium

CHEMICALS

1X TBS | 0.1 % Triton | 4% Paraformaldehyde (PFA) | Primary Antibody | Secondary Antibody | Direct Staining reagent (e.g. DAPI) | Blocking Buffer

DANGERS

Chemicals
Physical
Environmental

WARNINGS

PFA is harmful to your health.

PROTECTIVE GEAR

Laboratory Coat | Gloves

Step 4 [Time required 1.5 h]

Incubation of secondary anibody

- Prepare the proper dilution of your secondary antibody. I used 1:1000 for anti-rat (Ref: SAB4600186) and 1:1000 for anti-mouse (Ref: A-21235).
- Remove TBS and add secondary antibody solution. Incubate (upside down on parafilm to save material) for 1 h.
- Wash 3 times with TBS for 10 minutes each.

Step 5 [Time required 0.5 h]

Mounting on glass slides

- Clean glass slides with Ethanol and lab paper.
- Add 40 µL of mounting medium to your glass slide.
- Carefully put your coverslip on the glass slide with the cell side touching the mounting medium. This will prevent the fluorophores to bleach over time and preserve your sample. Use tweezers and try to avoid bubble formation.

NOTES